Vortex Fluidics Manipulation of Nanocarbon

By

Kasturi Vimalanathan (MSc Chemistry)

This thesis is presented for the degree of

Doctor of Philosophy of Chemistry

School of Chemical and Physical Sciences

Discipline of Chemistry

Flinders University

September 2016

SUMMARY

Carbon nanomaterials of various dimensionalities have gained a unique place in nanotechnology owing to their explicit physical and chemical properties. These include excellent optical and thermal properties, electrical conductivity and high mechanical strength. Such materials have a myriad of applications including for energy storage, sensors, drug delivery, field emission devices, electronic devices, as high strength materials and biomedical engineering. Carbon based nanomaterials have been widely used for decades in device and sensing technology and other related fields, but only recently have biological applications emerged. However, there are concerns about the toxicity of these nanomaterials, and exquisitely controlling their morphology, shapes and size is pivotal to harness their full potential. Following advances in fabrication and characterization techniques, graphene has emerged as a building block for other carbon nanomaterials other than nanodiamond, which include carbon nanotubes of single to multiple shells, fullerene C_{60} and C_{70} and carbon nanoonions.

Conventional processing methods have dominated the fabrication of carbon nanomaterials. This includes traditional “top down” and “bottom up” approaches which can involve long and tedious processing, the use of toxic and harsh chemicals, and the use of surface active molecules and chemical stabilizers. Although the methods can be high yielding and offer great opportunities in the market place, there are major concerns primarily around the high cost of fabrication, the generation of waste streams, high energy usage and the requirement for extensive down stream processing.

The key focus of this thesis is creating a paradigm shift in nanoscience, employing the use of process intensification as an alternative strategy towards the fabrication and manipulation of novel forms of carbon material at the nanoscale level. The research potentially hails a new frontier to the fabrication of different new carbon nanoforms which incorporate green chemistry metrics and is likely to create opportunities towards industrial applications. While addressing the issue of scalability beyond generating research quantities of carbon nanoforms, the ability to unequivocally manipulate high tensile carbon nanomaterials in particular poses a number of challenges. This includes the use of toxic organic chemicals, long and tedious processing times and the use of surfactant, and indeed overcoming these in

general is potentially a Holy Grail in material science.

With the limitations of traditional batch processing, the synthesis of nanocarbon potentially benefits from innovation in using novel energy efficient processing platform with controllable operating conditions. Recently the vortex fluidic device (VFD), as a microfluidic platform with dynamic thin films, has been developed as a versatile continuous flow processor. It has a number of novel and facile capabilities including controlling self assembly processes, and the fabrication and growth of carbon nanomaterials with distinct control over the morphology, shape and size of the nanostructures.

This thesis focuses on advancing the applications of the VFD in nanocarbon technology, specifically in fabricating carbon nanomaterials based on carbon nanotubes, fullerenes C_{60} and graphene. The controllable mechanoenergy within dynamic thin films in the VFD has been used to fabricate different forms of nanocarbon, with potential for a wide range of applications, from device technology to drug delivery, with a view of transferring the technology to the market place.

The thesis introduces the different forms of carbon nanomaterials and the extent of research developments in the area. The method of process intensification utilized to manipulate different carbon nanomaterials, namely vortex fluidic device (VFD) will be described. The research established that the VFD is effective for slicing carbon nanotubes in a controlled way while irradiated with a pulsed laser operating at 1064 nm wavelength, as a process incorporating green chemistry metrics, including scalability. In addition, the VFD was effective in fabricating toroidal arrays of single walled carbon nanotubes, the formation of self assembled arrays of fullerene C_{60} in the form of nanotubules which are superior sensing material for detecting small molecules, and the direct exfoliation of graphene into graphene scrolls. The extent of advances made in this research, in filling gaps in the scientific arena will be discussed.

TABLE OF CONTENTS

LIST OF FIGURES

LIST OF SUPPLEMENTARY FIGURES

ABBREVIATIONS

AFM	Atomic force microscopy
AsF_5	Arsenic pentafluoride
BZ	Brillouin zone
Br_2	Bromine
CVD	Chemical vapour deposition
CNT	Carbon nanotube
CNH	Carbon nanohorn
CNO	Carbon nanoonion
CNS	Carbon nanoscroll
CNF	Carbon nanofibre
DMF	N,N-dimethylformamide
DWCNT	Double walled carbon nanotube
DNA	Deoxyribonucleic acid
DGU	Density gradient ultracentrifugation
fcc	Face centred cubic
FETs	Field effect transistors
FWHM	Full width of half maximum
GO	Graphene oxide
HRTEM	High resolution transmission electron microscopy
HT-SDP	High temperature spinning disc processor
h-BN	Hexagonal boron nitride
hcp	Hexagonal close packed
HiPCO	High pressure CO disproportionation
ID	Inner diameter
$FeCl_3$	Iron (III) chloride
GPa	Gigapascal
KFM	Kelvin force microscopy
LLIP	Liquid liquid interfacial precipitation
LPE	Liquid phase exfoliation
MWCNT	Multiwalled carbon nanotube
MLG	Multilayer graphene

MFM	Magnetic force microscopy
MoS_2	Molybdenum disulfide
NMP	N-methyl pyrrolidone
NMR	Nuclear magnetic resonance
Nd:YAG	Neodymium-doped yttrium aluminium garnet
NIR	Near infrared
OD	Outer diameter
1D	One dimensional
PI	Process intensification
PEG	Poly(ethylene)glycol
QCM	Quartz crystal microbalance
RTP	Rotating tube processor
RBM	Radial breathing mode
SDP	Spinning disc processor
SAED	Selected area electron diffraction
SWCNT	Single walled carbon nanotube
SEM	Scanning electron microscopy
SANS	Small angle neutron scattering
SCs	Solar cells
WS_2	Tungsten disulfide
TEM	Transmission electron microscopy
TGA	Thermogravimetric analysis
TPa	Terapascal
2D	Two dimensional
UV-Vis	Ultraviolet visible spectroscopy
QD	Quantum dot
VFD	Vortex Fluidic Device
XRD	X-ray powder diffraction
0D	Zero dimensional

ACKNOWLEDGEMENTS

I wish to extend my gratitude to a number of people that have made this research a success. Firstly, I would like to thank my supervisor, Professor Colin Raston, for believing in me and being a great mentor. He has taught me that the key to a successful career is passion and hard work and for that I am sincerely grateful. During the last few years, his wisdom, immense knowledge and optimism has been a great motivation to me. He has created the foundation on which I have been able to build my research career on.

I would also like to thank my co-supervisors, Dr. Jason Gascooke and Professor Warren Lawarance for their guidance and encouragement. I would like to record my gratitude to Dr Jason Gascooke for guiding and working with me especially during the first few months of my PhD career, in particular with the design of the experiments. I appreciate the fact that he believed in my ideas and undoubtedly, the success in the outcome was achieved because I had the chance to work with such an inspiring team of colleagues.

To all the members of the Raston Research Group, not forgetting the ones who have embarked on a different path to pursue their respective careers, I would like to express my deepest appreciation. I believe that no research is a success without a great team. I would like to extend particular appreciation to Dr Ramiz Boulos for being a remarkable friend, colleague and mentor. I gained so much knowledge and skills from Dr Xianjue Chen during the tenure of my research career and for that my heartfelt gratitude goes to him.

I would like to also thank Dr Christopher Gibson for all his support and constant guidance particularly with the atomic force microscopy and Raman analysis. It has certainly helped me with a number of experiments and data analysis. A special thanks to Bob Northeast and Andrew Dunn from the faculty workshop for constantly solving the technical problems that surfaced time and again.

A big part of this research would not have been possible without keen collaborators from a number of local and international universities, most importantly Associate Professor Harshita Kumari for all the SANS characterisations, Dr Rekha Shrestha and Professor Jin Zou. I wish to extend my special thanks to Professor Tomonobu Nakayama for providing me with a

fellowship scholarship at the National Institute for Materials Science in Japan.

Last but not least, I am truly grateful to my parents and my sisters for truly believing in me and for providing me with a great support system. This thesis would not have been close to possible without their constant support and encouragement. I would like to thank them for being so patient and constantly reminding me to be proud of myself and everything that I have achieved thus far. I am truly blessed to be surrounded by so much love.

DETAILS OF PUBLICATIONS

JOURNAL ARTICLES

1 **K. Vimalanathan** and C.L. Raston, Controlling the fabrication of nanocarbon using dynamic thin films, **2016,** invited review article to be submitted to *Advanced Materials Technologies*

Author contributions: KV and CLR wrote and finalized the manuscript

2 **K. Vimalanathan**, R.G. Shrestha, Z. Zhang, J. Zou, T. Nakayama and C.L. Raston, Surfactant-free fabrication of fullerene C_{60} nanotubules under shear, **2016,** under review

Author contributions: KV, RGS and CLR designed the research. KV, RGS, ZZ performed 85%, 10% and 5% of the experimentations respectively. KV, RGS, JZ, TN and CLR finalised the manuscript.

3 **K. Vimalanathan**, J.R. Gascooke, I.S Martinez, N. Marks, H. Kumari, C.J. Garvey, J.L Atwood, W.D. Lawrance and C.L. Raston. Fluid dynamic lateral slicing of high tensile strength carbon nanotubes, *Sci. Rep.,* 2016, 6:22865

Author contributions: KV, JRG and CLR designed the research. KV, JRG, ISM, NM, HK, CJG performed 75%, 5%, 5%, 5%,5%, 5% of the experimentations respectively. KV, ISM, NM, HK, JLA, WDL and CLR finalized the manuscript.

4 **K. Vimalanathan**, X. Chen and C.L. Raston, Shear induced fabrication of intertwined single walled carbon nanotube rings, *Chem Commun.,* 2014, 50, 11295 (Cover illustrated).

Author contributions: KV and CLR designed the research. KV and XC performed 95% and 5% of the experimentations respectively. KV and CLR finalised the manuscript

5 M.H. Wahid, U.H. Stroeher. E. Eroglu, X. Chen, **K. Vimalanathan**, C.L. Raston and R.A Boulos, Aqueous based synthesis of antimicrobial decorated graphene, *J. Colloid and Interface Science*, 2015, 444, 88-96.

Author contributions: All authors designed the research. MHW, UHS, EE XC and VM performed 55%, 15%, 10%, 10% and 10% of the experimentations respectively. MHW, UHS, EE, KV and CLR finalised the manuscript.

6 P. Eggers, E. Eroglu, T. Becker, X. Chen, **K. Vimalanathan**, K.A. Stubbs, S.M. Smith and C.L. Raston, Nitrate uptake by *p*-phosphonic acid or p-(trimethylammonium) methyl calix[8] arene stabilized laminar materials, *RSC Adv.,* 2014, 4, 48348-48352.

Author contributions: PE, EE and CLR designed the research. PE performed 40% of the experimental, and EE, TB, XC and KV and VM each performed 12% of the experimentations. PE, EE, TB, KV, KAS and CLR finalised the manuscript.

CONFERENCE ABSTRACTS AND ORAL PRESENTATIONS

Conference Abstracts

Oral Presentations

1 **K. Vimalanathan**, J.R. Gascooke, I.S Martinez, N. Marks, H. Kumari, C.J. Garvey, J.L Atwood, W.D. Lawrance and C.L. Raston, *Fluid dynamic lateral slicing of high tensile strength carbon nanotubes,* International Conference for Nanoscience and Nanotechnology (ICONN), Canberra, **2016.**

2 **K. Vimalanathan**, J.R. Gascooke, I.S Martinez, N. Marks, H. Kumari, C.J. Garvey, J.L Atwood, W.D. Lawrance and C.L. Raston, *Fluid dynamic lateral slicing of high tensile strength carbon nanotubes,* International Chemical Congress of Pacific Basin Societies (PACIFICHEM), Honolulu, Hawaii, **2015.**

3 **K. Vimalanathan**, J.R. Gascooke, I.S Martinez, N. Marks, H. Kumari, C.J. Garvey, J.L Atwood, W.D. Lawrance and C.L. Raston, *Fluid dynamic lateral slicing of high tensile strength carbon nanotubes,* Advanced Materials and Nanotechnology Conference (AMN-7), Nelson, New Zealand, **2015.**

4 **K. Vimalanathan**, J.R. Gascooke, I.S Martinez, N. Marks, H. Kumari, C.J. Garvey, J.L Atwood, W.D. Lawrance and C.L. Raston, *Fluid dynamic lateral slicing of high tensile strength carbon nanotubes,* Royal Australian Chemical Institute (RACI) National Congress, **2014.**

5 **K. Vimalanathan**, X. Chen and C.L. Raston, Shear induced fabrication of intertwined single walled carbon nanotube rings, OzCarbon conference, Melbourne, Australia, **2013.**

Poster Presentations

6 **K. Vimalanathan**, R.G. Shrestha, Z. Zhang, J. Zou, T. Nakayama and C.L. Raston, Surfactant-free fabrication of fullerene C_{60} nanotubules under shear, Flinders Centre for NanoScale Science and Technology 6th Annual Conference, **2016**

7 **K. Vimalanathan**, J.R. Gascooke, I.S Martinez, N. Marks, H. Kumari, C.J. Garvey, J.L Atwood, W.D. Lawrance and C.L. Raston, *Fluid dynamic lateral slicing of high tensile strength carbon nanotubes,* International Chemical Congress of Pacific Basin Societies (PACIFICHEM), Honolulu, Hawaii, **2015.**

8 **K. Vimalanathan**, J.R. Gascooke, I.S Martinez, N. Marks, H. Kumari, C.J. Garvey, J.L Atwood, W.D. Lawrance and C.L. Raston, *Fluid dynamic lateral slicing of high tensile strength carbon nanotubes,* Flinders Centre for NanoScale Science and Technology 4th Annual Conference, **2014.**

9 **K. Vimalanathan**, J.R. Gascooke, I.S Martinez, N. Marks, H. Kumari, C.J. Garvey, J.L Atwood, W.D. Lawrance and C.L. Raston, *Fluid dynamic lateral slicing of high tensile strength carbon nanotubes,* International Conference of Nanoscience and Nanotechnology (ICONN), Adelaide, South Australia, **2014.**

DECLARATION

I certify that this thesis does not incorporate without acknowledgement any material previously submitted for a degree or diploma in any university; and that to the best of my knowledge and belief it does not contain any material previously published or written by another person except where due reference is made in the text.

Signed……

Date…….

1 INTRODUCTION

1.1 Overview

For decades, the fabrication of carbon nanomaterials, using the "top down" and "bottom up" approach has opened a myriad of possibilities in terms of developing novel and facile methods to afford nanomaterials of various dimensions, sizes and morphologies, to suit specific applications. Nanocarbon materials in different hybridization states (*sp*, sp^2 and sp^3) have exceptional utility in nanotechnology and material science. In addition, covalent bonds between the carbon atoms and its surroundings enable the formation of heterogeneous carbon nanostructures of various dimensionalities, which exhibit explicit properties with potential for a wide range of applications.[1-7] The unique properties of such carbon materials within nano and macro scale dimensions are merely dependent on their atomic structures and molecular interactions, and have bridged the gap between organic and biochemistry. There has been an exponential growth of interest in exploiting their unique properties, depending on dimensionalities, morphology, shape and size, as a basis for electronics, optoelectronics, photovoltaics and sensing applications,[8] as well as for incorporating into lipid bilayers for sensing,[9] for therapeutic applications, [10-12] and more.

In general, traditional batch processing methods have dominated the field of fabricating carbon nanostructures, but they can have limitations, specifically in terms of environmental issues, economical sustainability, scalability and the quality of the material. The ability to precisely control the formation of diverse range of functional materials at the nanoscale length, with scalability incorporated into the processing, is important for future uptake of material in the market place.

This thesis focuses on the novel approach of utilizing process intensification as an alternative route towards the fabrication, sorting and controlling the self assembly of carbon nanomaterials, while incorporating green chemistry metrics. This approach can alleviate some of the processing issues associated with traditional processing methods such as batch to batch variability. The primary goal is to develop new processing strategies in materials science for fabricating nanomaterials, within dynamic thin films under intense shear where the issue of scalability in incorporated into the process. Also considered at the inception of the science are economic and environmental sustainability issues. The thesis will describe in detail various

methods developed, for the “top down” and “bottom up” approach of fabricating carbon nanomaterials of various dimensionalities. This is using benign solvent systems, without the use of chemical stabilizers and toxic and harsh chemicals to avoid additional down stream processing.

1.2 Allotropes of carbon

Historically the discovery of fullerenes in 1985 and carbon nanotubes (CNTs) in 1991 sparked a journey of discovery for other carbon nanomaterials, which have properties beyond those of the classical allotropes of carbon. These include single walled carbon nanohorns,[13,14] carbon nano-onions,[15-17] carbon nanorings,[18-20] cup-stacked carbon nanotubes[21,22] and carbon hybrid materials.[23] Methods for fabricating carbon nanomaterials in general have been extensively studied, in establishing robust syntheses, which is important for their use in down stream applications. Conventional methods of fabricating these materials have evolved, using both the ‘top down’ and ‘bottom up’ approaches, with some advance towards developing more benign processes and addressing the often-vexing question of scalability, although this is rather challenging.

Centuries ago, elemental carbon was known to exist as two natural occurring allotropes, diamond and graphite, with each having different crystal structure and properties. These allotropes of carbon exhibit physical and chemical properties that are dependent on the arrangement of the carbon atoms. Diamond has a tetrahedral arrangement of sp^3 carbon atoms while graphite is comprised of stacked sheets of graphene held together by van der Waals interactions. Each graphene sheet consists of sp^2 carbon atoms arranged in two-dimensional hexagonal lattices. Diamond, the most well-known carbon allotrope, consists of carbon atoms with four valence electrons in each respective carbon atom occupying an sp^3 hybrid orbital. Carbon atoms are covalently bonded to four other carbon atoms forming a three dimensional (3D) tetrahedral lattice of six membered carbon rings. This hexagonal network of carbon atoms defined by covalent bonds contributes to diamond’s unique chemical and physical properties. Unlike graphite, diamond is notable for being an excellent transparent electrical insulator. Diamonds are also widely used as gemstones and in the jewellery industry because of the high refractive index and colourless appearance.[24]

Graphite, a black opaque soft material was the succeeding carbon allotrope identified after diamond. Under ambient temperature and pressure, graphite is the most stable form of carbon material.

Graphite is a layered material where each layer consists of carbon atoms arranged hexagonally in a planar condensed rings system. The carbon atoms in graphite are held together by three in-plane σ-bonds and one out-of-plane π-orbital. The presence of the two types of bonding arises due to the planar hexagonal network of carbon atoms and the weak inter-planar bonding between the multiple layers of graphite, known as van der Waals forces. The different bonding capacities of graphite allow it to exhibit a semi-metallic behaviour with remarkable electrical conductivity properties.[24]

The spark of a new era in allotropes of carbon beyond diamond and graphite began in 1985 with the discovery of fullerene C_{60}.[25,26] Since then other carbon nanomaterials consisting of sp^2 carbon atoms, with properties as exciting as those of C_{60} and other members of the fullerene family such as C_{70}, have been discovered. Of particular importance are the one-dimensional (1D) carbon nanotubes and isolated two dimensional (2D) graphene sheets, which have created new avenues in material science. The physical and chemical interactions of these carbon nanomaterials are determined mainly by their geometrical structure and method of synthesis.

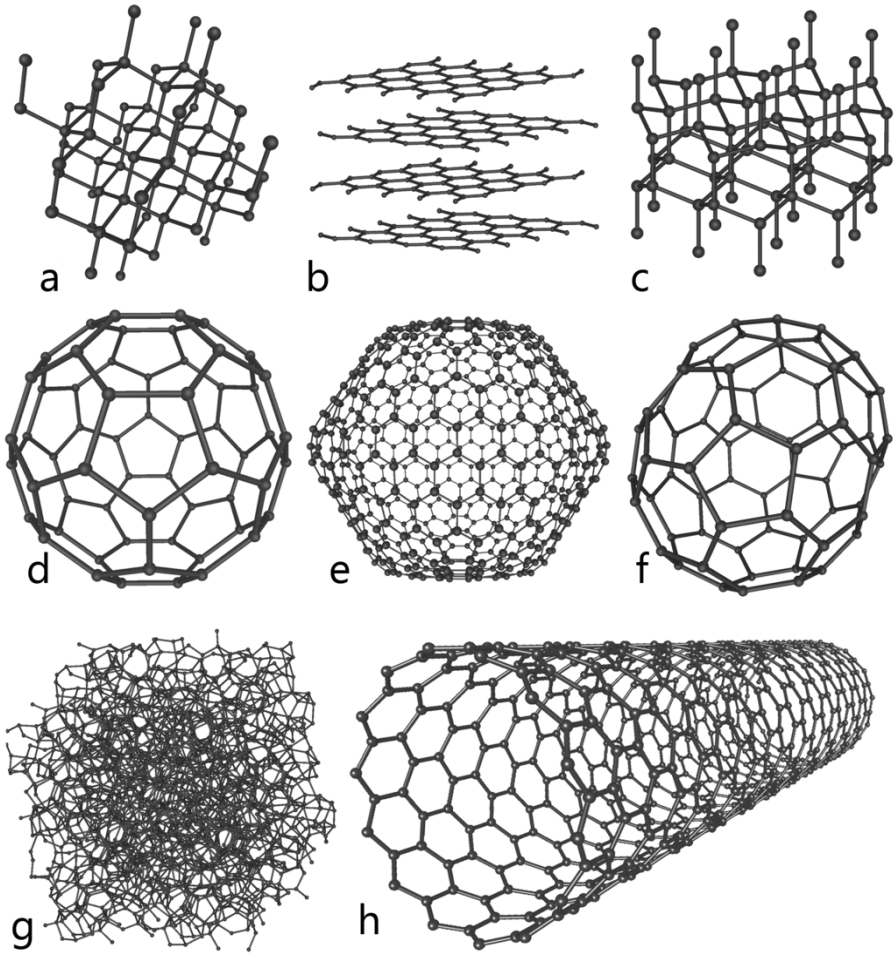

Figure 1 Different allotropes of carbon, (a) diamond, (b) graphite, (c) lonsdaleite, (d) fullerene C_{60}, (e) fullerene C_{540}, (f) fullerene C_{70}, (g) amorphous carbon, (h) single walled carbon nanotube (SWCNT).

1.3 The discovery of new forms of carbon

The quest towards the discovery of other carbon nanoforms beyond diamond and graphite then continued with more extensive understanding of the formation of these carbon-based materials in the bulk phase. This has led to the identification of a range of new carbon materials with exceptional intrinsic properties with diverse potential applications in varied fields. The spark of the new era in carbon technology began in 1985 with the discovery of fullerenes by researchers from Rice University. Thirty years on from the discovery of fullerenes (C_{60}) by Kroto *et al.*,[25] there has been an exponential advancement in discovering other carbon nanomaterials with unusual properties, as exciting as those of fullerenes.

The realisation of new carbon nanostructures, ranging from zero dimensional (0D) fullerenes through to one-dimensional (1D) carbon nanotubes and two dimensional (2D) graphene,

created new avenues of research in material science and allied areas. There have been extensive studies on these nanomaterials, in mapping out their exciting properties, which include excellent thermal, electrical, optical and mechanical properties. Exhibiting these exceptional properties and acquiring high aspect ratios and higher specific surface areas, they show promising capabilities for a plethora of applications. These include use in sensors, photovoltaics, field emission transistors, fuel cells, supercapacitors, composites, biomaterial composites, drug delivery and many others.[5,8-12,27-31]

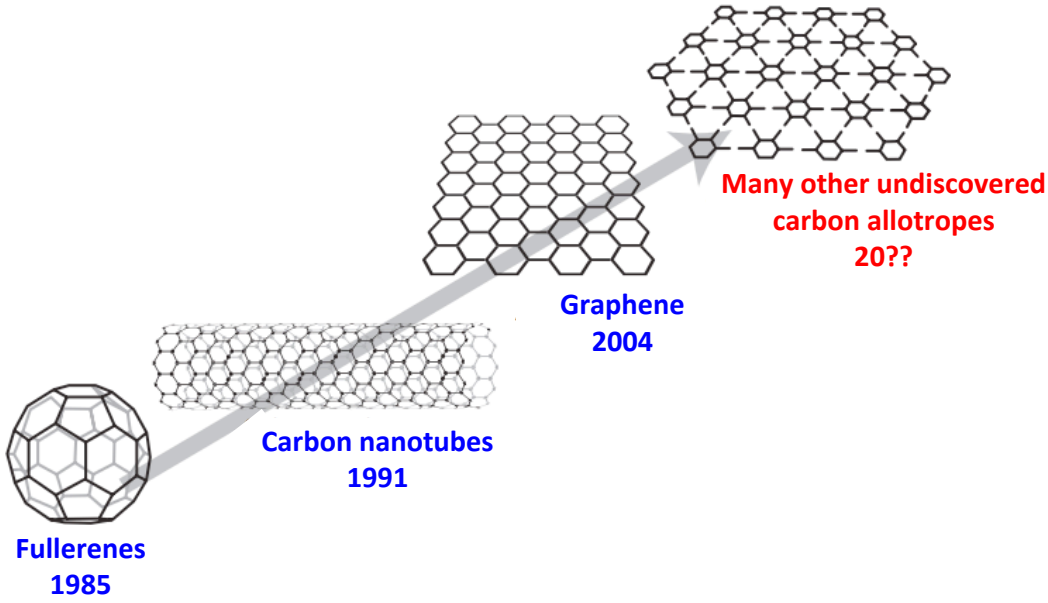

Figure 2 The new era of carbon allotropes which began with the discovery of fullerenes in 1985.[32]

On the nanoscale level, the physical and chemical interactions of these carbon nanomaterials are determined mainly by their geometrical structure and method of synthesis. Conventional batch processing methods have dominated the field of fabricating carbon nanostructures in various morphologies and dimensions for specific applications. For example, the different forms of carbon nanostructures that have been introduced and extensively studied beyond graphite, carbon nanotubes and fullerenes include carbon nanohorns and nanocones,[13,33,34] nanobowls,[35] nanotoroids,[19,20,36] nanotubules,[37,38] 'bamboo' tubes,[39] and many others. The synthetic approaches used can have limitations, in terms of environmental issues, economic sustainability, scalability and the quality of the material. The ability to precisely control the formation of diverse range of functional materials at the nanoscale length, with scalability incorporated into the processing, is important for future uptake in a myriad of applications, including those based on nanocarbon.

2 PROCESS INTENSIFICATION- CONTINUOUS FLOW PROCESSORS

Continuous flow processing can address scalability, as a form of process intensification (PI). This involves developing processing platforms with contrived surface areas with variation in rotational speed, which can provide versatility in equipment design and elevated acceleration environments, allowing the generation of high shear stress within thin films on surfaces with enhanced reactions despite having short reaction times.[40,41] PI can overcome imitations of conventional batch processing, for example, the uneven heat transfer and uneven mixing. With a number of novel carbon nanoforms representing a conceptually new class of nanomaterials, the ability to exquisitely control the size, morphology and dimensions is pivotal. This is possible using PI which can facilitate innovative pathways/methods in materials synthesis while addressing scalability and other green chemistry metrics for reducing negative impacts on the environment and ultimately translation of the processing into industrial applications. A number of continuous flow processors have been developed based on dynamic thin films for chemical and materials synthesis. These include the spinning disc processor (SDP), the rotating tube processor (RTP) and the more recently developed vortex fluidic device (VFD) (Figure 3), all of which are more versatile than conventional batch processing, and have been used to fabricate a diverse range of nanocarbon materials.

Dynamic thin films formed under centrifugal forces in the SDP and RTP allow exquisite control over the growth of nanoparticles,[42-46] accelerating chemical reactivity and selectivity,[47] drug formulation[48-50] and others.[51-52] Such control relates to the intense shear generated within the thin films, arising from the viscous drag as the liquid accelerates on the surface of a rapidly rotating disc on the SDP or as the liquid whirls along the tube in the RTP. An important feature of the thin films is their high mass and heat transfer. The VFD was developed with the initial design closely related to the horizontally aligned RTP, but with greater versatility than the RTP, and indeed the SDP, having a number of remarkable applications, and processing capabilities not possible using traditional batch approaches.

2.1 Spinning Disc Processor (SDP) and the Rotating Tube Processor (RTP)

The key component of the SDP (Figure 3a) is the horizontally oriented diameter-rotating disc, typically, ≥10 cm in diameter, with controllable speed and feed jets delivering reagents slightly away from the centre of the disc. Centrifugal acceleration generates thin films approximately 1-200 µm thick for operating speeds usually between 300-3000 rotations per minute (rpm). The thin film has a high surface area to volume ratio, which is a pivotal characteristic for favourable interactions between the film and its surroundings, enabling uniform heat transfer throughout the reaction mixture, in contrast to the uneven heating using conventional batch processing. Intense shear forces generated from the rapidly rotating disc creates turbulence and breaks the surface tension of the film, making waves and ripples which contribute to the efficiency of mixing and high heat and mass transfer. The films are also characterized by short residence times, with such times controlled by the size and surface texture of the disc, the viscosity of the liquid used and the flow rates.[40,53-55]

The high shear rates coupled with turbulent micromixing across the thin film have been effective in a number of applications that are inherently difficult using traditional batch methods. This includes free radical polymerization reactions,[56-57] condensation reactions,[58] synthesis and processing of nanoparticles,[42-46,59,60] disassembling hexameric molecules capsules,[55] and controlling chemical reactivity and selectivity.[41,47,61,62] In contrast to the SDP, the RTP (Figure 3b) has control over the residence time for reactions, with intense shear within thin films at high rotational speeds. The RTP has a horizontally aligned rotating tube which also generates intense micro mixing, but in a different way relative to the SDP. For the RTP, liquid swirls along the rapidly rotating tube (300 – 3000 rpm) with the thickness of the film depending on the viscosity of the liquid, the height of a ridge (if any) at the end of the tube and the rotational speed. The RTP allows single to multiple jet feeds to deliver solutions into the rotating tube at one end, slowly forcing the liquid out at the opposite end for collection. The residence time is therefore precisely controlled by the flow rate of each jet feed respectively. Multiple jet feeds in a single pass reaction is difficult using the SDP. The RTP offers major advantages over the SDP, specifically in terms of more precise control of the residence time, with potential for dramatically increasing the efficiency of any synthesis. The residence time of the RTP can be controlled, depending on the flow rates and the length of the tube. Applications of the RTP include biodiesel production,[63] the fabrication and formulation of drugs[48-50] and the decoration of nanorods with quantum dots.[51-52] The SDP and

RTP are effective for chemical synthesis and the fabrication of materials within nanoscale dimensions, but there are limitations. Most notably is that a large volume of liquid is required to achieve a constant shearing consistency within the fluid films, and the high cost of equipment construction. These have been overcome using the VFD.

2.2 The Vortex Fluidic Device (VFD)

The VFD (Figure 3c) is related to the above horizontally aligned RTP, but it has some distinctly different features and capabilities. Indeed, the VFD is effective in overcoming the drawbacks of both the SDP and RTP. The typical VFD has a rapidly rotating borosilicate glass tube, 20 mm in diameter which is opened at one end with rotational speeds ranging from 2000-10000 rpm, and with a variable inclination angle, θ, from 0°to 90°. High shear rates also prevail, which are governed by the rotational speed and inclination angle. The VFD can operate under the so-called confined mode of operation where a finite volume of liquid forms a thin film with high shear at high rotational speeds. Shearing in the thin films arises from the interplay between centrifugal and gravitational forces, and under the confined mode, Stewartson/Ekman layers form as the liquid flows upwards at the internal surface of the rotating tube and downwards close to the liquid surface, parallel to the axis of rotation of the rapidly moving fluid.[64,65,66,67] The VFD is also an effective continuous flow processor, where solutions are introduced through jet feeds to the base of the rotating tube under similar conditions, or at positions along the tube. Similar to the confined mode of operation, under the continuous flow and rapid rotation, dynamic thin films form, with the thickness ≥ 200 μm. The thickness of the film depends on the rotational speed, inclination angle and flow rates of the liquids. The continuous flow operation of the VFD imparts additional shear, which arises from the viscous drag as the liquid whirls up the tube.[64]

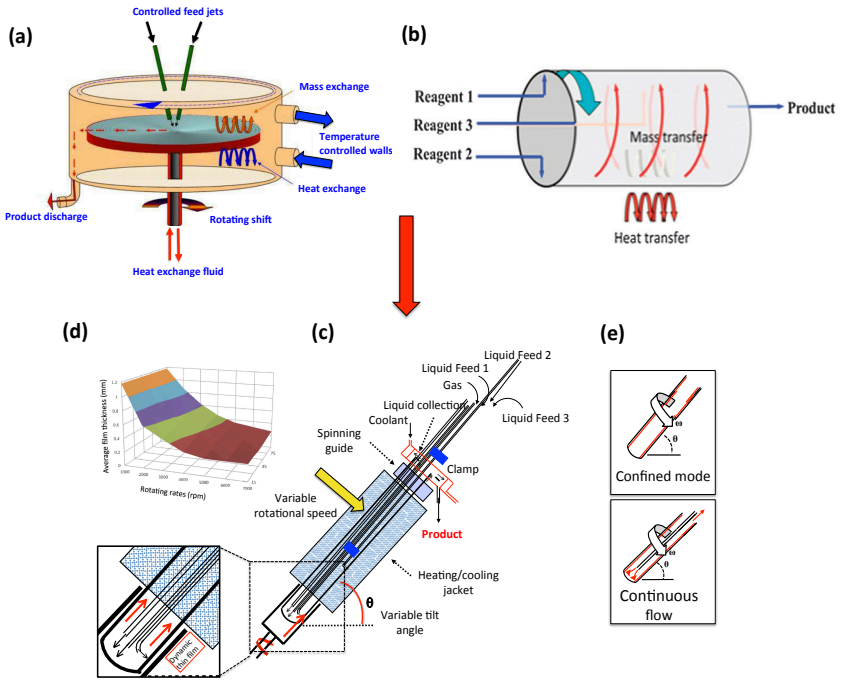

(f)

Continuous flow processors			
	SDP	**RTP**	**VFD**
Dimensions	60 mm- 500 mm (diameter of disc)	300 mm (length) and 60 mm (diameter)	10 mm (tube diameter)
Film thickness	1-200μm		200μm
Characteristics	• Uniform heat transfer • High shearing forces • Intense mixing • High mass transfer • Large volumes of liquid • Limiting operating conditions • High cost towards construction and development of equipment		• Uniform heat transfer • High shearing forces (2000rpm-1000rpm) • Intense mixing • High mass transfer • Submillilitre volumes of liquid • Low equipment cost and reduction of equipment size • Controllable residence time (confined mode) • Ability to scale up for industrial applications (continuous flow) • External attachments i.e. heating unit, real time fluorescence and optical absorbance measurements, laser and plasma probing • Precise controllable operating conditions

Figure 3 Schematic features of (a) a spinning disc processor (SDP), (b) a rotating tube processor (RTP),[65] (c) the vortex fluidic device (VFD), (d) average film thickness (≥ 200 μm) versus tilt angle (θ), (e) icons representing the different modes of operation of the VFD with jet feeds delivering reagents into the rotating tube in the continuous flow and (f) Overall comparison of the dimensions and characteristics of the different continuous flow processors. [64,65]

2.3 Dynamic thin film control in fabricating nanocarbon: A review

The VFD has high shear stress in the dynamic thin films, and is effective for a wide range of applications, from organic synthesis to the fabrication of materials for both 'top down' and 'bottom up' approaches. For example, the VFD is effective in exfoliating and scrolling single layered graphene and boron nitride sheets from the bulk material,[68,69] wrapping of bacteria and algal cells with graphene and magnetic polymer,[70-73] controlling the pore size and wall thickness of mesoporous silica[74,75] sol-gel synthesis of silica xerogel at room temperature and *in situ* incorporation of curcumin,[76] protein folding,[77] fabricating toroidal arrays of SWCNTs,[20] laterally 'slicing' CNTs[78] which work reported in this thesis, probing the structure of self organized systems,[79,80] biodiesel catalysis[81] and many others. The VFD is inexpensive relative to the SDP and RTP, with novel operating characteristics and is gaining prominence as a versatile microfluidic platform. A contemporary focus of chemistry is incorporating green chemistry metrics into the science at its inception, and using the VFD can greatly improve such metrics for a myriad of processes. The review is a comprehensive treatise on the processing of carbon nanomaterials under shear stress using the above continuous flow processors, namely the SDP, RTP and VFD. It is the basis of an invited review article to be submitted to *Advanced Materials Technologies*.

2.3.1 Decorating nanoparticles on carbon nanomaterials

Monodispersed uniformly sized metal nanoparticles have been of interest due to their high active surface area and surface to volume ratio, for applications in sensors, devices, energy storage and catalysis. Functionalized carbon nanomaterials, for example, coated with superparamagnetic iron oxide, Fe_3O_4, nanoparticles have been reported, adding other properties and potential applications, including drug delivery, as probes for magnetic interaction measurements and fillers in polymeric materials. The synthetic challenges with conventional methods include the need for prior oxidative functionalization of carbon nanotubes (CNTs), the use of inter-linkers and polymer wrapping agents to facilitate the loading of nanoparticles on the surface which necessitates down stream processing, and the high cost and inability to control the coating and loading density of the nanoparticles on the surface on the CNTs. Although *in situ* synthetic methods show promise in controlling the nanoparticle size and placement distribution, they still require high reaction temperatures, the use of toxic and high costing organic solvents and long and tedious processing methods. Other synthetic methods encompass more environmental and economical approaches,

typically including direct coating of the CNTs with Fe_3O_4 nanoparticles from solutions of Fe^{2+}/Fe^{3+} using either aqueous ammonia or sodium hydroxide, affording nanoparticles within a broad size distribution (25-80 nm) with the material exhibiting a ferromagnetic behaviour. Thus a primary challenge is controlling the particle size within a narrow distribution.

Continuous flow SDP processing is effective in synthesizing metal, organic and inorganic nanoparticles with precise control over the size and size distribution, and indeed shape, agglomeration and phase. Ultrafine Fe_3O_4 nanoparticles, 2-3 nm in diameter, can be decorated on SWCNTs *in situ* at room temperature with a high density loading of stabilized nanoparticles on the surface without the use of surfactants, Figure 4. The method involves chemical precipitation using oxidized SWCNTs dispersed in a solution of Fe^{2+}/Fe^{3+} delivered to the centre of the rotating disc through a jet feed with then deoxygenated aqueous ammonia introduced via a second jet feed under an atmosphere of high purity argon gas. The intense micromixing and viscous drag and the short and controllable residence time on the surface of the disc is effective in initiating nucleation and growth, circumventing aggregation of the nanoparticles. The strong shear forces from the viscous drag and intense mixing were also effective in controlling the nanoparticle size and distribution. The efficiency of the coating on the surface of the SWCNTs is related to the COO^- functional groups on their surface as sites for the spontaneous binding of the $Fe^{2+/3+}$ ions.[44]

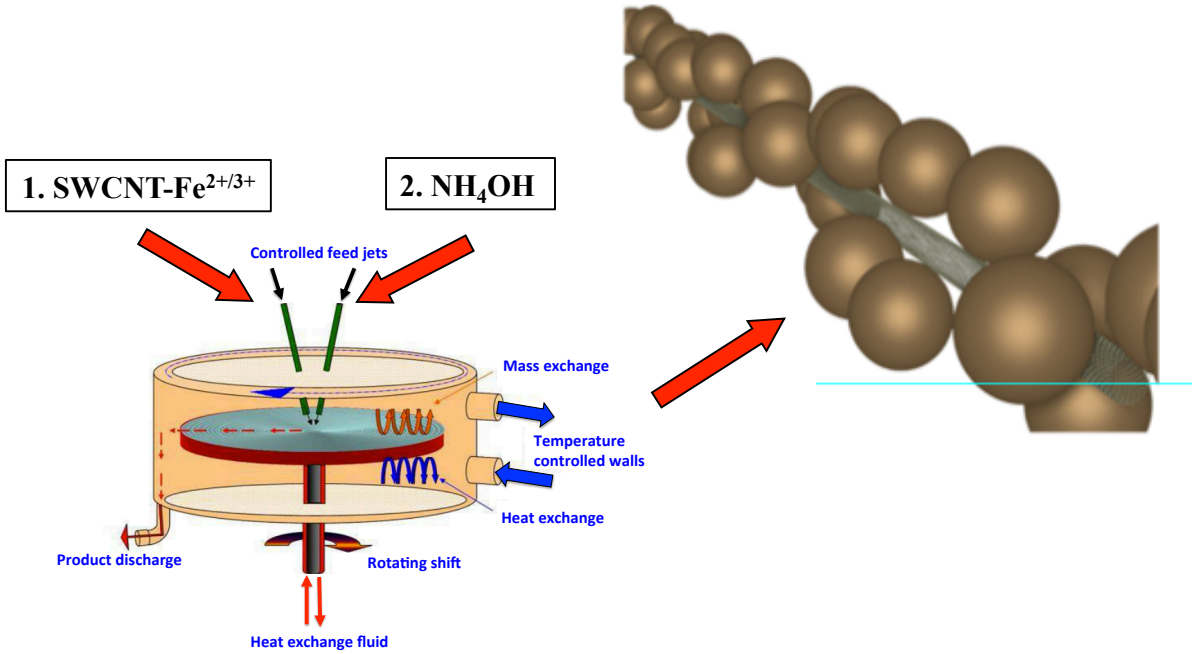

Figure 4 Schematic representation of the synthesis of ultrafine superparamagnetic Fe_3O_4 nanoparticles coated on SWCNT using a spinning disc processor.[44]

In variance to the method mentioned above, another more environmentally benign approach to decorate carbon nanomaterials with ultrafine noble metal nanoparticles was developed. The uniformity in the shear in the SDP results in a narrow sized distribution of the particles. Platinum (Pt) and palladium (Pd) nanoparticles have many applications, including energy storage, sensors and electrical devices, but they are prone to aggregation because of their high surface energy. This work using the SDP as a continuous flow reactor was followed soon after by developing use of the VFD to fabricate and stabilize nanoparticles *in situ* on carbon nanomaterials as a supporting material. While circumventing aggregation it also dramatically reduces the amount of noble metal nanoparticles required to achieve similar properties and performance relative to bulk nanoparticles of the same metal. This effectively reduces the cost in developing applications associated with the unique properties of precious metal nanoparticles.

Graphene, CNTs and carbon nano-onions (CNOs) are well known for their high surface area, excellent electrical, thermal and mechanical properties, and hybrid materials with noble metal nanoparticles can have enhanced properties relative to the properties of the separate components. A number of methods have been developed to systematically decorate such carbon nanomaterials, including in the use of a large macrocycle, *p*-phosphonic acid calixarene, as a surfactant, with shear within dynamic thin films a key towards controlling the dispersion and size distribution of the nanoparticles (Figure 5-7).[88-91] The surfactant stabilizes platinum and palladium nanoparticles on the surface of the 2D and 1D carbon nanomaterials, with high density loading arising from binding to the phosphonate moieties. In addition, the *p*-phosphonated calixarenes facilitates the exfoliation of 2D carbon nanomaterials for then non covalently functionalization them with a narrow size distribution of Pd and Pt nanoparticles in aqueous medium.[88-91] The driving force for homogenous nucleation of the nanoparticles is the level of local supersaturation. Thus, controllable and consistent intense micromixing within dynamic thin films in the SDP and VFD is effective in selectively controlling the growth of Pd and Pt nanoparticles, in the presence of either hydrogen gas or ascorbic acid as reducing agents. The size of the nanoparticles can be controlled by varying the rotational speed, with a higher rotational speed resulting in more nucleation sites for a finite amount of metal present, resulting in a narrower size distribution.[90]

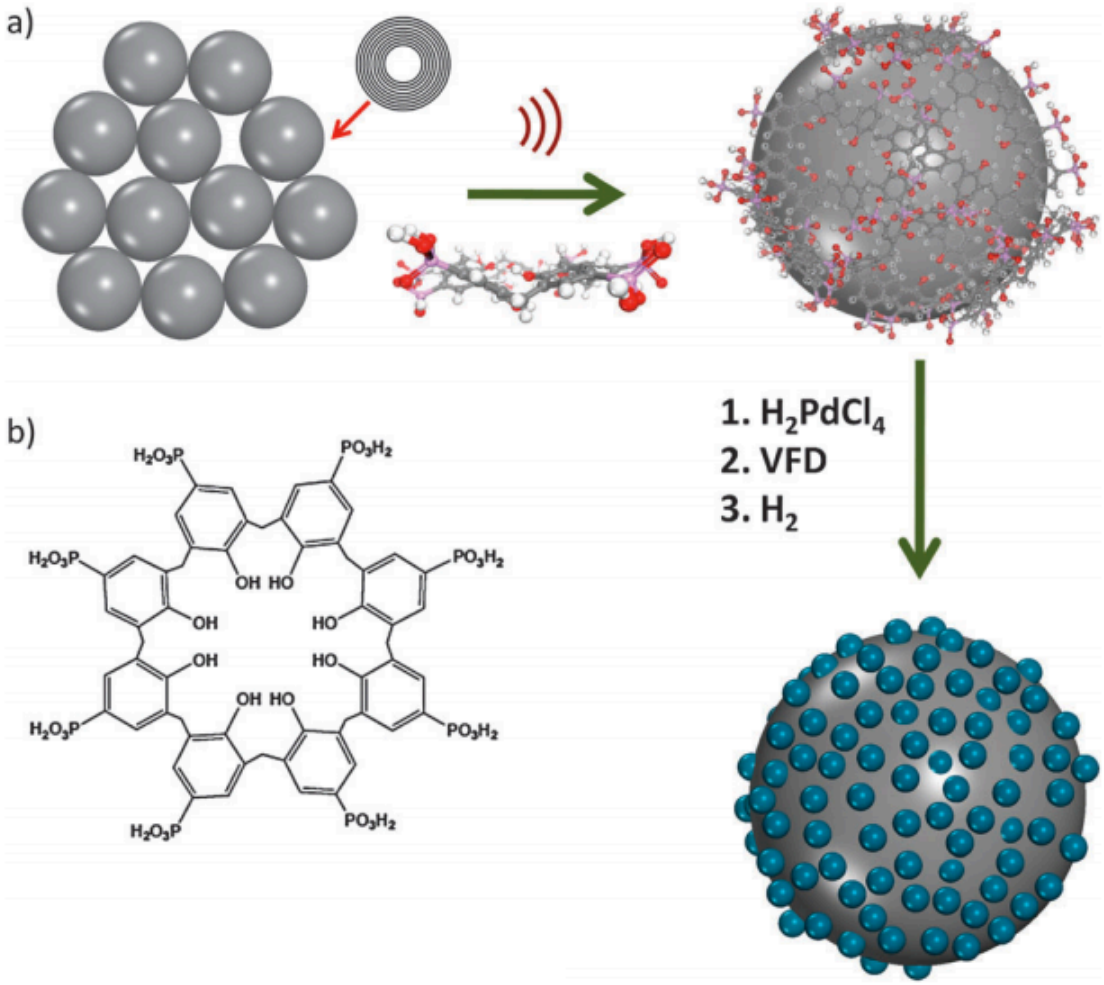

Figure 5 (a) Schematic of the decoration of CNOs with Pd nanoparticles, (b) *p*-phosphonic acid calix[8]arene using the vortex fluidic device.[90]

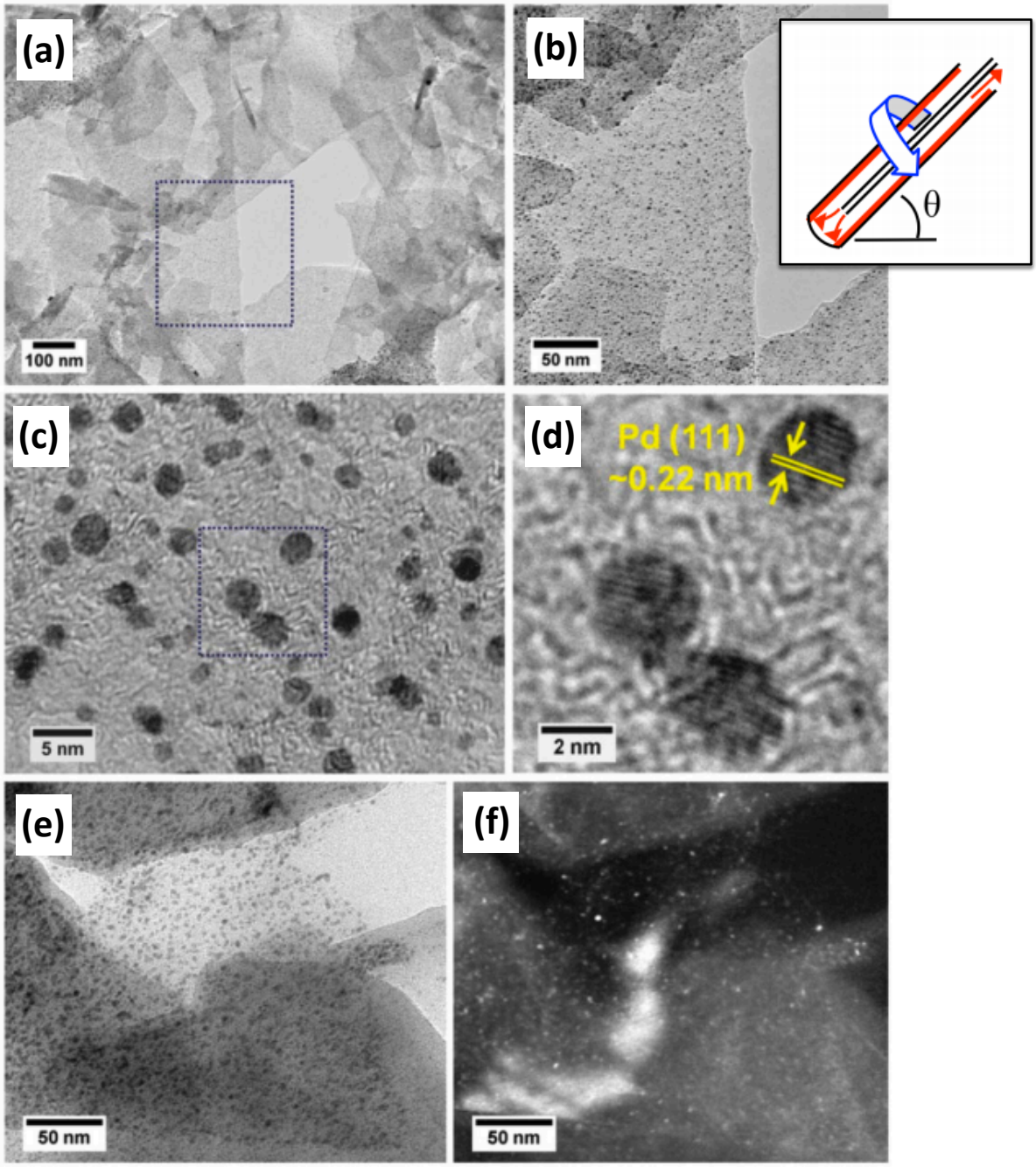

Figure 6 (a) and (b) TEM images of graphene sheets decorated with Pd nanoparticles prepared in the VFD, (c) HRTEM image of Pd nanoparticles on graphene sheets, (d) Zoomed-in image of the area indicated in (c), (e) Bright field and (f) dark field images of the Pd-graphene nanocomposite.[88]

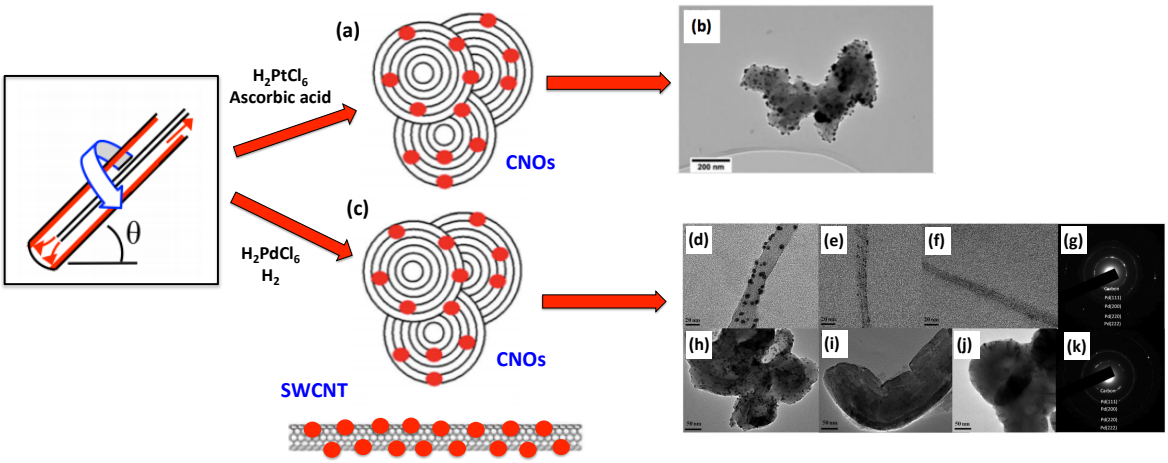

Figure 7 (a, c) Schematic of the formation of a nanocomposites in the 10 mm VFD tube, (b) TEM image of plasma treated CNOs with 0.2 mM H_2PtCl_6 in the VFD at an optimized rotational speed of 5000 rpm for a 10mm diameter tube using ascorbic acid as a reducing agent.[89] TEM images (d-g) of CNTs-Pd composite formed at 2000, 5000 and 7500 rpm respectively and the corresponding SAED (h-k) CNOs-Pd composite formed at 2000, 5000 and 7500 rpm respectively and the corresponding SAED. Hydrogen gas was used as a reducing agent.[91]

2.3.2 Lateral 'slicing' of carbon nanotubes

CNTs have high degrees of bundling and aggregation arising from the high aspect ratio and strong inter-tube van der Waals interaction as an effect of their growth process. Controlling the shortening of CNTs can require; (i) high temperature or high energy processing, (ii) the use of a suitable processing medium in overcoming their tendency to aggregate, for example using some common solvents such N-methyl-2-pyrollidone (NMP) and N,N-dimethylformamide (DMF), (iii) requiring polymer wrapping agents[92] and surfactants,[93] and (iv) covalent end and/or sidewall functionalization.[94,95] Improving the processing methods and potentially controlling the length of these cylindrical structures is important for applications that employ CNTs within a specific length distribution while preserving the pristine quality of the material.

Following the work of high density loading of Fe_3O_4 nanoparticles on the surface of CNTs, the SDP was used as a continuous flow reactor to fabricate metal plated SWCNTs and laterally slicing them in an aqueous media at room temperature, which at the time was surprising given the high tensile strength of SWCNTs, Figure 8. The SWCNTs can also be coated uniformly with metal nanoparticles (Ag, Au and Pt) using the SDP, for low concentrations of the noble metal. This processing takes advantage of the enhanced mixing and mass/heat transfer rates in the

microfluidic platform, with the nanoparticles generated with a narrow size distribution (2-3 nm). It is in the presence of excess ascorbic acid as a reducing agent to ensure complete reduction of the metal precursors. The mechanism of the lateral slicing was hypothesized to arise from the high shearing and centrifugal forces on the disc, which can twist and buckle CNTs with reversible elastic distortion. The presence of heavy metal loading with points of discontinuity of the metal on the surface of the CNTs provides break points where C-C bonds rupture occurs. In addition, Stone-Wales transformation under shear can contribute to the bond rotation defects, which is dictated by the chirality of the SWCNTs, surface tension of the liquid medium and temperature.[96]

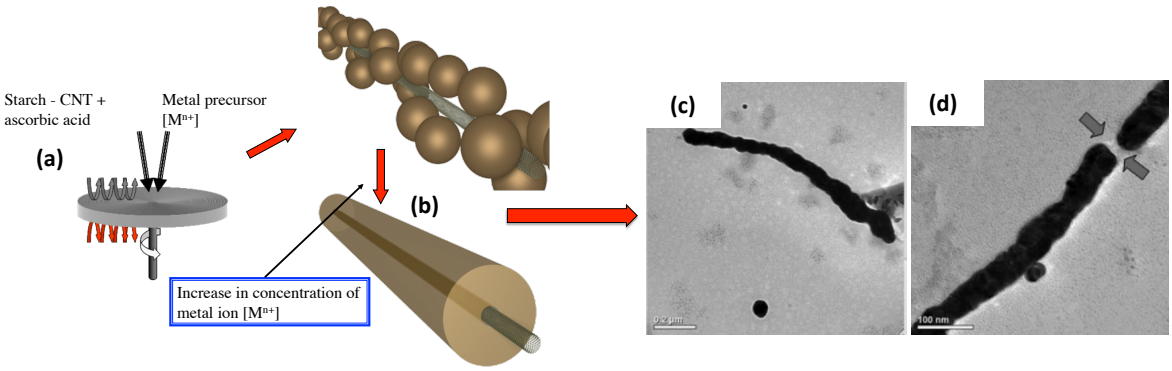

Figure 8 (a) Synthetic protocol for the fabrication and lateral slicing of SWCNT metal hybrids, (b) Controlling the metal nanoparticle decoration and metal plating of the CNTs by regulating the concentration of metal precursors in the jet feeds, and TEM images of (c) sliced Au plated CNT (10 Mm), (d) uncoated sites along the CNT that result slicing under shear.[80]

Use of the VFD was more efficient for laterally slicing SWCNTs, without the need for decorating SWCNTs with metal, as well as for double walled carbon nanotubes (DWCNTs) and multi-walled carbon nanotubes (MWCNTs). This was using a benign solvent system, a mixture of N-methyl pyrrolidone (NMP) and water, with the VFD simultaneous pulsed with a laser at 1064 nm wavelength at a specific laser power, Figure 9.[78] Importantly, the method minimizes the generation of defects on the surface of the CNTs, producing pristine sliced CNTs devoid of chemical stabilizers. Reducing the length of the nanotubes is more significant for SWCNTS, at 45 degree tilt angle under confined mode, down to a narrow size distribution, at a length scale of *ca* 100 nm which is at the length scale for drug delivery applications.[78] In general, the availability of SWCNTs, DWCNTs and MWCNTs is a paradigm shift for the advancement of applications of these materials, where a specific length scale is required. Furthermore, this processing is also novel in addressing scalability in operating under continuous flow, while

affording high quality materials devoid of surfactants with minimal defects on their surfaces. For the continuous flow processing, jet feeds are used to introduce colloidal suspensions of CNTs into the rapidly rotating tube, under specific operating parameters of the VFD, including speed at and a tilt angle of 45 degrees.

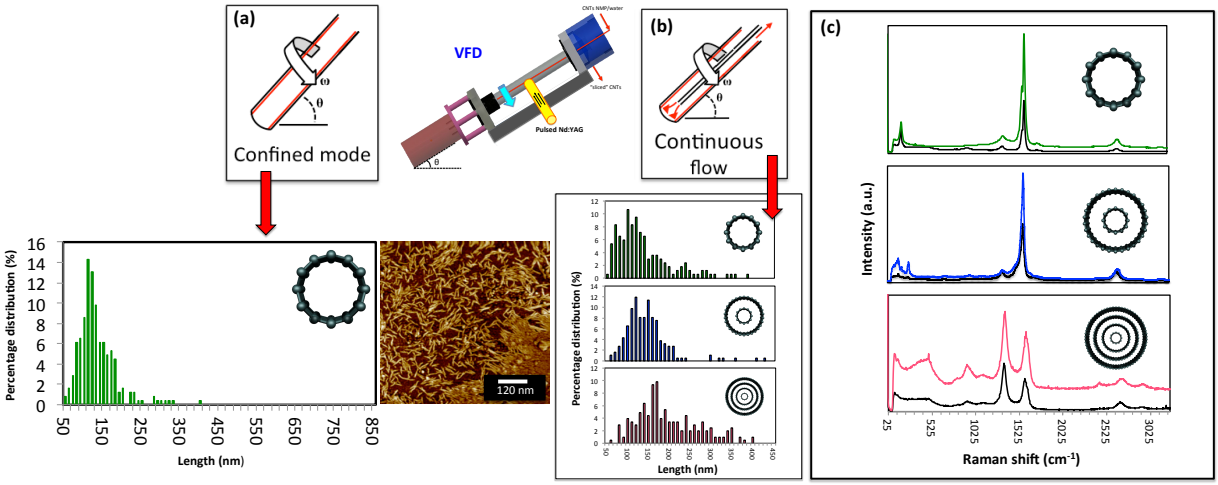

Figure 9 (a) Schematic of lateral slicing of CNTs using the VFD at a rotational speed of 7500 rpm and inclination angle at 45° while irradiated with a pulsed laser operating at a wavelength of 1064 nm and laser power of 260 mJ, (b) The ability to lateral slice CNTs under confined mode with the corresponding length distribution plot and AFM height image showing sliced SWCNTs at an average length of ~100nm, (c) Continuous flow operation at an optimised flow rate of 0.45 mL/min with the corresponding length distribution plots for sliced SWCNTs, DWCNTs and MWCNTs respectively, having average lengths of ~160-170 nm, (d) Raman spectra of SWCNTs, DWCNTs and MWCNTs, respectively, and the corresponding as received nanotubes (black) indicating minimal or no significant damage on the surface of the nanotubes post-processing.[78]

2.3.3 Exfoliation and scrolling of 2D carbon nanomaterial

Since the original 'scotch tape' method of exfoliating graphene was established, there has been significant effort in exfoliating the material, and 2D materials in general, while maintaining the integrity of the sheets for exploiting their remarkable properties. Issues pertaining to the methods of exfoliation involve the use of cavitation energy and the incorporation of functional groups that potentially results in significant damage to the materials, altering its properties and thereby limiting its applications. Thus, a more efficient 'top down' method was developed using an intense shearing process in the VFD in the presence of N-methyl pyrrolidone (NMP), exfoliating single layered graphene sheets and

similarly for iso-structural hexagonal-boron nitride (*h*-BN), Figure 10. The choice of organic solvent was related to its similar surface tension to graphitic material, and the solvent plays a role in the exfoliation, acting also as a stabilizing surfactant to avoid reassembling/restacking of the graphene sheets. The exfoliation mechanism involves a slippage process induced by the shear stress, with sufficient energy to lift the individual graphene sheets from the surface of the bulk material, occurring at the upper and/or lower layers of graphite, while being held centrifugally against the wall of the rapidly rotating tube. The use of a constant mechanoenergy source in the dynamic thin film in the VFD to exfoliate graphene sheets and other laminar materials offers scope for preparing defect free material for a range of applications.[68] Graphene sheets, and few layered graphene sheets, are one of the most promising materials in nanotechnology.[68]

Carbon nanoscrolls (CNS) exhibit distinct properties of both graphene and carbon nanotubes such as high carrier mobility and high mechanical strength. Although the physical structure of CNSs closely resembles the cylindrical structure of CNTs, the former shows superior electronic transport and electric current flow, with the interlayer spacing easily expandable or otherwise due to the open-ended structure. The unique structure of CNSs facilitates chemical doping and hydrogen storage and is regarded as an ideal material for supercapacitors and batteries.[97,98]

Shear forces within dynamic thin films generated in a SDP were effective in simultaneously exfoliating graphene and rolling it up into scrolls, Figure 11, and similarly *h*-BN, without inducing defects. SDP provides sufficient mechanoenergy to exfoliate the upper and/or lower layers of the graphene sheets with different degrees of scroll formation and folding occurring. According to theoretical considerations, if the edges of the sheets are lifted and come in contact with the inner surface of the same graphene sheets, spontaneous scrolling of graphene sheets will occur.[69] The use of mechanoenergy to exfoliate and produce scrolls was a new advance in gaining access to such material, with a higher yield of *h*-BN scrolls compared to graphene. This was related to the difference in particle size of the precursor material, graphene >> *h*-boron nitride. Scalability of scroll formation is possible using the SDP, particular in recycling liquids through the device, changing the texture of the surface of the disc and the choice of solvent(s).

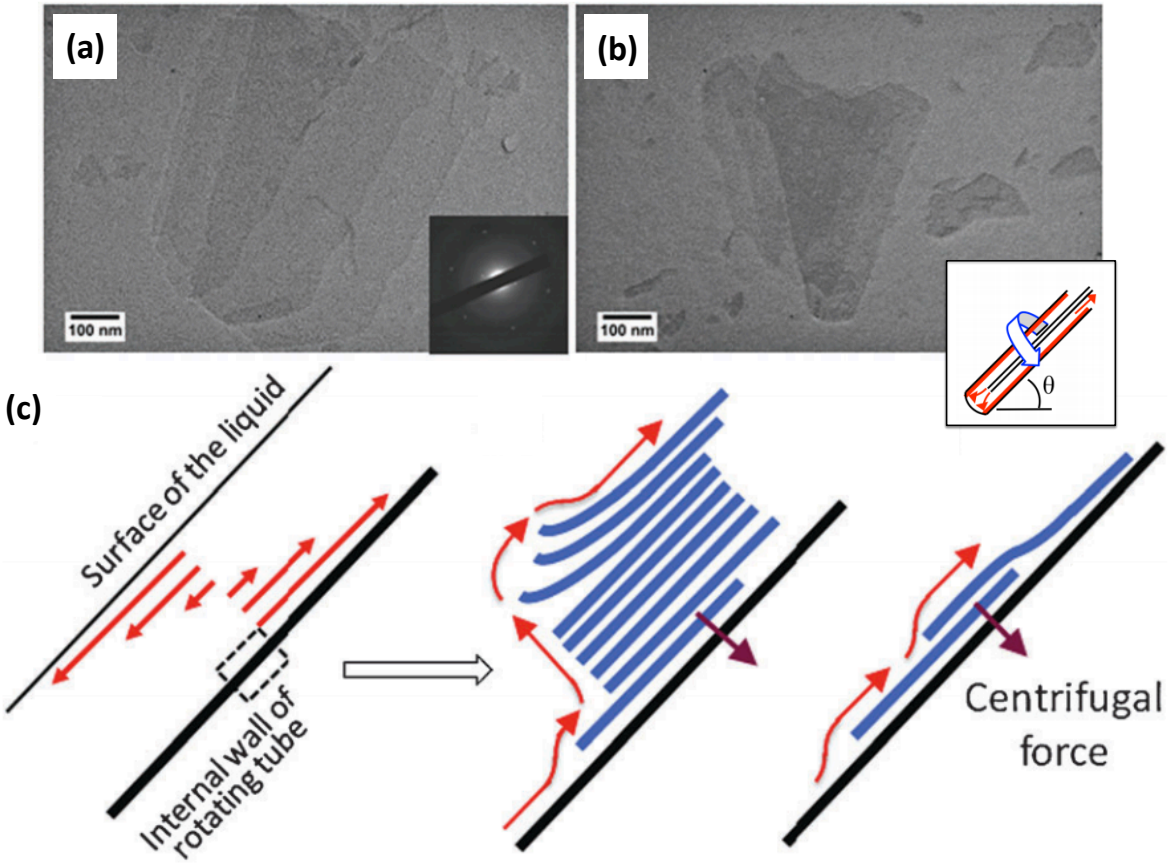

Figure 10 (a-b) TEM images of exfoliated graphene sheets (inset SAED pattern), (c) Schematic of the microfluidic flow velocity indicated by the red arrows for a section of the rotating tube, and the exfoliation process also involving slippage on the inner surface.[68]

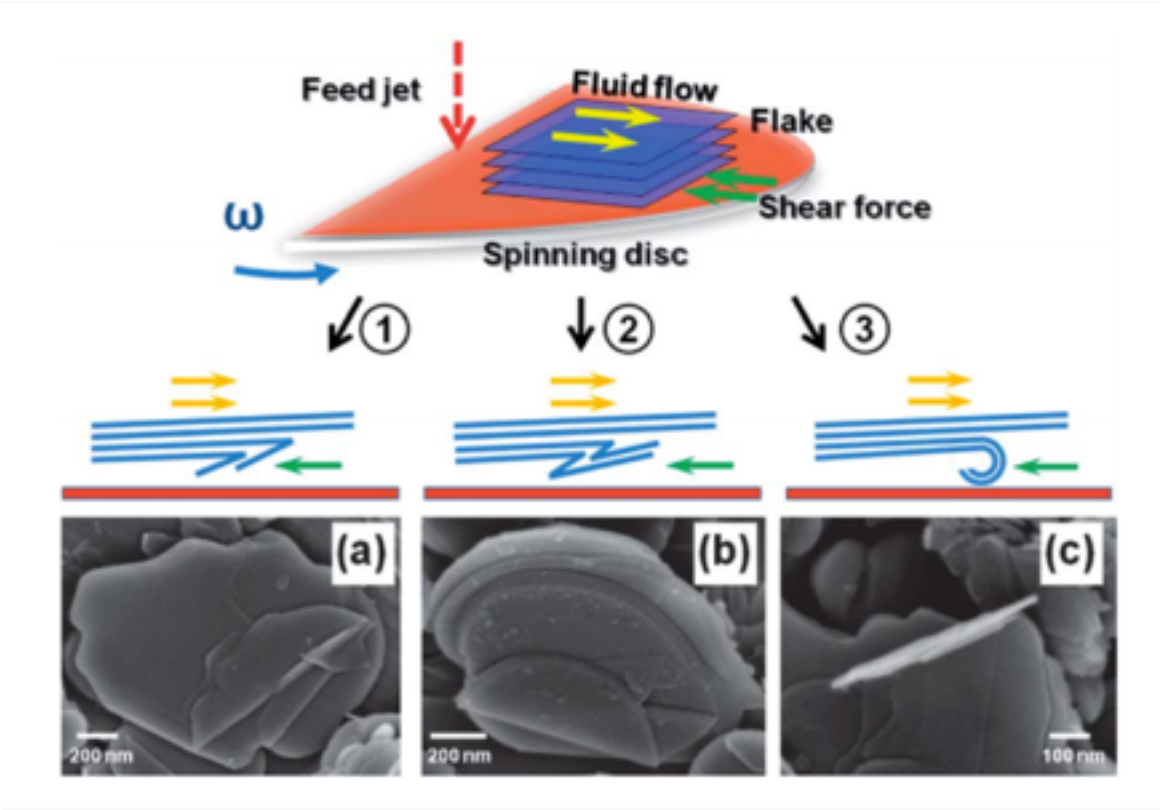

Figure 11 Proposed mechanism of exfoliation and scrolling of graphite and *h*-BN flakes using a SDP, with supporting SEM images.[69]

2.3.4 Synthesis of hybrid carbon nanomaterials involving microorganisms

Microorganisms such as microalgal and bacteria have growing interest for applications in the pharmaceutical industry and for the use in chemical processing. However, the utilization of these microorganisms depends on cultivation and harvesting methods, with their optimum activity affected by external environmental factors. A number of efforts have been devoted towards enhancing microorganism, but there are many limitations. With emerging advances in material science, conventional batch processing methods of forming hybrid structures between 2D material and biological cells have emerged, with exciting possibilities. Graphene and graphene oxide (GO) have remarkable properties on its own, including biodegradability, flexibility, transparency, amphiphilicity (GO only) and strong adhesion to the surface of the smoothest substrates, making it ideal as an interface with cells to promote their application while preserving biological activity. The growing number of applications of the VFD also includes manipulating live cells.[70-73] Following the

success in exfoliating graphene and other laminar materials within dynamic thin films, a two-step process of exfoliating graphene sheets into multi layer graphene (MLG) in water followed by hybridization with microalgal cells, *Chlorella vulgaris* was established.[70] The use of water

as the solvent here rather than NMP, as discussed above, resulted in MLG instead of single layered graphene under the confined mode operation of the device, being deemed necessary to preserve the viability of the cells. The shear stress in the VFD resulted in forming a hybrid material with algal cells under continuous flow, which had enhanced nitrate removal prowess compared to either graphene alone or just the microalgal cells. A simple process for the immobilization and encapsulation of microalgal cells and bacterial strains within graphene oxide (GO) layers was established, taking advantage of the hydrophilicity of the GO sheets with pH tuneable amphiphilic properties associated with the high degree of oxygen functionalities. This coupled with its high surface area makes it compatible with surface of cells. The hybrid material formed by wrapping GO around cells using a VFD, showed high colloidal stability while preserving the function of the cells, which began to replicate after 3 days. This confirms the non-toxic environment of the GO coating and the non-destructive nature of the shear stress in the VFD. The use of shear stress established a more uniform coating of the microalgae cells within GO layers compared to conventional methods, notably high energy sonication, offering a more efficient approach towards the immobilization of microalgae cells and nitrate removal, Figure 12.[70-73]

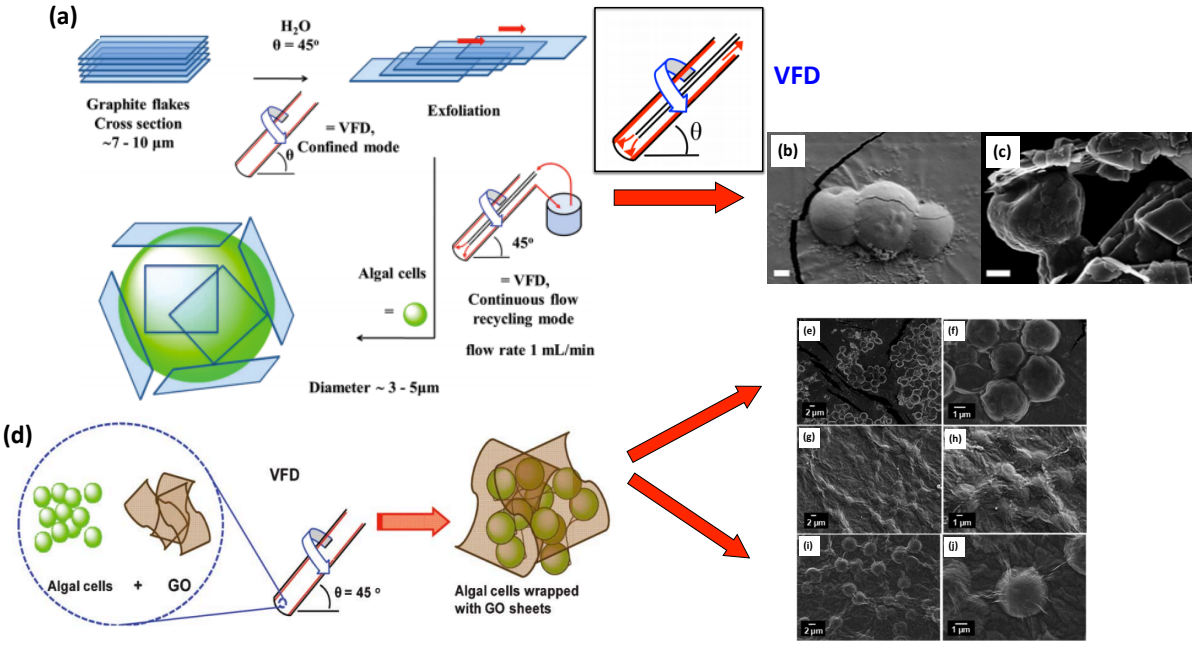

Figure 12 Synthesis of hybrid biomaterials in the VFD. (a) Schematic illustration of firstly the exfoliation of MLG under confined mode and then the hybridization of the microalgae cells and MLG under continuous flow in the VFD with the tube inclined at θ 45° and rotating at 7000 rpm for 30 minutes, for both modes of operation of the device. SEM images of (b) pristine microalgal cells (*Chlorella vulgaris*) processed in the VFD at 7000 rpm, (c) algae-graphene hybrid samples processing in the VFD at 7000 rpm, and (d) Schematic illustration of algal wrapping using GO in the VFD. SEM images; (e and f) pure algal cells, (g,h) GO wrapped algal cells using mild sonication, and (i and j) GO wrapped algal cells. Processing in (d) used a 10 mm OD borosilicate tube under the confined mode operation.[70,71]

Given the success of wrapping algal cells in the VFD, exploiting the high adsorptivity and surface area of GO, VFD-mediated GO encapsulation of different strains of bacterial cells with different morphologies, *Staphylococcus aureus* and *Rhodococcus opacus* with spherical and rod shaped respectively, was developed, Figure 13. The use of different morphologies of bacterial cells was pivotal towards the understanding of the extent of shear stress necessary to initiate the wrapping and subsequently maintaining the integrity of the cells. The efficacy of the bacteria was preserved in the resulting hybrid material which is a model system for protecting bacteria using 2D materials, for enhancing cell viability for delivery to targeted cells in a number of applications. Overall, use of the VFD offers a non-destructive approach towards increased efficiency of encapsulating bacterial strains, circumventing the use of chemical processing.[72]

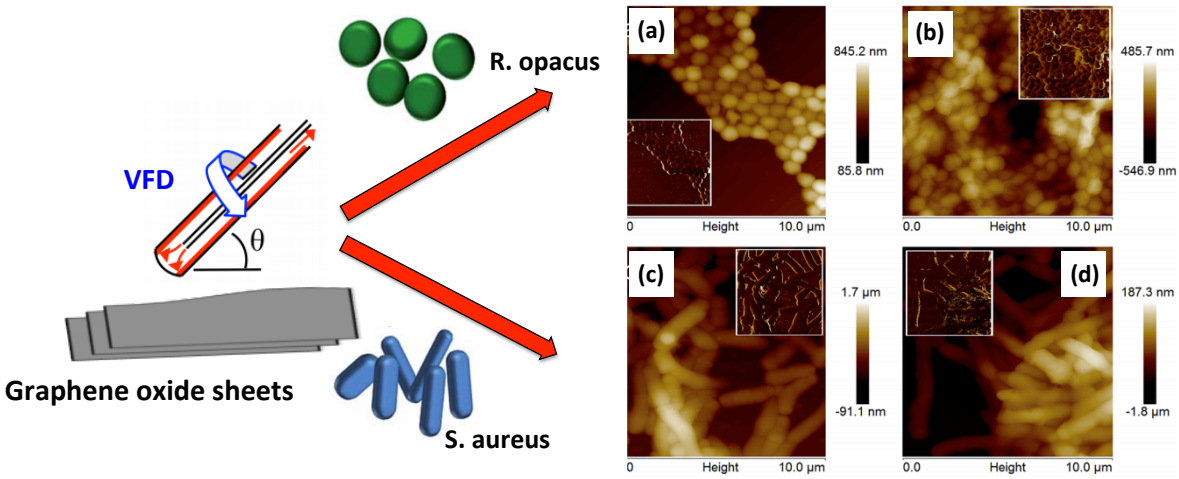

Figure 13 AFM images of bacteria (a) *S. aureus* only, (b) GO wrapped *S. aureus*, (c) *R. opacus,* and (d) GO wrapped *R. opacus.* Inset images display phase images of the same samples.[72]

2.3.5 Bottom up fabrication of other carbon nanoforms

The fabrication of novel carbon nanoforms such as carbon nanorings, carbon nanoonions and carbon nanofibres have been of interest for their unique properties that go beyond the properties of other carbon allotropes. A major challenge in the fabrication of such novel carbon nanoforms is the ability to precisely control the size and dimensions of the material, in fine-tuning their properties, depending on the applications. Traditional methods to fabricate such forms of nanocarbon have required the use of harsh chemicals, long and tedious processing methods, the addition of catalysts and the requirement for down stream processing.

To this end, the use of intense shear forces within dynamic thin films in a SDP operating at high temperature (HT-SDP) was explored, in gaining access to carbon nanofibres (CNFs) which is without precedent, Figure 14.[97] Here the rotating disc in a SDP is irradiated with a high intensity light source generated from a xenon arc discharge lamp creating a uniform temperature profile across the disc. Fructose was the precursor material of choice for generating carbon, in the absence of a catalyst, as a benign approach to the synthesis of carbon fibres. Meticulous control of temperature on the HT-SDP disc was important in

accessing this material, as was the short residence time to reduce the likelihood of degradation of the PEG 200 which was the choice of reaction medium.[99]

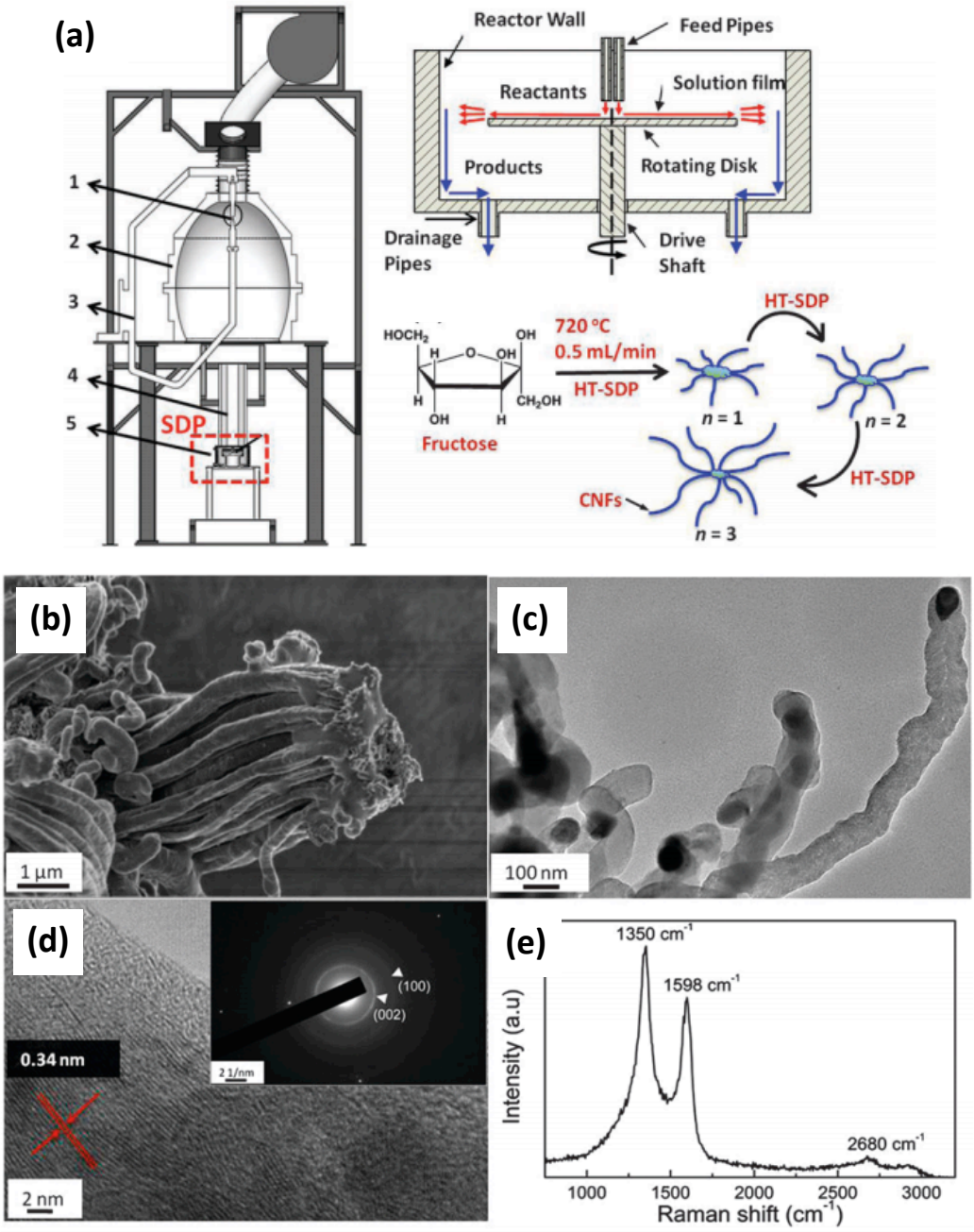

Figure 14 (a) Schematic illustration of the light-driven HT-SDP: (1) 7 kW xenon short arc discharge lamp, (2) hemi-ellipsoidal reflector, (3) manual XYZ micromanipulator, (4) hexagonal kaleidoscope flux homogenizer, and (5) a schematic illustration of the SDP and the growth of the CNFs via multiple *n* passes of fructose in PEG 200 through the SDP. Microstructure of CNFs obtained from fructose in PEG 200 at 720 °C, (b) SEM image of the CNF, (c) TEM image, (d) HRTEM image and SAED pattern (inset) and (d) Raman spectra.[99]

The controllable mechanoenergy within thin films on the VFD was investigated as an approach to overcome the high flexural rigidity of carbon nanomaterials. SWCNTs were transformed mainly into stable toroidal rings under ambient conditions, without the need for surfactants, Figure 15. This research is part of the work carried out in this thesis.

Shearing a mixture of toluene dispersed SWCNTs and water in the VFD afforded intertwined SWCNTs rings of various morphologies, namely torus, cross lattice and figure of '8' structures.[20] Different diameter nanorings can be prepared, between 300-700 nm and 100-200 nm, depending on the diameter of the rapidly rotating borosilicate tube, 20 mm and 10 mm OD respectively at θ 45°. For θ > 0° centrifugal forces accelerate the emulsion droplets and nanotubes up the side of the tube, with the shear stress overcoming the large van der Waals forces between the bundles of SWCNTs in exfoliating individual SWCNTs. Drop casting the water/toluene interfacial SWCNT laden material pre-VFD processing affords toroids with radiating SWCNTs, presumably as toluene containing hydrophobically matched SWCNTs. Under shear in the VFD, nanorings of compact intertwined SWCNTs at their van der Walls limit are formed, drawing in the radiating SWCNTs. They have smaller wall thickness (differences between the internal and external diameter) relative to the toroids formed from drop casting pre-VFD processing mixtures. For 10 mm diameter VFD tubes, the external diameter of the nanorings dramatically reduces relative to the size of the toluene toroids, i.e. a greater curvature of the SWCNTs. Nanorings of SWCNT with a controllable diameter have promise in a number of fields including in polymer composites, sensing devices and for the use in electronic circuits.

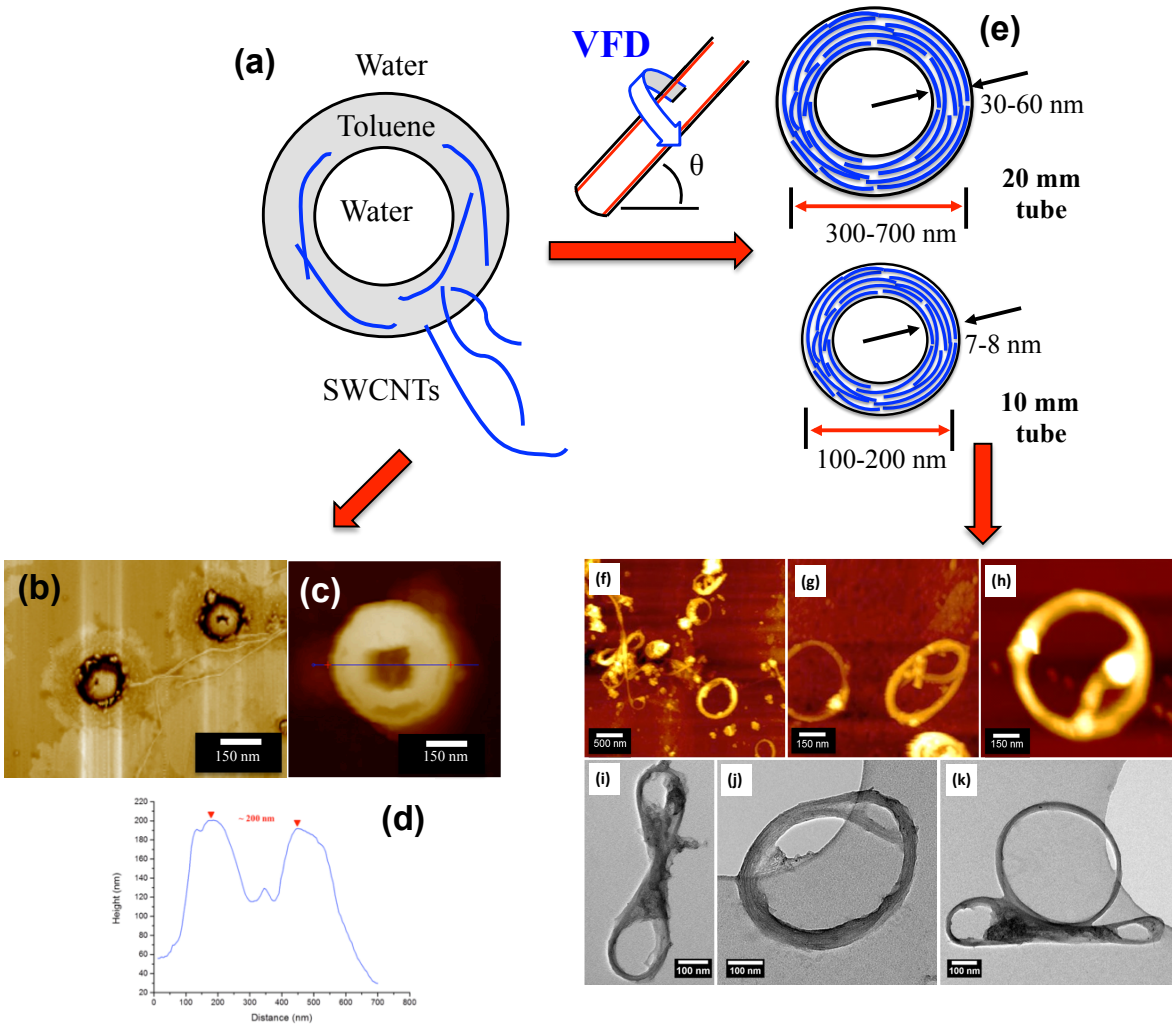

Figure 15 (a) Synthesis and proposed template mechanism of formation of nanorings of SWCNTs from a sonicated mixture of toluene and water; a toroidal structure with radiating SWCNTs, formed on drop casting the mixture from pre-VFD processing, (b) AFM phase image, (c) Height image and (d), and associated height profile, (e) SWCNT nanorings 300-700 nm and 100-200 nm in diameter generated using the 20 mm and 10 mm OD VFD tube respectively, (f-h) AFM height images of the rings, (i-k) TEM images of the different nanoring structures.[20]

2.3.6 Self assembly of C_{60} and C_{70} molecules

Continuous flow processing offers a more benign approach towards controlled self- assembly of fullerene, C_{60}. Nanowhiskers with approximately 5-8 nm in cross section and 250-350 nm in length are formed in reacting the ubiquitous starch-iodine complex with C_{60}. The nanowhiskers were then coated with silver nanoparticles using a SDP, with ascorbic acid used as the reducing agent, Figure 16.[46] TEM images confirmed uniformity of the silver coated nanowhiskers, with the starch acting as an effective stabilizing agent.[46]

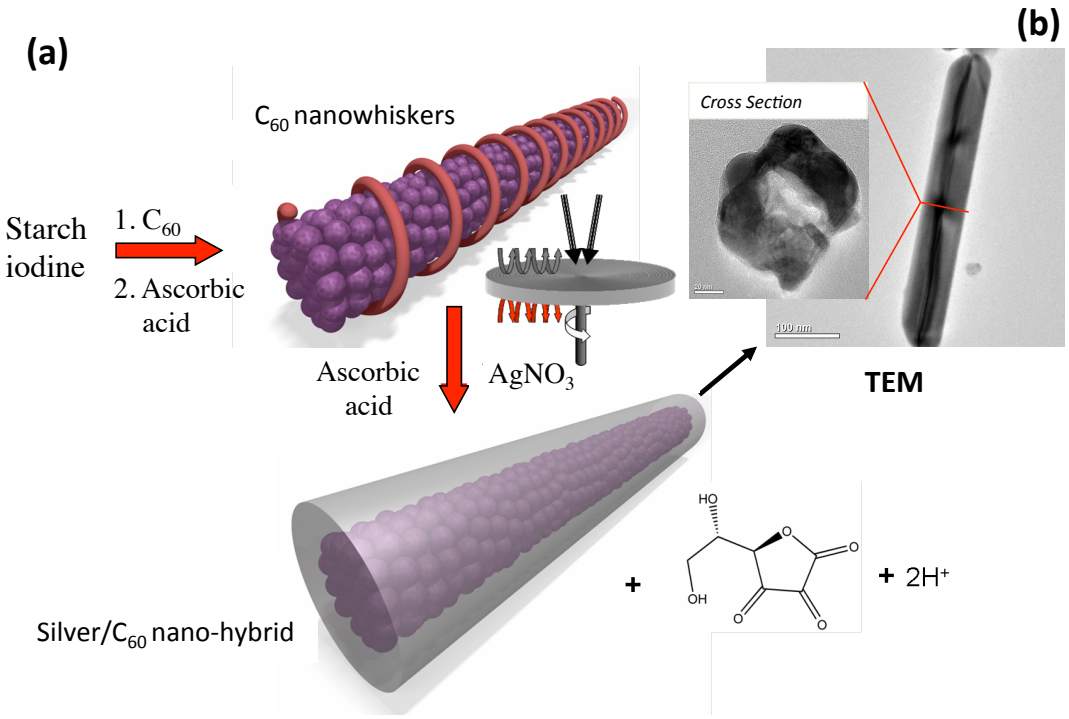

Figure 16 (a) Experimental protocol for the fabrication of C_{60} nanowhiskers and C_{60} silver nanohybrids, and (b) TEM image of the silver-C_{60} hybrid nanostructure. Inset: microtomed cross section of the silver C_{60} hybrid nanostructure.[46]

The starch-iodine complex has been used to solubilize SWCNTs in water,[44] and given the above findings on the formation of nanowhiskers of fullerene, C_{60},[46] the uptake and self assembly of C_{70} molecules in an aqueous medium was investigated. Ascorbic acid was also used as a reducing agent for iodine present in the solution and in reducing silver. Under shear in the SDP, nucleation and growth of silver nanoparticles 8-12 nm in diameter occurs inside a toroidal array of C_{70} molecules, Figure 17.[100]

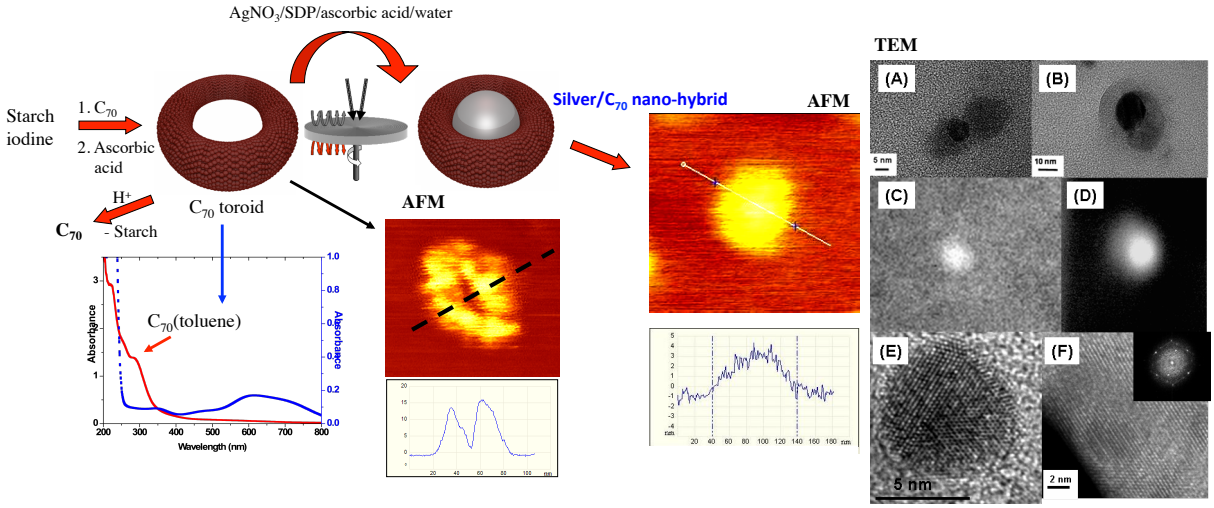

Figure 17 A schematic representation of a C_{70} nanoring and its utility as a nanoreactor to nucleate particle growth of silver metal within the central cavity to form silver/C_{70} nanohybrids using an SDP. The schematic illustrates the UV-Vis spectrum of the starch iodine complex (blue) and the C_{70}/starch nanocomposite (red) and SPM topography images for both the C_{70} toroids and the silver/C_{70} nanohybrid and the respective representative line scan across the AFM image as indicated by the dotted lines. TEM and HRTEM images are of the C_{70} torus nanostructures with an encapsulated silver nanoparticle. Figure (c,d) are dark field TEM image showing contrast between the core (silver) and the shell (C_{70}) for a single nanoparticle.[100]

Remarkably, the VFD is effective in controlling the self-assembly and the radial growth of nanotubules directly of *fcc* phase of C_{60}, without the need for stabilizing agents, and circumventing entrapment of solvent molecules during crystallization, Figure 18. This is also research undertaken in this thesis. The C_{60} nanotubules spontaneously self assemble in the presence of an immiscible solvent system of water and toluene forming micron length nanotubules of the fullerene with a hollow diameter of 100-400 nm.[101] The formation of these nanoporous microcrystals exhibits excellent sensitivity and selectivity towards different solvent molecules. The nanotubules spontaneously form at room temperature within 30 minutes of processing time, with the product readily collected, with no further processing required. In the case of continuous flow, the processing time is the amount of time taken for a finite volume of liquid delivered to the bottom of the tube to whirl up the tube and exit at the top. The direct formation of *fcc* C_{60} devoid of included solvent is particularly noteworthy, and while related nanotubules have been reported, they required heating to remove included

solvent, and also involve the use of surfactants. The choice of solvent mixture, the level of supersaturation difference of C_{60} in the toluene, the ratio of toluene to water, the rotational speed and flow rate (continuous flow mode) were systematically explored, with the optimized parameters critical for the formation exclusively of the hollow nanotubules of the fullerene.

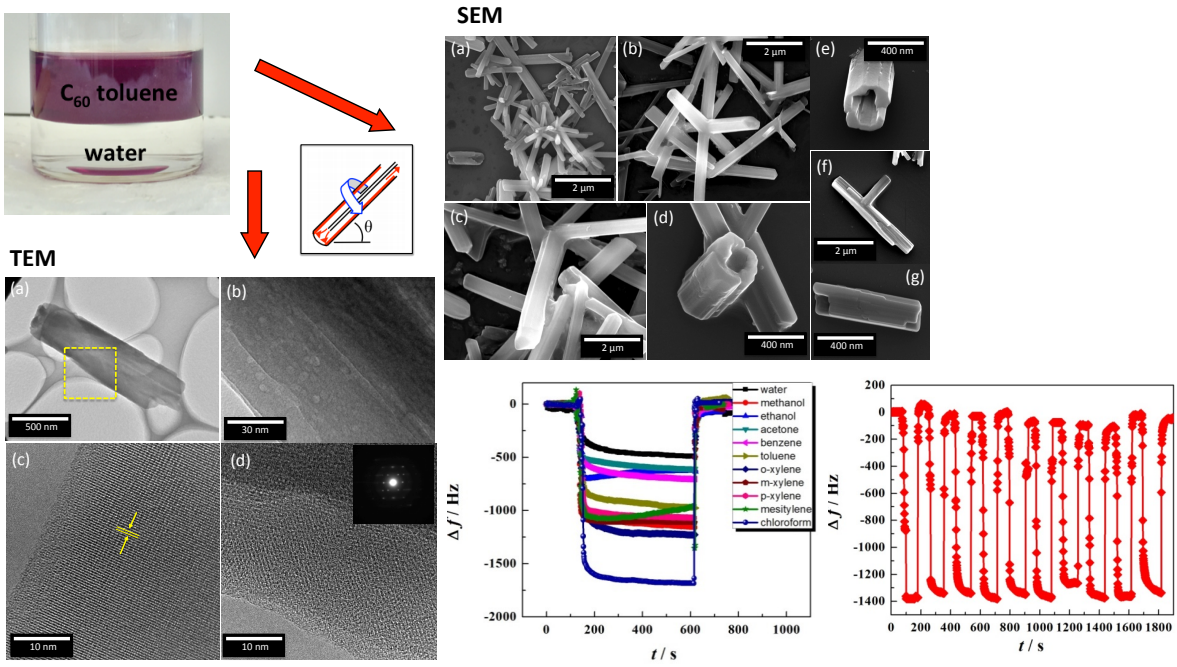

Figure 18 Schematic illustration of the fabrication of C_{60} nanotubules in the VFD at an inclination angle θ 45° and rotational speed of 7000 rpm for 30 minutes under confined mode and continuous flow at an optimized flow rate of 1 mL/min. SEM, TEM and HRTEM images resemble the nanotubules formed in the presence of shear stress. The nanotubules exhibit excellent sensitivity and selectivity towards different solvent molecules.[101]

2.4 Conclusion

Continuous flow processors, SDP and VFD, have revealed remarkable control in processing nanocarbon, and composites thereof. Clearly they have potential as an alternative more controllable approach to fabricating different forms of carbon nanomaterial, using the 'top down' or 'bottom up' approaches. The controllable mechanoenergy within dynamic thin films in these microfluidic platforms offers scope for controlling the shape, morphology and size of carbon nanomaterial, with high green chemistry metrics of the processing in general. This includes reducing the need for harsh and toxic chemicals, while avoiding additional down stream processing and energy usage. They have potential where conventional batch processing is limited in terms of practical convenience, and indeed where such novel forms of carbon and composites thereof are not accessible using traditional approaches. In addition, the VFD has the ability to scale down while still imparting high shear stress, which operating under confined mode, and this offers scope for gaining access to small quantities of materials, for example in wrapping of 2D material around cells, for use in medical research. The methods developed thus far establishes a paradigm shift in the ability to manipulate high tensile material in a controlled way while being attractive to industry in addressing scalability up front.

2.5 References

1 Lu, F. *et al.* Advances in Bioapplications of Carbon Nanotubes. *Advanced Materials* **21**, 139-152, (2009).

2 De Volder, M. F. L., Tawfick, S. H., Baughman, R. H. & Hart, A. J. Carbon Nanotubes: Present and Future Commercial Applications. *Science* **339**, 535-539, (2013).

3 Dreyer, D. R., Park, S., Bielawski, C. W. & Ruoff, R. S. The chemistry of graphene oxide. *Chemical Society Reviews* **39**, 228-240, (2010).

4 Georgakilas, V. *et al.* Functionalization of Graphene: Covalent and Non-Covalent Approaches, Derivatives and Applications. *Chemical Reviews* **112**, 6156-6214, (2012).

5 Feng, L., Wu, L. & Qu, X. New Horizons for Diagnostics and Therapeutic Applications of Graphene and Graphene Oxide. *Advanced Materials* **25**, 168-186, (2013).

6 Li, H., Kang, Z., Liu, Y. & Lee, S.-T. Carbon nanodots: synthesis, properties and applications. *Journal of Materials Chemistry* **22**, 24230-24253, (2012).

7 Li, L. *et al.* Focusing on luminescent graphene quantum dots: current status and future perspectives. *Nanoscale* **5**, 4015-4039, (2013).

8 Jariwala, D., Sangwan, V. K., Lauhon, L. J., Marks, T. J. & Hersam, M. C. Carbon nanomaterials for electronics, optoelectronics, photovoltaics, and sensing. *Chemical Society Reviews* **42**, 2824-2860, (2013).

9 Liu, L., Yang, C., Zhao, K., Li, J. & Wu, H.-C. Ultrashort single-walled carbon nanotubes in a lipid bilayer as a new nanopore sensor. *Nat Commun* **4**, (2013).

10 Bianco, A., Kostarelos, K. & Prato, M. Applications of carbon nanotubes in drug delivery. *Current Opinion in Chemical Biology* **9**, 674-679, (2005).

11 Zhang, W., Zhang, Z. & Zhang, Y. The application of carbon nanotubes in target drug delivery systems for cancer therapies. *Nanoscale Research Letters* **6**, 555, (2011).

12 Abdelbary M. A. Elhissi, W. A., Israr Ul Hassan, Vinod. R. Dhanak, and Antony D'Emanuele. Carbon Nanotubes in Cancer Therapy and Drug Delivery. *Journal of Drug Delivery,* (**2012).**

13 Zhu, S. & Xu, G. Single-walled carbon nanohorns and their applications. *Nanoscale* **2**, 2538-2549, (2010).

14 Miyawaki, J., Yudasaka, M., Azami, T., Kubo, Y. & Iijima, S. Toxicity of Single-Walled Carbon Nanohorns. *ACS Nano* **2**, 213-226, (2008).

15 Sano, N., Wang, H., Chhowalla, M., Alexandrou, I. & Amaratunga, G. A. J. Nanotechnology: Synthesis of carbon 'onions' in water. *Nature* **414**, 506-507, (2001).

16 Han, F.-D., Yao, B. & Bai, Y.-J. Preparation of Carbon Nano-Onions and Their Application as Anode Materials for Rechargeable Lithium-Ion Batteries. *The Journal of Physical Chemistry C* **115**, 8923-8927, (2011).

17 Cornejo, A. *et al.* Generating Hydrogen Gas from Methane with Carbon Captured as Pure Spheroidal Nanomaterials. *Chemistry – A European Journal* **17**, 9188-9192, (2011).

18 Martel, R., Shea, H. R. & Avouris, P. Ring Formation in Single-Wall Carbon Nanotubes. *The Journal of Physical Chemistry B* **103**, 7551-7556, (1999).

19 Martel, R., Shea, H. R. & Avouris, P. Rings of single-walled carbon nanotubes. *Nature* **398**, (1999).

20 Vimalanathan, K., Chen, X. & Raston, C. L. Shear induced fabrication of intertwined single walled carbon nanotube rings. *Chemical Communications* **50**, 11295-11298, (2014).

21 Saito, K., Ohtani, M. & Fukuzumi, S. Electron-Transfer Reduction of Cup-Stacked Carbon Nanotubes Affording Cup-Shaped Carbons with Controlled Diameter and Size. *Journal of the American Chemical Society* **128**, 14216-14217, (2006).

22 Kim, Y. A. *et al.* Effect of ball milling on morphology of cup-stacked carbon nanotubes. *Chemical Physics Letters* **355**, 279-284, (2002).

23 Nasibulin, A. G. *et al.* A novel hybrid carbon material. *Nat Nano* **2**, 156-161, (2007).

24 Falcao, E. H. L. & Wudl, F. Carbon allotropes: beyond graphite and diamond. *Journal of Chemical Technology & Biotechnology* **82**, 524-531, (2007).

25 Kroto, H. W., Heath, J. R., O'Brien, S. C., Curl, R. F. & Smalley, R. E. C60: Buckminsterfullerene. *Nature* **318**, 162-163, (1985).

26 Kratschmer, W., Lamb, L. D., Fostiropoulos, K. & Huffman, D. R. Solid C_{60}: a new form of carbon. *Nature* **347**, 354-358, (1990).

27 Chen, T. & Dai, L. Carbon nanomaterials for high-performance supercapacitors. *Materials Today* **16**, 272-280, (2013).

28 Shen, J., Zhu, Y., Yang, X. & Li, C. Graphene quantum dots: emergent nanolights for bioimaging, sensors, catalysis and photovoltaic devices. *Chemical Communications* **48**, 3686-3699, (2012).

29 Harrison, B. S. & Atala, A. Carbon nanotube applications for tissue engineering. *Biomaterials* **28**, 344-353, (2007).

30 Saito, N. *et al.* Carbon nanotubes: biomaterial applications. *Chemical Society Reviews*

38, 1897-1903, (2009).

31 Baughman, R. H., Zakhidov, A. A. & de Heer, W. A. Carbon Nanotubes--the Route Toward Applications. *Science* **297**, 787-792, (2002).

32 Hirsch, A. The era of carbon allotropes. *Nat Mater* **9**, 868-871, (2010).

33 Wang, H., Chhowalla, M., Sano, N., Jia, S. & Amaratunga, G. A. J. Large-scale synthesis of single-walled carbon nanohorns by submerged arc. *Nanotechnology* **15**, 546, (2004).

34 Yudasaka, M., Iijima, S. & Crespi, V. H. in *Carbon Nanotubes: Advanced Topics in the Synthesis, Structure, Properties and Applications* (eds Ado Jorio, Gene Dresselhaus, & Mildred S. Dresselhaus) 605-629, (Springer Berlin Heidelberg), (2008).

35 Zhang, Y. *et al.* Single-Crystalline C_{60} Nanostructures by Sonophysical Preparation: Tuning Hollow Nanobowls as Catalyst Supports for Methanol Oxidation. *Chemistry – A European Journal* **17**, 4921-4926, (2011).

36 Song, L. *et al.* Large-Scale Synthesis of Rings of Bundled Single-Walled Carbon Nanotubes by Floating Chemical Vapor Deposition. *Advanced Materials* **18**, 1817-1821, (2006).

37 Shrestha, L. K., Hill, J. P., Tsuruoka, T., Miyazawa, K. i. & Ariga, K. Surfactant-Assisted Assembly of Fullerene (C_{60}) Nanorods and Nanotubes Formed at a Liquid–Liquid Interface. *Langmuir* **29**, 7195-7202, (2013).

38 Shrestha, L. K. *et al.* Nanoporous Carbon Tubes from Fullerene Crystals as the π-Electron Carbon Source. *Angewandte Chemie International Edition* **54**, 951-955, (2015).

39 Li, Y. F. *et al.* Bamboo-shaped carbon tubes from coal. *Chemical Physics Letters* **366**, 544-550, (2002).

40 Aoune, A. & Ramshaw, C. Process intensification: heat and mass transfer characteristics of liquid films on rotating discs. *International Journal of Heat and Mass Transfer* **42**, 2543-2556, (1999).

41 Oxley, P., Brechtelsbauer, C., Ricard, F., Lewis, N. & Ramshaw, C. Evaluation of Spinning Disk Reactor Technology for the Manufacture of Pharmaceuticals. *Industrial & Engineering Chemistry Research* **39**, 2175-2182, (2000).

42 Hartlieb, K. J., Raston, C. L. & Saunders, M. Controlled Scalable Synthesis of ZnO Nanoparticles. *Chemistry of Materials* **19**, 5453-5459, (2007).

43 Anantachoke, N. *et al.* Fine Tuning the Production of Nanosized β-Carotene Particles Using Spinning Disk Processing. *Journal of the American Chemical Society* **128**, 13847-

13853, (2006).

44 Chin, S. F., Iyer, K. S. & Raston, C. L. Fabrication of carbon nano-tubes decorated with ultra fine superparamagnetic nano-particles under continuous flow conditions. *Lab on a Chip* **8**, 439-442, (2008).

45 Chin, S. F., Iyer, K. S., Raston, C. L. & Saunders, M. Size Selective Synthesis of Superparamagnetic Nanoparticles in Thin Fluids under Continuous Flow Conditions. *Advanced Functional Materials* **18**, 922-927, (2008).

46 Iyer, K. S., Raston, C. L. & Saunders, M. Hierarchical aqueous self-assembly of C60 nano-whiskers and C60-silver nano-hybrids under continuous flow. *Lab on a Chip* **7**, 1121-1124, (2007).

47 Smith, N. M., Corry, B., Swaminathan Iyer, K., Norret, M. & Raston, C. L. A microfluidic platform to synthesise a G-quadruplex binding ligand. *Lab on a Chip* **9**, 2021-2025, (2009).

48 Dev, S., Iyer, K. S. & Raston, C. L. Nanosized drug formulations under microfluidic continuous flow. *Lab on a Chip* **11**, 3214-3217, (2011).

49 Dev, S., Prabhakaran, P., Filgueira, L., Iyer, K. S. & Raston, C. L. Microfluidic fabrication of cationic curcumin nanoparticles as an anti-cancer agent. *Nanoscale* **4**, 2575-2579, (2012).

50 Dev, S. *et al.* Suppressing regrowth of microfluidic generated drug nanocrystals using polyelectrolyte coatings. *RSC Advances* **3**, 695-698, (2013).

51 Fang, J. *et al.* Sequential microfluidic flow synthesis of $CePO_4$ nanorods decorated with emission tunable quantum dots. *Lab on a Chip* **10**, 2579-2582, (2010).

52 Fang, J., Guo, Y., Lu, G., Raston, C. L. & Iyer, K. S. Instantaneous crystallization of ultrathin one-dimensional fluorescent rhabdophane nanowires at room temperature. *Green Chemistry* **13**, 817-819, (2011).

53 tailored rotating surfaces. *Heat Recovery Systems and CHP* **14**, 475-491, (1994).

54 Cafiero, L. M., Baffi, G., Chianese, A. & Jachuck, R. J. J. Process Intensification: Precipitation of Barium Sulfate Using a Spinning Disk Reactor. *Industrial & Engineering Chemistry Research* **41**, 5240-5246, (2002).

55 Swaminathan Iyer, K., Norret, M., Dalgarno, S. J., Atwood, J. L. & Raston, C. L. Loading Molecular Hydrogen Cargo within Viruslike Nanocontainers. *Angewandte Chemie International Edition* **47**, 6362-6366, (2008).

56 Boodhoo, K. V. K., Dunk, W. A. E. & Jachuck, R. J. Influence of centrifugal field on free-

radical polymerization kinetics. *Journal of Applied Polymer Science* **85**, 2283-2286, (2002).

57 Leveson, P., Dunk, W. A. E. & Jachuck, R. J. Numerical investigation of kinetics of free-radical polymerization on spinning disk reactor. *Journal of Applied Polymer Science* **90**, 693-699, (2003).

58 Boodhoo, K. V. K. & Jachuck, R. J. Process intensification: spinning disc reactor for condensation polymerisation. *Green Chemistry* **2**, 235-244, (2000).

59 Hostomsky, J. & Jones, A. G. Calcium carbonate crystallization, agglomeration and form during continuous precipitation from solution. *Journal of Physics D: Applied Physics* **24**, 165, (1991).

60 Hartlieb, K. J., Martin, A. D., Saunders, M. & Raston, C. L. Photochemical generation of small silver nanoparticles involving multi-functional phosphonated calixarenes. *New Journal of Chemistry* **34**, 1834-1837, (2010).

61 Vicevic, M., Jachuck, R. J. J., Scott, K., Clark, J. H. & Wilson, K. Rearrangement of [small alpha]-pinene oxide using a surface catalysed spinning disc reactor (SDR). *Green Chemistry* **6**, 533-537, (2004).

62 Boodhoo, K. V. K., Dunk, W. A. E., Jassim, M. S. & Jachuck, R. J. Thin film solvent-free photopolymerization of n-butyl acrylate. I. Static film studies. *Journal of Applied Polymer Science* **91**, 2079-2095, (2004).

63 Lodha, H., Jachuck, R. & Suppiah Singaram, S. Intensified Biodiesel Production Using a Rotating Tube Reactor. *Energy & Fuels* **26**, 7037-7040, (2012).

64 Yasmin, L., Chen, X., Stubbs, K. A. & Raston, C. L. Optimising a vortex fluidic device for controlling chemical reactivity and selectivity. *Scientific Reports* **3**, 2282, (2013).

65 Chen, X., Smith, N. M., Iyer, K. S. & Raston, C. L. Controlling nanomaterial synthesis, chemical reactions and self assembly in dynamic thin films. *Chemical Society Reviews* **43**, 1387-1399, (2014).

66 Bennetts, D.A. & Hocking, L.M. On nonlinear Ekman and Stewartson layers in a rotating fluid. *Proc. R. Soc. Lond. A.* **333,** 469-489, (1973).

67 Greenspan, H.P. The theory of rotating fluids. *Cambridge University Press,* **328,** (1968).

68 Chen, X., Dobson, J. F. & Raston, C. L. Vortex fluidic exfoliation of graphite and boron nitride. *Chemical Communications* **48**, 3703-3705, (2012).

69 Chen, X., Boulos, R. A., Dobson, J. F. & Raston, C. L. Shear induced formation of carbon and boron nitride nano-scrolls. *Nanoscale* **5**, 498-502, (2013).

70 Wahid, M. H., Eroglu, E., Chen, X., Smith, S. M. & Raston, C. L. Functional multi-layer graphene-algae hybrid material formed using vortex fluidics. *Green Chemistry* **15**, 650-655, (2013).

71 Wahid, M. H., Eroglu, E., Chen, X., Smith, S. M. & Raston, C. L. Entrapment of Chlorella vulgaris cells within graphene oxide layers. *RSC Advances* **3**, 8180-8183, (2013).

72 Wahid, M. H. *et al.* Microencapsulation of bacterial strains in graphene oxide nano-sheets using vortex fluidics. *RSC Advances* **5**, 37424-37430, (2015).

73 Eroglu, E., D'Alonzo, N. J., Smith, S. M. & Raston, C. L. Vortex fluidic entrapment of functional microalgal cells in a magnetic polymer matrix. *Nanoscale* **5**, 2627-2631, (2013).

74 Tong, C. L., Boulos, R. A., Yu, C., Iyer, K. S. & Raston, C. L. Continuous flow tuning of ordered mesoporous silica under ambient conditions. *RSC Advances* **3**, 18767-18770, (2013).

75 Tong, C. L. *et al.* Nitrate uptake using mesoporous silica embedded with zero-valent palladium nanoparticles. *RSC Advances* **5**, 20557-20561, (2015).

76 Tong, C. L., Stroeher, U. H., Brown, M. H. & Raston, C. L. Continuous flow vortex fluidic synthesis of silica xerogel as a delivery vehicle for curcumin. *RSC Advances* **5**, 7953-7958, (2015).

77 Yuan, T. Z. *et al.* Shear-Stress-Mediated Refolding of Proteins from Aggregates and Inclusion Bodies. *ChemBioChem* **16**, 393-396, (2015).

78 Vimalanathan, K. *et al.* Fluid dynamic lateral slicing of high tensile strength carbon nanotubes. *Scientific Reports* **6**, 22865, (2016).

79 Mo, J. *et al.* Shear induced carboplatin binding within the cavity of a phospholipid mimic for increased anticancer efficacy. *Scientific Reports* **5**, 10414, (2015).

80 Iyer, K. S. & Raston, C. L. Fabrication of laterally 'sliced' metal plated carbon nanotubes under aqueous continuous flow conditions. *Journal of Materials Chemistry* **17**, 4872-4875, (2007).

81 Britton, J. & Raston, C. L. Continuous flow vortex fluidic production of biodiesel. *RSC Advances* **4**, 49850-49854, (2014).

82 Yasmin, L., Stubbs, K. A. & Raston, C. L. Vortex fluidic promoted Diels–Alder reactions in an aqueous medium. *Tetrahedron Letters* **55**, 2246-2248, (2014).

83 Yasmin, L., Eggers, P. K., Skelton, B. W., Stubbs, K. A. & Raston, C. L. Thin film microfluidic synthesis of fluorescent highly substituted pyridines. *Green Chemistry* **16**,

3450-3453, (2014).

84 Gandy, M. N., Raston, C. L. & Stubbs, K. A. Towards aryl C-N bond formation in dynamic thin films. *Organic & Biomolecular Chemistry* **12**, 4594-4597, (2014).

85 Britton, J., Chalker, J. M. & Raston, C. L. Rapid Vortex Fluidics: Continuous Flow Synthesis of Amides and Local Anesthetic Lidocaine. *Chemistry – A European Journal* **21**, 10660-10665, (2015).

86 Britton, J., Dalziel, S. B. & Raston, C. L. The synthesis of di-carboxylate esters using continuous flow vortex fluidics. *Green Chemistry* **18**, 2193-2200, (2016).

87 Britton, J., Meneghini, L. M., Raston, C. L. & Weiss, G. A. Accelerating Enzymatic Catalysis Using Vortex Fluidics. *Angewandte Chemie International Edition*, (2016).

88 Chen, X. *et al.* Non-covalently modified graphene supported ultrafine nanoparticles of palladium for hydrogen gas sensing. *RSC Advances* **3**, 3213-3217, (2013).

89 Goh, Y. A. *et al.* Shear flow assisted decoration of carbon nano-onions with platinum nanoparticles. *Chemical Communications* **49**, 5171-5173, (2013).

90 Yasin, F. M. *et al.* Microfluidic size selective growth of palladium nano-particles on carbon nano-onions. *Chemical Communications* **48**, 10102-10104, (2012).

91 Yasin, F.M., Iyer, K. S. & Raston, C. L. Palladium nano-carbon-calixarene based devices for hydrogen sensing. *New Journal of Chemistry* **37**, 3289-3293, (2013).

92 Manivannan, S. *et al.* Dispersion of single-walled carbon nanotubes in aqueous and organic solvents through a polymer wrapping functionalization. *Journal of Materials Science: Materials in Electronics* **20**, 223-229, (2009).

93 Tkalya, E. E., Ghislandi, M., de With, G. & Koning, C. E. The use of surfactants for dispersing carbon nanotubes and graphene to make conductive nanocomposites. *Current Opinion in Colloid & Interface Science* **17**, 225-232, (2012).

94 Mickelson, E. T. *et al.* Solvation of Fluorinated Single-Wall Carbon Nanotubes in Alcohol Solvents. *The Journal of Physical Chemistry B* **103**, 4318-4322, (1999).

95 Boul, P. J. *et al.* Reversible sidewall functionalization of buckytubes. *Chemical Physics Letters* **310**, 367-372, (1999).

96 Nardelli, M. B., Yakobson, B. I. & Bernholc, J. Brittle and Ductile Behavior in Carbon Nanotubes. *Physical Review Letters* **81**, 4656-4659, (1998).

97 Mpourmpakis, G., Tylianakis, E. & Froudakis, E. Carbon Nanoscrolls: A Promising Material for Hydrogen Storage. *Nano Lett* **7,** 1893-1897, (2007)

98 Zeng, F., Kuang Y., Liu, G., Liu,R., Huang, Z., Fu, C. & Zhou, H. Supercapacitors based on

high quality graphene scrolls. *Nanoscale* **4,** 3997-4001, (2012)

99 Lu, H.B. *et al.* Carbon nanofibres from fructose using a light-driven high-temperature spinning disc processor. *Chemical Communications* **50**, 1478-1480, (2014).

100 Iyer, K. S., Saunders, M., Becker, T., Evans, C. W. & Raston, C. L. Nanorings of Self-Assembled Fullerene C70 as Templating Nanoreactors. *Journal of the American Chemical Society* **131**, 16338-16339, (2009).

101 Vimalanathan, K., Shrestha, G. R., Zhang, Z., Zou, J., Nakayama, T. & Raston, C.L. Surfactant free fabrication of fullerene C_{60} nanotubules under shear (Under Review)

3 RESEARCH PROGRAM

The main concept of this thesis relates to the ability to manipulate carbon materials within nanoscale dimensions to harness their explicit properties for wide range of applications, specifically in medicine and device technology. The properties of carbon nanomaterials can be tailored based on their size, shape and morphology. Thus, employing the use of controllable mechanoenergy generated from a microfluidic platform, the VFD, this research probes the development of novel methods to gain access to new forms of nanocarbon material using green chemistry metrics, which includes incorporating scalability at the inception of science. This approach takes attempts to ensure environmental and economical feasibility of the resulting technology.

The specific aims of this research are as follows:-

- To investigate the nucleation and growth of supramolecular assemblies of fullerene molecules in the bulk phase, in gaining access to nano and micron sized structures with control over size, shape and morphology, for application in devices.
- To develop novel methods to fabricate 2D materials in manipulating their morphology, for harnessing their properties for applications in energy storage.
- To develop novel methods of overcoming the high flexural rigidity of CNTs, while controlling their length, diameter and chirality, potentially for a diverse range of application.

There has been rapid advancement in materials chemistry, specifically in the field of carbon nanomaterials using conventional batch processing methods. Carbon nanomaterials have been extensively explored due to their limitless and extraordinary properties that can be utilized in a diversity of fields. Although there has been significant breakthrough in developing novel methods to control the growth, manipulate the morphology and control the self-assembly of nanomaterial, there are a number of limitations that are yet to be addressed.

The subsequent chapters in this thesis will provide a detail description of the development of novel methods using a green chemistry or sustainability metrics strategy to overcome

the limitations of conventional processing methods for nanocarbon material processing. The processing of carbon nanomaterials of various dimensionalities using intensive shear within dynamic thin films will be explored with the aims of developing environmentally benign processing methods, which includes minimizing energy usage and reducing the generation of waste, and avoiding the need for additional down stream processing.

The carbon nanomaterials that will feature in this thesis includes, 0D fullerene C_{60} and C_{70} molecules, 1D carbon nanotubes of single to multiple coaxial shells and 2D graphene sheets. The approaches in this thesis was designed specifically to eliminate the use of toxic and harsh chemicals, surfactants and chemical stabilisers with scalability incorporated into the process from the outset, with a view that it will facilitate transferring the technology to the market place.

A number of key characterization techniques were employed in the research, and includes the atomic force microscopy (AFM), Raman spectroscopy, scanning electron microscopy (SEM), transmission electron microscopy (TEM) and high resolution transmission electron microscopy (HRTEM), small angle neutron scattering (SANS), thermogravimetric analysis (TGA) and X-ray powder diffraction (XRD).

The structure of this thesis is in the following order, along with a brief summary of the content of each chapter.

Chapter 4, **Fullerene, C_{60} and C_{70}**, has an introduction into fullerene chemistry and the various approaches employed towards controlling the self assembly of fullerene molecules using various architectures. Chapter 4 then provides a detailed study and explanation on the use of shear stress in the VFD to exquisitely control the self assembly of C_{60} molecules to form stable micron size nanotubules devoid of surfactants.

Chapter 5, **Graphene**, describes an introduction into 2D graphene and the current methods explored to exfoliate high yielding graphene sheets of high quality and controlling their morphology to harness, for potential in harnessing its properties for applications. Chapter 5 will then discuss a novel method developed to form graphene scrolls under shear stress using an immiscible solvent system in high yield while maintaining the structural integrity of

the material.

Chapter 6, **Manipulation of carbon nanotubes**, provides a detailed introduction towards the various methods of growth of CNTs, their physical and electrical properties in a bulk mixture and the current limitations in the field. Four essential factors that will be addressed in this chapter are: (i) Lateral slicing of SWCNT, DWCNT and MWCNT to narrow length distributions using a benign solvent system while ensuring the quality of the material is preserved, (ii) Converting (interconverting) a bulk mixture of SWCNTs, affording chirality enriched monochiral SWCNTs. (iii) Dethreading DWCNT and MWCNTs by removing the inner shells from the outer shells as a strategy for gaining access to CNTs of larger diameters. (iv) Overcoming the high flexural rigidity of SWCNTs using a combination of shear stress and an immiscible solvent system to afford stable SWCNT toroids with controllable diameters and with different morphologies, and importantly devoid of surfactants.

4 FULLERENE

Among the different dimensionalities of carbon nanomaterials that have been discovered to date, 0D fullerenes are particularly unique materials for their definitive molecular structure with vast potential in diverse fields. The applicability of fullerenes are sometimes an issue for particular applications due to its sparing solubility in a number of solvent systems and the strong aggregation that is easily formed.[1] Since its discovery in 1985 by Kroto *et al*.,[2] fullerenes have been one of the most exciting and extensively studied carbon materials in the family of carbon allotropes due to its excellent redox, optical and optoelectronic.[3] This functional material requires controlled assembly into well ordered 1D or 2D nanostructures to further enhance its electronic and optical properties for the applicability in applications. For example, the development of next generation of electronic and photonic devices such as field effect transistors (FETs) and solar cells (SCs) that are lightweight, cost effective, have flexibility in being implemented into the system and most importantly with potential of scalability of the processing.[4-7] Thus, highly conjugated organic molecular systems in the form of crystalline structures would be useful as these sorts of applications requires materials with a specific band gap with geometrically well-defined shapes and sizes in order to be able to modulate the optical properties of the material.

Zero dimensional (0D) fullerenes are the smallest and most stable carbon allotrope in the carbon family. This 0D molecule is an example of a type of highly conjugated organic molecule that has attracted much attention for its semiconducting and superconducting properties.[8,9] Fullerenes were first discovered when a laser was used to vaporize graphite rods in an atmosphere of helium gas. In 1990, Krätschmer *et. al.* were successful in establishing a simple technique using an electric arc to produce fullerene in macroscopic conditions which then created a new paradigm in fullerene chemistry.[10]

Fullerene molecules consist of a cage like structure of carbon atoms ranging from 18 atoms to hundreds of atoms large. The most extensively studied fullerene to date has been the buckyball (in the shape of a soccer ball) (Figure 19) consisting of 60 carbon atoms, with each carbon atom being bonded to three (3) other carbon atoms via sp^2 hybridised bonds. C_{60}, a truncated icosahedron (I_h) is a polygon with 60 vertices and 32 faces forming a spheroid shape

with bond lengths calculated to be 1.40 Å and 1.46Å respectively; the diameter of a C_{60} molecule has been calculated to be 7.09 Å.[11,12] C_{60} molecules consist purely of carbon atoms located at the nodes of a series of hexagons and pentagons arranged in a caged lattice defined by alternating single and double bonds. They are electron deficient (i.e. electron accepting) molecules due to the energetically unstable double bonds within the pentagon rings.[13] The curvature induced by the cage structure increases the energy associate with the double bonds, along with electron accepting capabilities which enhances the reactivity of the molecule and offers great potential for the use in a variety of applications specifically for ferromagnetic of superconducting materials,[14,15] for the use in photoinduced electron transfer[16] and in medicinal chemistry[17,18]. C_{60} has been considered as a large spherical organic molecule considering its solubility in organic solvents.[1]

Another key property of the C_{60} molecules is its ability in quenching various free radicals compared to conventional antioxidants, making it an excellent material for biological applications.[19] However, the hydrophobic nature of these molecules offers limitations in such applications. This has been overcome over the years using synthetic methods of substitution and functionalization of ionic and non-ionic functional groups, in increasing its water solubility.[20] These water-soluble fullerenes have been useful for studying the interactions between organofullerenes and DNA, proteins and living cells and the encapsulation of C_{60} molecules in supramolecular structures containing a host moiety such as cyclodextrin, surfactants, gels and polymers.[21] It is noteworthy that C_{60} molecules polymerize under high temperature and pressure and when exposed to UV irradiation.[22,23]

Several other fullerenes were subsequently discovered including C_{20}, C_{70}, and even larger species. Among these other fullerenes, the study of geometrically well-defined C_{70} molecules also features in the present study, with an aim to precisely control the shape and morphology at the nano and micro scale dimension. C_{70} exhibits superior properties such as fluorescence, enhanced conductivity and photoconductivity and optical limiting performance, which is beyond that of C_{60} molecules.[24,25] C_{70} is the next most common (abundant) fullerene after Buckminsterfullerenes C_{60}. It has a 'belt' of additional 10 benzene hexagons in its structure relative to C_{60}, having an ellipsoidal structure, departing slightly from the spherical structure of C_{60}.[26] Morphology controlled crystallization of C_{70} has been scarcely studied due to its ellipsoidal molecular shape and the coexistence of energetically similar phases at room

temperature which makes the crystallization at nanoscale dimesions challenging to control.[27,28]

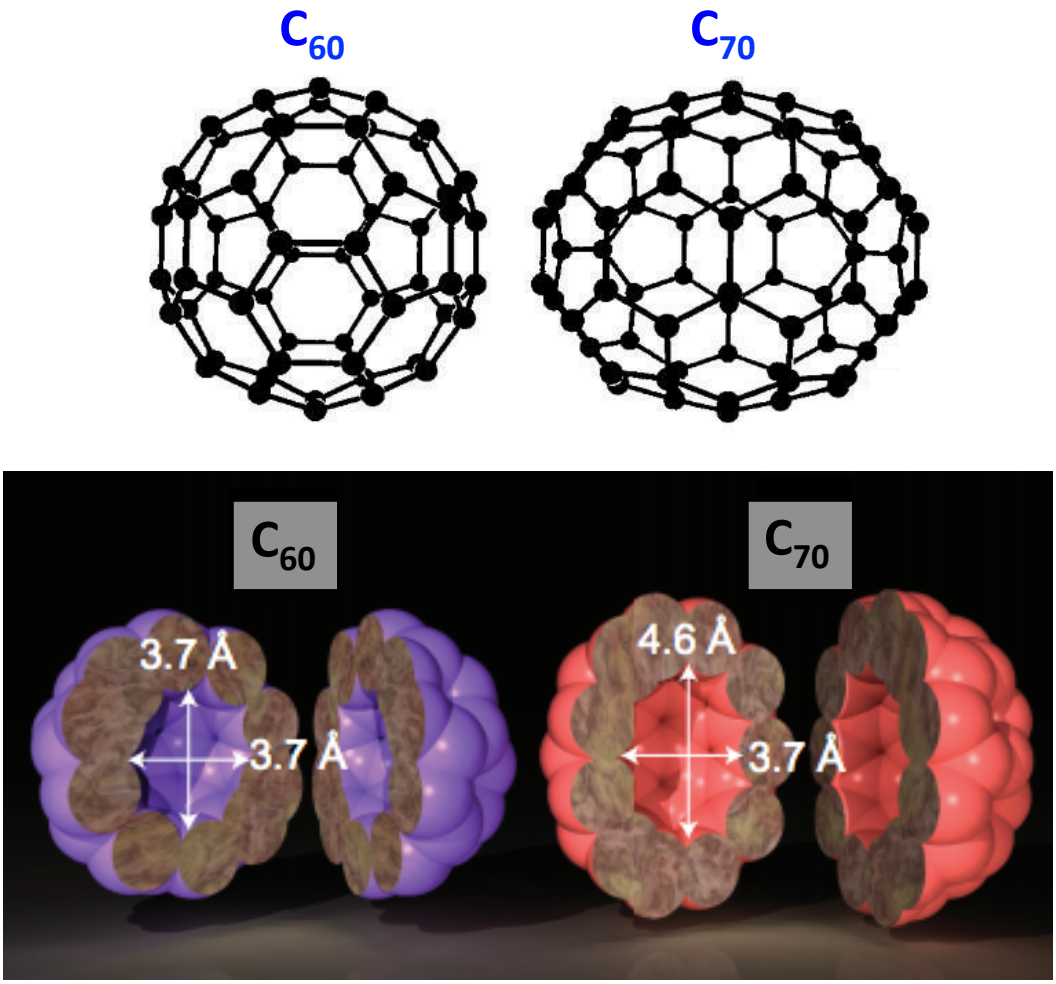

Figure 19 Structures of fullerene, C_{60} and C_{70}. [29]

4.1 Controlled self organization of fullerene, C_{60}

Spontaneous supramolecular self-assemblies of fullerene C_{60} molecules, based on π stacking interactions offers new methods towards the tunable fabrication of nanomaterials of higher complexity. Research efforts into the development of self-assembled C_{60} carbon nanostructures, has initiated structural diversity with molecular level precision. These nanostructures afford excellent optoelectronic properties beyond that of pristine $C_{60.}$ Several methods have been developed to afford C_{60} nanostructures of different shapes and sizes. With the crystal structure highly dependent on the method of preparation, the most common methods of synthesis include the vapor driven crystallization and solution driven self-assemblies such as the liquid-liquid interfacial precipitation (LLIP) method,[30,31] the template assisted dip drying method[32] and the drop drying process.[33] For example, slow evaporation of C_{60} solutions afford 1D nanowhiskers with the aspect ratio controlled by varying the evaporation rate and the molecular shape of the solvent used. A sublimation method yields C_{60} crystals with a 2D platelike morphology. For these different methods of assembling C_{60}, it is essential to understand the formation of the various close packed structures of the molecule involving three-dimensional (3D) π-π interactions. The morphology of nano/microstructures being highly dependent on the method of preparation, with a number of recent reports having established the formation of C_{60} crystals with specific geometries and dimensionalities. LLIP has been most common synthetic method for gaining access to different crystalline morphologies. Miyazawa *et al.* incorporated an LLIP method for the synthesis of microporous nanowhiskers[30] and hexagonal nanosheet[34] while Masuhara *et al.* reported fine crystals with tunable shapes and sizes by changing the antisolvent to solvent mixing ratio and temperature.[35] Jeong *et al.* used the LLIP method involving different types of alcohols to precisely control the dimensionalities of the C_{60} crystals.[36]

All these aforementioned methods are systematic approaches towards the tuning of dimensions, shapes and sizes of the C_{60} crystals, involving varying (i) the nature of the solvent, (ii) C_{60} concentration, (iii) the volume ratios of the binary solvent system and (iv) the crystallization temperature. Shrestha *et al.* demonstrated that the presence of amphiphilic molecules such as surfactants can drive the assembly of 3D flower like microcrystals at the liquid-liquid interface. Surfactants resemble surface-active molecules that adsorb at the air-liquid interface, altering the interfacial free energy of the solvent system.[37] In this work, the growth of C_{60} nanotubes at the interface of the binary solvent system was dominated by the

presence of these surface-active molecules preferably adsorbed in the central regions of the nanotubes of the fullerene, thereby facilitating radial growth.[37] Iyer *et al.* demonstrated another well established bottom up assembly with the use of fullerene-based superstructures using silver nanoparticles as 'nanoreactors'.[38] Interestingly, all these micron and nano structures of C_{60} molecules have not only maintained but could also exhibit enhanced electrical and optical properties relative to the bulk pristine C_{60}.

Thus, there has been considerable effort towards developing novel methods of self assembly of fullerene C_{60} to obtain exquisite control over the micron architectures of the material, with a view of tailoring their properties for specific applications. The next section of this chapter will describe a novel method of controlling the self-assembly of C_{60} molecules using a binary solvent system devoid of surfactants, using a VFD. The key concept was to design and develop a simple method to afford micron-structured nanotubules of the C_{60} in high yield with scalability, economic and environmental sustainability incorporated into the process. The method was devised to control the growth of the C_{60} molecules without chemical stabilizers and surfactants. The method was also extended to controlling the growth of fullerene C70 into novel self assembled arrays.

4.2 VFD-mediated self assembly of C_{60} molecules

This section was adapted from a publication entitled 'Surfactant free fabrication of fullerene C_{60} nanotubules under shear,' authored by **Kasturi Vimalanathan**, Rekha G. Shrestha, Zhi Zhang, Tomonobu Nakayama and Colin L. Raston, which has been submitted to *Angiewandte Chemie* and is currently under review.

Abstract: A method for controlling the self-assembly of fullerene C_{60} into nanotubules in the *fcc* phase, devoid of entrapped solvent has been established in a thin film vortex fluidic device. The micron length C_{60} nanotubules with individual hollow diameters 100 to 400 nm are formed under continuous flow processing during high shear micromixing of water and a toluene solution of the fullerene, in the absence of surfactant, and without the need for further down stream processing. HRTEM revealed pores on the surface of the nanotubules, and the isolated material has much higher response to small molecule sensing than for analogous material formed using multistep batch processing.

Fullerene (C_{60}) can assemble into a variety of architectures which have potential in electronic, magnetic and photonic applications.[3,39-40] A number of different methods for their synthesis have been developed including the vapour driven crystallization, solution driven self-assembly and liquid-liquid interfacial precipitation (LLIP). Well defined morphologies of C_{60} nanowhiskers/nanorods,[30, 41-44] nanowires,[45] nanobowls,[46] fullerene flowers,[36,37] nanotubes[47,48,49] and nanosheets of various shapes[34,50] have been extensively studied. Most of the methods use supersaturated solutions of C_{60} in solvent systems, amphiphilic surfactants to control crystal growth,[37] and toxic solvents such as benzene[37,44] and dichlorobenzene.[48]

In this work we establish the ability to organize C_{60} into hollow micron sized crystalline nanotube structures (nanotubules) under shear. This is within an immiscible benign binary solvent system, toluene and water, and in the absence of any surfactant, which is important for surface responsive applications of the materials. The formation of the nanotubules was amplified by the mechanoenergy within dynamic thin films in a vortex fluidic device (VFD), Figure 20. This microfluidic platform can operate under the so-called confined mode of operation for a finite volume of liquid or under continuous flow, Figure 20, where scalability of the process is addressed up front. The shear stress within the VFD, under either mode of operation, is effective in controlling chemical reactivity and selectivity,[52,53] exfoliating

graphene and boron nitride,[53] protein folding,[54] fabricating toroidal arrays of SWCNTs,[55] laterally 'slicing' single and multiple shell CNTs,[56] other materials proceesing,[58] probing the structure of self organised systems,[58,59] and accelerating enzymatic reactions.[6]

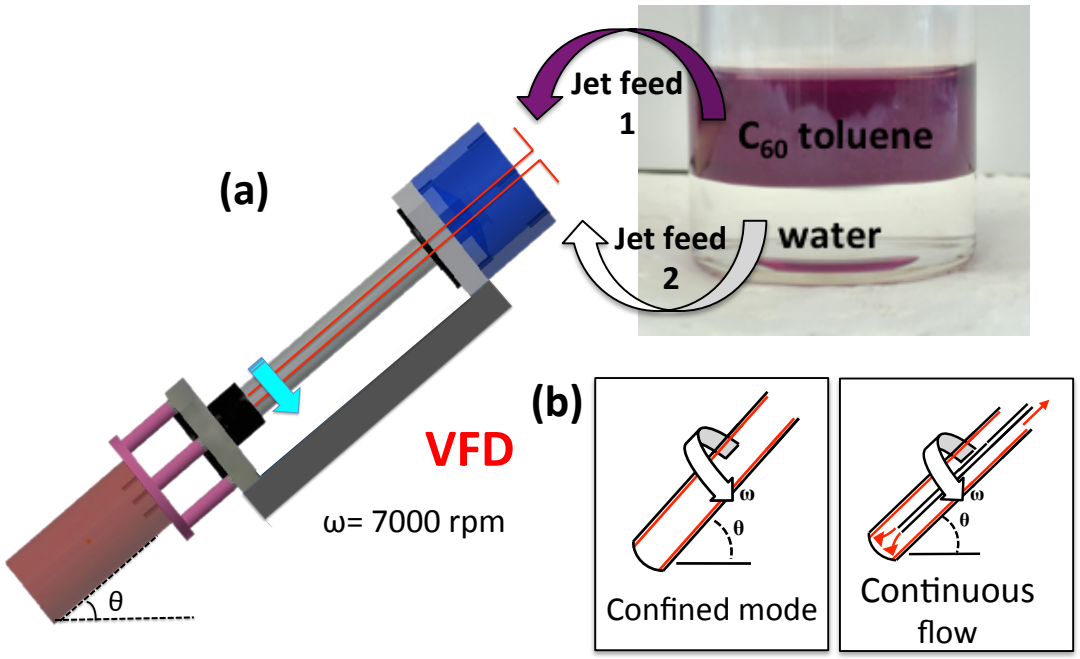

Figure 20 (a) Schematic of a VFD at the optimized conditions for fabricating C_{60} nanotubules (θ 45° and ω 7000 rpm) using a toluene solution of C_{60} (2 mg/L) and water in a 1:1 ratio, under (b) the confined mode for a finite volume of the two liquids in the rapidly rotating tube, or continuous flow where water and a toluene solution of C_{60} are delivered to the bottom of the tube.

Stable nanotubules, with pores of uniform size on the surface, Figure 21 and 22, rapidly form at room temperature within minutes of processing time, with the product readily collected. For continuous flow, the processing time is for a finite volume of liquid delivered to the bottom of the tube to whirl up the tube and exit at the top. The direct formation of face centered cubic (*fcc*) C_{60} devoid of included solvent is particularly noteworthy, and while related nanotubules have been reported, they required heating to remove included solvent,[50] and can involve the use of surfactants.[37] The choice of solvent mixture, the level

of supersaturation difference of C_{60} in toluene, the ratio of toluene to water, the rotational speed and flow rate (continuous flow) were systematically optimized for exclusive formation of hollow nanotubules. Their size and shape were established using SEM, Figure 21, being ca 0.4 to 3 µm in length, with a hollow inner diameter *ca* 100 to 400 nm.

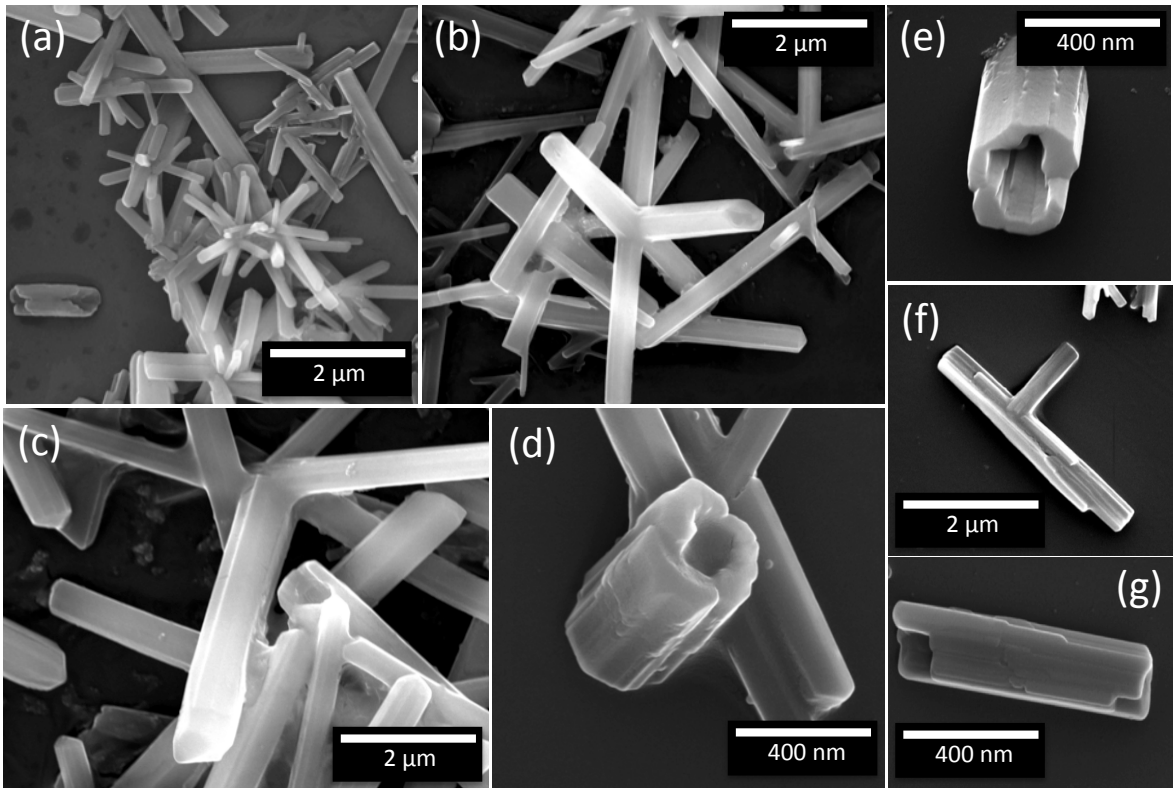

Figure 21 SEM images of C_{60} nanotubules ~0.4 to 3 µm long with a hollow inner diameter ~100 to 400 nm.

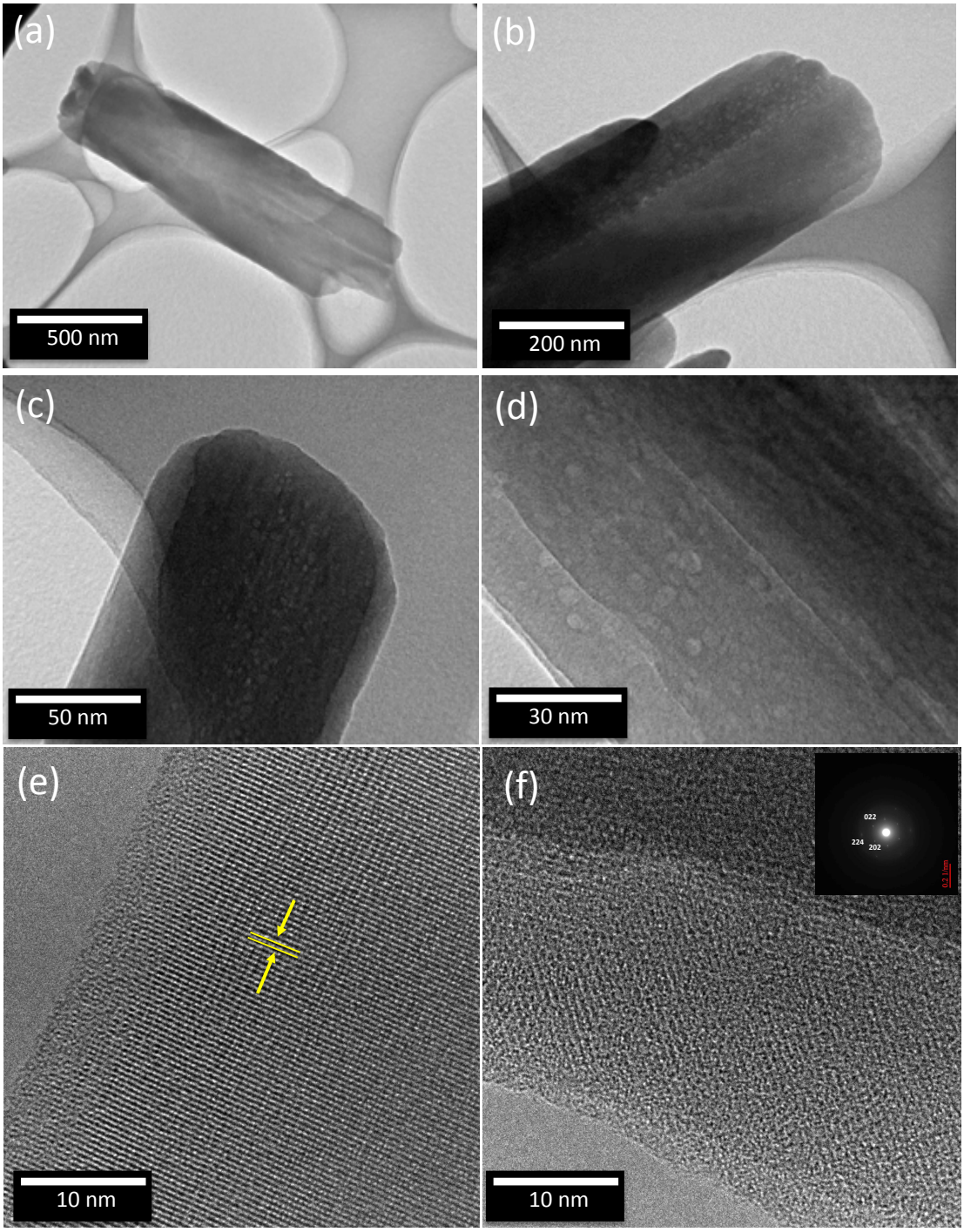

Figure 22 (a-f) TEM images, SAED patterns and HRTEM images of C_{60} nanotubules afforded in the VFD. The distance marked in the HRTEM of figure (e) is 0.88 nm.

Raman spectra (Figure 23) have characteristic peaks for pristine C_{60} corresponding to the typical A_g and H_g vibrational modes. The major bands at 500 and 1471 cm^{-1} correspond to the A_g vibrational modes, which are comparable to those of as received $C_{60,}$ at 495 and 1467 cm^{-1} respectively. Other distinct bands at 271, 431, 712, 770, 1431, and 1569 cm^{-1}, correspond to the active H_g vibrational modes. There was no distinct red shift for the band centered at 1467 cm^{-1}, which corresponds to the A_g mode, and unequivocally confirms that the nanotubules are comprised of self assembled C_{60} molecules.[61,62] Any significant downshift of the pentagonal pinch mode (the peak at ~ 1467 cm^{-1}) would be indicative of polymerized C_{60}, as a [2+2] cycloaddition product.[37,45]

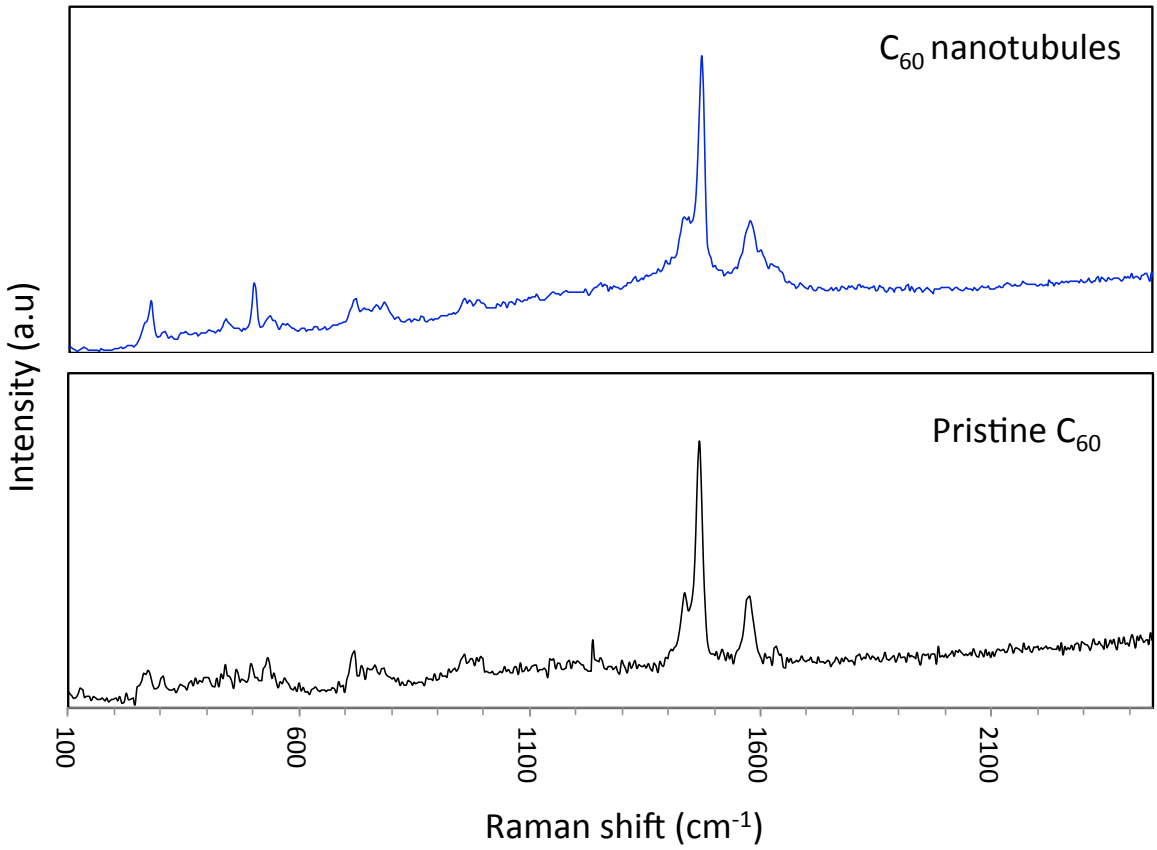

Figure 23 Raman spectra for as-received pristine C_{60} and the nanotubules respectively, obtained using a 532 nm laser at room temperature.

The powder XRD patterns, Figure 24, of the nanotubules and as received C_{60} are in agreement. The major peaks at 2θ 10.8°, 17.7° and 20.8° correspond to the (111), (220) and the (311) planes respectively, and the calculated lattice constant, a, is 14.18 ± 0.01 Å which corresponds to *fcc* C_{60}.[30,44] The SAED pattern, Figure 22f, of the nanotubules can be indexed to the (022), (224) and (202) crystallographic planes along the (111) zone axis of

the *fcc* structure which is devoid of included solvent[48] and is consistent with the XRD data. This is in contrast to the need for annealing to remove or allow for the evaporation of included solvent for tubules prepared using conventional batch processing.[37,43,49]

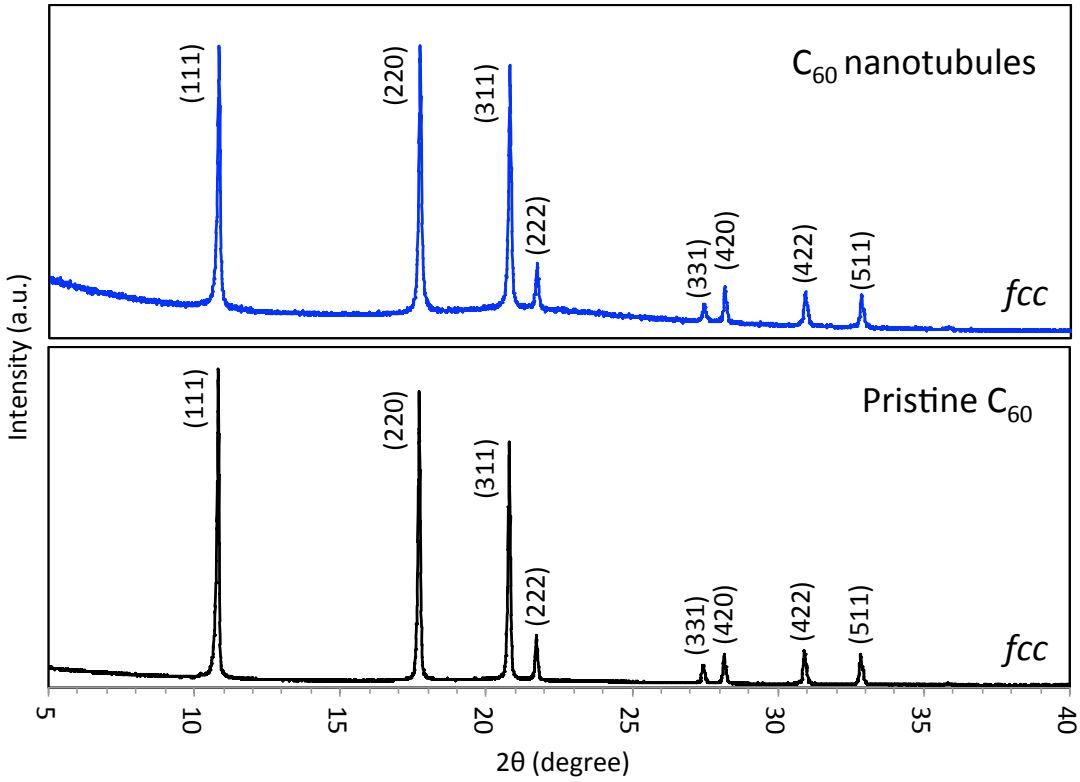

Figure 24 XRD patterns of the nanotubules (and pristine C_{60}) establishing the *fcc* phase.

Thermogravimetric analysis (TGA) (Appendix G) in air showed a slight ~4.3 wt% weight loss between 60° to 200°C which could be due to the presence of physisorbed toluene and/or water. The XRD and SAED results unequivocally establish *fcc* C_{60} for which the interstices are too small to accommodate toluene molecules. A significant weight loss of ~83.4 wt, occurred at 650°C which corresponds with the expected sublimation of C_{60}, with a final residual weight of approximately 3.6% of the starting mass at 950°C.

SEM and the HRTEM images (Figure 21 and 22) establish that the majority of the nanotubules are connected into flower-like structures, with small amounts of freestanding nanotubules. The growth of C_{60} nanorods has been extensively studied using the LLIP method, with the growth self assembled 1D structured rods/whiskers at the interface of a variety of binary solvent systems.[30,36,37,41-49] Depending on the nature and concentration of surfactants, the growth of hollow C_{60} nanotubes at the interface under ultrasonication also affords flower-like structures.[37] Here formation arises from adsorption of surfactants, particularly in the middle

regions of the nanotubes rather than in the ends, which controls the direction of growth.[11] In the present study the growth of the nanotubules is in the absence of surfactants. Presumably the interfacial tension between toluene and water plays an important role. Under shear the otherwise immiscible liquids in the VFD appear uniformly mixed, but post VFD processing they spontaneously phase separate, a feature which has been established for a number of immiscible systems post VFD processing.[63,64] We propose that micelles of water provide templates for the growth of the toluene around them, noting that the inner surface of the tubules are smooth rather than faceted, unlike the outer edges, which approximate to flat surfaces intersecting in hexagonal rods.

Although much work is still to be done to further confirm this occurrence, the hypothesis remains that these structures that form at the interface carry hydrophobic and hydrophilic characteristics. Thus, the hydrophobicity of carbon nanomaterials causes selective growth around such templates at the van der Waals limit. The Raston research group is currently working on real-time SANS experiments to establish and confirm the formation of such nanostructures at the interface of toluene and water which would then further corroborate our findings. This is a major research project in its own right.

The use of an immiscible toluene/water solvent system at a 1:1 volume ratio relates to our previous work on the formation of stable self assembled toroids of single walled carbon nanotubes (SWCNTs) rings with controllable diameter.[55] This also involves the use of the VFD, with the shear resulting in tightly coiled toroids. The concentration of the solvated C_{60} molecules in toluene, close to 2 mg/mL and the 1:1 volume ratio of toluene/water was critical for their formation with other concentrations and volume ratios resulting in mixtures of nanostructures with no control over their morphologies (Appendix E). The shear generated within the VFD was effective in generating uniform nanotubules for a rotational speed of 7000 rpm with the tube inclined a 45°. Other rotational speeds and inclination angles, other than the optimized conditions for the formation of the nanotubules, resulted in a mixture of nanostructures with no control over the morphologies (Appendix E). The optimized conditions are in accordance with the presence of a mechanical resonance present within the device around 6950 rpm.[52] This mechanical resonance is a driving force towards the generation of Faraday wave like fluidic responses, which can dramatically increase the yields of organic reactions.[51,52] The operating condition critical towards the formation of these C60

nanotubules in high yield was the residence time of the fluid in the hemisphere at the bottom of the tube which is governed by the rotational speed, inclination angle and flow rate. At high shear rates, a helical wave is formed within dynamic thin films, which is likely to provide additional shearing from the viscous drag as the liquid whirls up the tube, in forming the C_{60} nanotubules, which is in high yield. Interestingly the use of ultrasonication as another form of mechanical energy is effective for the formation of similar nanotubules,[37,49] but this requires the use of surfactants and heating post processing to remove included solvent molecules. Overall the VFD is efficient in controlling the radial growth of the nanotubules, directly into the *fcc* phase of C_{60}.

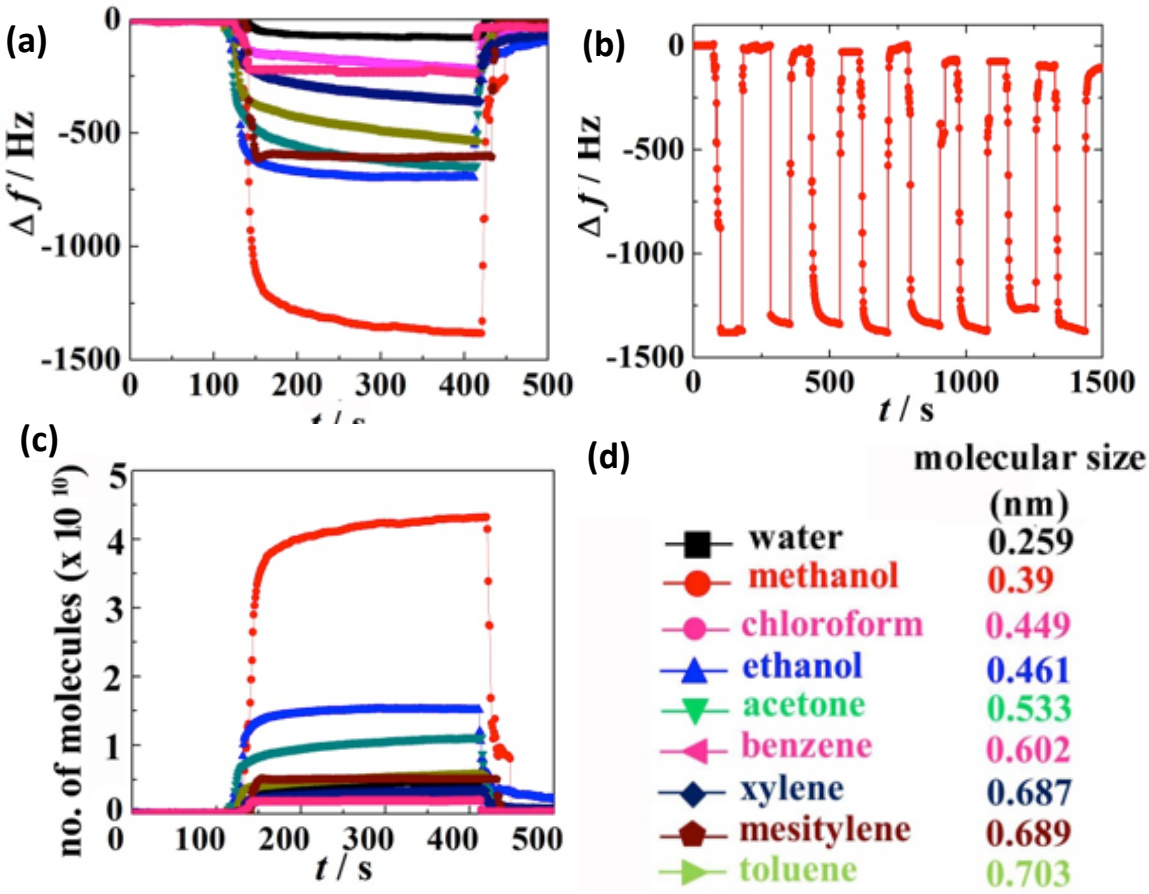

Figure 25 (a) QCM frequency shifts of C_{60} nanotubules with uniform pores coated electrode upon exposure to different solvent vapors, (b) repeatability test of the electrode upon exposure and removal of methanol vapors, (c) number of molecules adsorbed with time, and (d) the legends common for figures (a) to (c) shown in the order of their molecular sizes that are estimated by considering molecular structure and atomic radii of the solvents.

These C_{60} nanotubules with relatively uniform pores have potential for vapour entrapment and effective sensing. To this end, we measured their vapour-sensing capacities for different solvent molecules using the quartz crystal microbalance (QCM) technique, Figure 25, and compared the sensing capacities with nanotubules fabricated using the previously published LLIP method (Appendix E).[49] Results of typical time dependent frequency shifts for the nanotubules (prepared in the VFD) coated QCM electrode upon exposure to water, methanol, ethanol, acetone, benzene, toluene, mesitylene, xylene and chloroform are shown in Figure 25a. The results show that upon exposure of electrode to different solvent vapors, frequency shifts occur at a fast rate and the magnitude of frequency shifts depends on the nature of the molecules. Smaller organic solvent molecules such as chloroform and methanol gave a large decrease in frequency arising from strong physical adsorption whereas water resulted in a relatively lower change in the frequency; the frequency shifts for the electrode are 80 Hz for water, 1380 Hz for methanol, 700 Hz for ethanol, 645 Hz for acetone, 530 Hz for toluene, 220 Hz for benzene, 360 Hz for xylene, 610 Hz for mesitylene, and 240 Hz for chloroform (Figure 25a). The repeatability of the fullerene nanotube coated electrode was investigated by recording frequency shifts upon alternate exposure and removal of the methanol. Good repeatability and reproducibility upon alternate exposure and removal of methanol vapor have been demonstrated for the electrode (Figure 25b). Figure 25c shows that smaller the molecule of solvent higher is the adsorption. However, water and chloroform show some discrepancies. Considering the polar nature of water and chloroform (comparing other organic solvents), these molecules find hard to enter the voids present inside the crystals of fullerene, showing less adsorption. These values for water and chloroform are very close to that for without voids (Appendix E) confirming that whatever the adsorption occurs that occurs on to the surface only. This establishes a higher selectivity of the fullerene tubes towards smaller aromatic solvents and less selectivity towards polar solvents. The change in frequencies for the nanotubules with and without pores (Appendix E) as a result of solvent adsorption indicates that the presence of pores on the surface enhances the physi-adsorption. The formation of these pores was only possible in dynamic thin films in the VFD.

We have established a facile one step method for the controlled growth of stable nanotubules of fullerene C_{60} within a vortex fluidic device, as a thin film microfluidic platform. Importantly, *fcc* material is obtained directly in the absence of surfactants in the conventional sense, and without the incorporation of solvent molecules. This avoids the need for post-processing

heating to remove the solvent, and the material is more suitable for various applications, in the absence of surface contaminating surfactants. The use of an immiscible solvent system in the presence of shear in controlling the growth of complex nanostructures is without precedent, and the scene is set to use this bottom up strategy for the growth of a diverse range of materials, with the likelihood of accessing different morphologies, and size and shape of the particles of the materials. This is further encouraged by the application of the self-assembled material in a sensor, with the presence of pores on the surface being able to enhance the physic-adsorption of solvent vapours
compared to traditional methods of processing.

4.2.1 Experimental design of the fabrication of surfactant free fullerene C_{60} nanotubules

In a typical experiment C_{60} (99685-96-8, 99+%, BuckyUSA) was added to toluene (2 mg/mL) and the mixture was allowed to stand overnight, whereupon it was filtered to remove any undispersed C_{60} and impurities. A mixture of a toluene solution of C_{60} (0.5 mL) with water (0.5 mL) was placed in a glass tube (as a readily available borosilicate nuclear magnetic resonance (NMR) tube (ID 16.000 ± 0.013 mm), which was spun for 30 minutes at an optimized speed of 7000 rpm and inclination angle of 45 degrees. For the confined mode of operation, a finite volume of total liquid is required which was set at 1 mL. This ensures that a vortex is maintained to the bottom of the tube for moderate rotational speeds to avoid different shear regimes, and without any liquid exiting at the top the tube. Stewartson/Ekman layers prevail in the dynamic thin films, which arise from the liquid accelerating up the tube with gravitational force acting against them.[52] The scalability of the process was then investigated under continuous flow, using two jet feeds, one delivering the above toluene solution of C_{60} and the other water, both at the combined optimised flow rate of 1 mL/min with intense micromixing resulting in the formation of what appears to be a single phase with then spontaneous phase separation as the liquid exits the tube. A systematic evaluation of the flow rates was carried out with 1mL/min affording the highest yield (~ 85 %) of hollow C_{60} nanotubules. The formation of the nanotubules is facilitated initially at the hemispherical bottom of the tube where there is instability of the liquid boundary layer.[52] The viscous drag as the liquid whirls up the tube creates shear and facilitates micromixing, along with that from the Stewartson/Ekman layers.

4.2.2 Quartz Crystal Microbalance (QCM) Test

Sample preparation for quartz crystal microbalance studies

QCM electrode was prepared as follows: 2.0 mg of C_{60} nanotube was dispersed in toluene (1 mL). The mixture was then sonicated for 3 minutes (mild intensity) in a bath sonicator, and the integrity of the nanotubules was confirmed using SEM. 3 µL of this dispersion was drop casted on the QCM Au electrodes. The electrode was dried at 60 °C in vacuum for 24 hours before measurements. The modified QCM electrode then was attached to the QCM instrument and exposed to the solvent in a sealed space to prevent the escape of the vapors during the adsorption measurements. Between measurements, the electrode was exposed to air to desorb the solvent vapor. The recovery of the initial frequency value was taken as an indication of complete desorption. The change in mass, m ($g.cm^{-2}$) of the material deposited on the surface of the QCM electrode (due to adsorption and desorption of solvent molecules) is related to the change in the oscillating frequency of the quartz electrode. A resonance frequency of 9 MHz (AT-cut) was used and the frequency of the modified QCM electrode (fullerene coated on Au QCM electrode) was recorded upon exposure to different solvent vapors at 25 °C.

The frequency change (Δf) corresponds to the sample amount loaded (m) on the QCM electrodand can be calculated from Sauerbrey equation[65]

$$\Delta f = (2 f_0^2 / \sqrt{\rho_Q \mu_Q}) m`$$

Equation 1

where f_o (Hz) is the natural frequency of the quartz crystal, ρ is the quartz density (2.649 g cm^{-3}), and μ_Q is the shear modulus (2.947×10^{11} g $cm^{-1}s^{-2}$).

4.2.3 Acknowledgements

The authors gratefully acknowledge support of this work by the Australian Research Council and the Government of South Australia, and the Australian Microscopy & Microanalysis Research Facility (AMMRF) for accessing microscopic facility. The authors would also like to thank Dr. Jack Evans for providing the XRD data and Professor Allan Pring for valuable discussions.

4.3 References

1 Ruoff, R. S., Tse, D. S., Malhotra, R. & Lorents, D. C. Solubility of fullerene (C_{60}) in a variety of solvents. *The Journal of Physical Chemistry* **97**, 3379-3383, (1993).

2 Kroto, H. W., Heath, J. R., O'Brien, S. C., Curl, R. F. & Smalley, R. E. C_{60}: Buckminsterfullerene. *Nature* **318**, 162-163, (1985).

3 Prato, M. [60] Fullerene chemistry for materials science applications. *Journal of Materials Chemistry* **7**, 1097-1109, (1997).

4 Hoppe, H. & Sariciftci, N. S. Morphology of polymer/fullerene bulk heterojunction solar cells. *Journal of Materials Chemistry* **16**, 45-61, (2006).

5 Babu, S. S., Mohwald, H. & Nakanishi, T. Recent progress in morphology control of supramolecular fullerene assemblies and its applications. *Chemical Society Reviews* **39**, 4021-4035, (2010).

6 Itaka, K. *et al.* High-Mobility C_{60} Field-Effect Transistors Fabricated on Molecular-Wetting Controlled Substrates. *Advanced Materials* **18**, 1713-1716, (2006).

7 Segura, J. L., Martin, N. & Guldi, D. M. Materials for organic solar cells: the C_{60}/π-conjugated oligomer approach. *Chemical Society Reviews* **34**, 31-47, (2005).

8 Haddon, R. C., Brus, L. E. & Raghavachari, K. Electronic structure and bonding in icosahedral C_{60}. *Chemical Physics Letters* **125**, 459-464, (1986).

9 Hebard, A. F. *et al.* Superconductivity at 18 K in potassium-doped C_{60}. *Nature* **350**, 600-601, (1991).

10 Kratschmer, W., Lamb, L. D., Fostiropoulos, K. & Huffman, D. R. Solid C_{60}: a new form of carbon. *Nature* **347**, 354-358, (1990).

11 Jensen, A. W., Wilson, S.R. & Schuster, D.I. Biological Application of Fullerenes. *Bioorganic and Medical Chemistry* **4**, 767-779, (1996).

12 Dresselhaus M.S., Dresselhaus G. & Eklund P.C. Science of Fullerenes and Carbon Nanotubes. (*Academic Press*), (1996).

13 Georgakilas, V., Perman, J. A., Tucek, J. & Zboril, R. Broad Family of Carbon Nanoallotropes: Classification, Chemistry, and Applications of Fullerenes, Carbon Dots, Nanotubes, Graphene, Nanodiamonds, and Combined Superstructures. *Chemical Reviews* **115**, 4744-4822, (2015).

14 Allemand, P.-M. *et al.* Organic Molecular Soft Ferromagnetism in a Fullerene C_{60}. *Science* **253**, 301-302, (1991).

15 Schön, J. H., Kloc, C., Haddon, R. C. & Batlogg, B. A Superconducting Field-Effect Switch. *Science* **288**, 656-658, (2000).

16 Martín, N., Sánchez, L., Illescas, B. & Pérez, I. C_{60}-Based Electroactive Organofullerenes. *Chemical Reviews* **98**, 2527-2548, (1998).

17 Da Ros, T. & Prato, M. Medicinal chemistry with fullerenes and fullerene derivatives. *Chemical Communications*, 663-669, (1999).

18 Bisaglia, M. *et al.* C_3-Fullero-tris-Methanodicarboxylic Acid Protects Cerebellar Granule Cells from Apoptosis. *Journal of Neurochemistry* **74**, 1197-1204, (2000).

19 Krusic, P. J., Wasserman, E., Keizer, P. N., Morton, J. R. & Preston, K. F. Radical Reactions of C_{60}. *Science* **254**, 1183-1185, (1991).

20 Nakamura, E. & Isobe, H. Functionalized Fullerenes in Water. The First 10 Years of Their Chemistry, Biology, and Nanoscience. *Accounts of Chemical Research* **36**, 807-815, (2003).

21 Diederich, F. & Gomez-Lopez, M. Supramolecular fullerene chemistry. *Chemical Society Reviews* **28**, 263-277, (1999).

22 Núñez-Regueiro, M., Marques, L., Hodeau, J. L., Béthoux, O. & Perroux, M. Polymerized Fullerite Structures. *Physical Review Letters* **74**, 278-281, (1995).

23 Rao, A. M. *et al.* Photoinduced Polymerization of Solid C_{60} Films. *Science* **259**, 955-957, (1993).

24 Wang, Y. Photoconductivity of fullerene-doped polymers. *Nature* **356**, 585-587, (1992)

25 Wei, X. *et al.* New chemical method for selective generation of C_{70}^{n-} (n=1,2,3) anions and formation and properties of an aqueous colloidal solution of C_{70}. *Journal of the Chemical Society, Perkin Transactions 2*, 121-126, (1999)

26 McKenzie, D. R., Davis, C. A., Cockayne, D. J. H., Muller, D. A. & Vassallo, A. M. The structure of the C_{70} molecule. *Nature* **355**, 622-624, (1992).

27 Meingast, C., Gugenberger, F., Roth, G., Haluška, M. & Kuzmany, H. Structural phase transitions in 'hcp' C_{70} single-crystals. *Zeitschrift für Physik B Condensed Matter* **95**, 67-71, (1994).

28 Vaughan, G. B. M. *et al.* Orientational Disorder in Solvent-Free Solid C_{70}. *Science* **254**, 1350-1353, (1991).

29 Zhang, R. *et al.* Synthesis of a distinct water dimer inside fullerene C_{70}. *Nature Chemistry* **8**, 435-441, (2016).

30 Miyazawa, K., Kuwasaki, Y., Obayashi, A. & Kuwabara, M. C_{60} Nanowhiskers Formed by

the Liquid–liquid Interfacial Precipitation Method. *Journal of Materials Research* **17**, 83-88, (2002).

31 Miyazawa, K., Minato, J., Yoshii, T., Fujino, M. & Suga, T. Structural characterization of the fullerene nanotubes prepared by the liquid–liquid interfacial precipitation method. *Journal of Materials Research* **20**, 688-695, (2005).

32 Liu, H. *et al.* Imaging As-Grown [C_{60}]Fullerene Nanotubes by Template Technique. *Journal of the American Chemical Society* **124**, 13370-13371, (2002).

33 Wang, L. *et al.* Highly Enhanced Luminescence from Single-Crystalline C_{60} m-xylene Nanorods. *Chemistry of Materials* **18**, 4190-4194, (2006).

34 Marappan, S. & Miyazawa, K. Size-Tunable Hexagonal Fullerene (C_{60}) Nanosheets at the Liquid−Liquid Interface. *Journal of the American Chemical Society* **129**, 13816-13817, (2007).

35 Akito, M., Zhenquan, T., Hitoshi, K., Hachiro, N. & Hidetoshi, O. Fullerene Fine Crystals with Unique Shapes and Controlled Size. *Japanese Journal of Applied Physics* **48,** (2009).

36 Jeong, J., Kim, W.-S., Park, S.-I., Yoon, T.-S. & Chung, B. H. Synthesis and Characterization of Various-Shaped C60 Microcrystals Using Alcohols As Antisolvents. *The Journal of Physical Chemistry C* **114**, 12976-12981, (2010).

37 Shrestha, L. K., Hill, J. P., Tsuruoka, T., Miyazawa, K. I. & Ariga, K. Surfactant-Assisted Assembly of Fullerene (C_{60}) Nanorods and Nanotubes Formed at a Liquid–Liquid Interface. *Langmuir* **29**, 7195-7202, (2013).

38 Iyer, K. S., Saunders, M., Becker, T., Evans, C. W. & Raston, C. L. Nanorings of Self-Assembled Fullerene C_{70} as Templating Nanoreactors. *Journal of the American Chemical Society* **131**, 16338-16339, (2009).

39 Guss, W., Feldmann, J. & Gobel, E.D. Fluorescence from *X* traps in C_{60} single crytals. *Phys. Rev. Lett.,* **72,** 2644-2647, (1994).

40 Saito, R., Fujita, M., Dresselhaus, G. & Dresselhaus, M.S. Electronic structure of on graphene tubules based on $C_{60.}$ *Phys. Rev. B.*, **46,** 1804-1811, (**1992).**

41 Tachibana, M., Kobayashi, K., Uchida, T., Kojima, K., Tanimura, M. & Miyazawa, K. Photoassisted growth and polymerization of C_{60} nanowhiskers. *Chem. Phys. Lett.* **374,** 279-285, (2003).

42 Miyazawa, K., Kuwasaki, Y., Hamamoto, K., Nagata, S., Obayashi, A & Kuwabara, M. Structural characterization of C_{60} nanowhiskers formed by the liquid/liquid interfacial precipitation method. *Surf. Interface Anal.* **35,** 117-120, (2003).

43 Minato, J. & Miyazawa, K. Solvated structure of C_{60} nanowhiskers. *Carbon* **43,** 2837-2841, (2005).

44 Marappan, S., Miyazawa, K & Sasaki, T. Nanoporous fullerene nanowhiskers. *Chem. Mater.* **19,** 2398-2400, (2007).

45 Geng, J., Zhou, W., Skelton, P., Yue, W., Kinloch, I.A., Windle, A.H. & Johnson, B.F.G. Crystal structure and growth mechanism of unusually long fullerene (C_{60}) nanowires. *J. Am. Chem. Soc.* **130,** 2527-2534, (2008).

46 Zhang, Y., Jiang, L., Li, H., Fan, L., Hu, W., Wang, C., Li, Y. & Yang, S. Single crystalline C_{60} nanostructures by sonophysical preparation: tuning hollow nanobowls as catalyst supports for methanol oxidation. *Chem. Eur. J.* **17,** 4921-4926, (2011).

47 Marrapan, S. & Miyazawa, K. Selective precipitation of tubular like short fullerene (C_{60}) whiskers at liquid liquid interface. *CrystEngComm* **12,** 4146-4151, (2010).

48 Barzegar, H.R., Nitze, F., Malolepszy, A., Stobinski, L., Tai, C.W. & Wågberg, T. Water assisted growth of C_{60} rods and tubes by liquid-liquid interfacial precipitation method. *Molecules.* **17,** 6840-6853, (2012).

49 Shrestha, L.K., Shrestha, R.G., Yamauchi, Y., Hill, J.P., Nishimura, T, Miyazama, K., Kawai, T., Okada, S., Wakabayashi, K & Ariga, K. Nanoporous carbon tubes from fullerene crystals as the π-electron carbon source. *Angew. Chem. Int. Ed.* **54**, 951-955, (2015).

50 Marrapan, S., Miyazawa, K, Hill, J.P. & Ariga, K. Solvent engineering for shape shifter pure fullerene (C_{60}). *J. Am. Chem. Soc.* **131,** 6372-6373, (2009).

51 Britton, J., Chalker, J.M. & Raston, C.L. Rapid vortex fluidics: Continuous flow synthesis of amides and local anaesthetic lidocaine. *Chem. Eur. J.* **21,** 10660-10665, (2015).

52 Britton, J., Dalziel, S.B., & Raston, C.L. Continuous flow Fischer esterifications harnessing vibrational-coupled thin films fluidics. *RSC Advances.* **5**, 1655-1660, (2015).

53 Chen, X., Dobson, J.F. & Raston, C.L. Vortex fluidic exfoliation of graphite and boron nitride. *Chemical Communication* **48**, 3703-3705, (2012).

54 Yuan, T.Z., Ormonde, C.F.G., Kudlacek, S.T., Kunche, S., Smith, J.N., Brown, W.A., Pugliese, K.M., Olsen, T.K., Iftikhar, M., Raston, C.L. & Weiss, G.A. Shear stress-mediated refolding of proteins from aggregates and inclusion bodies. *ChemBioChem*.

16, 393-396, (2015).

55 Vimalanathan, K., Chen, X. & Raston, C.L. Shear induced fabrication of intertwined single walled carbon nanotube rings. *Chemical Communication* **50,** 11295-11298, (2014).

56 Vimalanathan, K., Gascooke, J.R., Suarez-Martinez, I., Marks, N.A., Kumari, H., Garvey, C.J., Atwood, J.L., Lawrance, W.D. & Raston, C.L. Fluid dynamic lateral slicing of high tensile strength carbon nanotubes. *Scientific Reports* **6,** (2016).

57 Tong, C.L., Boulos, R.A., Yu, C., Iyer, K.S. & Raston, C.L. Continuous flow tuning of ordered mesoporous silica under ambient conditions. *RSC Advances,* **3**, 18767-18770, (2013).

58 Mo, J., Eggers, P.K., Chen, X., Ahamed, M.R.H., Becker, T., Lim, L.Y. & Raston, C.L. Shear induced carboplatin binding within the cavity of a phospholipid mimic for increased anticancer efficacy. *Scientific Reports* **5**, 10414, (2015).

59 Iyer, K.S. & Raston, C.L. Fabrication of laterally 'sliced' metal plated carbon nanotubes under aqueous continuous flow conditions. *J. Mater. Chem.* **17**, 4872-4875, (2007).

60 Britton, J., Meneghini, L. M., Raston, C. L. & Weiss, G. A. Accelerating Enzymatic Catalysis Using Vortex Fluidics. *Angew. Chem*. **2016**, doi:10.1002/ange.201604014

61 Kuzmany, H., Pfeiffer, R., Hulman, M. & Kramberger, C. Raman spectroscopy of fullerenes and fullerene nanotube composites. *Philos. Trans. R. Soc. London, Ser. A.* **362,** 2375-2406, (2004).

62 Martin, M.C., Koller, D., Rosenberg, A., Kendziora, C. & Mihaly, L. Infrared and Raman evidence for dimers and polymers in RbC_{60}. *Phys. Rev. B: Condens. Matter,* **51**, 3210, (1995).

63 Britton, J. & Raston, C.L. Continuous flow vortex fluidic production of biodiesel. *RSC Advances* **4,** 49850-49854, (2014).

64 Luo, X., Smith, P., Raston, C.L. & Zhang, W. Vortex Fluidic Device- Intensified aqueous two phase extraction of C-Phycocyanin from *Spirulina Maxima. ACS Sustainable Chem. Eng.* **4***,* 3905-3911, **(**2016).

65 Sauerbrey, G. Verwendung von Schwingquarzen zur Wägung dünner Schichten und zur Mikrowägung. *Zeitschrift für Physik* **155**, 206-222, (1959).

5 GRAPHENE

5.1 Introduction

Graphene is the most recently isolated carbon nanostructure, representing a conceptually new class of materials that is only one atom thick and is a building block for other carbon nanomaterials with different dimensionalities. Graphene can be wrapped up into 1D nanotubes or stacked into 3D graphite.[1] In 2004, Andre Geim and Konstantin Novoselov mechanically exfoliated single layered graphene sheets from bulk graphite using the 'scotch tape' method.[2] Since then graphene has been the most enticing nanomaterial, being extensively explored in terms of developing new techniques to exfoliate single layered sheets, precisely control the morphology of the nanomaterial, the formation of hybrid materials amongst others, to be used in a wide range of applications. Its extraordinary properties include excellent electrical, thermal, mechanical, electronical and optical properties, with a high specific surface area, high chemical stability, high optical transmittance, high elasticity, high porosity, biocompatibility and it has a tuneable band gap.[1,3-5]

Graphene has other remarkable properties including (i) half-integer room temperature quantum Hall effect, (ii) long range ballistic transport, (iii) almost ten times greater electron mobility than of silicon (Si), (iv) behaves as a massless relativistic quasi particle charge carrier (Dirac fermion), and (v) quantum confinement giving rise to a finite band gap and Coulomb blockade effect.[2,6-9] Graphene is an example of a zero-bandgap conductor with approximately linear electron dispersion at the vicinity of the Fermi level at two points in the Brillouin zone (BZ). The negligible fraction of single layered graphene sheets was experimentally confirmed to consist of charge carriers that were indeed massless Dirac fermions, with carrier mobilities up to 200,000 $cm^2 V^{-1} s^{-1}$.[10-12] Applications of graphene are many and varied, including high frequency electronics, conductive coatings, composite fillers, energy generation and storage and bioapplications.[7,13-20] Graphene is also an ideal material for low cost electrode material in solar cells, batteries and sensors and as a transparent electrode in a liquid crystal device.[1,21-28]

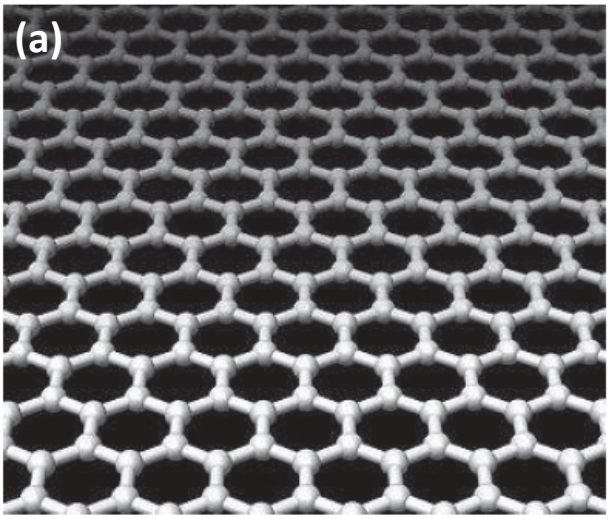

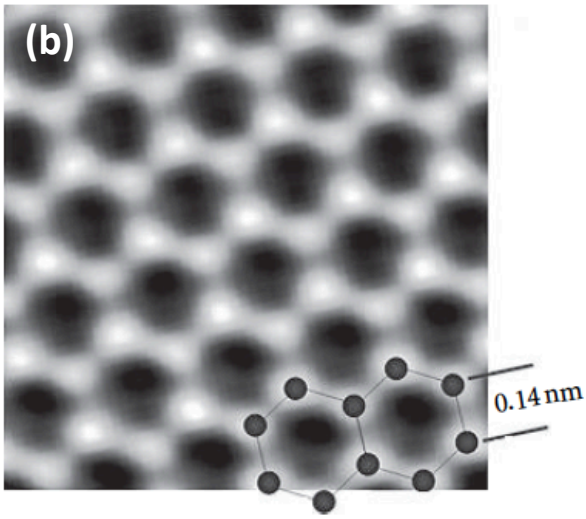

(c)

Properties	Graphene
Young's modulus	~1100 GPa
Fracture strength	125 GPa
Thermal conductivity	~5000 $Wm^{-1} K^{-1}$
Mobility of charge carrier	200000 $cm^2 V^{-1} s^{-1}$
Specific surface area	2630 $m^2 g^{-1}$

Figure 26 (a) Graphene, a flat monolayer of carbon atoms tightly packed into a two-dimensional (2D) honeycomb lattice, (b) high resolution transmission electron microscopy (HRTEM) of graphene, and (c) Physical properties of graphene.[5]

Mechanical exfoliation was the first method discovered to generate single layer graphene, as a form of micromechanical cleavage.[2] This so called 'Scotch tape' method, uses cellophane tape to peel off graphene layers from highly oriented pyrolytic graphite flakes, as defect free single layered graphene sheets. Defect free single, and also bi-layer, graphene sheets, have been fabricated using 'top down' and 'bottom up' approaches. The latter involves chemical and physical processes to form the 2D networks from small molecular blocks used in chemical vapour deposition method (CVD),[29,30] molecular beam epitaxy[31,32] or anodic bonding.[33,34] The 'top down' approach involves breakdown of bulk graphitic material into graphene sheets, usually achieved by mechanical exfoliation,[35] ball-milling,[36] electrochemical exfoliation,[37,38] oxidative intercalation exfoliation,[39-41] liquid

phase exfoliation[42-47] and the reduction of graphene oxide.[48] Although, the 'bottom up' approach has made significant contributions towards producing graphene sheets, the processes are high costing with the issue of scalability still a major challenge. On the contrary, the 'top down' approach using liquid phase exfoliation (LPE) shows greater potential to produce large quantities of defect free graphene. Overcoming the non covalent van der Waals interactions arising from the overlap of π orbital is required for exfoliation, and for a single sheet this has a high energy requirement. The ability to achieve this depends on a number of factors including the choice of solvent system coupled with shear forces to provide energy sufficient to balance the solvent-graphene interaction and intercalation of molecules or functionalization of the bulk graphite.[49] For exfoliation in a liquid medium, the choice of solvent is pivotal, in enhancing the affinity towards the carbon surface. Taking this into consideration, only a number of solvents are effective, namely N-methyl-pyrollidinone (NMP), N,N-dimethylformamide (DMF), benzyl benzoate and Y-butyrolactone.[44] Avoiding restacking of graphene sheets post exfoliation, arising from the strong π-π interactions between the layers of the bulk material is a common challenge to overcome. It can be circumvented using surface-active molecules or intercalation molecules such as phosphonated calixarenes,[50] lignin molecules,[51] and porphyrins.[52,53]

Graphite is most often intercalated with oxidizing acids or molecular oxidants as an interlayer of both neutral and ionized guest species.[41] The energetics of intercalation describes the complementing nature of both molecules with the energy required for exfoliation, balanced by the electron affinity and lattice energy of the ionic guest molecule. Neutral molecules such as Br_2, AsF_5 or $FeCl_3$ stabilize the exfoliated sheets by screening the repulsion between the negative charged guest species. Although the exfoliation via oxidization methods has high yielding outcomes, the functionalization of hydroxyls and epoxides on the surface of the sheets and intercalation molecules disrupts the electronic structure; defects on the basal planes also disrupts its electronic properties.[41]

Thus, it is without a doubt that research on producing high yielding synthetic methods to produce suspensions of pristine defectless single and bi-layer graphene sheets has been a key area of research. Such a focus on the production of high quality graphene, is driven by a commercial need for this 2D material to be used in applications in varying fields. The next

section of this chapter will describe a novel and facile templated method of simultaneously exfoliating and scrolling of graphene sheets in the presence of controllable mechanoenergy in the VFD, to facilitate the lifting and bending of the 2D sheets.

5.2 VFD mediated graphene scrolls formation from graphite

This section is the basis of a manuscript to be submitted for publication entitled, 'VFD induced templated graphene scroll formation from graphite,' authored by **Kasturi Vimalanathan**, Christopher Gibson, Xianjue Chen and Colin L. Raston.

Abstract: This section of the thesis describes the use of mechanoenergy within dynamic thin films whereby graphene scrolls are accessible directly from graphite flakes in a mixture of toluene and water in the absence of surfactants, in ca. 30% yield. Their formation occurs within dynamic thin films in a microfluidic vortex fluidic device where a uniform mixture of the otherwise immiscible solvents prevails. The simultaneous exfoliation and scrolling of individual sheets of graphene arises from the expected interfacial surface tension between toluene and water under high shear. Intra-layer spacing in the scrolls is 3.40 nm, which is beyond the van der Waals limit of graphene sheets, and it is consistent with unprecedented nano-dimensional solvent structures in the intensely mixed solvents acting as template.

Two dimensional (2D) graphene sheets have captured the attention of the research community due to their exquisite electrical, thermal and mechanical properties,[54-58] having promising capabilities of the material in many and diverse applications.[59-65] Graphene has a high Young's modulus (~ 1.100 GPa)[54] yet in some cases it can roll up to form graphene scrolls of varying compactness.[66-71] Less extreme flexibility is evident, for example, in wrapping graphene around fullerene C_{60} molecules,[72] the direct formation of 3D fullerenes from single layered graphene sheets[73] in the presence of magnetic nanoparticles,[74] and the inclusion of self-assembled molecules inside the scrolls.[75] Access to rolled up 1D graphene scrolls is important given they can take on properties of both carbon nanotubes and graphene sheets, as well as exhibiting more enhanced carrier mobility and mechanical strength.[71] Although graphene scrolls possess a tubular structure as for carbon nanotubes, they have more specific applications, especially in hydrogen storage[76,77] and in supercapacitors,[78] with the interlayer spacing within the scrolled graphene sheets being tunable, depending on the scrolling mechanism.[70] A variety of methods have been reported for exfoliating graphene sheets and

their conversion to graphene scrolls of various lengths, depending on the dimensions of the precursor graphite flakes.[66-71] However, these either afford composite materials or afford scrolls in low yield in bulk samples.

The challenge is to be able yet to gain access to graphene scrolls in high yield, ideally avoiding the use of damaging forms of mechanoenergy which can occur using long periods of sonication for example, avoiding the use of surfactants, the use of scroll enhancing nanoparticles such and fullerene (C_{60})[73] and magnetite,[74] and the growth and inclusion of other molecules.[75] These methods can limit potential application of graphene scrolls with potential damage to the surface and limited sustainability metrics given they are likely to generation waste streams or require post processing and purification.

We have developed a simple high yielding one step method under ambient conditions for fabricating stable graphene scrolls directly from graphite flakes, which are 7 to 10 μm in cross section in the basal plane. This involves the use of a mixture of water and toluene under shear, in the absence of surfactants and other auxiliary reagents such as scroll directing nanoparticles. Scroll formation arises from the expected liquid-liquid interfacial tension created from a mixture of immiscible liquids, which is amplified by the 'soft' mechanoenergy in dynamic thin films in the recently developed energy efficient microfluidic vortex fluidic device (VFD) (Figure 27). It is noteworthy that although the toluene/water nanorods are essential towards the fabrication of the graphene scrolls, they would be easily removed to obtain pristine scrolls and thus reducing the amount of wastes produced post processing

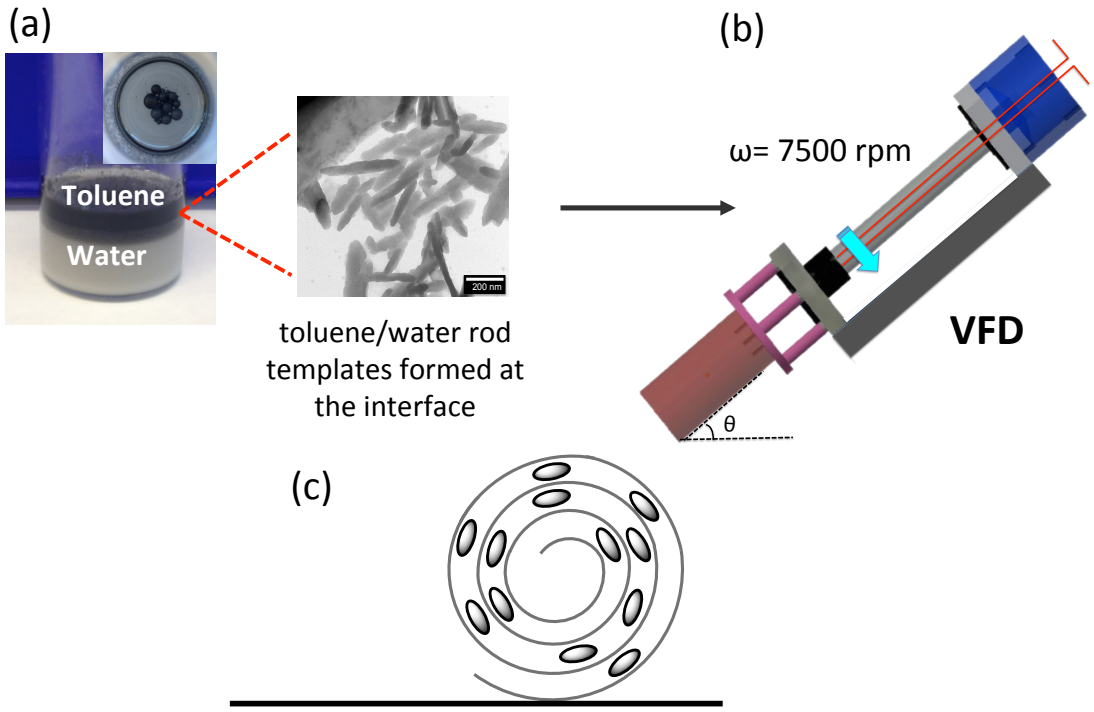

Figure 27 (a) Photograph image of the graphite toluene/water dispersion. Inset: photograph of the toluene water droplets, and TEM image of the toluene water nano-rod templates at the interface of the solvent mixture, (b) Schematic of the vortex fluidic device, which is at a 45° inclination angle and at the optimised rotational speed, 7500 rpm in the 20 mm OD glass tube, for the formation of graphene scrolls, and (c) Cartoon of the proposed composite structure involving the intercalation of nano-rod templates within the successive layers of the graphene scroll.

The VFD has a rapidly rotating tube with variable orientation relative to the horizontal position, θ, within which liquids form dynamic thin films for finite sub-millilitre volumes of liquid, as the so-called confined mode of operation of the device. The shear intensity in the films depends on a number of parameters, including the inclination angle θ and the rotational speed, which collectively define the interplay between centrifugal and gravitational forces within the films. The confined mode of operation of the VFD results in the formation of a thin film for a specific volume of liquid within the tube, which is 1 mL in the present study. Importantly there is a minimum threshold speed, which is required to maintain a vortex to the bottom of the tube, otherwise there are different regimes of shear within the liquid.[79] The VFD can also operate under continuous flow where jet feeds deliver solutions to the bottom of the tube which results in intense micro mixing, and collectively with the confined mode of operation, a number of applications of the device have been established. These operations of

the VFD is effective for a diversity of applications of the device. These include formation of toroidal arrays of SWCNTs,[80] controlling chemical reactivity and selectivity in organic synthesis,[79,81,82] exfoliation of graphene and *h*-BN in N-methylpyrollidinone (NMP),[47] generating mesoporous silica at room temperature with control of pore size and wall thickness,[83] controlling the polymorphs of calcium carbonate,[84] protein folding,[85] and probing the structure of self organized processes.[86,87]

The scrolls were stable in solution with reduced amount of graphite flakes remaining, with an estimated percent conversion of *ca* 30.0%. Control experiments established that the concentration of the starting materials was critical for effective and highest yield of formation of the scrolls of graphene sheets, with the minimal concentration of graphite set at 0.1 mg/mL. The maximum concentration of the initial graphene/toluene dispersion was optimised to be of 0.5 mg/mL with higher concentrations affording much lower yields or with no scrolls observed. This could be related to the high concentration of starting material perturbing the complex fluid dynamics, which is effective for scroll formation and/or the formation of the nano-rod structures which appear to template the formation of the scrolls (Appendix F).

The formation of graphene scrolls was established using atomic force microscopy (AFM) (Figure 28), transmission electron microscopy (TEM) and scanning electron microscopy results (Figure 29). The lengths of the scrolls are seemingly determined by the cross section dimensions of the precursor graphite flakes, with no evidence for lateral slicing of the scrolls. Indeed, the scrolls resemble the structural appearance of multi-walled carbon nanotubes (MWCNT) (Figure 30), which can be sliced in the VFD, but this requires additional energy from a pulsed Nd:YAG laser operating at 1064 nm.[88] Lateral slicing for the scrolls would require breaking a continuous array of carbon-carbon bonds across a micron or more, as a higher energy process relative to breaking a limited number of such bonds in slicing carbon nanotubes. The ratio of the two solvents was optimized, with an equal volume ratio of toluene and water yielding the aforementioned 30% yield (Figure 28 and 29).

The van der Waals interactions (tip/sample convolution effects) between the graphene scrolls and the AFM tip is likely to cause substantial deformations to the material being imaged. This is well known for CNTs, and such elastic deformation is expected for the scrolls. In addition, the relatively strong interactions between the scrolls and the substrate as well as the

reciprocal pressure from the bundled graphene scrolls stacked on each other is expected to contribute to their radial and axial deformations (Figure 28). The larger the diameter of the scroll the larger the expected deformation due to the high binding energies between the AFM tip and sample, which has been experimentally determined for CNTs, and is expected to decrease the width and height of the scrolls.[89-91]

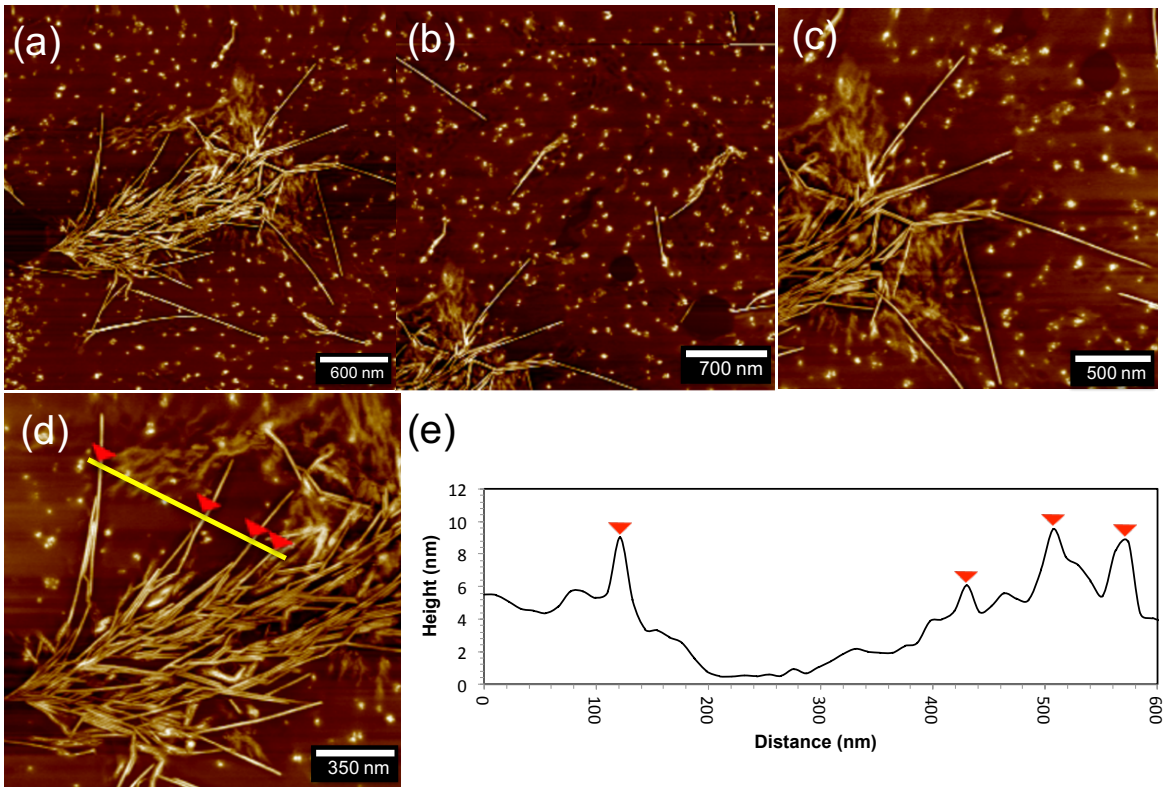

Figure 28 (a) – (d) AFM images of the graphene scrolls, and (e) associated height profile, with each scrolls having a height of *ca* 6-10 nm.

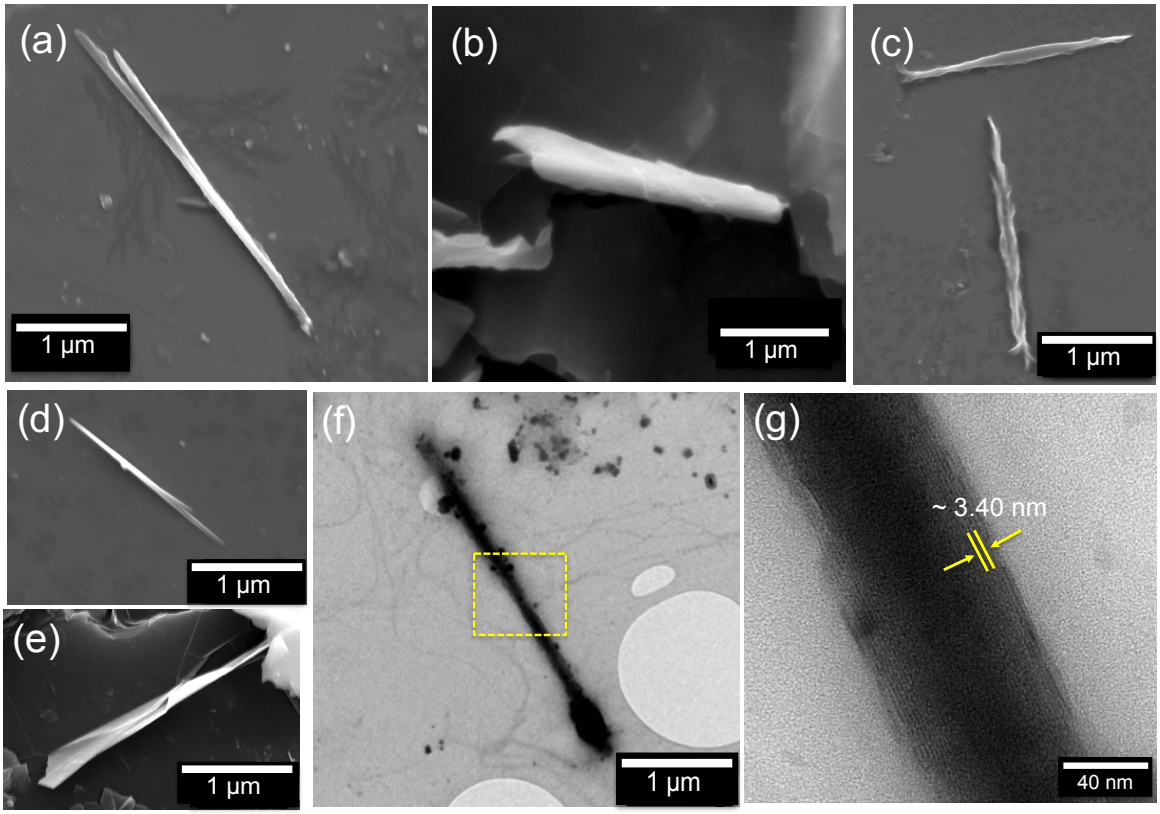

Figure 29 TEM and SEM images of the graphene scrolls; (a-e) SEM images, (f) TEM and (g) HRTEM of the area indicated in (f).

Previously, tightly scrolled graphene sheets were fabricated using shear forces in a related microfluidic spinning disc processor (SDP). However, the challenge endured, besides the low yield of scrolls, was the shredding and ripping of the graphene sheets resulting in much shorter length scrolls regardless of the dimensions of the starting material.[66] The mechanism of exfoliation and simultaneous scrolling of graphene sheets in the present work relates to a combination of both the controllable mechanoenergy generated within the dynamic thin films in the VFD and the presence of the interfacial tension arising from the immiscible solvent system under diffusion control. The shear forces would enable the dispersed graphite flakes to accelerate rapidly up the tube by the large centrifugal force and then downwards creating Stewartson/Ekman layers within the dynamic thin films.[47] Besides providing the energy for exfoliating the graphene sheets, the large shear forces within the VFD is likely to result in local bending of graphitic material in the presence of toluene and water. This relates to our previous work of the formation of stable self assembled toroids of single walled carbon nanotube (SWCNTs) rings of controllable diameter under shear, using the same VFD microfluidic platform in confined mode of operation.[80]

Drop casting the interfacial graphite material onto a silicon wafer resulted in the formation of toluene water rod-like nanostructures, as established using AFM and TEM (Appendix F**)**. Although the formation of these rod-like nanostructures has yet to be reported and needs further investigation, they are possibly acting as templates in assisting in the scroll formation. Control experiments established that changing the volume ratio of toluene to water resulted in either the formation of higher amounts of the toluene/water rod-like nanostructures with partial scroll formation or no scrolls, with evidence of exfoliation of the graphene sheets (Appendix F**)**. Thus, we propose that the lifting/bending of the graphene sheets into scrolls involves intercalation of these rod templates, Figure 27c, forming a close contact with the inner surface of the graphene sheets, overcoming the large van der Waals forces between the sheets.[47] This relates to water nanodroplets on the surface of graphene nanostructures facilitating bending/folding of graphene nanostructures.[92]

HRTEM (Figure 29) established the inside void of the scrolls to be approximately ~30 nm in diameter with the interlayer distance between the layers within each scroll *ca* ~3.40 nm, which is much larger than the typical interlayer distance of graphitic material (0.33 nm). This is consistent with intercalation of these toluene water rod present in solution after processing, which act as templates within the lattice spacing of the scrolls. The toluene water rod-like nanostructures were of approximately 200-300 nm in length and ~4-6 nm in height (Appendix F**)**. Residual traces of the solvents (toluene/water) surrounding the scrolls as well as physisorbed on the surface of the scrolls was observed, as established using Raman spectroscopy (Figure 30).

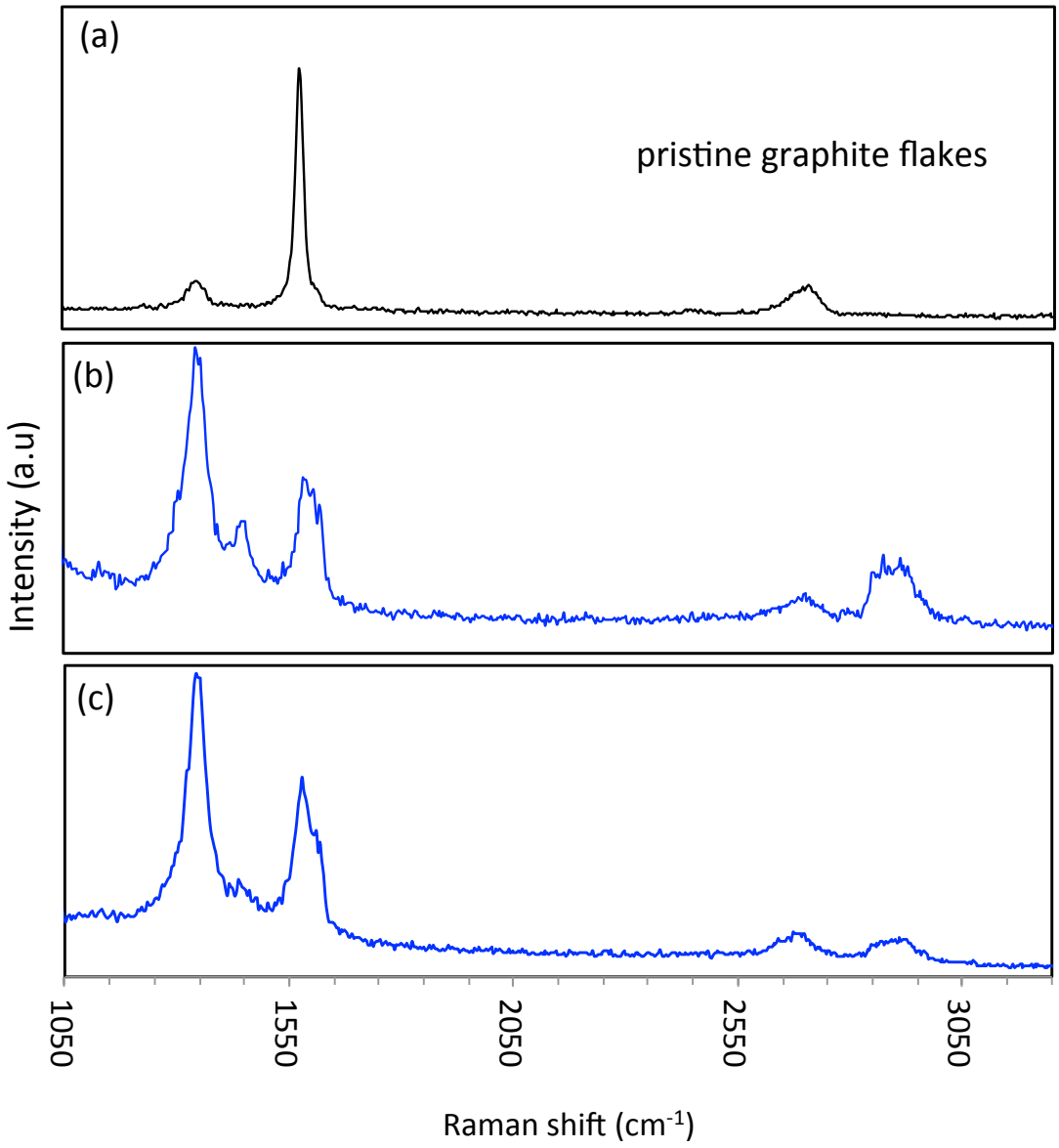

Figure 30 Raman spectroscopy of (a) he as received graphite flakes, and (b,c) of the graphene scrolls

Conformal Raman mapping (Figure 30) of the individual nanoscrolls deposited on SiO_2/silicon substrates confirmed the presence of the carbon nanoscroll structures, rather than unlikely MWCNTs for which they resemble in lateral length and cross section. The Raman spectra of these carbon nanoscrolls show a typical graphitic spectrum, D band (1338.2 cm^{-1}), G band (1574.7 cm^{-1}) and a 2D band (2678.4 cm^{-1}). A significant increase in the averaged Raman I_D/I_G ratio (corresponding to the D-band and G-band intensities) of the nanoscrolls compared to the as received graphite flakes were observed to be approximately 0.99 and 0.58 respectively,

suggesting a significant increase in the density defects of the scroll structures which can be well attributed to the scrolled edges.[93,94,95] A red shift of the G band (~20.8 cm^{-1}) was prominently observed for the nanoscrolls which is often related to the increasing number of graphene layers and disoriented stacked layers of graphene within the structures. As the graphene sheets scroll up, the changes of the C-C bond and phonon dispersion shifts the G band.[70] A broadening of the G band from the activation of the doubly degenerate zone centre E_{2g} phonon mode was also consistent with scroll formation, having a broader full width of half maximum (FWHM) observed within a range of 40 cm^{-1} to 90 cm^{-1} compared to pristine graphite flakes, which was approximately 20 cm^{-1}. The broadening of the G band was consistent with the blue shift of the 2D band which also coincides with the formation of graphene scrolls, which are presumably made up of a number of graphene sheets rolled up.[70] The Raman spectra of the carbon nanoscrolls were easily distinguishable from small diameter CNTs (SWCNT) from the absence of splitting of the G peaks into 2 degenerate modes, G^+ and G^-. This indicates that regardless of the high tensile strain of the carbon nanoscrolls, the confinement and curvature of these scroll structures have no significant effect on the carbon-carbon intra-atomic force constants.[70] Other that the prominent peaks corresponding to the graphitic material, additional peaks were observed in the Raman spectra at approximately 1436 cm^{-1} and 2870 cm^{-1}. Control experiments were able assign the position and the shape of peaks to the silicon substrate and the toluene/water solvent used respectively (Appendix F). The presence of small amounts of exfoliated graphene sheets other than the high quantities of the scrolls were noticed within the post processed sample indicating the conversion of exfoliated graphene as scrolls was high yield but not of 100% (Appendix F**)**.

In conclusion, we have developed a facile one-step method of fabricating graphene scrolls with large interlayer spacing between the successive layers, which are formed under intense shear generated within dynamic thin films in a vortex fluidic device. The stable graphene scrolls were produced in high yield, in the absence of auxiliary surfactants, nano-materials, and other chemicals, and with minimal processing times. The larger interlayer distance of the scrolls is foreseen to have potential in a number of fields, specifically in hydrogen and other gas storage purposes, especially given the possibility of scaling up the processing under continuous flow mode of operation of the VFD.

5.2.1 Experimental design for the fabrication of graphene scrolls.

In a typical experiment, graphite flakes (1 mg, particles size 7-10 μm in lineal dimension of the planar flakes) was dispersed in toluene (0.5 mg/mL). MilliQ water (0.5 mL) was then added to the graphite/toluene dispersion (0.5 mL) in the borosilicate glass tube (10 mm OD, 7.100 ± 0.013 mm ID). The volume ratio of the graphite/toluene dispersion to water was optimised to a 1:1 ratio. The optimum confined mode VFD operating parameters for generating high yield graphene scrolls were inclination angle, θ at 45 ^{o} for a rotational speed of 7500 rpm with a reaction time of 30 minutes. Centrifugation (g=3.22) of the post-processed material removed any residual graphite flakes and contaminants present in the sample.

5.2.2 Acknowledgements

The authors gratefully acknowledge support of this work by the Australian Research Council and the Government of South Australia, and the Australian Microscopy & Microanalysis Research Facility (AMMRF) at the Centre for NanoScale Science and Technology, Flinders University

5.3 References

1 Geim, A. K. & Novoselov, K. S. The rise of graphene. *Nature Materials* **6**, 183-191,(2007).

2 Novoselov, K. S. *et al.* Electric Field Effect in Atomically Thin Carbon Films. *Science* **306**, 666-669, (2004).

3 Rao, C. N. R., Sood, A. K., Subrahmanyam, K. S. & Govindaraj, A. Graphene: The New Two-Dimensional Nanomaterial. *Angewandte Chemie International Edition* **48**, 7752 7777, (2009).

4 Han, M. Y., Özyilmaz, B., Zhang, Y. & Kim, P. Energy Band-Gap Engineering of Graphene Nanoribbons. *Physical Review Letters* **98**, 206805, (2007).

5 Rasool, H. I., Ophus, C., Klug, W. S., Zettl, A. & Gimzewski, J. K. Measurement of the intrinsic strength of crystalline and polycrystalline graphene. *Nature Communication* **4,** (2013).

6 Zhang, Y., Tan, Y.-W., Stormer, H. L. & Kim, P. Experimental observation of the quantum Hall effect and Berry's phase in graphene. *Nature* **438**, 201-204, (2005).

7 Novoselov, K. S. *et al.* Two-dimensional gas of massless Dirac fermions in graphene. *Nature* **438**, 197-200, (2005).

8 Novoselov, K. S. *et al.* Room-Temperature Quantum Hall Effect in Graphene. *Science* **315**, 1379-1379, (2007).

9 Du, X., Skachko, I., Duerr, F., Luican, A. & Andrei, E. Y. Fractional quantum Hall effect and insulating phase of Dirac electrons in graphene. *Nature* **462**, 192-195, (2009).

10 Bolotin, K. I. *et al.* Ultrahigh electron mobility in suspended graphene. *Solid State Communications* **146**, 351-355, (2008).

11 Morozov, S. V. *et al.* Giant Intrinsic Carrier Mobilities in Graphene and Its Bilayer. *Physical Review Letters* **100,** (2008).

12 Du, X., Skachko, I., Barker, A. & Andrei, E. Y. Approaching ballistic transport in suspended graphene. *Nature Nanotechnology* **3**, 491-495, (2008).

13 Westervelt, R. M. Graphene Nanoelectronics. *Science* **320**, 324-325, (2008).

14 Bonaccorso, F., Sun, Z., Hasan, T. & Ferrari, A. C. Graphene photonics and optoelectronics. *Nature Photonics* **4**, 611-622, (2010).

15 Su, Y. *et al.* Impermeable barrier films and protective coatings based on reduced graphene oxide. *Nature Communications* **5**, (2014).

16 Kim, Y. *et al.* Strengthening effect of single-atomic-layer graphene in metal–graphene nanolayered composites. *Nature Communications* **4,** (2013).

17 Huang, X., Qi, X., Boey, F. & Zhang, H. Graphene-based composites. *Chemical Society Reviews* **41**, 666-686, (2012).

18 Sun, Y., Wu, Q. & Shi, G. Graphene based new energy materials. *Energy & Environmental Science* **4**, 1113-1132, (2011).

19 Pumera, M. Graphene-based nanomaterials for energy storage. *Energy & Environmental Science* **4**, 668-674, (2011).

20 Bonaccorso, F. *et al.* Graphene, related two-dimensional crystals and hybrid systems for energy conversion and storage. *Science* **347,** (2015).

21 Geim, A. K. Graphene: Status and Prospects. *Science* **324**, 1530-1534, (2009).

22 Novoselov, K. S. *et al.* A roadmap for graphene. *Nature* **490**, 192-200, (2012).

23 Kavan, L., Yum, J. H. & Grätzel, M. Optically Transparent Cathode for Dye-Sensitized Solar Cells Based on Graphene Nanoplatelets. *ACS Nano* **5**, 165-172, (2011).

24 Pumera, M. Electrochemistry of graphene: New horizons for sensing and energy storage. *The Chemical Record* **9**, 211-223, (2009).

25 Keeley, G. P. *et al.* Electrochemical ascorbic acid sensor based on DMF-exfoliated graphene. *Journal of Materials Chemistry* **20**, 7864-7869, (2010).

26 Blake, P. *et al.* Graphene-Based Liquid Crystal Device. *Nano Letters* **8**, 1704-1708, (2008).

27 Dua, V. *et al.* All-Organic Vapor Sensor Using Inkjet-Printed Reduced Graphene Oxide. *Angewandte Chemie International Edition* **49**, 2154-2157, (2010).

28 Schedin, F. *et al.* Detection of individual gas molecules adsorbed on graphene. *Nat Mater* **6**, 652-655, (2007).

29 Li, X. *et al.* Large-Area Synthesis of High-Quality and Uniform Graphene Films on Copper Foils. *Science* **324**, 1312-1314, (2009).

30 Kim, K. S. *et al.* Large-scale pattern growth of graphene films for stretchable transparent electrodes. *Nature* **457**, 706-710, (2009).

31 Moreau, E., Ferrer, F. J., Vignaud, D., Godey, S. & Wallart, X. Graphene growth by molecular beam epitaxy using a solid carbon source. *Physica Status Solidi (a)* **207**, 300-303, (2010).

32 Al-Temimy, A., Riedl, C. & Starke, U. Low temperature growth of epitaxial graphene on SiC induced by carbon evaporation. *Applied Physics Letters* **95**, 231907, (2009).

33 Moldt, T. *et al.* High-Yield Production and Transfer of Graphene Flakes Obtained by Anodic Bonding. *ACS Nano* **5**, 7700-7706, (2011).

34 Shukla, A., Kumar, R., Mazher, J. & Balan, A. Graphene made easy: High quality, large-area samples. *Solid State Communications* **149**, 718-721, (2009).

35 Novoselov, K. S. *et al.* Two-dimensional atomic crystals. *Proceedings of the National Academy of Sciences of the United States of America* **102**, 10451-10453, (2005).

36 Leon, V. *et al.* Few-layer graphenes from ball-milling of graphite with melamine. *Chemical Communications* **47**, 10936-10938, (2011).

37 Parvez, K. *et al.* Electrochemically Exfoliated Graphene as Solution-Processable, Highly Conductive Electrodes for Organic Electronics. *ACS Nano* **7**, 3598-3606, (2013).

38 Parvez, K. *et al.* Exfoliation of Graphite into Graphene in Aqueous Solutions of Inorganic Salts. *Journal of the American Chemical Society* **136**, 6083-6091, (2014).

39 Hong, Y., Wang, Z. & Jin, X. Sulfuric Acid Intercalated Graphite Oxide for Graphene Preparation. *Scientific Reports* **3**, 3439, (2013).

40 Osváth, Z. *et al.* Graphene layers from thermal oxidation of exfoliated graphite plates. *Carbon* **45**, 3022-3026, (2007).

41 Kovtyukhova, N. I. *et al.* Non-oxidative intercalation and exfoliation of graphite by Brønsted acids. *Nature Chemistry* **6**, 957-963, (2014).

42 Ciesielski, A. & Samori, P. Graphene via sonication assisted liquid-phase exfoliation. *Chemical Society Reviews* **43**, 381-398, (2014).

43 Hernandez, Y. *et al.* High-yield production of graphene by liquid-phase exfoliation of graphite. *Nature Nanotechnology* **3**, 563-568, (2008).

44 Haar, S. *et al.* Enhancing the Liquid-Phase Exfoliation of Graphene in Organic Solvents upon Addition of n-Octylbenzene. *Scientific Reports* **5**, 16684, (2015).

45 Paton, K. R. *et al.* Scalable production of large quantities of defect-free few-layer graphene by shear exfoliation in liquids. *Nature Materials* **13**, 624-630, (2014).

46 Matsumoto, M., Saito, Y., Park, C., Fukushima, T. & Aida, T. Ultrahigh-throughput exfoliation of graphite into pristine 'single-layer' graphene using microwaves and molecularly engineered ionic liquids. *Nature Chemistry* **7**, 730-736, (2015).

47 Chen, X., Dobson, J. F. & Raston, C. L. Vortex fluidic exfoliation of graphite and boron nitride. *Chemical Communications* **48**, 3703-3705, (2012).

48 Zhou, X. & Liu, Z. A scalable, solution-phase processing route to graphene oxide and graphene ultralarge sheets. *Chemical Communications* **46**, 2611-2613, (2010).

49 Israelachvili, J. N. *Intermolecular and surface forces*. 3rd edn, (Academic Press), (2011).

50 Chen, X., Boulos, R. A., Eggers, P. K. & Raston, C. L. *p*-Phosphonic acid calix[8]arene assisted exfoliation and stabilization of 2D materials in water. *Chemical Communications* **48**, 11407-11409, (2012).

51 Liu, W. *et al.* Lignin-assisted direct exfoliation of graphite to graphene in aqueous media and its application in polymer composites. *Carbon* **83**, 188-197, (2015).

52 Brinkhaus, L. *et al.* Tuning the Stability of Graphene Layers by Phthalocyanine-Based OPPV Oligomers Towards Photo- and Redoxactive Materials. *Small* **9**, 2348-2357, (2013).

53 Malig, J. *et al.* Direct exfoliation of graphite with a porphyrin - creating functionalizable nanographene hybrids. *Chemical Communications* **48**, 8745-8747, (2012).

54 Lee, C., Wei, X., Kysar, J.W. & Hone, J. Measurement of the elastic properties and intrinsic strength of monolayer graphene. *Science* **321**, 385-388, (2008).

55 Nardeccia, S., Carriazo, D., Ferrer, M.L., Gutierrex, M.C. & Monte, F.D. Three dimensional macroporous architectures and aerogels built of carbon nanotubes and/or graphene: Synthesis and applications. *Chem. Soc. Rev.* **42**, 794-830, (2013).

56 Edwards, R.S. & Coleman, K.S. Graphene synthesis: relationship to applications. *Nanoscale* **5**, 38-51, (2013).

57 Allen, M.J. Tung, V.C. & Kaner, R.B. Honeycomb carbon: A review of graphene. *Chem. Rev.* **110**, 132-145, (2012).

58 Dikin, D.A. *et al.* Preparation and characterization of graphene oxide paper. *Nature* **448**, 201-204, (2005).

59 Stankovich, S. *et al.* Graphene based composite materials. *Nature* **442**, 282-286, (2008).

60 Park, S. *et al*. Graphene oxide papers modified by divalent ions-Enhancing mechanical properties via chemical cross linking. *ACS Nano* **2B,** 572-578, (2008).

61 Bunch, J.S. *et al*. Electrochemical resonators of graphene sheets. *Science* **315**, 490-493, (2007).

62 Ramanathan, T. *et al*. Functionalisation graphene sheets for polymer nanocomposites. *Nature Nanotechnology* **3**, 327-331, (2008).

63 Blake, P. *et al*. Graphene based liquid crystal device. *Nano Lett.* **8**, 1704-1708 (2008).

64 Zhang, Y., Tan, Y.W., Stormer, H.L. & Kim, P. Experimental observation of the quantum Hall effect and Berry's phase in graphene. *Nature* **438**, 457-460, (2007).

65 Stoller, M.D., Park, S., Zhu, Y., An. J. & Ruoff, R.S. Graphene based ultracapacitors. *Nano Lett.* **8**, 3498-3502, (2008).

66 Chen, X., Boulos, R.A., Dobson, T.F. & Raston, C.L. Shear induced formation of carbon and boron nitride nanoscrolls. *Nanoscale* **5**, 498-502, (2013).

67 Zeng, F. Kuang, Y., Liu, G., Liu, R., Huang, Z., Fu, C. & Zhou, H. Supercapacitors based on high quality graphene scrolls. *Nanoscale* **4**, 3997-4001, (2012).

68 Yao, K., Manjare, M., Barreett, C.A., Yang, B., Salguero, T.T. & Zhao, Y. Nanostructure scrolls from graphene oxide for microjet engines. *J. Phys. Chem. Lett.* **3**, 2204-2208, (2012).

69 Zeng, F., Kuang, Y., Wang, Y., Huang, Z., Fu,C. & Zhou, H. Facile preparation of high quality graphene scrolls from graphite oxide by a microexplosion method. *Adv. Mater.* **23**, 4929-4932, (2011).

70 Xie, X., Ju,L., Feng, X., Sun, Y., Zhou, R., Liu, K., Fan, S., Li, Q. & Jiang, K. Controlled fabrication of high quality carbon nanoscrolls from monolayer graphene. *Nano Lett.* **9**, 2565-2510, (2009).

71 Viculis, L.M., Mack, J.J. & Kaner, R.B. A chemical route to carbon nanoscrolls. *Science* **299**, 1361, (2003).

72 Yang, J. Heo, M., Lee, H.J., Park, S.M., Kim, J.Y. & Shin, H.S. Reduced graphene oxide wrapped fullerene (C_{60}) wires. *ACS Nano*, **5**, 8365-8371, (2011).

73 Chuvilin, A., Kaiser, U., Bichoutskaia, E., Besley, N.A. & Khlobystor, A.N. Direct transformation of graphene to fullerene. *Nature* **2**, 450-453, (2010).

74 Shanfi, T., Gracia-Espino, E., Barzegar, H.R., Jia, X. Nitze, F, Hu, G., Nordblad, P., Tai, C.W. & Wagberg, T. Formation of nitrogen-doped graphene nanoscrolls by adsorption of magnetic Fe_2O_3 nanoparticles. *Nature Commun.* **4,** (2013).

75 Hwang, D.Y., Yook, J.Y. & Suh, D.H. Inclusion and exclusion of self assembled molecules inside graphene scrolls. *RSC Adv.* **4,** (2014).

76 Mpourmpakis, G., Tylianakis, E. & Froudakis, G.E. Carbon nanoscrolls: A promising material for hydrogen storage, *Nano Lett.* **7**, 1893-1897, (2007).

77 Coluci, V.R., Braga, S.F. Baughman, R.H. & Galvao, D.S. Prediction of the hydrogen storage capacity of carbon nanoscrolls. *Phys. Rev. B.* **75**, 12504, (2007).

78 Yang, X., He, Y.S., Jiang, G., Liao, X.Z. & Ma, Z.F. High voltage supercapacitors using hydrated graphene film in a neutral aqueous electrolyte. *Electro. Chem.* **13**, 1166-1169, (2011).

79 Yasmin, L., Chen, X., Stubbs, K. A. & Raston, C. L. Optimising a vortex fluidic device for controlling chemical reactivity and selectivity. *Sci. Rep.* **3**, 2282, (2013).

80 Vimalanathan, K, Chen, X & Raston, C.L. Shear induced fabrication of intertwined single walled carbon nanotube rings. *Chem. Commun.* **50,** 11295-11298, (2014).

81 Britton, J., Chalker, J.M. & Raston, C.L. Rapid vortex fluidics: Continuous flow synthesis of amides and local anaesthetic lidocaine. *Chem. Eur. J.,* (2015).

82 Britton, J., Dalziel, S.B., & Raston, C.L. Continuous flow Fischer esterifications harnessing vibrational-coupled thin films fluidics*. RSC Adv.* **5**, 1655-1660, (2015).

83 Tong, C.L., Boulos, R.A., Yu, C., Iyer, K.S. & Raston, C.L. Continuous flow tuning of ordered mesoporous silica under ambient conditions. *RSC Adv.,* **3**, 18767-18770, (2013).

84 Boulos, R.A. Zhang, F., Tjandra, E.S., Martin, A.D., Spagnoli, D. & Raston, C.L. Spinning up polymorphs of calcium carbonate. *Scientific Reports* **4**, 3616, (2013).

85 Yuan, T.Z., Ormonde, C.F.G., Kudlacek, S.T., Kunche, S., Smith, J.N., Brown, W.A., Pugliese, K.M., Olsen, T.J., Iftikhar, M., Raston, C.L., & Weiss, G.A. Shear-stress-mediated refolding of proteins from aggregates and inclusion bodies. *ChemBioChem*. **16**, 393-396, (2015).

86 Mo, J., Eggers, P.K., Chen, X., Ahamed, M.R.H., Becker, T., Lim, L.Y. & Raston, C.L. Shear induced carboplatin binding within the cavity of a phospholipid mimic for increased anticancer efficacy. *Scientific Reports* **5**, 10414, (2015).

87 Iyer, K.S. & Raston, C.L. Fabrication of laterally 'sliced' metal plated carbon nanotubes under aqueous continuous flow conditions. *J. Mater. Chem.* **17**, 4872-4875, (2007).

88 Vimalanathan, K. *et al.* Fluid dynamic lateral slicing of high tensile strength carbon nanotubes. *Scientific Reports* **6**, 22865, (2016).

89 Hertel, T., Walkup, R.E. & Avouris, P. Deformation of carbon nanotubes by surface van der Waals forces. *Physical Review B* **58,** 13870-13873 (1998).

90 Shapiro, I.R., Solares, S.D., Esplandiu, M.J., Wade, L.A., Goddard, W.A. & Collier, C.P. Influence of elastic deformation on single walled carbon nanotube atomic force microscopy probe resolution. *Journal Physical Chemistry B* **108,** 13613-13618, (2004).

91 Alizadegan, R., Liao, A.D., Xiang, F., Pop, E & Hsia, K.J. Effect of tip-nanotube interactions on atomic force microscopy imaging of carbon nanotubes. *Nano Research* **5,** 1235-1247, (2012)

92 Patra, N., Wang, B. & Kral, P. Nanodroplet activated and guided folding of graphene nanoscturctures. *Nano Lett.* **9,** (2009).

93 Carotenuto, G., Longo, A., Nicola, S.D., Camerlingo, C. & Nicolais, L. A simple mechanical technique to obtain carbon nanoscrolls from graphite nanoplatelets. *Nano Lett.* **8,** (2013).

94 Zheng, J., Liu, H., Wu, B., Guo, Y., Wu, T., Yu, G., Liu, Y. & Zhu, D. Production of high quality carbon nanoscrolls with microwave spark assistance in liquid nitrogen. *Adv. Mater.* **23,** (2011).

95 Roy, D., Tactay, E.A., Brown, R.J.C., Spencer, S.J., Fry, T., Dunton, T.A., Young, T. & Milton, M.J.T. Synthesis and Raman spectroscopic of carbon nanoscrolls. *Chem. Phys. Lett.* **465,** 254-257, (2008).

96 Zhou, H.Q., Qiu, C.Y., Yang, H.C., Yu, F., Chen, M.J., Hu, L.J., Guo, Y.J. & Sun, L.F. Raman spectra and temperature dependent Raman scattering of carbon nanoscrolls. *Chem. Phys. Lett.* **501,** 475-479, (2011).

6 MANIPULATING CARBON NANOTUBES

6.1 Structure and Properties of Carbon Nanotubes

Carbon nanotubes (CNTs) were discovered by Iijima[1-3] and offer exciting pathways towards developing novel and facile methods of other unique nanostructures with complexity in morphology and excellent properties. Thereafter, various other methods were used to grow CNTs utilizing the 'bottom up' approach, which includes the initial arc-discharge[4] and laser ablation[5] method followed by the chemical vapour deposition (CVD) approach.[6] Both the arc discharge and the laser ablation method involved condensation of carbon atoms generated from the evaporation of solid carbon sources at the high melting point temperature of graphite 3000-4000 °C. The CVD approach then established the ability to grow bulk SWCNTs at much lower temperatures compared to the former. The growth process involved the use of a catalyst at temperature of about 550-750 °C in a tube furnace in the presence of a hydrocarbon gas flowing through the tube reactor. Commercially available CNTs grown using the CVD method includes the HiPCO and CoMoCAT. These methods typically afford CNTs millimetres in length with high degrees of bundling and aggregation of the strands through van der Waals forces.[4,7,8] Their explicit chemical and physical properties such as high surface area, chemical stability and high electrical conductivity make them an ideal material for many applications specifically for hydrogen storage, electronic devices, hybrid material, biomedicine and device technology, including high performance transistors.[9-15]

Among the many properties, the most enticing property compared to other nanomaterials is its excellent electrical characteristics which is highly dependent on a few factors such as the synthetic method of production, defects on the surface of the nanotubes and degree of crystallinity.[16] A few limitations that over ride their excellent properties for specific applications are the structural heterogeneity of the CNTs grown using these methods and the strong van der Waals interactions between the long bundled ropes. CNTs, molecular scale tubes of graphite carbon, are the strongest and stiffest materials with a Young's modulus of 1 TPa and a maximum tensile strength of 63 GPa.[17-19]

Depending on the method of growth and the experimental conditions, CNTs can be thought of as a concentric arrangement of single or multi layered stacked graphene sheets with a hexagonal lattice of sp^2 carbon atoms wrapped up into seamless cylindrical structures along an (*n,m*) lattice vector in the graphene plane.[9] It is this (*n,m*) lattice vector that determines the diameter and chirality of the resulting nanotubes. The number of sheets rolled up to form CNTs defines the number of consisting coaxial concentric layers and are accordingly called single (SWCNT), double (DWCNT) or multi walled (MWCNT). There is a constant interlayer spacing between the graphene sheets of 3.40 Å, which is in agreement with the interlaying spacing of graphite.

CNTs with two concentric layers are known as double walled (DWCNT) possessing properties of both the SWCNT and MWCNT making it ideal for applications that require more than one concentric layer but not requiring multiple layers. With close structural resemblance to the SWCNTs, DWCNTs also possess unique capabilities and properties. For example, they exhibit a much higher mechanical stability compared to SWCNTs and most importantly they allow for functionalization of the outer tube ensuring the pristine nature of the inner tube to exploit its mechanical and electrochemical properties.[20,21]

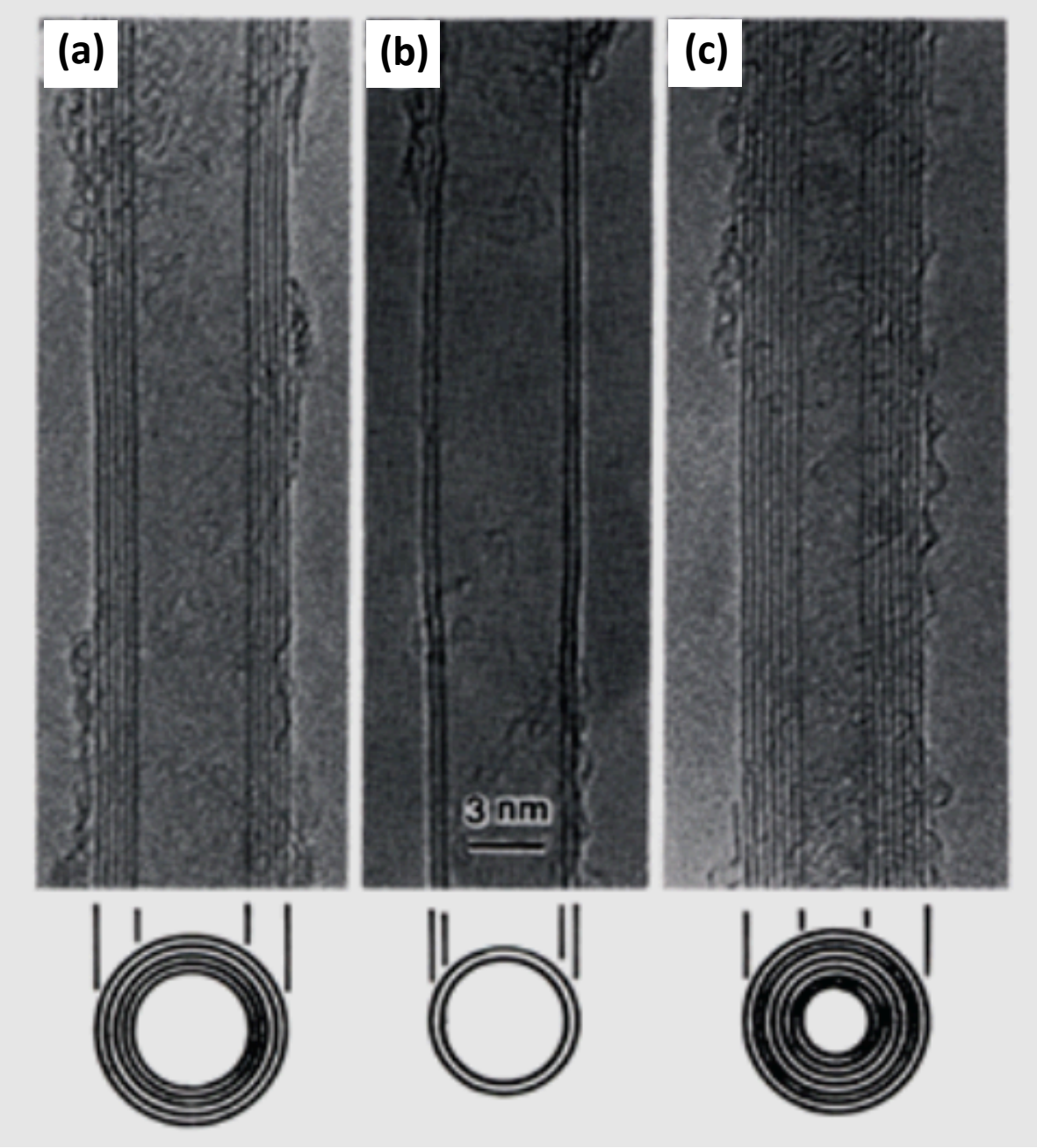

Figure 31 Electron micrographs of the microtubules of graphitic carbon discovered by Iijima *et al.* Illustration of each figure corresponds to a cross section of the nanotubes made up of a particular number of graphene sheets; (a) CNT consisting of five (5) graphitic sheets (6.7 nm diameter), (b) CNT consisting of two (2) graphene sheets (2.2 nm diameter), and (c) CNT consisting of seven (7) graphene sheets (6.5 nm diameter). Being made up of a number of concentric layers, the nanotube in figure (c) has the smallest hollow core, corresponding to a diameter of 2.2 nm.[3]

Although CNTs consisting of multiple numbers of shells are used for a variety of applications, SWCNTs stand out, having attracted significant attention due to their excellent electronic and optical properties. The typical experimentally observed SWCNT diameter is between 0.6 nm and 2.0 nm.[22]

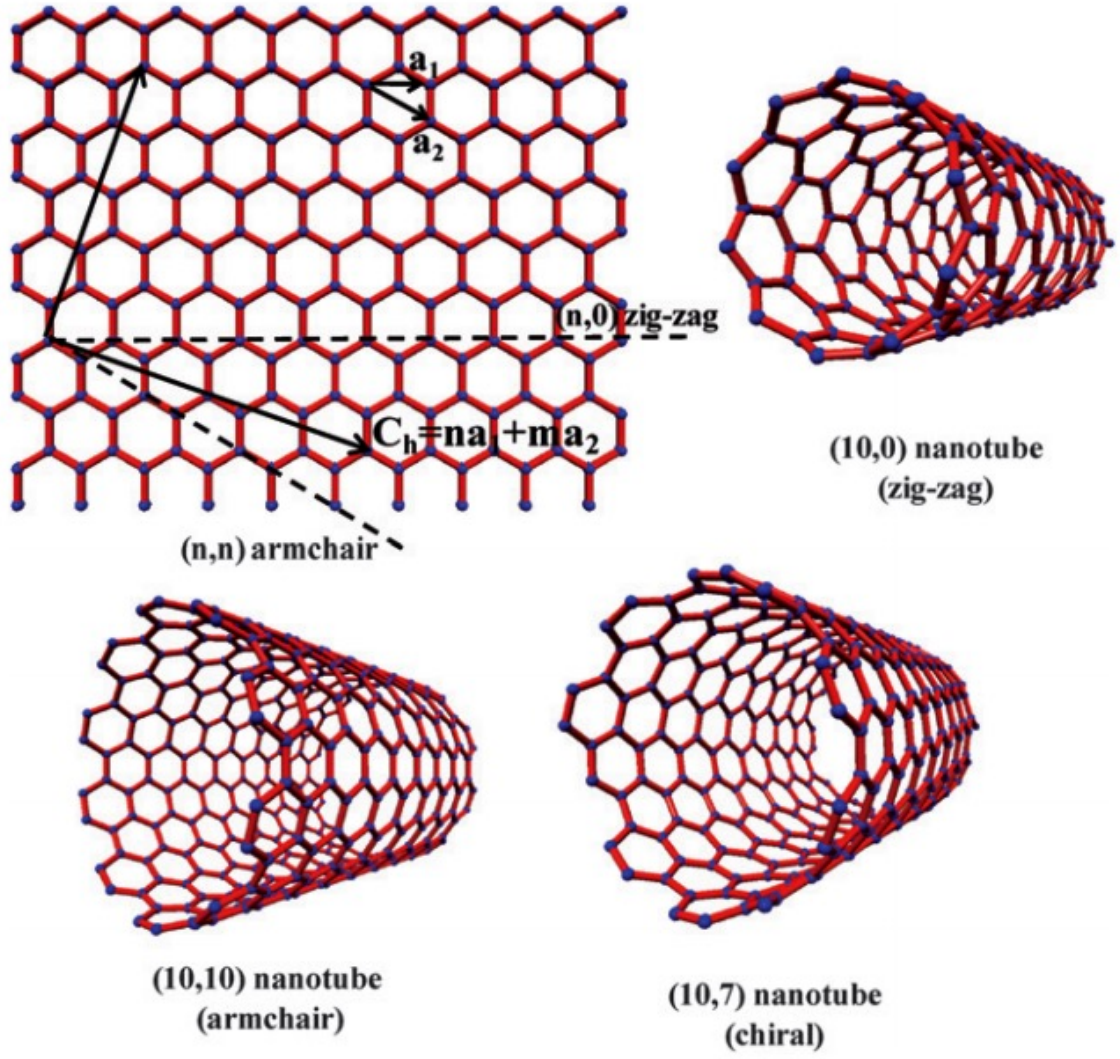

Figure 32 SWCNT formed by rolling up a graphene sheet along a chiral vector to form a cylindrical shaped 1D structure. The different chiralities (*n,m*) are defined by rolling angle and the diameter, affording either semiconducting or metallic configuration.[23]

6.2 Geometric structure

As previously noted, cylindrical shaped CNTs are derived from graphene sheets consisting of a hexagonal planar network of carbon atoms. One of the most unique features of SWCNTs is related to their electronic and optical properties which are strongly dependent on the how the graphene sheet is rolled up to form the the one-dimensional structure.[24] Thus, depending on the rolling angle (θ) and diameter (d_t), CNTs can exhibit either semiconducting (S) or metallic (M).[25] Upon rolling up, the circumference of a carbon nanotube is determined by a chiral vector, C_h , which is used to identify the two equivalent lattices that meet to form a nanotube of a particular helicity. The chiral vector is defined by equation 2,

$$C_h = na_1 + ma_2 \qquad \textbf{Equation 2}$$

whereby (*n,m*) are a pair of integers corresponding to the number of steps along the zig-zag carbon bonds and $\mathbf{a_1}$ and $\mathbf{a_2}$ are graphene lattice vectors. The pair of integers and the graphene lattice vectors is used to identify the two equivalent lattices that meet to form a nanotube of a particular helicity. Each point on the lattice represents a unique (*n,m*) assignment corresponding to a nanotube structure (armchair, zigzag and chiral) and the bandgap of the SWCNT. This nanotube structure and diameter with a unique assignment of (*n,m*) is determined by equation 3,

$$d_t = \frac{|C_h|}{\pi} = \frac{a(n^2 + m^2 + nm)^{1/2}}{\pi} \qquad \textbf{Equation 3}$$

where $a = \sqrt{3a_{c-c}}$, $\sqrt{3a_{c-c}}$, corresponds to the carbon- carbon bond length of approximately 1.42 Å.[26]

For example, nanotubes with chiral vectors of (*n, 0*) are defined as zigzag nanotubes, (*n,n*) vectors are defined as armchair nanotubes, and (*n,m*) vectors where m≠n, 0, are defined as chiral nanotube vectors. [9,27-31] Zigzag nanotubes can be categorised as either a zero gap semiconductor (quasi metallic nanotube) or a finite bandgap semiconductor. Armchair

nanotubes however exhibit metallic characteristics. All other integer pairs (*n,m*) are defined as chiral nanotubes, whereby those in agreement with |n-m| =3q is quasi metallic and have a small band gap and all other chiral nanotubes are semiconducting (whereby q is a non zero integer).

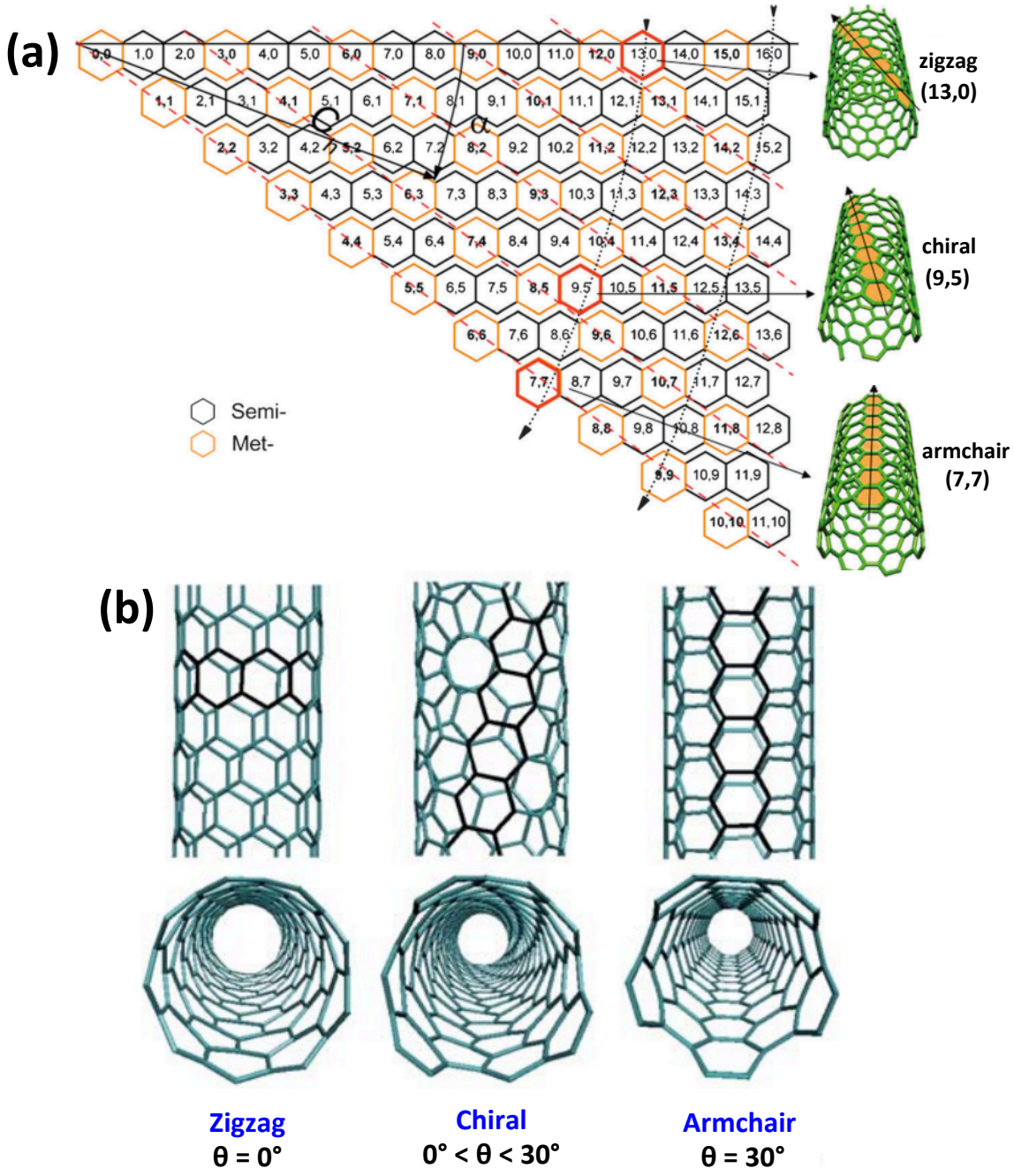

Figure 33 Chirality map of semiconducting and metallic SWCNTs. The three (3) typical types of SWCNTs are the zigzag, chiral and armchair corresponding to a unique (*n,m*) chiral indices. The example provided in this figure include zigzag (13,0), chiral (9,5) and armchair (7,7).[32,33]

6.3 Fluid dynamic lateral slicing of high tensile strength carbon nanotubes

This section is based on a publication published in *Nature's Scientific Reports* entitled 'Fluid dynamic lateral slicing of high tensile strength carbon nanotubes,' authored by **Kasturi Vimalanathan**, Jason R. Gascooke, Irene Suarez-Martinez, Nigel Marks, Harshita Kumari, Chris J. Garvey, Jerry L. Atwood, Warren D. Lawrance and Colin L. Raston.

Abstract: Lateral slicing of micron length carbon nanotubes (CNTs) is effective on laser irradiation of the materials suspended within dynamic liquid thin films in a microfluidic vortex fluidic device (VFD). The method produces sliced CNTs with minimal defects in the absence of any chemical stabilizers, having broad length distributions centred at *ca* 190, 160 nm and 171 nm for single, double and multi walled CNTs respectively, as established using atomic force microscopy and supported by small angle neutron scattering solution data. Molecular dynamics simulations on a bent single walled carbon nanotube (SWCNT) with a radius of curvature ≤ 12 nm results in tearing across the tube upon heating, highlighting the role of shear forces which bend the tube forming strained bonds which are ruptured by the laser irradiation. CNT slicing occurs with the VFD operating in both the confined mode for a finite volume of liquid and continuous flow for scalability purposes.

The processing of cylindrical carbon nanotubes (CNTs) for exploiting their exceptional thermal, mechanical, and electrical properties[34] poses a number of challenges. This includes overcoming a high degree of bundling and aggregation arising from their high aspect ratio and strong inter-tube van der Waals interactions. The CNTs are microns to millimetres in length, and may have single or multiple layers, described as single walled (SWCNTs), double walled (DWCNTs) or multi walled (MWCNTs). They have low density, and high stiffness and axial strength[35] with an exceptionally high Young's modulus, 1.0 to 1.28 TPa.[17-19] CNTs are produced using a number of techniques, including arc-discharge, laser ablation and chemical vapour deposition (CVD),[4,7,8] typically affording arrays of nanotubes in various lengths. However, the availability of shorter lengths without compromising quality is important for many applications, for example, in incorporating them into lipid bilayers for molecular sensing[2], and for enhancing the efficiency of electronic devices,[17,18,36] for solar cell applications[10] and for chirality separation.[38-40] There has thus been considerable work directed at shortening CNTs towards sub-micron lengths, but this has

proved challenging, currently requiring the use of high-energy sonication, lengthy processing times and the use of toxic chemicals.[41-51] Moreover, such conditions can chemically alter the surface of the CNTs with consequential change in their properties, thereby limiting their applications. Controlling the shortening of CNTs requires the use of a suitable processing medium in overcoming their tendency to aggregate, with some common solvents such N-methyl-2-pyrollidone (NMP) and N,N-dimethylformamide (DMF) being effective dispersants for such purpose. The colloidal stability of individual CNTs usually requires polymer wrapping agents[52] and surfactants,[53] and covalent end and/or sidewall functionalization.[54,55]

We have established a new means to achieve shortening of CNTs that avoids many of these problems. Despite their high tensile strength, CNTs can be laterally sliced in solution by applying intense shear within dynamic thin films in a vortex fluidic device (VFD) while irradiating at 1064 nm using a pulsed Q-switch Nd:YAG laser (Figure 34). The VFD microfluidic platform generates controllable mechanoenergy within the liquid medium, as thin films around the internal walls of a rapidly rotating tube, which for practical purposes was a 20 mm diameter (ID 16.000 ± 0.013 mm) borosilicate nuclear magnetic resonance (NMR) glass tube. In general, the optimal performance of the VFD occurs at high rotational speeds (2000 rpm to 9000 rpm) and inclination angles, $\theta > 0°$, with a 45° tilt angle corresponding to the maximum cross vector of centrifugal force and gravity, being the optimum setting for a diverse number of applications of the device.[56-62]

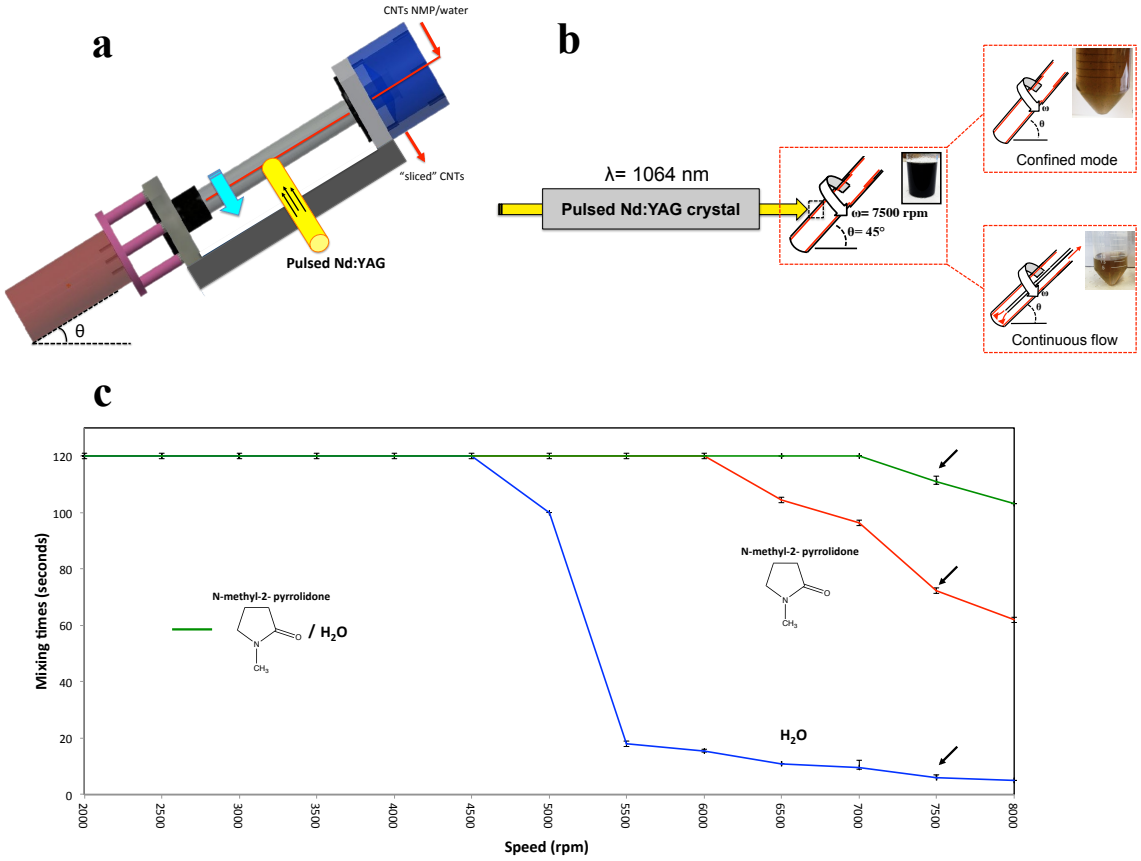

Figure 34 VFD laser processing and mixing time data. (a) Schematic of the vortex fluidic device (VFD). (b) Experimental set up for laser Nd:YAG processing operating at 1064 nm wavelength, for confined and continuous flow modes of operation of the VFD. (c) Variation of mixing times of pure NMP, water and NMP/water at a 1:1 ratio. Mixing times were measured by placing 1 mL of the solvent in the VFD operating at an inclination angle of 45° and varying the rotational speed (2000-9000 rpm) and then measuring the time taken for a drop of dye to uniformly mix with the bulk liquid (measured in triplicates).

Both the confined and continuous modes of operation of the VFD are effective in slicing of the CNTs. In the confined mode a finite volume of liquid is wholly contained within the tube during processing while ensuring that a vortex is maintained to the bottom of the tube for moderate rotational speeds, and without any liquid exiting at the top the tube. This minimises the formation of different shear regimes. In this mode, Stewartson/Ekman layers prevail in the resulting dynamic thin films, which arise from the liquid accelerating up the tube, with gravitational force acting against them.[57] In the continuous flow mode of operation of the VFD, jet feeds deliver one or more solutions (normally) to the bottom of

the tube where there is intense micromixing, with instability of the liquid boundary layer in the hemispherical sphere at the bottom of the tube. The viscous drag as the liquid whirls up the tube creates shear, in addition to that from the Stewartson/Ekman layers. For the the purpose of slicing CNTs, the continuous flow mode of operation was employed to show scalability of the work, affording a yield of ~95%. Both modes, confined and continuous flow modes of operation yielded CNTs of similar lengths ~160-170 nm. Yes, there is drag for both modes of operation, but it follows that it must be greater under continuous flow, for the liquid to exit the tube.

These unique fluidic properties of the VFD have led to a number of applications including control of chemical reactivity and selectivity in organic synthesis,[56,57] exfoliating graphene and boron nitride,[58] protein folding,[59] fabricating toroidal arrays of SWCNTs,[60] forming mesoporous silica at room temperature with control of pore size and wall thickness[61], and probing the structure of self organised processes.[62,63]

6.3.1 Experimental design of the lateral slicing of CNTs

The volume of liquid for confined mode studies was set at 1 mL with the speed and tilt angle varied to establish the lowest time for two liquids to homogenously mix. This was important to optimise exposure of the CNTs in the solution to the 8 mm diameter laser beam used in the 'slicing' experiments, as well as providing the maximum shear for debundling of the tubes. The minimum time taken for a homogenous mixture of water and NMP (1:1 ratio) to uniformly mix (visually estimated for solutions containing a dye, in the range 2000 to 9000 rpm, was for a rotational speed of 7500 rpm (Figure 34) for θ 45°. The choice of a 1:1 ratio of water and NMP was based on overcoming the low mixing time for NMP, in which the CNTs are readily dispersed, versus the fast mixing times in water, in which there is little dispersion of CNTs. These VFD parameters (θ 45°, 7500 rpm rotational speed) also correspond to the optimal processing parameters (*vide infra*).

Energy absorption from the pulsed laser source was essential to laterally slice the CNTs. The laser produces 1064 nm pulses of 5 ns duration and operates at a repetition rate of 10Hz. In the confined mode, the optimised irradiation conditions were found to be at laser power of 260 mJ/pulse for 30 minutes of processing. This was established by determining CNT length distributions using AFM on isolated samples (Appendix G). At high laser powers, ≥400 mJ, only small amounts of sliced nanotubes were evident, along with bundled and aggregated long

nanotubes. Here the extra heat provided by the laser pulse disturbs the fluid flow, with a clear band which is presumably largely devoid of CNTs at the point of laser irradiation. Decreasing the laser power to <200 mJ for 30 minutes was ineffective in slicing the CNTs and no clear band was observed at the irradiation site. (Appendix G).

The optimal VFD processing parameters (inclination angle θ and rotational speed) were determined following a number of control experiments. For rotational speeds below 6000 rpm, the as-received aggregated bundles of CNTs (SWCNTs, DWCNTs and MWCNTs) remained unaffected in both the presence and absence of laser irradiation. At 6000 rpm and 45° tilt, a significant amount of debundling of the nanotubes occurred (as shown through AFM observations), but laser irradiation led to non-uniformity of the sliced CNTs, and the persistence of longer tubes. Uniform slicing of the CNTs occurred between 7500 rpm and 8000 rpm when irradiated by the pulsed laser. A tilt angle of 45° angle was found to be optimal, with minimal lateral slicing at other angles between 0 and 90°. For these optimised VFD processing parameters (θ 45°, rotational speed 7500 rpm), in the absence of the laser pulses there was no evidence for slicing, with the length of the CNTs unchanged, although there was significant debundling (Appendix G). In decoupling the effect of the VFD and the laser irradiation, a pulsed laser beam of the same optimised power was directed towards the CNTs in a 1:1 mixture of water and NMP in a glass cuvette rather than in a VFD. This resulted in fragmentation of the CNTs nanotubes into (i) large and irregular shapes for the SWCNTs, (ii) large bundles and aggregates for the DWCNTs, and (iii) irregular slicing of MWCNTs with bundles and aggregates present (Appendix G). In addition, there was no evidence of slicing the CNTs with the laser wavelength set to 532 nm (Appendix G). Thus, the optimised parameters for laterally slicing the different CNTs to lengths below *ca* 450 nm are established as a 45° tilt angle of the VFD tube rotating at 7500 rpm under confined mode for 30 minutes, with the 10 Hz pulsed laser operating at a wavelength of 1064 nm and 260 mJ per 5 ns pulse. These conditions were found to be independent of the concentration of CNTs in the solution up to a maximum concentration of 0.1 mg/mL, above which presumably the dynamics in the thin film are affected by the CNTs.

A time dependant study taking samples at 10 minute intervals during 1064 nm laser irradiation at 260 mJ/pulse, and the VFD operating in the confined mode, was also undertaken for the three types of CNTs. Over time, more slicing and debundling was observed, with SWCNTs

resulting in a narrower length distribution, but not so for DWCNTs and MWCNTs (Figure 35), although here slightly higher yields of sliced CNTs were evident.

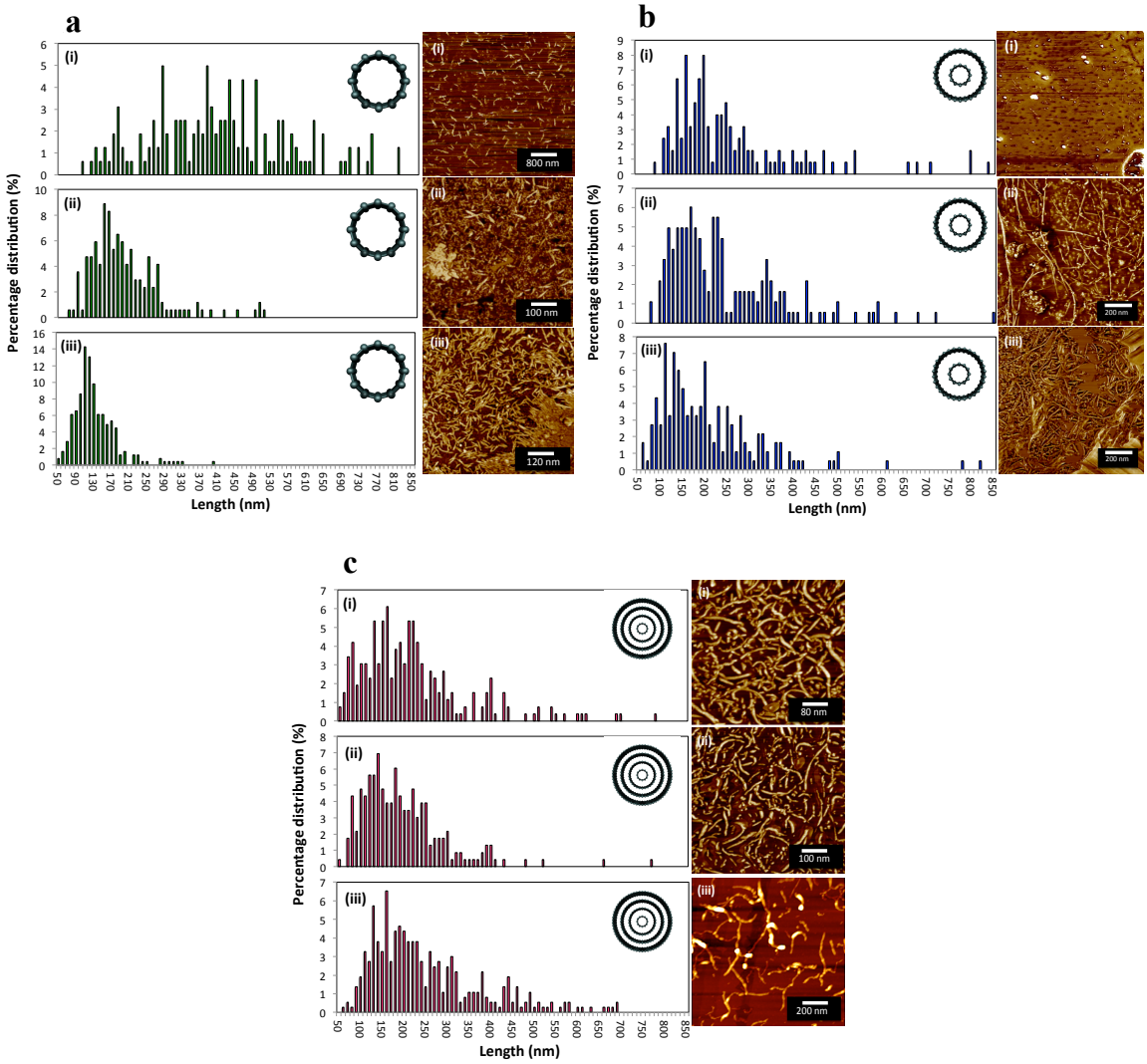

Figure 35 Slicing of SWCNTs, DWCNTs and MWCNTs at θ = 45° and rotational speed of 7500 rpm. AFM height images of laterally sliced CNTs with its associated length distribution plots for reaction times of (i) 10 minutes, (ii) 30 minutes and (iii) 1 hour for SWCNTs (a), DWCNTs (b) and MWCNTs (c). The NanoScope Atomic Force Microscopy software was used to measure the dimensions of the nanotubes. An average of 200-300 nanotubes were measured for each length distribution plot.

Experiments under confined mode established the potential for laser irradiation of CNTs in a VFD to produce unbundled, short CNTs, but for generating practical quantities of the materials, continuous flow processing is desirable. Here a jet feed of CNTs dispersed in a 1:1 mixture of water and NMP was directed into the bottom of the rapidly rotating 20 mm tube at a low flow rate of 0.45 mL/min, using the same concentration of CNTs as for the confined

mode. The low flow rate was necessary for sufficient exposure time of the CNTs to the 8 mm diameter laser beam, while ensuring droplets of the suspension of the CNTs were striking the hemispherical bottom of the tube rather than a continuous stream of the liquid. Such droplets result in instability of the resulting thin film, which imparts additional shear compared to the confined mode of operation of the VFD.[57] Under continuous flow there is a dramatic increase in yield of the sliced CNTs, typically 95%, with a length distribution of 100-400 nm, for SWCNTs, DWCNTs and MWCNTs (Figure 38b). Also noteworthy is that all the samples are devoid of long bundled nanotubes, unlike the outcome for confined mode of operation of the VFD.

6.3.1.1 Characterization techniques

Raman analysis

Raman spectroscopy (Figure 36a) established that any damage to the walls of the CNT products is minimal for confined mode and continuous flow operation of the VFD, irrespective of the number of shells of cylindrical graphene. Distinct peaks for CNTs include the radial breathing mode region (RBM), the tangential mode G band, its second harmonic G′ band and the disorder-induced D-band. The average ratio of intensities of the G and D bands (I_D/I_G) of the sliced SWCNT, DWCNT and MWCNT was ~0.2, ~0.3 and 1.2, respectively, which are similar to that of the starting pristine nanotubes which were ~0.2, ~0.2 and ~1.3, respectively, confirming that tube damage was minimal.

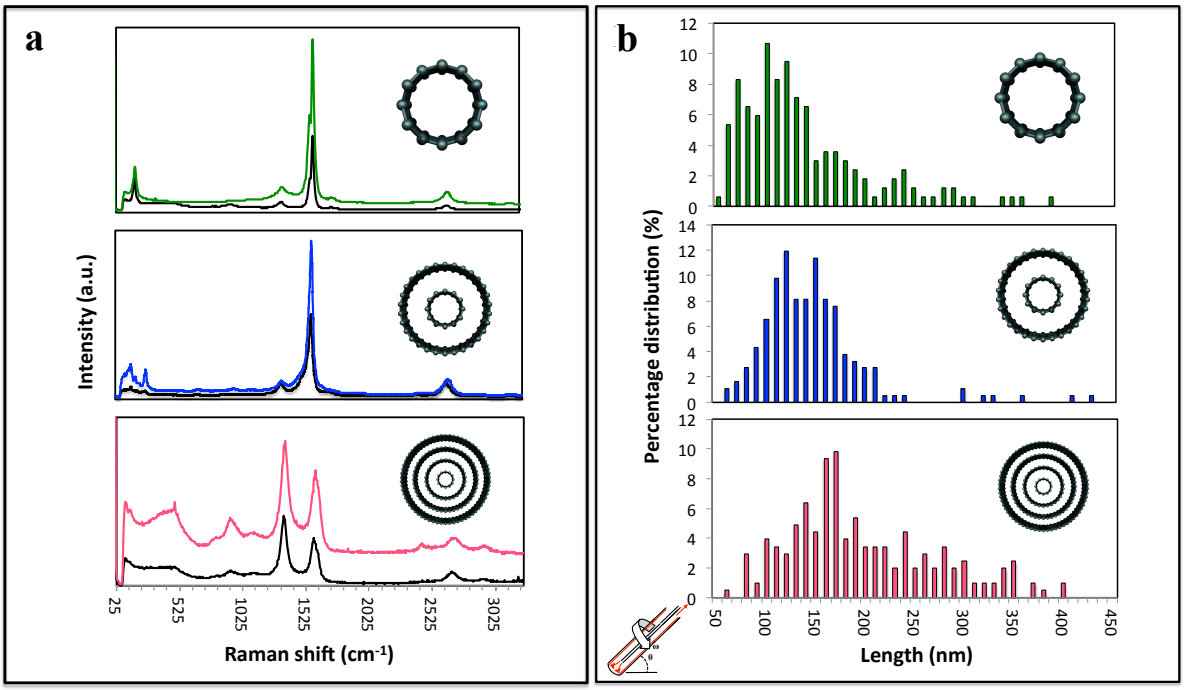

Figure 36 Raman spectroscopy and length distribution plots. (a) Raman spectra of SWCNTs, DWCNTs and MWCNTs, respectively, and the corresponding as received nanotubes (black), and (b) Length distribution plots of the sliced SWCNTs, DWCNTs and MWCNTs under continuous flow operation of the VFD at a flow rate of 0.45 mL/min.

Small angle neutron scattering analysis

The average size of the sliced CNTs in solution was analysed using small angle neutron scattering (SANS). The radius of SWCNTs treated with the laser alone and laser and VFD (confined mode, 10, 30 and 60 min) was 0.7 ± 0.2 nm, which is consistent with AFM results (0.7 to 1.4 nm). For shorter treatment times the nanotubes were longer, and in the absence of VFD processing there is either complete disruption of SWCNTs or no slicing, with the results consistent with the AFM data (Appendix G). Overall, SWCNTs irradiated and subject to shear are broken down to smaller length scales (Appendix G), as is the case for the DWCNTs (Appendix G) and MWCNTs (Appendix G), to 160 nm and 171 nm respectively (Appendix G), which is again consistent with AFM data.

Theoretical calculations

CNTs subjected to the shear forces created in the VFD result in local bending, as established by the observation that toroidal arrays of SWCNTs are produced in a mixture of toluene and water in the VFD in the absence of laser irradiation.[60] Bending is not surprising given the very high aspect ratio for SWCNTs, and when combined with heating from the laser it is likely to result in rupture of multiple bonds. To explore this further in understanding the mechanism of slicing, molecular dynamics simulations were carried out for SWCNTs, with hairpin-shaped tubes created to mimic the bending occurring in the VFD. Figure 37a shows a (10,0) nanotube with a bending radius R of 2.5 nm and an arm-length L of 10 nm. When relaxed near room temperature (Figure 37b & Movie S1) (Appendix G), the hairpin unfolds and no defects are created. However, when the system is raised to a high temperature (Figure 37c and d & Movie S2) (Appendix G) a large tear occurs in the bent region and other defects appear nearby. The damage is produced by the extra energy provided by the elevated temperature resulting in breaking of bonds that are already strained.

The number of defects induced has been explored for different bending radii as a function of temperature. Figure 37e shows data for the same (10,0) chirality with four bending radii, R=3, 6, 8 and 10 nm. Ten simulations were performed at each temperature and radius to gather statistics. Defects are counted as atoms with a potential energy 10% higher than the cohesive energy of graphene or with a coordination number other than three. Below a critical temperature few defects are created, and in many instances no damage is created at all. As the radius increases, the critical temperature above which many defects are created becomes higher, as the bonds are less strained and require additional thermal activation to damage the nanotube. At large radii few defects are observed (Figure 37f), even at high temperatures.

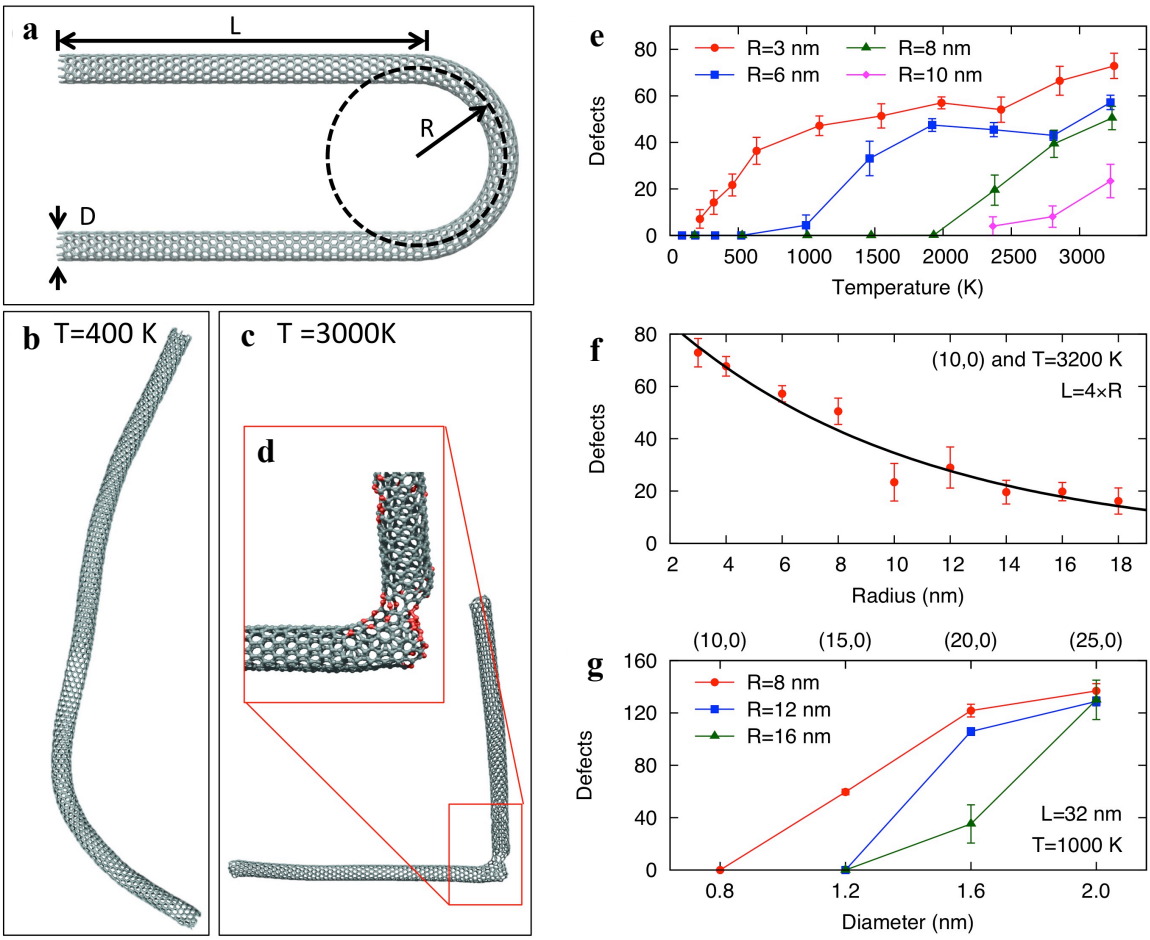

Figure 37 Theoretical calculations. (a) Initial bent structure of geometrical model of a nanotube showing the bending radius, R. and an arm-length, L, and nanotube diameter, D. (**b**) and (**c**) Snapshots of a (10,0) nanotube model after annealing at 400K and 3000K respectively, with inset (d) showing a zoom-in of the defected sliced part of the nanotube. (e) Plot of the number of defects as a function of temperature for the (10,0) nanotube with different bending radii. (f) Plot of the number of defects as a function of radius for the (10,0) nanotube at a constant temperature of 3200 K, and (g) Plot of number of defects at constant temperature as a function of diameter for different chiralities.

These observations explain the experimental result that slicing occurs in the VFD with the laser irradiation but not with laser irradiation alone. Without the shear forces provided by the VFD, there is no localized bending or strained bonds for the laser to rupture. The simulations also suggest that the diameter D of the nanotube plays a role. Experimentally, this varies between 1 and 2 nm for the SWNTs. Figure 37g shows defect-vs-diameter data for three different bending radii. Chiralities of (10,0), (15,0), (20,0) and (25,0) were chosen

with diameters spanning 0.78 to 2.0 nm. For all three bending radii shown, the number of defects increases for nanotubes with larger diameter. This behaviour is quite distinct from the radius effect in Figure 37f and occurs because the larger diameter tubes are much more easily deformed. We expect that these simulations of SWCNTs are also applicable to DWCNTs and MWCNTs, and we note that once the outer tube of the MWCNT is breached then the mechanical force either side would provide a point for the spontaneously slicing through the inner tubes.

It is noteworthy that more in depth experimental details on the complex shear stress in the liquid, the actual heat absorbed by the CNTs, and how they dissipate the heat are being currently studied using real time neutron imaging and small angle neutron scattering at ANSTO, which is also a major research project in their own right.

6.3.2 Conclusion

In summary, we have established the ability to laterally slice carbon nanotubes within dynamic thin films, irrespective of the number of concentric layers in the material. This is without precedent, and further highlights the unique capabilities of the recently developed vortex fluidic device. Importantly, the method minimizes the generation of defects on the CNTs, producing pristine material devoid of chemical stabilizers, and we have demonstrated that there is potential for scalability of the process under continuous flow mode of operation of the VFD. In this work, chemical stabilizers are referred to as other chemicals/solvents that are added in addition to the existing organic solvent to facilitate the slicing process. Controlling the lengths of the shorter nanotubes is more significant for SWCNTs, under confined mode, affording a narrow size distribution at a length scale suitable for drug delivery applications. In general, the availability of short single, double or multi-walled CNTs is poised for the advancement of their applications where specific length scale is paramount.

6.3.3 Acknowledgements

The authors thank Dr. Paul Eggers for his technical assistance, Associate Professor Amanda Ellis for discussions on the optical absorbance characterisations. The authors also thank Australian Research Council and The Government of South Australia for support of the work.

6.4 VFD-mediated chirality enriched single walled carbon nanotubes

The remarkable electrical and optical properties of SWCNTs are strongly dependent on its geometrical parameters. As previously noted, the chiral angle and the diameter of the cylindrical shaped 1D structures are defined by the direction and magnitude of rolling vector of graphene sheets, affording either the semiconducting (S) or metallic (M) configurations. Typically, bulk as received SWCNTs consist of a mixture of metallic and semiconducting configurations whereby their respective properties contribute to the use in diverse range of applications, ranging from electronic and device technology to biomedical applications. For optimum exploitation of their remarkable properties, high purity monostructured SWCNTs of a specific configuration/chirality are ideal, specifically for applications in sensors, optical devices, high performance field effect transistors, conductive films, nanoscale circuit, biological imaging and others.[65-74] For most of these applications, the use of highly pure semiconducting or metallic CNTs is required and for this purpose they need to be separated/purified from the bulk mixture. Over the past decade, numerous studies have focused on the separation and purification of bulk as received SWCNTs based on its electronic configuration. The current methods employ the use of complex chromatographic methods using various surfactants and chemical stabilizers,[75,76,77-80] DNA wrapping chromatography methods,[75-85] density gradient ultracentrifugation,[74,86-88] the synthesis of metal coordination complexes,[89] the use of copolymers,[90-93] polymers using weak field ultracentrifugation[94] and dielectrophoresis.[95] In addition to overcoming the issues of low dispersibility of SWCNTs in organic solvents and the high degree of bundling and aggregation of the up to millimetre long strands, chirality separation of bulk SWCNTs has been another issue that has sparked significant amounts of interest in the research arena. This is because of the exceptional properties of the individual chiralities.

Although the abovementioned methods have been well-established, the major concerns with these protocols are the complex and tedious methods involved, the need for the destruction of metallic CNTs in order to separate the semiconducting configuration, the need for the use of a variety of surfactants of different concentrations which is high costing, and the issues of scalability and purity of sample. These are actively being addressed. Although there is much hype with the advanced potentials of semiconducting SWCNTs specifically, in device technology and other electronic applications, what is yet to be realized is the importance and the properties that metallic SWCNTs also exhibit. Thus, it is important to ensure that any

process or method developed to separate and purify SWNCTs based on their diameter and chirality should allow for the metallic SWCNTs to also be separated and collected instead of being destructively eliminated during the separation process. There are a number of studies to date, focused on the separation of metallic CNTs from a bulk mixture, mostly using the density gradient ultracentrifugation (DGU) and the gel column chromatography method to selectively separate either single chirality armchair metallic SWCNTs of specific chiralities, in particular (6,6) and (7,7) or the non-armchair single chirality as in (7,4). These methods have established the ability to separate these specific chiralities using wrapping DNA sequences[96] and an aqueous two phase separation process.[97]

With the various current methods of growth consisting of a complex mixture of both the semiconducting and metallic chiralities, there is a need to separate or convert (interconvert) them, to accordingly manipulate their properties. Thus, to avoid the need for surfactants and other chromatographic methods of separation that are low yielding and high costing, feasibility studies illustrate a simple and novel method to enrich sliced SWCNTs into the metallic and semiconducting configuration on a large scale.

6.4.1 Experimental design

The method involves the use of controllable mechanoenergy within dynamic thin films in the VFD while the tube is irradiated with a pulsed Nd:YAG laser operating at a wavelength 1064 nm at a laser power of ~260 mJ. The experimental conditions are similar to the slicing experiments in Section 6.3. SWCNTs are dispersed in solvent mixture of NMP and water at a 1:1 ratio. Under both confined mode and continuous flow modes of operation of the device, as received SWCNTs comprising of a mixture of semiconducting and metallic chiralities undergoes lateral slicing and *in situ* conversion (interconversion) to afford metallic enriched SWCNTs. For the confined mode of operation, a finite volume of total liquid is required which was set at 1 mL. This ensures that a vortex is maintained to the bottom of the tube for moderate rotational speeds to avoid different shear regimes, and without any liquid exiting at the top the tube. Stewartson/Ekman layers prevail in the dynamic thin films, which arise from the liquid accelerating up the tube with gravitational force acting against them. The effectiveness of the process was then investigated under continuous flow, using jet feeds delivering the SWCNT dispersion into the rapidly rotating tube at a flow rate of 0.45 mL/min. These preliminary experiments used similar optimised conditions to what was established for

the lateral slicing of CNTs. The VFD was at an inclination angle of 45° and a rotational speed of 7500 rpm.

6.4.2 Characterization techniques and discussion

Figure 38a depicts the optical absorption spectra of the separated SWCNT fraction after one pass under the continuous flow operation in the VFD with a simultaneous 1064 nm wavelength pulsed laser operating at a power of 260 mJ. The absorption peaks around 850-1350 nm, 500-850 nm, 330-450 nm and 300-400 nm are derived from first (S_{11}), second (S_{22}), third (S_{33}) and fourth (S_{44}) optical transitions of semiconducting SWCNTs respectively. The absorbance peaks around 400-650 nm represents the first optical transition of metallic SWCNTs (M_{11}). Absorption at shorter wavelengths (200-300 nm corresponds to the ultraviolet optical absorption characteristics of the nanotubes.[98] Although the ultraviolet region of the spectra was not clearly identified in this study, for the purpose of future optimization work, the UV region can play a pivotal role in determining the intensity of the semiconducting configuration of nanotubes present in the sample. Theoretical calculations by Takagi and Okada highlight that the intensity of the peaks within this UV region is strongly dependent on the diameter and the chirality of the nanotubes present post separation.[98] It is theoretically understood that the UV spectral features characteristics of the interband transitions near the M point of the hexagonal Brillouin zone of graphene.[98]

Thus, in the case of confirming chirality separation, the UV optical absorption feature can be considered as an additional technique to determine the electronic and optical properties of a highly enriched sample of monochiral nanotubes.[98] The optical absorption spectra of both the pristine SWCNT and the sliced SWCNTs demonstrate the disappearance of the semiconducting S_{11} (900-1350 nm) and S_{22} (600-900 nm) peaks and the emergence of a M_{11} peak (approximately 400-600 nm). The absence of semiconducting peaks in the optical absorption spectra of the sliced SWCNTs sample was intriguing and provides an indication that the sample is enriched with SWCNTs with metallic chirality.

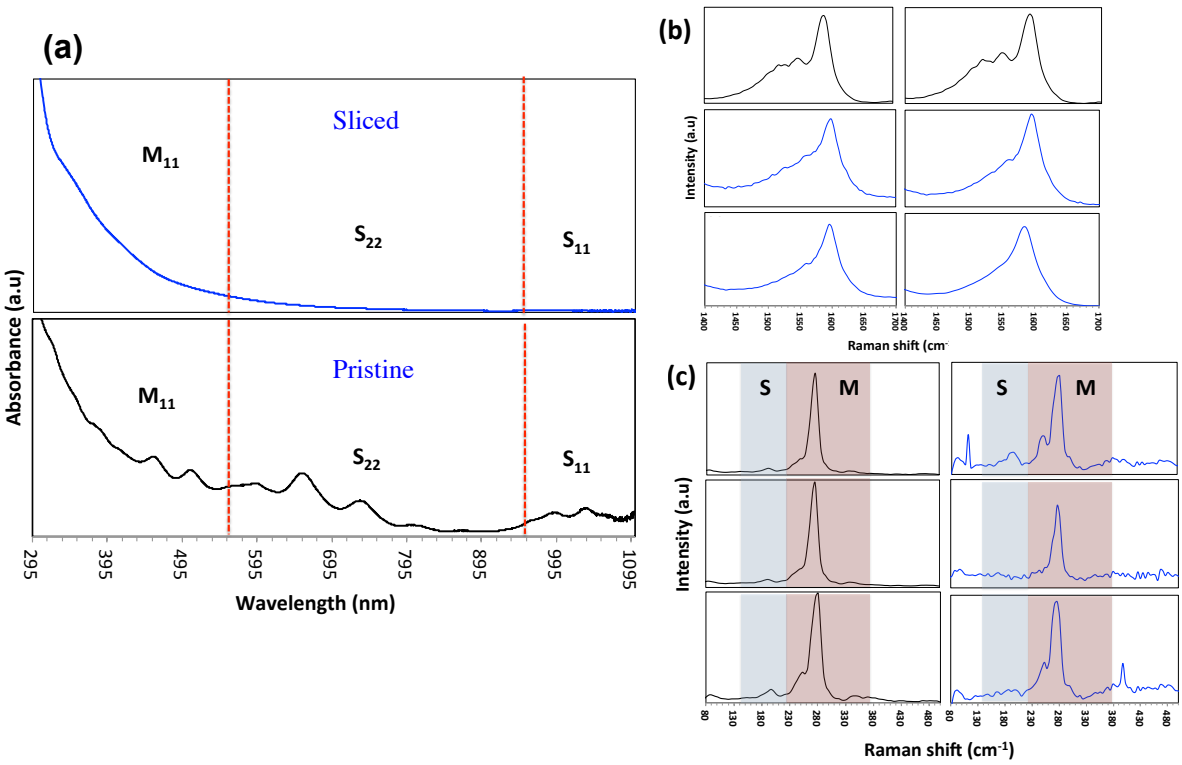

Figure 38 Optical absorption spectra and Raman analysis. (a) Ultraviolet-visible-infrared absorption spectra of as received semiconducting and metallic SWCNTs (black line) and the separated SWCNTs with the majority of the tubes of metallic chirality and the semiconducting S_{22} chirality (blue line), (b) The G-mode region of as received SWCNTs (black line) and the separated metallic SWCNTs (blue line), and (c) Radial breathing mode (RBM) analysis of the as received SWCNTs (black line) and the separated metallic SWCNTs (blue line).

Raman spectroscopy was then employed to confirm that the sample was enriched with metallic SWCNTs. Raman spectra (Figure 38b and c) were measured using the 532 nm laser excitation wavelength. A comparison of the G band regions, of the as received SWCNTs and the separated metallic SWCNTs. For both semiconducting and metallic configurations, there are characteristic differences between the G bands, with two dominant features between 1500 and 1600 cm^{-1} corresponding to the vibrations along the circumferential direction (ω_{G-}) and a high frequency component attributed to vibrations along the direction of the nanotube axis (ω_{G+}).[101] The as received SWCNTs show both the ω_{G-} and ω_{G+} peaks in a Lorenzian lineshape with the ω_{G+} being stronger in intensity compared to the ω_{G-} peak.

Upon slicing, both of these peaks merge and exhibit a much broader band, exhibiting an asymmetric Breit-Wigner-Fano line shape, which is in agreement with the presence of

enriched metallic nanotubes in the sample (Figure 38b). The frequency of the radial breathing mode (RBM) is proportional to the inverse diameter of the CNTs, with the diameter and the chiral angle used to define the (*n,m*) integers of the CNTs. All metallic SWCNTs have RBM frequencies in the range between 200-280 cm^{-1} while the semiconducting SWCNTs range between 160-200 cm^{-1}. The RBM peaks of the sliced SWCNTs were analysed and the peaks corresponding to the semiconducting CNTs (~186 cm^{-1}) disappear with an additional prominent metallic peak (~248 cm^{-1}) observed (Figure 38c).

The sliced SWCNT sample was also characterized using photoluminescence (PL) contours (Figure 39). The results indicated that although there was evidence that the sliced SWCNT sample were enriched with the metallic configuration (optical absorbance and Raman analysis), the PL contour plots established that process induced the adsorption of the (9,4) chirality in specific with the other semiconducting chiralities losing their adsorbability and diminishing within the sample. These results are observed just after a single pass in the VFD under continuous flow in the presence of a pulsed laser at ~260 mJ. This demonstrates the ballistic pulses from the pulsed laser at 260 mJ laser power overcomes the large barrier of energy for interconverting different configurations of SWCNTs. This process is effectively changing the magnitude and rolling vector of the semiconducting nanotubes affording SWCNTs enriched with metallic characteristics with a specific semiconducting chirality still present.

This section of the thesis is still in the preliminary stages. Although the mechanism of this interconversion is not yet clearly understood, our findings at this stage show that the laser energy not only facilitates the breaking of the C-C bonds at points of defect, but also provides sufficient energy to convert/interconvert the CNTs to obtain monochiral CNTs. At this stage, we assume that interconverting the remaining semiconducting chiralities to metallic via a second or additional passes in the VFD under continuous flow will eventually be effective in converting all semiconducting tubes to metallic tubes. This is for future studies.

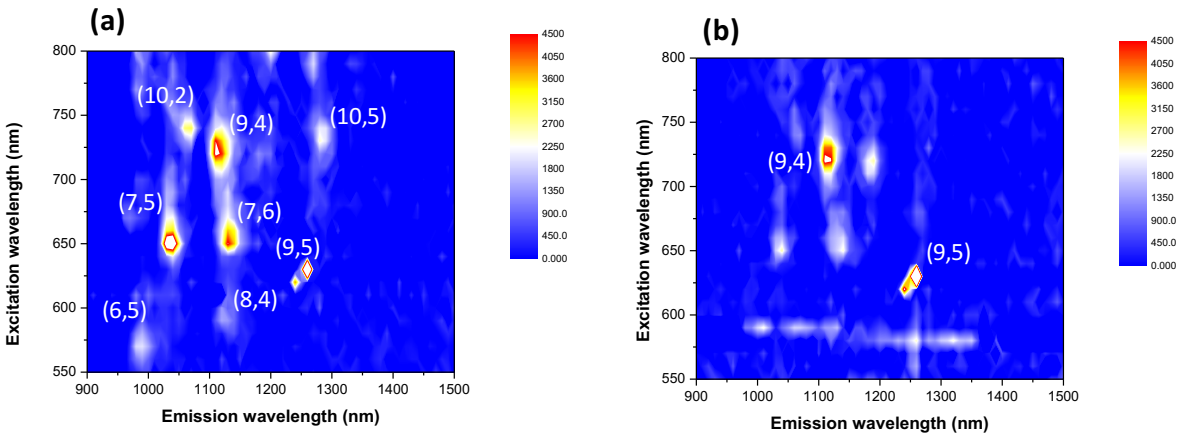

Figure 39 Photoluminescence excitation spectra of (a) pristine as received SWCNTs and (b) separated SWCNTs after a single pass in the VFD while simultaneous pulsed with a Nd:YAG laser operating at 1064 nm and 260 mJ.

In summary, although these results are still preliminary, the method developed thus far creates a new avenue for research in materials science, with the ability to interconvert one configuration to another via a simple and novel step, devoid of the use of surfactants, and using long and tedious chromatographic methods and chemical stabilizers. One of the most interesting features of this non-destructive method is that it avoids the use of toxic chemicals, high temperature processing and tedious and complex chromatographic methods to facilitate the separation and purification of monochiral SWCNTs. These preliminary results open new pathways towards optimizing the conditions to be able to interconvert metallic CNTs to semiconducting as well as the ability to afford monochiral SWCNTs under continuous flow.

6.5 VFD mediated dethreading of DWCNT and MWCNT/ removing the inner shells

DWCNTs and MWCNTs are made up of multiple coaxial cylindrical layers with a high aspect ratio (10^3-10^8).[99] Each layer is geometrically unique, exhibiting different electrical properties, being either semiconducting or metallic. The electronic complexity that is often a limitation using SWCNTs is the inability to grow SWCNTs of a specific diameter and chirality with a view of controlling their respective electronic properties. Bulk SWCNTs grown using a bottom up approach consists of a mixture of diameters and chirality making use for some specific applications problematic.

Thus, besides developing a novel method to separate or convert (interconvert) SWCNTs of different chiralities, as presented in Section 6.4 in this chapter, an alternative method would be to selectively displace the different shells as a dethreading process. Selectively removing the inner shells from the outer shells would enable the ability to exquisitely tailor the properties of the resulting SWCNTs. DWCNTs and MWCNTs are composed of more than one shell, which are held together by van der Waals interactions with non local nature of the π-π dispersion forces.[100] The extremely low friction between the shells, indeed super-lubricity offers scope for sliding or rotating the inner shells with respect, in removing the inner shells from the outer shells and exploit the individual properties of now SWCNTs of specific diameters and chirality.[101-104]

A number of methods have been developed for the purpose of removing the inner shells of multi layer CNTs, including using a scanning bias voltage,[105] complex electrical procedures,[106] the use of solution phase extraction facilitated by cavitation energy and surfactants [107] or by nanomanipulation using atomic force microscopy.[100] However, these methods have limited practicality in terms of making viable quantities of dethreaded CNTs, although theoretical considerations suggest that removing the inner shells from the outer shells would provide great avenues in materials science for a diverse range of applications.[100,101,108-111] For example, the "sword-in-sheath" method involves the breaking of the outer most shells to analyse the sliding of the inner shells.[101,108,111-113] Significant progress in the sliding behaviour of MWCNTs has recently been demonstrated with centimetres long DWCNTs whereby the inner-shell pull-out was determined to be independent of the pull-out length.[114]

As part of the research undertaken in this thesis, a novel and facile method of dethreading of

DWCNTs during *in situ* slicing in the presence of shear stress in the VFD and a pulsed laser operating at a wavelength of 1064 nm and a designer surfactant, or post VFD processing on addition of the same surfactant. The dethreading of sliced DWCNTs and MWCNTs is likely to be more favoured than for long, as received material, on the basis that the evidence suggests that laser processing in the VFD limits the defects present in the material, and any defects may circumvent dethreading. Moreover, shorter CNTs are less likely to have defect limited dethreading sites relative to long CNTs.

In this work, the focus was on micron length DWCNTs in the first instance as the simplest dethreading scenario, for then translating the processing to MWCNTs. The method developed involves the spontaneous removal of the inner shells to gain access to single walled carbon nanotubes of progressively larger diameters. Spontaneous removal of the inner shells in small quantities was observed from the sliced sample CNT sample. A large hydrophobic designer surfactant, *p*-H_2O_3 phoshonated-calix[8]arene, was employed to further facilitate the dethreading (and maintain colloidal stability) of the CNTs. The choice of calixarene was based on the use of the same calixarene and phosphonated calixarenes in general to separate different diameter SWCNTs.[115]

6.5.1 Calixarenes

Since their discovery in the 1940's by Zinke and Ziegler, the unique 3D surface of calixarenes has attracted considerable amounts of attention due to their diverse applications, including acting as surfactants and chemoreceptors.[116] Calixarenes are a class of cyclooligomers, typically formed via an oligomerisation reaction involving a phenol-formaldehyde condensation reaction. The molecular structure of these macrocyclic receptors resembles a 'cup' like shape, divided into three main segments, the upper rim, the central annulus and the lower rim (Figure 40). The central annulus is made of cyclic arrays of [n] phenol moieties bridged by methylene groups,[117] with both the upper and lower rim accessible for functionalization, widening their potential applications. The unique molecular structure of calixarenes, having a rigid conformation, n = 4, or flexible conformation as n increase, and highly hydrophobic nature of the varying cavity size of the macrocycle, makes them candidates as host molecule in host-guest chemistry and supramolecular chemistry in general.[118] For example, the calix[8]arene bearing Bu-t moieties in the *p*-positions is effective in selectivity binding and purifying fullerene C_{60}.[119] Indeed, the versatility of these macromolecules in

molecular recognition is almost limitless, featuring in ion sensitive electrodes or sensors, optical sensors, chiral recognition devices for solid phase extraction as a stationary phase and modifiers.[116,120,121]

In targeting more benign methods to the processing of carbon nanomaterials, water soluble calixarenes bearing water-soluble functional groups at the lower and upper rims have been developed. The most widely investigated class of such macrocycles are the sulfonic acids[122,123] or phosphonic acid moieties on the upper rim.[124,125] Solubilisation of carbon nanomaterial in water rather than in organic solvents has resulted in a number of novel and facile methods to fabricate and manipulate hydrophobic carbon nanomaterials to enhances the green chemistry metrics of the processing, with economic and environmental sustainability, minimizing energy usage, reduction in down stream processing and dramatically reduction in the cost of processing with scope for scaling up the the process. The high level of conformational flexibility of functionalized water-soluble calix[8]arenes offers the opportunity to process carbon nanomaterial in water devoid of any other chemical stabilizers, without compromising the quality of the nanocarbon product targeted. Although *p*-sulfonated calixarenes and other sulfonated calixarenes will be explored in future, this section of the chapter will focus on the addition of *p*-phosphonated calix[8]arenes, to facilitate the removal of inner shells from the outer shells of multi walled CNTs.

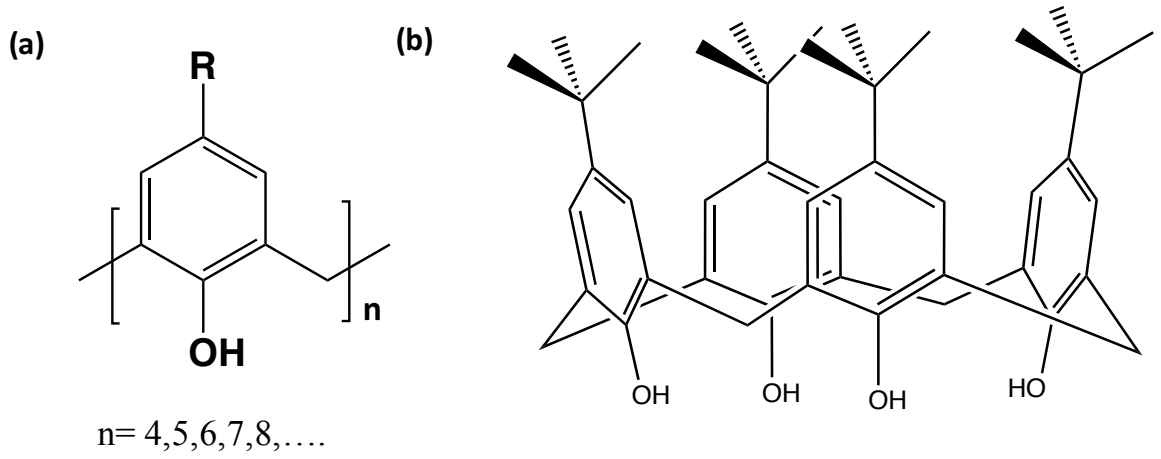

Figure 40 (a) General formula of calix[*n*]arenes, R can be a wide range of substituents, and (b) cone conformation of the Bu-t-calix[4]arene.

6.5.2 *p*-Phosphonated calixarenes

The versatility of *p*-phosphonated calix[n]arenes (n= 4, 5, 6 and 8) (Figure 41) with different lower and upper rim functionalization is highlighted by a number of recent reports on the processing of nano-carbon.[126] *p*-Phosphonated calix[n]arenes are effective in facilitating the exfoliation graphene and also stabilising the individual graphene sheets.[127] Other recent work have established the use of these macrocycles to efficiently solubilized SWCNTs in water and selectively afford enriched SWCNTs based on diameter,[115] as surfactants facilitating the exfoliation and stabilising of 2D material over a wide pH range,[127] facilitating the decoration of palladium (Pd) and platinum (Pt) nanoparticles on graphene sheets[128-130] and on carbon nano onions (CNO).[131] This relates to its simple method of synthesis and biocompatibility. In this section of the chapter, the focus is on the use of *p*-phosphonated calix[8]arene, for which a robust synthesis was developed much later, in 2008, and like the other members of the family of calixarenes, n = 4, 5 and 6, it is non-toxic.[126]

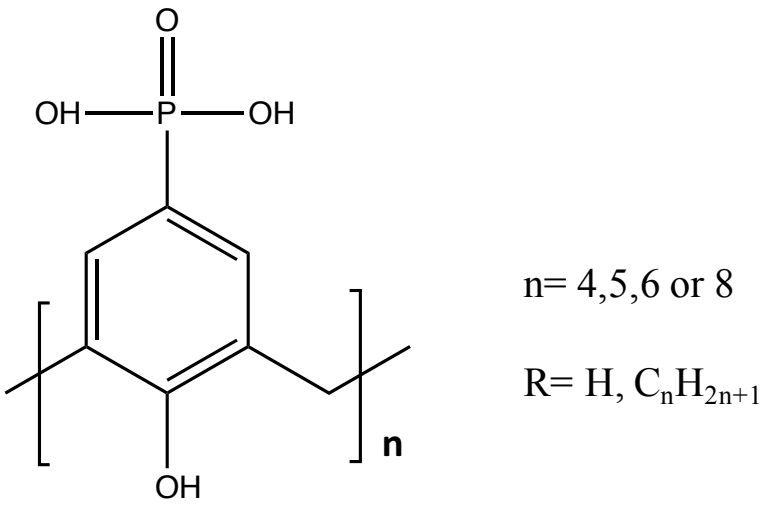

Figure 41 General structure of *p*-phosphonic acid calix[n] arenes

6.5.3 Experimental design

A novel and facile method of removing the inner shells of DWCNTs in water is developed, noting earlier studies established that it is effective in solubilizing and stabilising nanocarbon material in general.[115,127-131] Indeed the *p*-phosphonated calix[8]arenes is effective in overcoming the inter-shell interplay involving van der Waals interactions, as a simple method to easily remove the inner shells from the outer shells, under the shear stress in dynamic thin film son the VFD. The inner shells of the DWCNTs are dethreaded from the outer walls in water by applying shear stress within dynamic thin films in the VFD while irradiating at 1064 nm

using a pulsed Q-switch Nd:YAG laser, in the presence of the calixarene (Figure 42). The VFD is a microfluidic platform that generates controllable mechanoenergy within a liquid medium, as thin films are formed around the internal walls of a rapidly rotating tube, which for practical purposes was a 20 mm diameter (ID 16.000 ± 0.013 mm) borosilicate glass tube. In general, the optimal performance of the VFD occurs at high rotational speeds (2000 rpm to 9000 rpm) and inclination angles, θ > 0°, with a 45° tilt angle corresponding to the maximum cross vector of centrifugal force and gravity. For this work, the optimized conditions for removing the inner shells from the outer shells was θ 45° for a rotational speed of 7500 rpm.

Preparation of aqueous suspensions of CNTs. DWCNTs were purchased from Carbon Allotropes with an as received purity >99%. *p*-Phosphonic acid calix[8] arene (*p*-H_2O_3 P-calix[8] arene) (Figure 42b) was synthesized following the literature method[129]. Millli-Q water was used for preparing the 10 mL aqueous suspensions of CNTs. Aqueous dispersions of DWCNT (1mg) in water (6mL) were prepared in the presence of *p*-phosphonic acid calix[8] arene (1 mg/mL). Each solution mixture was ultrasonicated for 5 minutes, affording a black stable dispersion. Under the confined mode of operation of the VFD, the solution mixture (1 mL) was then placed in the glass tube and rotated at 7500 rpm, at a tilt angle of 45 degrees. Simultaneously, a nanosecond pulsed laser processing system with an energy of approximately 260 mJ was applied to the rapidly rotating system for 30 minutes. Under continuous flow mode, jet feeds with a flow rate at 0.45 mL/min (optimized) deliver the CNT suspension (similar concentration, as for the confined mode) into the rapidly rotating tube. Centrifugation (g= 3.22) of the resulting dispersion for the confined mode of operation was required to remove any large agglomerates, bundled CNTs and impurities in the sample. The suspension of DWCNTs was then further ultracentrifugated (g ~16900) for 30 minutes to remove the excess calixarene. The centrifuge-washing step was repeated 3 times to ensure there was no excess calixarenes present. The above method was then repeated using a mixture of NMP and water (6 mL) at a 1:1 ratio.

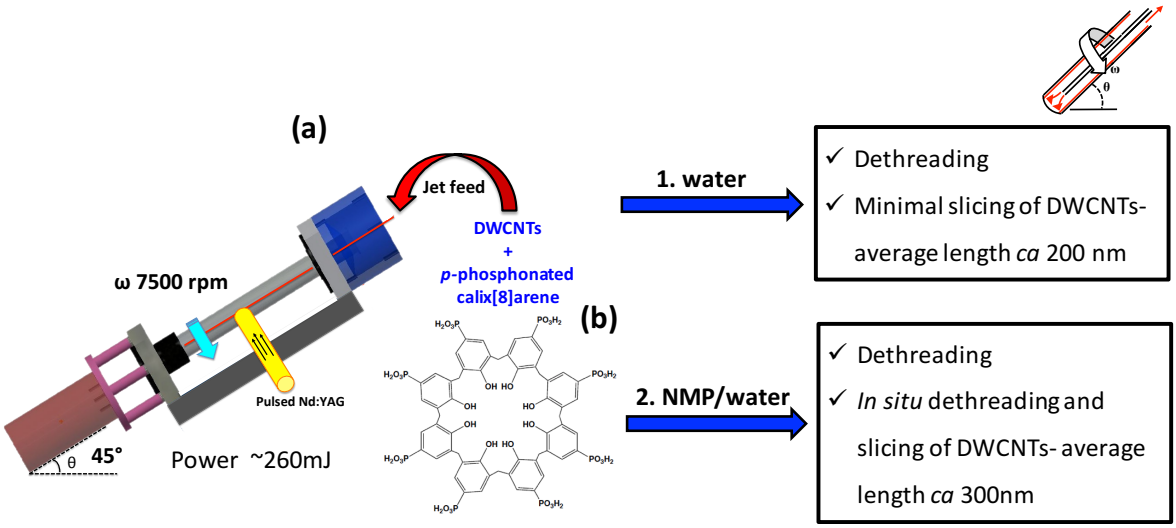

Figure 42 Schematic of the vortex fluidic device and chemdraw of *p*-phosphonated calix[8]arene.

6.5.4 Characterization techniques and discussion

The results establish that the inner shell has been removed from the outer shells, based mainly using Raman spectroscopy measurements. Thus under the experimental conditions of shear stress coupled with irradiation with a pulsed laser in the presence of the calixarene there is dethreading of the inner SWCNT. For the purpose of characterization, the CNTs solubilized by the calixarene were ultra centrifuged (refer to experimental design) and the supernatant solution was drop casted on a glass slide. The radial breathing mode (RBM) frequencies (100-300 cm^{-1}) of the Raman spectra provides detailed information with regards to the diameter of CNTs present within a sample.[133] In order to precisely determine the diameter of CNTs, the frequencies of the radial breathing mode of the as received multi walled CNTs were compared with RBM frequencies obtained upon the addition of the *p*-H_2O_3 phosphonated calix [8]arene.

The relationship between the RBM frequency and the inverse nanotube diameter has been well explored and is determined using the mathematical formula below:

$$\nu_{RBM} = \frac{A}{d_t} + B$$

Equation 4

where ν_{RBM} is the RBM frequency in cm^{-1}, d_t is the tube diameter in nm and the parameters A= 223.5 cm^{-1} and B= 12.5 cm^{-1} were experimentally determined.[131] A summary of the calculated diameters of CNTs present in the as received sample and the sample upon removing the shells were systematically tabulated in Figure 43 (DWCNT dispersed in water) and 44 (DWCNT dispersed in a mixture of NMP and water). It is noteworthy that Raman spectra were obtained for control experiments consisting of just the *p*-H_2O_3 phosphonated calix[8]arene, establishing that the calixarenes are not Raman active and this is in agreement with previously reported work.[115] The RBM frequencies with the highest intensities after dethreading are at 129.8 cm^{-1} (1.91 nm), 148.9 cm^{-1} (1.64 nm), 182.2 cm^{-1} (1.31nm), 271.7 cm^{-1} (0.86nm), 304.5 cm^{-1} (0.77 nm), 309.2 cm^{-1} (0.75nm), and 323.0 cm^{-1} (0.72 nm) (Figure 43). Broad RBM bands were observed with the as received DWCNT compared to the narrow sharp peaks observed with the sample post processing. The broad bands observed are possibly due to a superposition of a few Lorentzian components related to CNTs consisting of different diameters.[115]

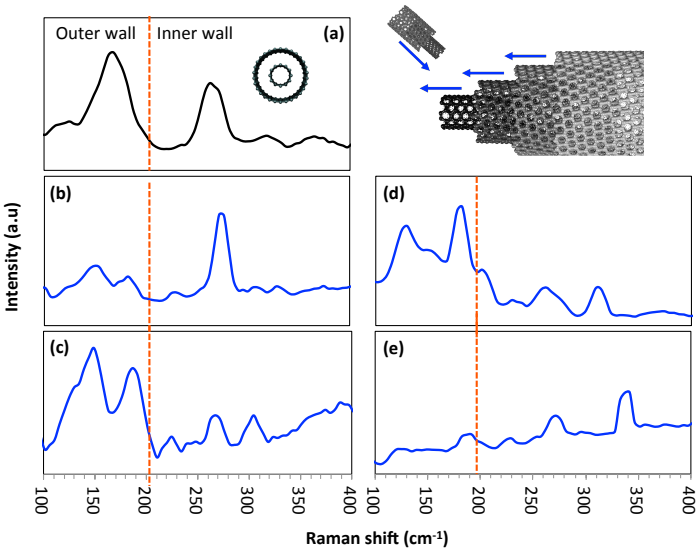

ω_{RBM} as received DWCNT (cm^{-1})	Diameter, d (nm)
163.2	1.48
262.4	0.89

ω_{RBM} DWCNT after dethreading (cm^{-1})	Diameter, d (nm)
129.8	1.91
148.9	1.64
177.4	1.36
182.2	1.31
201.1	1.19
220.0	1.08
229.4	1.03
257.7	0.91
271.7	0.86
304.5	0.77
309.2	0.75
323.0	0.72
383.6	0.61

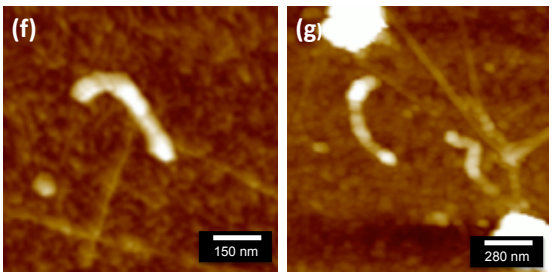

Figure 43 Raman analysis of the radial breathing mode (RBM) region of SWCNTs in water: (a) as received DWCNTs, (b-e) DWCNT after dethreading, (f-g) AFM height images of sliced SWCNTs in water.

Thus, we established a method whereby the addition of *p*-phosphonated calix[8]arene effectively removes the inner shells from the outer shells in water and with low yields of slicing observed, *ca* 200 nm in length (Figure 43). Using a mixture of water an NMP as used in the original slicing work reported earlier in this chapter allowed for *in situ* dethreading and high yield of slicing, with an average length of *ca* 370 nm (Figure 44).

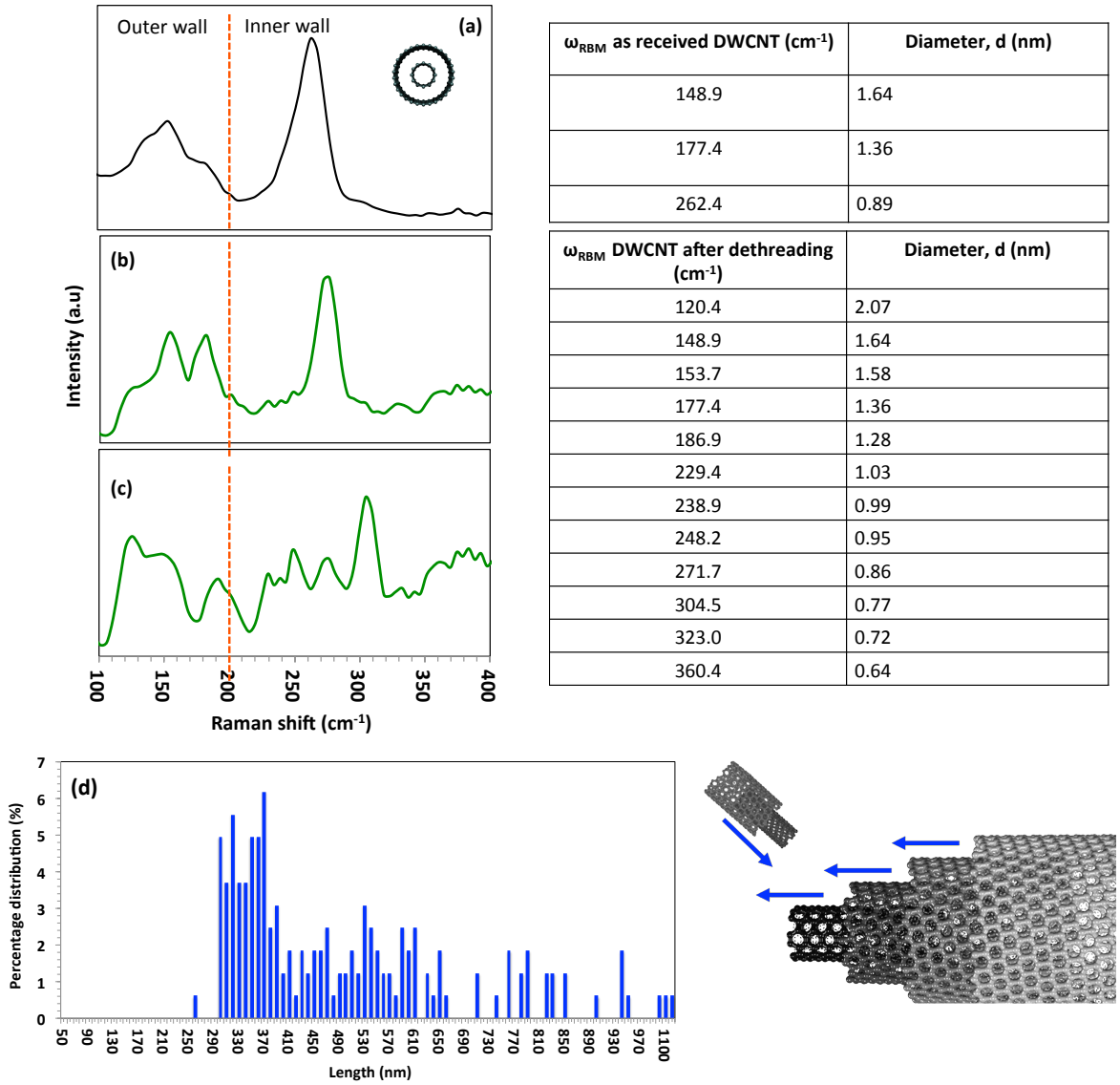

ω_{RBM} as received DWCNT (cm^{-1})	Diameter, d (nm)
148.9	1.64
177.4	1.36
262.4	0.89

ω_{RBM} DWCNT after dethreading (cm^{-1})	Diameter, d (nm)
120.4	2.07
148.9	1.64
153.7	1.58
177.4	1.36
186.9	1.28
229.4	1.03
238.9	0.99
248.2	0.95
271.7	0.86
304.5	0.77
323.0	0.72
360.4	0.64

Figure 44 Raman analysis of the radial breathing mode (RBM) region of SWCNTs in a mixture of NMP/water: (a) as received DWCNTs, (b-c) DWCNT after dethreading *in situ*, and (d) length distribution plot of sliced SWCNTs with an average length of *ca* 370 nm.

6.5.5 Conclusion

The method established is an *in situ* dethreading and slicing of DWCNTs in water in the presence of the calixarene. Other solubilising surfactants may also be effective, in also avoiding the use organic solvents. Removing the inner shells from the outer shells of DWCNTs, and in future MWCNTs, provides a novel pathway towards gaining access to larger diameter SWCNTs with potential use for drug delivery and as protein delivery vehicles.[135] The feasibility studies establishes that the dethreading is solvent dependent with the designer calixarene facilitating the rotation and sliding of the outer shells from the inner shells. It is also important to note that shortening of the nanotubes could somewhat have an effect on the ease of intertube sliding relative to long, bundled nanotubes.

6.6 VFD mediated fabrication of intertwined single walled carbon nanotube rings.

This section is based on a publication published in Chemical Communication entitled, 'Shear induced fabrication of intertwined single walled carbon nanotube rings,' authored by **Kasturi Vimalanathan**, Xianjue Chen and Colin L. Raston.

Abstract: Thin film microfluidic shearing of a mixture of toluene dispersed single walled carbon nanotubes (SWCNTs) and water in a vortex fluidic device results in SWCNT nanorings (and related structures), diameters 100 to 200 nm or 300 to 700 nm in diameter, for respectively 10 mm or 20 mm diameter rotating tubes.

Single walled carbon nanotubes (SWCNTs) continue to attract attention, having exceptional mechanical and electrical properties in high performance electronics[136] and applications in scanning probe microscopy,[137] fuel cells,[17] composites,[34] chemical,[138] biological,[139] and physical sensors.[140] They are available as long fibres, centimetres in length and beyond, and tend to aggregate into large bundles because of the relatively strong inter-SWCNT van der Waals interactions. Indeed, difficulties in generating individual strands of SWCNTs are an issue in optimizing their mechanical, thermal, and electronic properties.[141,142] Carbon nanotubes have in general extremely high flexural rigidity,[17,34] and permanently bending them in a controlled way into well-ordered nanorings/toroidal structures is challenging,[143] with the potential to circumvent or control the aforementioned aggregation and impart different functionality. A variety of techniques have been reported on generating such structures with control over their diameters.[144-148] However, they mostly involve long periods of high-energy sonication, chemical modifications and lengthy physical processing as well as the use of highly reactive chemicals such as concentrated sulphuric acid and hydrogen peroxide, which are potentially damaging to the SWCNTs. In this context, the development of more benign methods is warranted, as is the ability to scale up the conversion of SWCNTs in particular, into the nanorings, with control over their diameter while maintaining a high level of purity. Hydrophobic carbon nanotubes and hydrophilic palladium nanowires form coils in the presence of a water/oil mixture, and this establishes the utility of an immiscible solvent mixture and the associated interfacial surface tension as an important consideration in overcoming high flexural rigidity of these one dimensional materials.[146]

We now report a simple and novel one-step method to produce nanorings of SWCNTs in high yield, where liquid-liquid interfacial area involving a mixture of water and toluene is amplified using mechanoenergy from a recently developed energy efficient microfluidic vortex fluidic device (VFD), Figure 45.[149] Well-defined nanorings of SWCNTs with the average diameters depending on the diameter of the tube, being accessible down to ca 100 nm. The ability to control the diameter of such rings, and the ability to scale up, has implications for applications in electronic devices.[143]

The VFD has a rapidly rotating tube, within which liquids form dynamic thin films for finite sub-millilitre volumes of liquid, as the so-called confined mode of operation of the device.[149] The shear intensity in the films depends on a number of parameters, including inclination angle relative to the horizontal position, θ, and the rotational speed,[149] which collectively define the interplay between centrifugal and gravitational forces within the films.[64] The confined mode of operation of the VFD results in the formation of a thin film for a defined volume of liquid (herein 1 mL) within the tube, at least above a threshold speed such that a vortex is maintained to the bottom of the tube, otherwise there are different regimes of shear within the liquid.[149]

The VFD can also operate under continuous flow where jet feeds deliver solutions to the bottom of the tube which results in intense micro mixing, and collectively with the confined mode of operation, a number of applications of the device have been established. These include controlling chemical reactivity and selectivity in organic synthesis,[149] exfoliation of graphene and boron nitride,[64] controlling the decoration of palladium nanoparticles on carbon nano-onions and graphene sheets,[128-131,150] generating graphene algae hybrid material for nitrate removal,[151] generating mesoporous silica at room temperature with control of pore size and wall thickness,[67] and more.

6.6.1 Experimental design

SWCNTs produced by a catalytic chemical deposition synthesis method with > 90% purity were purchased from Thomas Swan and Co. (UK), and used as received. Toluene was purchased from Sigma Aldrich and also used as received. SWCNTs (1.0 mg) were dispersed in toluene (3 mL) and added to MilliQ water (3 mL). Sonication for 10 minutes afforded a stable two-phase dispersion with the top phase black and the bottom phase milky (Figure 1(a)). A 1 mL portion

of the mixture under sonication was collected to ensure that it was a uniform mixture of the three components, and was placed in a 20 mm (I. D= 20.000 ± 0.013 mm) or 10 mm (I. D= 7.100 ± 0.013 mm) diameter VFD tube, as standard borosilicate glass NMR tubes.

A systematic evaluation of the operating parameters of the VFD was carried out to ascertain the optimal parameters for the formation of the nanorings. These were established as an inclination angle of 45° with the 20 mm VFD tube rotating at 7500 rpm, for a reaction time of 20 minutes. At other rotational speeds and inclination angles, ie. higher or lower than the optimized conditions, the formation of the nanorings was either in low yield or not evident (Appendix H). The diameters of the rings produced were within the range of 300 to 700 nm, as established using atomic force microscopy (AFM) and transmission electron microscopy (TEM). Optimisation of the operating parameters were also established for a 10 mm diameter tube, which resulted in the formation of nanorings with a significantly smaller diameter range, 100 to 200 nm.

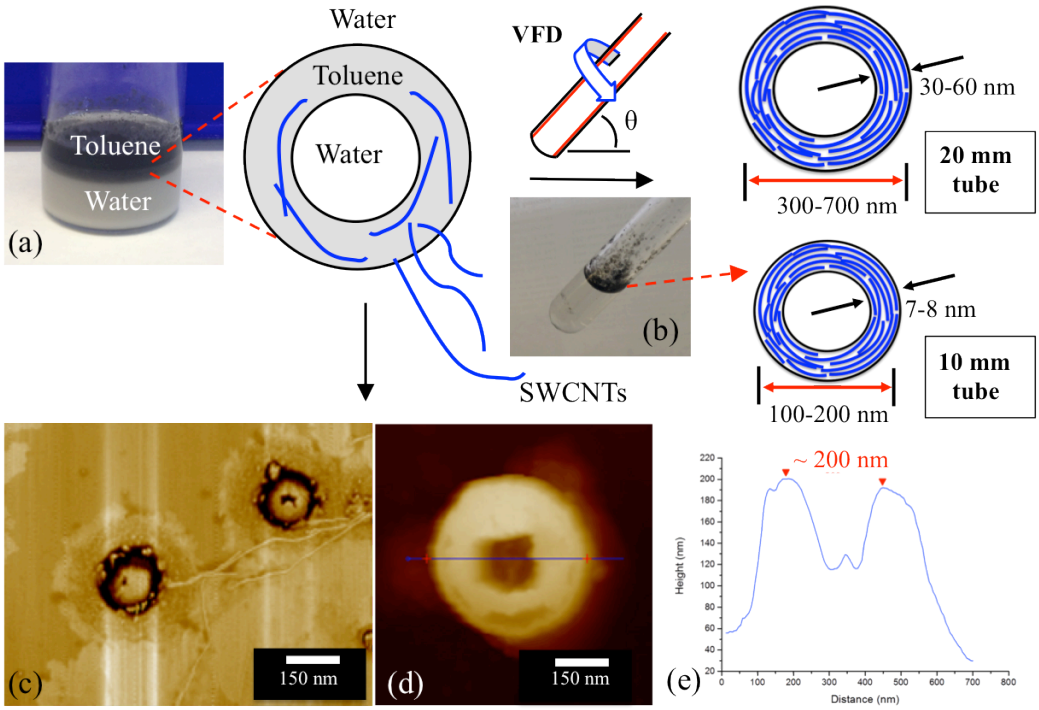

Figure 45 (a) Synthesis and proposed templated mechanism of formation of nanorings of SWCNTs from a sonicated mixture of toluene and water, (b) photograph of SWCNT/toluene/water mixture post-VFD processing, θ 45° and pre-VFD processing AFM phase image, (c) height image, (d) and associated height profile, (e) of a toroidal structure with radiating SWCNTs, formed on drop casting the mixture from (a).

Overall the nanorings formation (Figure 46 and 47) is at a high conversion. There was no evidence of non-coiled SWCNTs, with some different morphologies generated, namely nanorings, figure of "8" shaped rings and crossed lattice rings.[141]

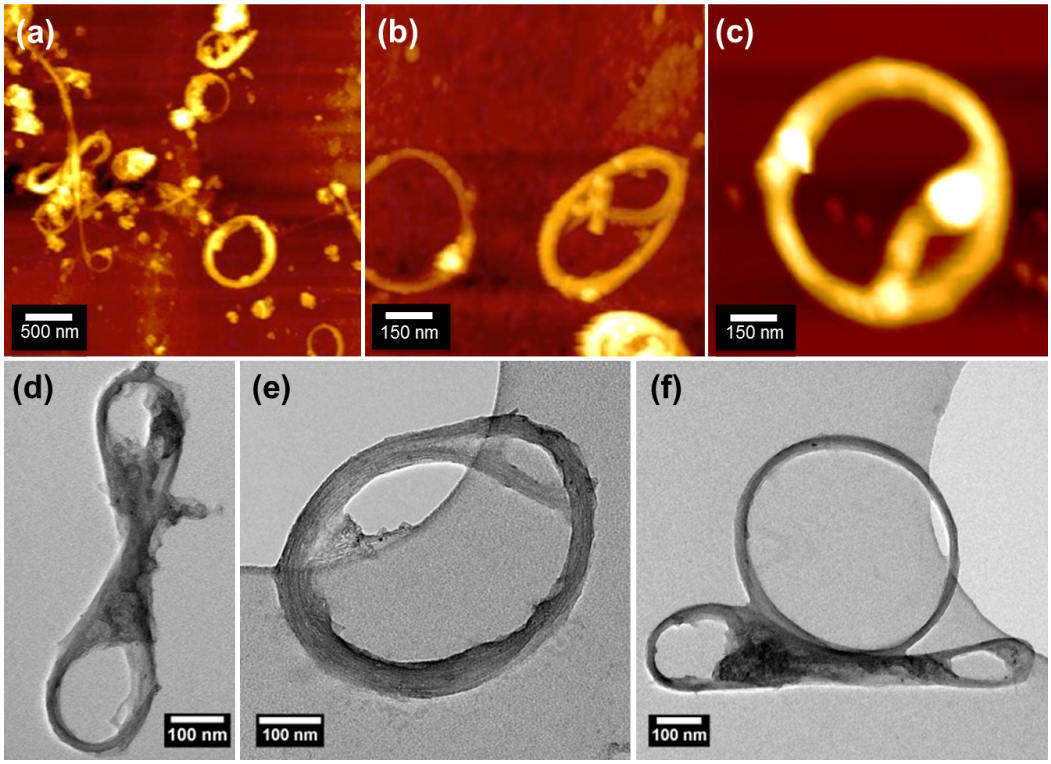

Figure 46 SWCNT nanorings 300 to 700 nm in diameter, generated using a 20 mm VFD tube: (a-c) AFM height images of the rings, (d-f) TEM images of the different nanoring structures.

Processing in the smaller internal diameter tube afforded smaller rings, 100 to 200 nm in diameter, Figure 47, for a reaction time of an hour under the same VFD operating parameters (namely 45 degree inclination angle, 7500 rpm rotational speed). Small amounts of toroidal structures based on a single SWCNT are also present (Figure 47f), where it appears that SWCNTs 'bite' their tail, with the diameter of the toroid at approximately 100 nm. This corresponds to a length of 314 nm for a straight SWCNT, from which the toroid presumably originates, Figure 46f, and this has implications on the nature of processes involved in the dynamic thin films in the VFD. It is noted that the initial lengths of these as-received SWCNTs were approximately 1-2 μm in length, and thus in forming these structures based on a single SWCNT there has been some lateral slicing in generating shorter lengths.

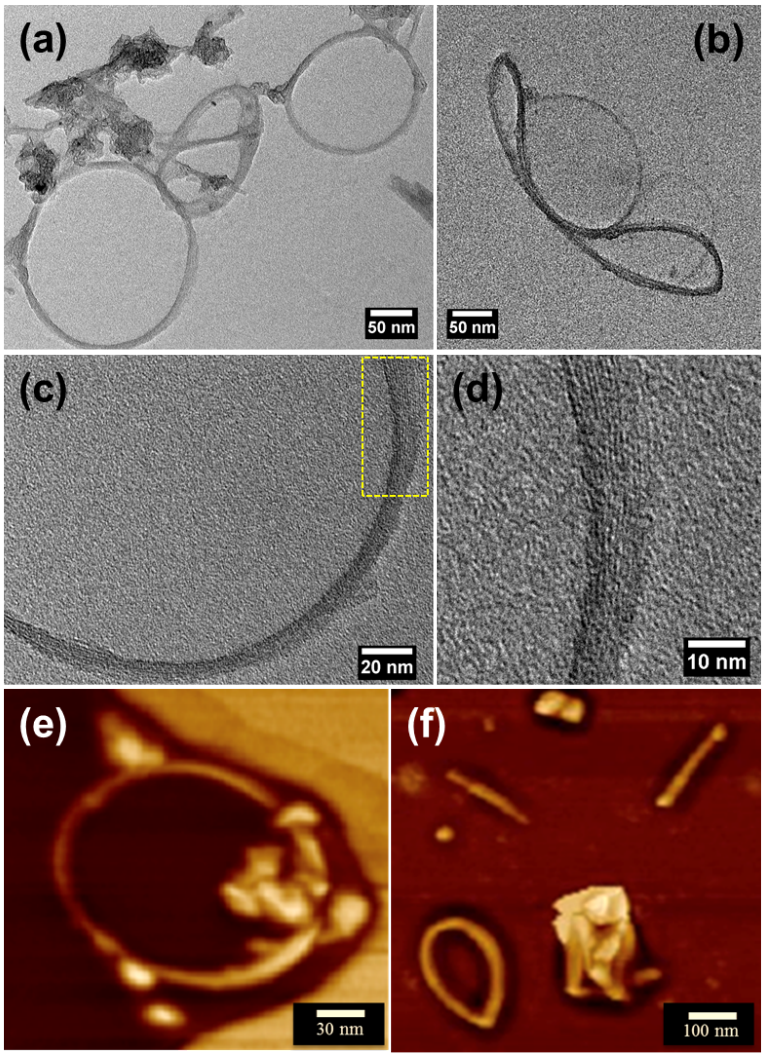

Figure 47 SWCNT nanorings 100 to 200 nm in diameter (10 mm diameter VFD tube): (a-b) TEM images of the nanorings, (c-d) HRTEM images. AFM height images (e) nanoring, and (f) single SWCNT 'biting' its tail (lower left) along with some short SWCNTs, *ca* 120 nm in length.

Shear forces in the VFD are effective under both confined mode and continuous flow modes of operation in controlling the fabrication of nanomaterials,[64,67,150,151] including exfoliation of carbon nanomaterials such as graphite.[64] In the confined mode at $\theta > 0^{o}$, centrifugal forces accelerate the emulsion droplets and nanotubes to the bottom of the tube. The ensuing shear can overcome the large van der Waals forces between the bundles of SWCNTs and thus facilitate exfoliation of individual SWCNTs, with the shear then also responsible for their lateral slicing.

Drop casting the interfacial SWCNT laden material in Figure 45(a) affords toroids with radiating SWCNTs, as established using AFM, Figure 45(c) – (e). This suggests that toroids of toluene

containing hydrophobically matched SWCNTs are present pre-VFD processing, and under shear nanorings of compact intertwined SWCNTs at their van der Walls limit are formed, drawing in the radiating SWCNTs. These nanorings were characterised using AFM and TEM, Figure 46 and 47. They have smaller wall thickness (differences between the internal and external diameter) relative to the toroids formed from drop casting pre-VFD processing mixture. For 10 mm diameter VFD tubes, the external diameter of the nanorings dramatically reduces relative to the size of the toluene toroids, and thus there is greater curvature in the SWCNTs.

Interestingly, the long axis of the figure of "8" structures is approximately twice the external diameter of the nanorings, and possibly arise from two toroids of SWCNT laden toluene in contact through common SWCNTs, at their limiting size under intense shear. Previous researchers have noted that the different structures of nanorings depend on the method of sample preparation, with rings collapsing at the edge of the substrate prior to solvent evaporation in forming the figure of "8" structure.[146] Formation of these structures has also been ascribed as resulting from further coiling and twisting of the toroid rings, as a secondary structure.[148]

As a control, sonication of a suspension of SWCNTs in toluene showed de-bundling of the nanotubes with occasional ring structures. However, these rings were unstable and slowly collapsed back post-sonication (Appendix H**)**. Also SWCNTs in toluene, in the absence of water, and without the application of sonic energy, undergo aggregation/restacking. Clearly, sonication is essential to obtain a well-dispersed SWCNT toluene/water dispersion, generating templating toroids of toluene en route to forming the compact nanorings of SWCNTs under shear. In the absence of the liquid-liquid interface, the SWCNTs dispersed in pure toluene under shear using similar VFD processing conditions does not afford nanorings of SWCNTs, thereby establishing that the surface tension between the otherwise immiscible liquids is essential for generating nanorings of SWCNTs (Appendix H**)**.

High-resolution TEM (HRTEM) images show that the nanorings are comprised of SWCNTs of diameters in the range 1 to 2 nm (Figure 47c and 47d). These results are consistent with micro-Raman spectroscopy (Figure 48), at an excitation wavelength of 532 nm (≤ 5 mW).
The radial breathing mode (RBM) (Figure 48 inset) as well as the G- and D-band on the spectra

are markers for determining the diameters of the SWCNTs.[152] The peaks at 1353 cm^{-1} and the peak at 1593 cm^{-1} correspond to the D- and the G-bands respectively (Figure 48). The D-band is the disorder-induced band which provides information regarding amorphous impurities and is a measure of the amount of disorder and defects on the walls of the nanotubes, whereas the G-band (graphite band) corresponds to the graphite E_{2g} symmetry band, affirming the structural integrity of the sp^2 hybridized carbon atoms of the nanotubes.[115] Focusing on the RBM of the spectra, the frequencies at ca 97.3 cm^{-1}, 164.1 cm^{-1}, 182.1 cm^{-1} and 277.8 cm^{-1} respectively, $v_{RBM} = A/d_t + B$, where the RBM frequency is in cm^{-1}, d_t is the diameter of the CNT, and A= 223.5 cm^{-1} and B= 12.5 cm^{-1} which have been determined experimentally,[134] enable the determination of the diameter of the SWCNTs forming the rings. Thus, the frequencies of the RBM region correspond to SWCNTs present approximately 2.64 nm, 1.47 nm, 1.32 nm and 0.86 nm in diameter respectively, in accordance with HRTEM data.

The irregular thicknesses (Figure 46 and 47) of the ring walls relate to aggregation of more than one nanotube, consisting of semiconducting and metallic nanotubes of a range of diameters, stacked at the van der Waals limit. The rings produced in the 20 mm VFD had a nanoring wall thickness of ca 30 to 60 nm, comprised of approximately 20 to 30 stacks of nanotubes of diameters between 1 to 2 nm, noting that some of the nanotubes are likely to coil more than once in each nanoring. The smaller diameter rings, generated using a 10 mm diameter VFD tube, have 7.0 to 8.0 nm thick walls, being similarly built up of about 3 to 8 stacks of nanotubes of 1 to 2 nm in diameter.

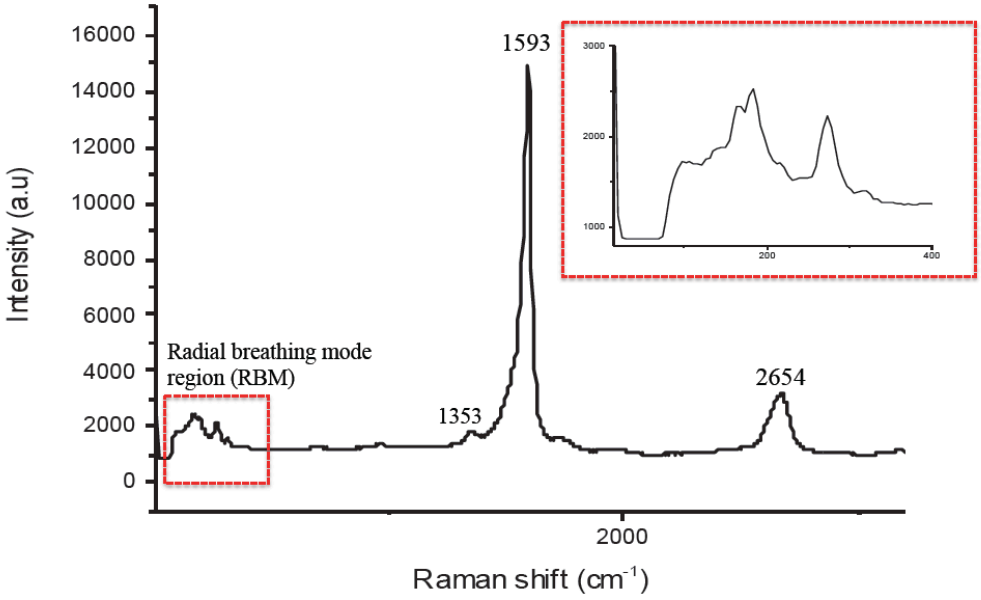

Figure 48 Raman spectra of SWCNT nanorings deposited on a glass slide. Inset: Radial breathing mode region whereby the frequencies correspond to diameter of the SWCNTs.[148]

6.6.2 Conclusion

In summary, we have developed a simple and novel one-step method to fabricate SWCNT nanorings using the shear generated in thin films within a vortex fluidic device. This is under ambient conditions and avoids the use of reactive chemicals for processing, and the need for surfactants to stabilize the nanorings, with the ability to control the ring size, depending on the diameter of the rapidly rotating tube. Nanorings of SWCNT have promise in a number fields including in polymer composites, sensing devices and more importantly electronic circuits,[142-144] and this is closer to a realization with the availability of such material herein, which can be readily scaled up.

6.6.3 Acknowledgements

The authors gratefully acknowledge support of this work by the Australian Research Council and the Government of South Australia, and the Australian Microscopy & Microanalysis Research Facility (AMMRF) at the Centre for NanoScale Science and Technology, Flinders University

6.7 References

1 Iijima, S. & Ichihashi, T. Single-shell carbon nanotubes of 1-nm diameter. *Nature* **363**, 603-605, (1993).

2 Bethune, D. S. *et al.* Cobalt-catalysed growth of carbon nanotubes with single-atomic-layer walls. *Nature* **363**, 605-607, (1993).

3 Iijima, S. Helical microtubules of graphitic carbon. *Nature* **354**, 56-58, (1991).

4 Ebbesen, T. W. & Ajayan, P. M. Large-scale synthesis of carbon nanotubes. *Nature* **358**, 220-222, (1992).

5 Thess, A. *et al.* Crystalline Ropes of Metallic Carbon Nanotubes. *Science* **273**, 483-487, (1996).

6 Charlier, J.-C. & Iijima, S. Growth in Carbon Nanotubes. *Springer* 55-81, (2001).

7 Guo, T., Nikolaev, P., Thess, A., Colbert, D. T. & Smalley, R. E. Catalytic growth of single-walled manotubes by laser vaporization. *Chemical Physics Letters* **243**, 49-54, (1995).

8 Endo, M. *et al.* The production and structure of pyrolytic carbon nanotubes (PCNTs). *Journal of Physics and Chemistry of Solids* **54**, 1841-1848, (1993).

9 Dai, H. Carbon Nanotubes: Synthesis, Integration, and Properties. *Accounts of Chemical Research* **35**, 1035-1044, (2002).

10 Liu, Z., Tabakman, S., Welsher, K. & Dai, H. Carbon nanotubes in biology and medicine: In vitro and in vivo detection, imaging and drug delivery. *Nano Research* **2**, 85-120, (2009).

11 Prato, M., Kostarelos, K. & Bianco, A. Functionalized Carbon Nanotubes in Drug Design and Discovery. *Accounts of Chemical Research* **41**, 60-68, (2008).

12 Tuncel, D. Non-covalent interactions between carbon nanotubes and conjugated polymers. *Nanoscale* **3**, 3545-3554, (2011).

13 Sgobba, V. & Guldi, D. M. Carbon nanotubes-electronic/electrochemical properties and application for nanoelectronics and photonics. *Chemical Society Reviews* **38**, 165-184, (2009).

14 Katz, E. & Willner, I. Biomolecule-Functionalized Carbon Nanotubes: Applications in Nanobioelectronics. *ChemPhysChem* **5**, 1084-1104, (2004).

15 Zhang, W.-D., Xu, B. & Jiang, L.-C. Functional hybrid materials based on carbon nanotubes and metal oxides. *Journal of Materials Chemistry* **20**, 6383-6391, (2010).

16 Roche, S. Carbon nanotubes: Exceptional mechanical and electronic properties.

Annales de Chimie Science des Matériaux **25**, 529-532, (2000).

17 Treacy, M. M. J., Ebbesen, T. W. & Gibson, J. M. Exceptionally high Young's modulus observed for individual carbon nanotubes. *Nature* **381**, 678-680, (1996).

18 Krishnan, A., Dujardin, E., Ebbesen, T. W., Yianilos, P. N. & Treacy, M. M. J. Young's modulus of single-walled nanotubes. *Physical Review B* **58**, 14013-14019, (1998).

19 Kashyap, K. T. & Patil, R. G. On Young's modulus of multi-walled carbon nanotubes. *Bulletin of Materials Science* **31**, 185-187, (2008).

20 Pumera, M. Electrochemical properties of double wall carbon nanotube electrodes. *Nanoscale Research Letters* **2**, 87-93, (2007).

21 Moore, K. E. *et al.* Separation of Double-Walled Carbon Nanotubes by Size Exclusion Column Chromatography. *ACS Nano* **8**, 6756-6764, (2014).

22 Han, J. Carbon nanotubes: science and application (Ed.: M.Meyyappan), *CRC Press,* (2005).

23 Rao, C. N. R., Voggu, R. & Govindaraj, A. Selective generation of single-walled carbon nanotubes with metallic, semiconducting and other unique electronic properties. *Nanoscale* **1**, 96-105, (2009).

24 Dai, H. Carbon nanotubes: opportunities and challenges. *Surface Science* **500**, 218-241, (2002).

25 Mildred S. Dresselhaus, Dresselhaus, G., Avouris, P. Carbon Nanotubes Synthesis, Structure, Properties and Applications. *Springer,* (2001).

26 Dresselhaus, M., Dresselhaus, G. & Saito, R. Physics of carbon nanotubes. *Carbon* **33**, 883-891, (1995).

27 Ajayan, P. M. Nanotubes from Carbon. *Chemical Reviews* **99**, 1787-1800, (1999).

28 Andrews, R., Jacques, D., Qian, D. & Rantell, T. Multiwall Carbon Nanotubes: Synthesis and Application. *Accounts of Chemical Research* **35**, 1008-1017, (2002).

29 Charlier, J.-C., Blase, X. & Roche, S. Electronic and transport properties of nanotubes. *Reviews of Modern Physics* **79**, 677-732, (2007).

30 Belin, T. & Epron, F. Characterization methods of carbon nanotubes: a review. *Materials Science and Engineering: B* **119**, 105-118, (2005).

31 Odom, T. W., Huang, J.-L., Kim, P. & Lieber, C. M. Atomic structure and electronic properties of single-walled carbon nanotubes. *Nature* **391**, 62-64, (1998).

32 Liu, C.-H., Liu, Y.-Y., Zhang, Y.-H., Wei, R.-R. & Zhang, H.-L. Tandem extraction strategy for separation of metallic and semiconducting SWCNTs using condensed benzenoid

molecules: effects of molecular morphology and solvent. *Physical Chemistry Chemical Physics* **11**, 7257-7267, (2009).

33 Galano, A. Carbon nanotubes: promising agents against free radicals. *Nanoscale* **2**, 373-380, (2010).

34 Wong, E.W., Sheehan, P.E. & Lieber, C.M. Nanobeam Mechanics: Elasticity, Strength and Toughness of Nanorods and Nanotubes. *Science*. **277**, 1971-1975, (1997).

35 Liu, L., Yang, C., Zhao, K., Li, J. & Wu, H.C. Ultrashort single walled carbon nanotubes in a lipid bilayer as a nanopore sensor. *Nature Commun.* **4, (**2013).

36 Javey, A., Guo, J., Paulsson, M., Wang, Q., Mann, D., Lundstrom, M. & Dai, H. High Field Quasiballistic Transport in Short Carbon Nanotubes. *Phys. Rev. Lett.* **92,** 16804, (2004).

37 Kalita, G., Adhikari, S., Aryal, H.R., Umeno, M., Afre, R., Soga, T. & Sharon, M. Cutting carbon nanotubes for solar cell applications. *Appl. Phys. Lett.* **92,** 12358, (2008).

38 Farkas, E., Anderson, M.E., Chen, Z. & Rinzler, A.G. Length sorting cut single walled carbon nanotubes by high performance liquid chromatography. *Chem. Phys. Lett.* **363,** 111-116, (2002).

39 Sanchez-Valencia, J.R., Dienel, T., Groning, O., Shorubalko, I., Mueller, A. Jansen, M., Amsharov, K., Ruffleux, P & Fasel, R. Controlled synthesis of single chirality carbon nanotubes. *Nature,* **512,** 61-64, (2014).

40 Casey, J.P., Bachilo, S.M., Moran, C.H. & Weisman, R.B. Chirality-resolved length analysis of single walled carbon nanotube samples through shear aligned photoluminescence anisotropy. *ACS Nano,* **2,** 1738-1746, (2008).

41 Minati, L., Speranza, G., Bernagozzi, I., Torrengo, S., Toniutti, L., Rossi, B., Ferrari, M. & Chiasera, A. Investigation on the Electronic and Optical Properties of Short Oxidised Multiwalled Carbon Nanotubes. *J.Phys. Chem. C.* **114,** 11068-1107, (2010).

42 Tran, M.Q., Tridech, C., Alfrey, A. Bismarck, A. & Shaffer, M.S.P. Thermal oxidative cutting of multiwalled carbon nanotubes. *Carbon*. **45**, 2341-2350, (2007).

43 Wang, C., Guo, S., Pan, X., Chen, W. & Bao, X. Tailored cutting of carbon nanotubes and controlled dispersion of metal nanoparticles inside their channels. *J. Mater. Chem.* **18**, 5782-5786, (2008).

44 Yudasak, M., Zhang, M., Jabs, C. & Iijima,S. Effect of an organic polymer in purification and cutting of single walled carbon nanotubes. *App. Phys. A.* **71**, 449-451, (2000).

45 Zhang, J., Zou, H., Qing, Q., Yang, Y., Li, Q., Liu, Z., Guo, X. & Du, Z. Effect of chemical oxidation on the structure of single walled carbon nanotubes. *J. Phys. Chem. B.* **107**,

3712-3718, (2003).

46 Liu, J., Rinzler, A.G., Dai, H., Hafner, J.H., Bradley, R.K., Boul, P.J., Lu, A., Iverson, T., Shelimov, K., Huffman, C.B., Rodriguez-Macias, F., Shon, Y.S., Lee, T.R., Colbert, D.T. & Smalley, R.E. Fullerene pipes. *Science.* **280**, 1253-1256, (1998).

47 Gu, Z., Hauge, R.H., Smalley, R.E. & Margrave, J.L. Cutting single walled carbon nanotubes through fluorination. *Nano Letters.* **2**, 1009-1013, (2002).

48 Pierard, N., Fonseca, A., Colomer, J.F., Bossuot, C., Benoit, J.M., Tendeloo, G.V., Pirard, J.P. & Nagy, J.B. Ball milling effect on the structure of single walled carbon nanotubes. *Carbon*. **42**, 1691-1697, (2004).

49 Chen, Z., Kobashi, K., Rauwald, U., Booker, R., Fan, H., Hwang, W.F. & Tour, J.M. Soluble ultra-short single walled carbon nanotubes. *J. Am. Chem. Soc.* **128**, 10568-10571, (2006).

50 Yi, X.J., Nadeem, A.M., Dong, B.H., Ying, L.H. & Tai, Y.W. Concentration and temperature controlled oxidation and cutting of single walled carbon nanotubes by ammonium persulfate. *Sci Chi.* **53,** 2026-2032, (2010).

51 Zhao, J., Liu, P., Yang, Z., Zhou, P. & Zhang, Y. One-step cutting of multiwalled carbon nanotubes using nanoscissors. *Nano-Micro Lett.* **2,** 86-90, (2011).

52 Manivannan, S., Jeong, I.O, Ryu, J.H., Lee, C.S., Kim, K.S., Jang, J. & Park, K.C. Dispersion of single walled carbon nanotubes in aqueous and organic solvents through polymer wrapping functionalisation. *J. Mater. Sci.* **20**, 223-229, (2009).

53 Tkalya, E.E., Ghislandi, M., With, G.D. & Koning, C.E. The use of surfactants for dispersing carbon nanotubes and graphene to make conductive nanocomposites. *Curr. Opin. Coll. Inter.* **17**, 225-232, (2012).

54 Mickelson, E.T., Chiang, I.W., Zimmerman, J.L., Boul, P.J., Lozano, J., Liu, J., Smalley, R.E., Hauge, R.H. & Margrave, J.L. Solvation of flourinated single walled carbon nanotubes in alcohol solvents. *J. Phys. Chem. B.* **103**. 4318-4322, (1999).

55 Boul, P.J., Liu, J., Mickelson, E.T., Huffman, C.B., Ericson, L.M., Chiang, I.W., Smith, K.A., Colbert, D.T., Hauge, R.H., Margrace, J.L. & Smalley, R.E. Reversible sidewall functionalisation of bucky tubes. *Chem. Phys. Lett.* **310**, 367-372, (1999).

56 Britton, J., Chalker, J.M. & Raston, C.L. Rapid vortex fluidics: Continuous flow synthesis of amides and local anaesthetic lidocaine. *Chem. Eur. J.* **21,** 10660-10665, (2015).

57 Britton, J., Dalziel, S.B., & Raston, C.L. Continuous flow Fischer esterifications harnessing vibrational-coupled thin films fluidics. *RSC Adv.* **5**, 1655-1660, (2015).

58 Chen, X., Dobson, J.F. & Raston, C.L. Vortex fluidic exfoliation of graphite and boron nitride. *Chem. Commun.* **48**, 3703-3705, (2012).

59 Yuan, T.Z., Ormonde, C.F.G., Kudlacek, S.T., Kunche, S., Smith, J.N., Brown, W.A., Pugliese, K.M., Olsen, T.J., Iftikhar, M., Raston, C.L., & Weiss, G.A. Shear-stress-mediated refolding of proteins from aggregates and inclusion bodies. *ChemBioChem*. **16**, 393-396, (2015).

60 Vimalanathan, K., Chen, X, & Raston, C.L. Shear induced fabrication of intertwined single walled carbon nanotube rings. *Chem Commun.* **50**, 11295-11298, (2014).

61 Tong, C.L., Boulos, R.A., Yu, C., Iyer, K.S. & Raston, C.L. Continuous flow tuning of ordered mesoporous silica under ambient conditions. *RSC Adv.* **3**, 18767-18770, (2013).

62 Mo, J., Eggers, P.K., Chen, X., Ahamed, M.R.H., Becker, T., Lim, L.Y. & Raston, C.L. Shear induced carboplatin binding within the cavity of a phospholipid mimic for increased anticancer efficacy. *Sci. Rep.* **5**, 10414, (2015).

63 Iyer, K.S. & Raston, C.L. Fabrication of laterally 'sliced' metal plated carbon nanotubes under aqueous continuous flow conditions. *J. Mater. Chem.* **17**, 4872-4875, (2007).

64 Marks, N.A. Generalizing the environment-dependent interaction potential for carbon. *Phys. Rev. B*. **63**, (2000).

65 Wu, Z. *et al.* Transparent, Conductive Carbon Nanotube Films. *Science* **305**, 1273-1276, (2004).

66 Green, A. A. & Hersam, M. C. Colored Semitransparent Conductive Coatings Consisting of Monodisperse Metallic Single-Walled Carbon Nanotubes. *Nano Letters* **8**, 1417-1422, (2008).

67 Javey, A., Guo, J., Wang, Q., Lundstrom, M. & Dai, H. Ballistic carbon nanotube field-effect transistors. *Nature* **424**, 654-657, (2003).

68 Barone, P. W., Baik, S., Heller, D. A. & Strano, M. S. Near-infrared optical sensors based on single-walled carbon nanotubes. *Nat Mater* **4**, 86-92, (2005).

69 Weisman, R. B. Fluorimetric characterization of single-walled carbon nanotubes. *Analytical and Bioanalytical Chemistry* **396**, 1015-1023, (2010).

70 Avouris, P. & Martel, R. Progress in Carbon Nanotube Electronics and Photonics. *MRS Bulletin* **35**, 306-313, (2010).

71 Yang, L. *et al.* Efficient photovoltage multiplication in carbon nanotubes. *Nat Photon* **5**, 672-676, (2011).

72 Jain, R. M. *et al.* Polymer-Free Near-Infrared Photovoltaics with Single Chirality (6,5) Semiconducting Carbon Nanotube Active Layers. *Advanced Materials* **24**, 4436-4439, (2012).

73 Robinson, J. T. *et al.* High Performance In Vivo Near-IR (>1 μm) Imaging and Photothermal Cancer Therapy with Carbon Nanotubes. *Nano research* **3**, 779-793, (2010).

74 Green, A. A. & Hersam, M. C. Nearly Single-Chirality Single-Walled Carbon Nanotubes Produced via Orthogonal Iterative Density Gradient Ultracentrifugation. *Advanced Materials* **23**, 2185-2190, (2011).

75 Yomogida, Y. *et al.* Industrial-scale separation of high-purity single-chirality single-wall carbon nanotubes for biological imaging. *Nat Commun* **7**, (2016).

76 Liu, H., Nishide, D., Tanaka, T. & Kataura, H. Large-scale single-chirality separation of single-wall carbon nanotubes by simple gel chromatography. *Nat Commun* **2**, (2011).

77 Zhang, J., Gui, H., Liu, B., Liu, J. & Zhou, C. Comparative study of gel-based separated arcdischarge, HiPCO, and CoMoCAT carbon nanotubes for macroelectronic applications. *Nano Research* **6**, 906-920, (2013).

78 Takeshi, T., Hehua, J., Yasumitsu, M. & Hiromichi, K. High-Yield Separation of Metallic and Semiconducting Single-Wall Carbon Nanotubes by Agarose Gel Electrophoresis. *Applied Physics Express* **1**, 114001, (2008).

79 Tanaka, T., Urabe, Y., Hirakawa, T. & Kataura, H. Simultaneous chirality and enantiomer separation of metallic single-wall carbon nanotubes by gel column chromatography. *Analytical chemistry* **87**, 9467-9472, (2015).

80 Liu, H., Tanaka, T., Urabe, Y. & Kataura, H. High-efficiency single-chirality separation of carbon nanotubes using temperature-controlled gel chromatography. *Nano letters* **13**, 1996-2003, (2013).

81 Zheng, M. *et al.* DNA-assisted dispersion and separation of carbon nanotubes. *Nat Mater* **2**, 338-342, (2003).

82 Zheng, M. *et al.* Structure-Based Carbon Nanotube Sorting by Sequence-Dependent DNA Assembly. *Science* **302**, 1545-1548, (2003).

83 Zheng, M. & Semke, E. D. Enrichment of Single Chirality Carbon Nanotubes. *Journal of the American Chemical Society* **129**, 6084-6085, (2007).

84 Tu, X., Manohar, S., Jagota, A. & Zheng, M. DNA sequence motifs for structure-specific recognition and separation of carbon nanotubes. *Nature* **460**, 250-253, (2009).

85 Kato, Y., Inoue, A., Niidome, Y. & Nakashima, N. Thermodynamics on Soluble Carbon Nanotubes: How Do DNA Molecules Replace Surfactants on Carbon Nanotubes? *Scientific Reports* **2**, 733, (2012).

86 Ghosh, S., Bachilo, S. M. & Weisman, R. B. Advanced sorting of single-walled carbon nanotubes by nonlinear density-gradient ultracentrifugation. *Nat Nano* **5**, 443-450, (2010).

87 Arnold, M. S., Green, A. A., Hulvat, J. F., Stupp, S. I. & Hersam, M. C. Sorting carbon nanotubes by electronic structure using density differentiation. *Nat Nano* **1**, 60-65, (2006).

88 Kazuhiro, Y., Yasumitsu, M. & Hiromichi, K. Optical and Conductive Characteristics of Metallic Single-Wall Carbon Nanotubes with Three Basic Colors; Cyan, Magenta, and Yellow. *Applied Physics Express* **1**, 034003, (2008).

89 Toshimitsu, F. & Nakashima, N. Semiconducting single-walled carbon nanotubes sorting with a removable solubilizer based on dynamic supramolecular coordination chemistry. *Nat Commun* **5**, (2014).

90 Wang, H. *et al.* Scalable and Selective Dispersion of Semiconducting Arc-Discharged Carbon Nanotubes by Dithiafulvalene/Thiophene Copolymers for Thin Film Transistors. *ACS Nano* **7**, 2659-2668, (2013).

91 Chen, J. *et al.* Noncovalent Engineering of Carbon Nanotube Surfaces by Rigid, Functional Conjugated Polymers. *Journal of the American Chemical Society* **124**, 9034-9035, (2002).

92 Khripin, C. Y., Fagan, J. A. & Zheng, M. Spontaneous Partition of Carbon Nanotubes in Polymer-Modified Aqueous Phases. *Journal of the American Chemical Society* **135**, 6822-6825, (2013).

93 Mistry, K. S., Larsen, B. A. & Blackburn, J. L. High-Yield Dispersions of Large-Diameter Semiconducting Single-Walled Carbon Nanotubes with Tunable Narrow Chirality Distributions. *ACS Nano* **7**, 2231-2239, (2013).

94 Reis, W. G. *et al.* Highly Efficient and Scalable Separation of Semiconducting Carbon Nanotubes via Weak Field Centrifugation. *Scientific Reports* **6**, 26259, (2016).

95 Krupke, R., Hennrich, F., Löhneysen, H. v. & Kappes, M. M. Separation of Metallic from Semiconducting Single-Walled Carbon Nanotubes. *Science* **301**, 344-347, (2003).

96 Tu, X., Hight Walker, A. R., Khripin, C. Y. & Zheng, M. Evolution of DNA sequences toward recognition of metallic armchair carbon nanotubes. *Journal of the American*

Chemical Society **133**, 12998-13001, (2011).

97 Fagan, J. A. *et al.* Isolation of Specific Small-Diameter Single-Wall Carbon Nanotube Species via Aqueous Two-Phase Extraction. *Advanced Materials* **26**, 2800-2804, (2014).

98 Takagi, Y. & Okada, S. Theoretical calculation for the ultraviolet optical properties of single-walled carbon nanotubes. *Physical Review B* **79**, 233406 (2009).

99 Zhang, R. *et al.* Interwall Friction and Sliding Behavior of Centimeters Long Double-Walled Carbon Nanotubes. *Nano Letters* **16**, 1367-1374, (2016).

100 Hong, B. H. *et al.* Extracting subnanometer single shells from ultralong multiwalled carbon nanotubes. *Proceedings of the National Academy of Sciences of the United States of America* **102**, 14155-14158, (2005).

101 Cumings, J. & Zettl, A. Low-Friction Nanoscale Linear Bearing Realized from Multiwall Carbon Nanotubes. *Science* **289**, 602, (2000).

102 Li, Y. *et al.* Molecular mechanics simulation of the sliding behavior between nested walls in a multi-walled carbon nanotube. *Carbon* **48**, 2934-2940, (2010).

103 Xia, Z. & Curtin, W. A. Pullout forces and friction in multiwall carbon nanotubes. *Physical Review B* **69**, 233408, (2004).

104 Zheng, Q. & Jiang, Q. Multiwalled Carbon Nanotubes as Gigahertz Oscillators. *Physical Review Letters* **88**, 045503, (2002).

105 Li, Q. & Wang, T. Removal of shells of multi-wall carbon nanotubes by repeatedly scanning bias voltage. *Science in China Series E: Technological Sciences* **47**, 1-5, (2004).

106 Collins, P. G. & Avouris, P. Multishell conduction in multiwalled carbon nanotubes. *Applied Physics A* **74**, 329-332, (2002).

107 Choi, D. H. *et al.* Fabrication and Characterization of Fully Flattened Carbon Nanotubes: A New Graphene Nanoribbon Analogue. *Scientific Reports* **3**, 1617, (2013).

108 Yu, M.-F., Yakobson, B. I. & Ruoff, R. S. Controlled Sliding and Pullout of Nested Shells in Individual Multiwalled Carbon Nanotubes. *The Journal of Physical Chemistry B* **104**, 8764-8767, (2000).

109 Kis, A., Jensen, K., Aloni, S., Mickelson, W. & Zettl, A. Interlayer Forces and Ultralow Sliding Friction in Multiwalled Carbon Nanotubes. *Physical Review Letters* **97**, 025501, (2006).

110 Fennimore, A. M. *et al.* Rotational actuators based on carbon nanotubes. *Nature* **424**, 408-410, (2003).

111 Yu, M.-F. *et al.* Strength and Breaking Mechanism of Multiwalled Carbon Nanotubes

Under Tensile Load. *Science* **287**, 637, (2000).

112 Seiji, A. & Yoshikazu, N. Extraction of Inner Shell from Multiwall Carbon Nanotubes for Scanning Probe Microscope Tip. *Japanese Journal of Applied Physics* **42**, 3933, (2003).

113 Legoas, S. B. *et al.* Molecular-Dynamics Simulations of Carbon Nanotubes as Gigahertz Oscillators. *Physical Review Letters* **90**, 055504, (2003).

114 Zhang, R. *et al.* Superlubricity in centimetres-long double-walled carbon nanotubes under ambient conditions. *Nat Nano* **8**, 912-916, (2013).

115 Hubble, L. J., Clark, T. E., Makha, M. & Raston, C. L. Selective diameter uptake of single-walled carbon nanotubes in water using phosphonated calixarenes and 'extended arm' sulfonated calixarenes. *Journal of Materials Chemistry* **18**, 5961-5966, (2008).

116 Gillian McMohan, S. O. M., Kieran Nolan & Dermot Diamond. Important calixarene derivatives-their synthesis and application. *Arkivoc*, 23-31, (2003).

117 Beer, P. D., Gale, P. A. & Smith, D. K. *Supramolecular chemistry*. *Oxford University Press,* (1999).

118 Vicens, J. & Bohmer, V. Calixarenes: a versatile class of macrocycle compounds. *Springer Science and Business Media* **3,** (2012).

119 Atwood, J.L., Koutsantonis, G.A. & Raston, C.L. Purification of C_{60} and C_{70} by selective complexation with calixarenes. *Nature* **368,** 229-231, (1994).

120 Lynam, C. *et al.* Tuning and Enhancing Enantioselective Quenching of Calixarene Hosts by Chiral Guest Amines. *Analytical Chemistry* **74**, 59-66, (2002).

121 Egorov, V. V. & Sin'kevich, Y. V. pH-ISEs with an expanded measuring range based on calix[4]arenes: specific features of the behaviour and description of the electrode response. *Talanta* **48**, 23-38, (1999).

122 Makha, M. & Raston, C. Direct synthesis of calixarenes with extended arms: p-phenylcalix[4,5,6,8]arenes and their water-soluble sulfonated derivatives. *Tetrahedron Letters* **42**, 6215-6217, (2001).

123 Makha, M. & Raston, C. Synthesis of p-benzylcalix[4]arene and its sulfonated water soluble derivative. *Chemical Communications* **2001**, 2470-2471, (2001).

124 Shinkai, S., Mori, S., Koreishi, H., Tsubaki, T. & Manabe, O. Hexasulfonated calix[6]arene derivatives: a new class of catalysts, surfactants, and host molecules. *Journal of the American Chemical Society* **108**, 2409-2416, (1986).

125 Shinkai, S., Mori, S., Tsubaki, T., Sone, T. & Manabe, O. New water-soluble host molecules derived from calix [6] arene. *Tetrahedron letters* **25**, 5315-5318, (1984).

126 Martin, A.D. & Raston, C.L. Multifunctional *p*-phosphonated calixarenes. *Chemical Communication,* **47,** 9764-9772, (2011).Hubble, L. J., Clark, T. E., Makha, M. & Raston, C. L. Selective diameter uptake of single-walled carbon nanotubes in water using phosphonated calixarenes and 'extended arm' sulfonated calixarenes. *Journal of Materials Chemistry* **18**, 5961-5966, (2008).

127 Chen, X., Boulos, R. A., Eggers, P. K. & Raston, C. L. p-Phosphonic acid calix[8]arene assisted exfoliation and stabilization of 2D materials in water. *Chemical Communications* **48**, 11407-11409, (2012).

128 Chen, X. *et al.* Self-assembled calixarene aligned patterning of noble metal nanoparticles on graphene. *Nanoscale* **6**, 4517-4520, (2014).

129 Chen, X. *et al.* Non-covalently modified graphene supported ultrafine nanoparticles of palladium for hydrogen gas sensing. *RSC Advances* **3**, 3213-3217, (2013).

130 Chen, X., Zang, W., Vimalanathan, K., Iyer, K. S. & Raston, C. L. A versatile approach for decorating 2D nanomaterials with Pd or Pt nanoparticles. *Chemical Communications* **49**, 1160-1162, (2013).

131 Md Yasin, F., Iyer, K. S. & Raston, C. L. Palladium nano-carbon-calixarene based devices for hydrogen sensing. *New Journal of Chemistry* **37**, 3289-3293, (2013).

132 Clark, T. E. *et al.* Self-organised nano-arrays of p-phosphonic acid functionalised higher order calixarenes. *New Journal of Chemistry* **32**, 1478-1483, (2008).

133 Rao, A. M. *et al.* Diameter-Selective Raman Scattering from Vibrational Modes in Carbon Nanotubes. *Science* **275**, 187 (1997).

134 Bachilo, S. M. *et al.* Structure-Assigned Optical Spectra of Single-Walled Carbon Nanotubes. *Science* **298**, 2361, (2002).

135 Mousavi, S.Z., Amjad-Iranagh, S., Nademi, Y. & Modarress, H. Carbon nanotube-encapsulated drug penetration through the cell membrane: an investigation based on steered molecular dynamic simulation. *The Journal of Membrane Biology.* **246,** 697-704, (2013).

136 Appenzeller, J. Carbon Nanotubes for High Performance Electronics-Progress and Prospect. *Proceeding of the IEEE* 2008 **483**, 201-211, (2008).

137 Dai H., Hafner, J.H., Rinzler, A.G., Colbert, D.T. and Smalley, R.E.. Nanotubes as nanoprobes in Scanning Probe Microscopy. *Nature* **384**, 147-150, (1996).

137 Hafner, J.H., Cheung, C.L. and Lieber, C.M. Direct Growth of Single Walled Carbon Nanotubes Scanning Probe Microscopy Tips. *J.Am.Chem.Soc* **121**, 147-150, (1999).

139 Girishkumar, G., Hall, T.D., Vinodgopal, K. and Kamat, P.V. Single walled Carbon Nanotube Supports for Portable Direct Methanol Fuel Cells. *J.Phys.Chem* **110**, 107-114, (2006).

140 Breuer, O. and Sundararaj, U. Big returns from small fibres: A review of polymer/ carbon nanotube composites. *J.Phys.Chem* **25**, 630-645, (2004).

141 Snow, E.S., Perking, F.K., Houser, E.J., Badescu, S.C. and Reinecke, T.L. Chemical Detection with a Single Walled Carbon Nannotube Capacitor. *Science* **307**, 1942-1945, (2005).

142 Allen, B.L., Kichambare,V. and Star, A. Carbon Nanotube Field Effect Transistor Based Biosensors. *Adv. Mat* **19**, 1439-1451, (2007).

143 Wood J.R. and Wagner, H.D. Single walled carbon nanotubes as molecular pressure sensors. *App. Phy. Lett* **76**, 2883-2885, (2000).

144 T. Hasan, V. Scardaci, P. Tan, A.G. Rozhin, W.I. Milne and A.C. Ferrari. stabilization and debundling of single walled carbon nanotubes dispersions in N-methyl-2-pyrollidinone (NMP) by polyvinylpyrollidinone (PVP). *J. Phys. Chem C* **111**, 12594-12602, (2007).

145 Song, L., Ci, L., Sun, L., Jin, C., Liu, L., Ma, W., Liu, D., Zhao, X., Luo, S., Zhang, Z., Xiang, Y., Zhou, J., Zhou, W., Ding, Y., Wang, Z. and Xie, S.. Large scale synthesis of rings of bundled single walled carbon nanotubes by floating chemical vapor deposition. *Adv. Mater* **18**, 1817-1821, (2006).

146 Wang, W., Laird, E.D., Gogotsi, Y. and Li, C.Y.. Bending single walled carbon nanotubes into nanorings using a Pickering emulsion based process. *Carbon* **50**, 1769-1775, (2012).

147 Martel, R., Shea, H.R. and Avouris, P. Ring formation in single walled carbon nanotubes. *J. Phys.Chem* **103**, 7551-7556, (1999).

148 Chen, L., Yu, S., Wang, H., Xu, J., Liu, C., Chong, W. H. and Chen, H.. General methodology of using oil in water and water in oil emulsions for coiling nanofilaments. *J.Am.Chem.Soc* **135**, 835-843, (2012).

149 Yasmin, L., Chen, X., Stubbs, K.A. and Raston, C.L. Optimizing a vortex fluidic device for controlling chemical reactivity and selectivity. *Sci. Rep.* **3**, 2282, (2013).

150 Yasin, F.M., Boulos, R.A., Hong, B.Y., Cornejo, A., Iyer, K.S., Gao, L., Chua, H. T. and Raston, C.L.. Microfluidic size selective growth of palladium nanoparticles on carbon nano-onions. *Chem. Comm* **48**, 10102-10104, (2012).

151 Wahid, M.H., Eroglu, E., Chen, X., Smith, S.M. and Raston, C.L. Functional multilayer

graphene-algae hybrid material formed using vortex fluidics. *Green Chemistry* **15**, 650-655, (2012).

152 Dresselhaus, M.S., Dresselhaus, G., Saito, R. and Jorio, A. Raman spectroscopy of carbon nanotubes. *Phys Rep* **409**, 4799, (2005).

7 CONCLUSIONS AND FUTURE DIRECTIONS

The research undertaken using thin film microfluidics within the vortex fluidic device (VFD) has established a paradigm shift in materials science processing as applied to carbon nanomaterials. This has opened new possibilities of fabricating carbon nanomaterial of various dimensions and architectures. The past few years of research, delving into the development of methods to control the growth and self assembly of 0D, 1D and 2D carbon nanomaterials, has resulted in significant advances in the field with the ability to exquisitely tailor the chemical and physical properties for targeted applications.

Controlling the fabrication of carbon nanomaterials using conventional processing methods has greatly influenced the field of nanotechnology, in bridging the gap between biochemistry and organic chemistry. The aim of the research herein was to develop new methods for fabricating carbon nanomaterial in a more benign way with a view that this will facilitate transferring the technology to the market place. Although most of the conventional methods are significant innovations in science and in their respective fields, the main issues and limitations that are yet to be addressed are the generation of high levels of waste, high energy usage, often the need for down stream processing, and limited scope for scaling up the processes. The use of chemical stabilisers and surface active molecules in many of the methods is pivotal for controlling the growth and stabilising the structures within nanoscale dimensions. However, when addressing potential for scalability of a process, these requirements raise concerns due to the high costs and the difficulties of down stream processing. In the present study, these issues have been addressed at the inception of the science.

To summarize the findings in this thesis, the use of process intensification as an alternative route to conventional processing methods has resulted in significant advancement, establishing more environmentally benign methods of processing, with scalability incorporated into the processes. The research provides an in-depth study on the use of shear stress generated within dynamic thin films in the VFD to manipulate and process carbon nanomaterials with control over the shapes, size and dimensions of the material. The main advantage of the VFD relates to controllable mechanoenergy within dynamic thin films (≥ 200

μm thick) to control the fabrication of nanomaterials under continuous flow.

A number of significant advancements have been made in the field of materials chemistry herein, firstly in controlling the self assembly of fullerene molecules, as detailed in Chapter 4. Since the 90's there has been extensive studies on controlling the self assembly of fullerene C_{60}, with remarkable precision in manipulating the architectures with distinct morphologies and sizes.[1-9] Thin film processing in the VFD establishes a new way of controlling the self assembly of C_{60} molecules, forming nanotubules using an immiscible solvent system of toluene and water. These nanotubules are stable and devoid of surfactants, and have uniform nanopores on their surfaces. The formation of these distinct architectures devoid of surfactants is without precedent, and their accessibility is directly related to the high shear forces in the thin films in the VFD, which in turn is related to the optimal operating parameters of the device, including rotational speed, using a saturated solution of C_{60} in toluene and water as an immiscible solvent.

The intense micromixing and the formation of what appears to be a uniform phase of otherwise immiscible solvents, presumable as an antisolvent effect, in dramatically lowering the solubility of the fullerene, resulting in controlled nucleation and growth of the nanotubules. Moreover, the shear stress created *fcc* C_{60} directly which is devoid of included solvent, rather than the hexagonal phase containing interstitial toluene molecules, thereby circumventing the need for down stream processing post-VFD processing. The dynamic nature of the liquid also results in solvent evaporation under shear because of the waves and ripples in the thin film, but for the toluene/water mixture, such evaporation would be minimal. Overall, the ability to fabricate functional nanocarbon material in this way is significant in the field in eliminating the need for annealing the nanostructures at high temperature for generating the *fcc* phase, and to remove any surfactants used to control the radial growth under diffusion controlled batch processing.

Reports on the self assembly of C_{70} are limited, which relates to its ellipsoidal molecular shape and the coexistence of energetically similar phases at room temperature, thus making its nucleation and growth inherently difficult to control.[10-13] Using similar conditions to what was achieved for the above self assembly of $C_{60,}$ feasibility studies show promising results of being able to employ similar conditions, affording hollow tubes of self assembled C_{70} molecules

generated under continuous flow conditions. However this was possible using a mixture of toluene and isopropanol as the miscible solvent system (Figure 49), rather than the immiscible water and toluene system used for C_{60}, which gave non-uniform material. Unlike conventional methods,[10-13] the VFD established controllable self assembly of C_{70} molecules into nanotubules of microns in length with an orthorhombic lattice.[10] The phase transition from the hexagonal of pristine C_{70} (Figure 49e) is possibly related to mechanism of the nucleation and growth of these molecules, controlled by the shear stress and the nature of the miscible solvent system. Is the phase transformation observed with C_{70} an indication of trapped solvents within the nanostructure and could this be related to the ellipsoidal molecular shape of C_{70}? This will be be explored further to understand the mechanism of the self assembly and how it differs to that of the C_{60} molecules, as will be controlling the growth of mixed fullerene material, ie. studying ratios of C_{60} and C_{70}, and the affect this has on the structure and the properties.

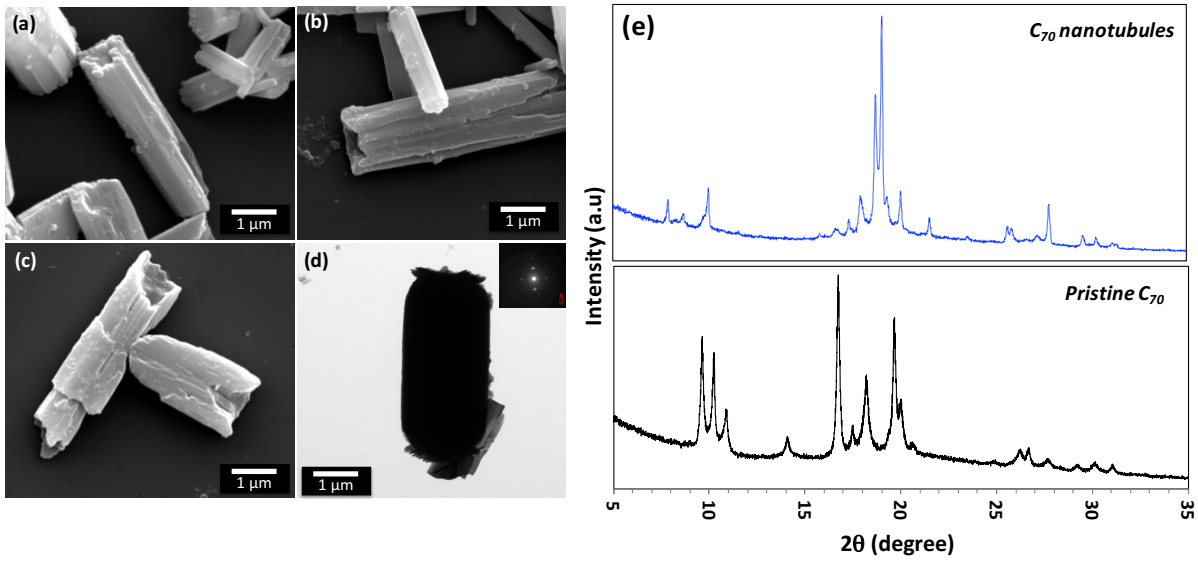

Figure 49 (a-c) SEM images of C_{70} micron length tubules formed in the presence of a binary solvent system of toluene and isopropanol at a 1:1 ratio. (d) TEM image of the C_{70} tubules (inset: SAED pattern), and (e) XRD pattern of both the pristine C_{70} (hexagonal phase) and C_{70} nanotubules (orthorhombic phase) respectively.

Thus, it is evident that controllable mechanoenergy generated in the VFD shows great potential for the fabrication and self assembly of novel architectures based on fullerene C_{60} and higher fullerene molecules. This method now allows for translating this novel process towards affording novel hybrid nanomaterials, which includes composites of fullerenes and sliced CNTs[14] and composites of fullerenes C_{60} and higher fullerenes, especially C_{70}. The VFD

provides an opportunity to control the size, shape, morphology of hybrid materials, for example, *in situ* slicing of CNTs in the presence of fullerenes. This will provide a robust method to physically merge both nanomaterials, whereby the presence of C_{60} molecules for instance may facilitate the slicing process, simultaneously forming covalent bonds either to the outer surface of the CNTs or to the dangling bonds at the ends of the tubes, arising from the the high vibrational energy induced by a NIR laser. Novel hybrid material formed will possess properties beyond those for structures based on fullerenes and CNTs alone.

Another significant advance was the ability to exfoliate graphene and indeed exfoliate with simultaneously formation of graphene nanoscrolls in relatively high yield, as detailed in Chapter 5. Although there are a number of published methods for exfoliating graphene,[15-17] they involve the use of intercalation molecules, surfactants and toxic organic solvent, which limits the utility of the material even when scalability of the process is addressed. Similar to graphene sheets, exhibiting exceptional thermal, mechanical and electrical properties for a diverse range of applications, graphene nanoscrolls have also emerged as material having properties beyond that of carbon nanotubes, with potential for use in supercapacitors and for hydrogen storage.[18-20] The research focused on exploiting the properties of graphene nanoscrolls by means of fabricating directly from graphite flakes with the shear stress lifting and facilitating the rolling process. Conventional processing generates graphene scrolls in low yield, and uses contaminating surfactant. VFD scroll formation featured the use of an immiscible toluene and water solvent mixture within dynamic thin films, as for the above controlling of the fullerene self assembly. Although a detailed mechanism of this process is yet to be realised with the spacing between the layers at 3.34 nm, dramatically larger than at the van der Waals limit, at 0.34 nm. Nevertheless, a remarkable finding is the formation of rod shape structures at the interface of the otherwise immiscible solvent when subjected to mild cavitation, without the use of the VFD. If such rod shape structures also prevail in the VFD, they could act as templates in the scrolling process and account for the large separation between layers in each scroll. This needs to be investigated in details using real time small angle neutron scattering (SANS) experiments, which is being explored within the Raston research group as a major research program, noting real time SANS under shear has not been reported. A number of other issues also need to be addressed, including characterising the rods using other techniques, including AFM, SEM and TEM, but this is also is a major research program in its own right. In addition, upon formation of the nanoscrolls, is there rapid

evaporation of the solvent(s) affording pristine nanoscrolls, and can they be compressed with then van der Waals contacts between layers? In conclusion here, the apparent stabilized micelle templates in the presence of shear stress in the liquid represents a new route towards the fabrication of graphene nanoscrolls in relatively high yield (~30%) compared to conventional low yielding methods currently available, for then testing the above applications. The challenges that will be further systematically addressed for the exfoliation and scrolling of graphene sheets includes (i) high volume fabrication –scaling up, (ii) further direct exfoliation devoid of surfactants and toxic and harsh chemicals, (iii) exquisite control over the morphology of the graphene sheets affording tightly formed scrolls, (iv) the possibility of lateral slicing of the graphene scrolls using a NIR (1064 nm) laser.

Chapter 6 provides a detailed study on the use of shear within dynamic thin films to process, manipulate and control the chemical and physical properties of CNTs. However, the method of growth and their physical complexity in bulk mixture can limit their applications. VFD mediated processing of CNTs has advantageous in being able to accentuate certain properties without compromising the quality of the material. The primary gap in materials science of CNTs is applications specifically in the biological arena and device technology,[21-24] which is in consequence of the inability to avoid bundling and control their lengths. With dispersibility in solvents being critical for most processing, the ability to overcome the high flexural rigidity of CNTs has been overcome. The controlled bending under intense shear was not only essential to afford stabilized CNT toroids of varying diameters and morphologies, for the use in electronic device and sensors, but was the primary step towards developing a method for lateral slicing. The mechanism is well understood through high level theoretical calculations where shear stress in the VFD provides sufficient energy to overcome the high flexural rigidity of SWCNTs (Figure 50b) . The ability to slice SWCNTs to a length *ca* 300 nm allows for the shear to bend the SWCNTs to an extent that that the ends come in contact and fuse affording rings with a diameter of *ca* 120 nm. The persistent current flow and exceptional magnetic responses of such novel nanostructures would be pioneering work with theoretical calculations well understood[25] (Figure 50c). These SWCNTs rings have interesting magnetic properties as determined through preliminary magnetic force microscopy measurements (MFM) (Figure 50d) exhibiting surface potentials that dependent on the size and morphology of the rings (Figure 50d). Surface potential measurements were obtained using the Kelvin force microscopy technique (KFM) (Figure 50d).

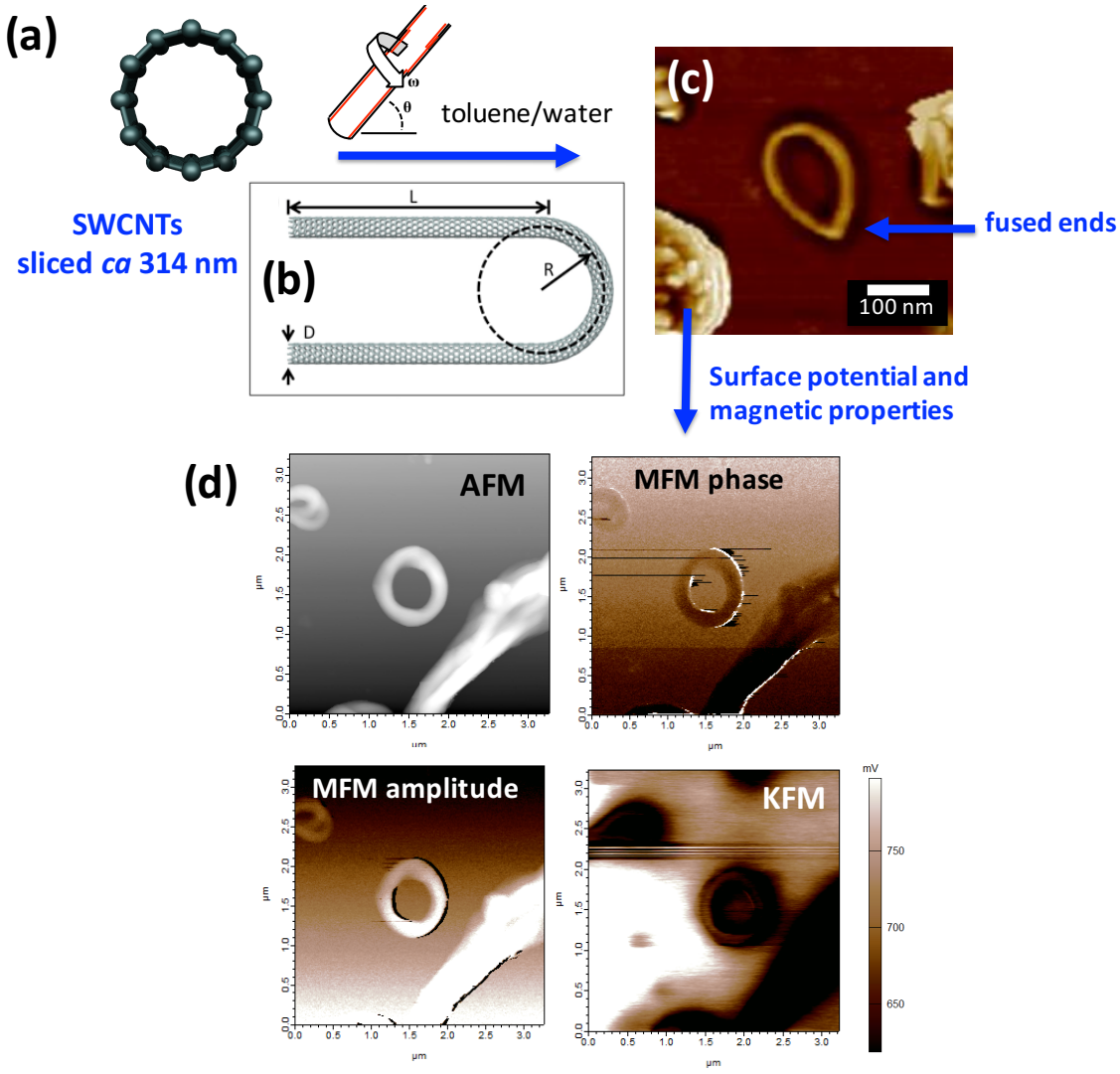

Figure 50 Schematic of feasibility studies for studying the use of shear stress in the VFD to fuse two ends of SWCNTs, with surface potential and magnetic properties determined *via* Kelvin force microscopy (KFM) and magnetic force microscopy (MFM).

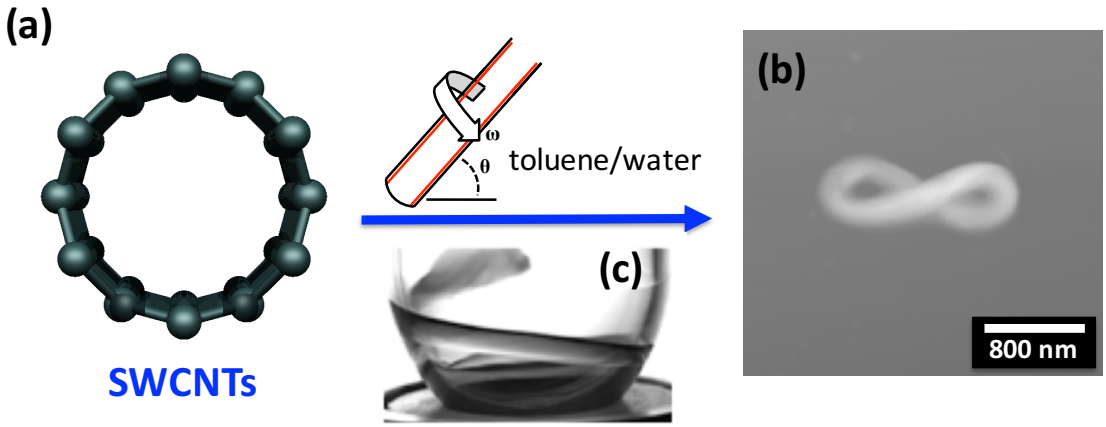

Figure 51 Schematic of feasibility studies for the studying the use of shear stress in the VFD to induce chirality into the nano-carbon structures

With extended exposure to shear stress in the VFD, chiral 'figure of 8' nanostructures are observed (Figure 51). It is remarkable that the nanostructures, as illustrated in Figure 51b appear to exhibit the same absolute chirality, and it is hypothesized that this arises from chiral nature of the fluid flow in the VFD, which is being explored within the Raston research group. With the recent use of mechanical vortexes to tune the chirality of nano-carbon material,[26] the above observations, although at this stage still preliminary, would be a further step towards inducing chirality into the nano-carbon structures, with control over the absolute stereochemistry.

A pulsed Nd:YAG laser operating in the NIR was used as an alternative to high temperature processing in establishing a novel route to break and rupture the C-C bonds at points of high curvature associated with the bending under shear. The advantage of continuous flow VFD mediated processing is the scalability of the process with minimal or no significant defects formed on the surface of the nanotubes. This has been beyond the bounds of possibility using conventional methods. Now that an efficient means of lateral slicing single, double and multi walled carbon nanotubes has been established, succeeding work will involve precisely controlling the length to suit specific applications. For example, with the understanding of the slicing mechanism, the thin films allow for the possibility of controlling the shear thereby imparting different radii of curvature of the CNTs, which then under optimised laser powers would be an efficient route towards affording CNTs of controllable lengths and specificity to suit biomedical, bioengineering and for device technology respectively.

CNTs are defined by their varied diameters and chirality, which dictate their unique electrical and optical properties. Single chirality SWCNTs show great promise in applications in device technology, biomedical and other biological applications. Given that different chiralities have different chemical, physical and electrical properties, the use of single chirality CNTs would offer as a more efficient route for different applications. After establishing the VFD mediated slicing of CNTs with control in the length distribution, the focus was then to convert (interconvert) the chiralities to approach single chirality SWCNTs. The separation of the different chiralities of CNTs have been extensively studied, as monochiral SWCNTs with enhance and improve efficiency.[27-34] The aim of this part of the research was to optimize conditions accordingly to (a) convert the bulk mixture of SWCNTs to purely semiconducting chiralities, and (b) convert the bulk mixture of SWCNTs to purely metallic chiralities. At this stage, a non-destructive method of enriching the sample of sliced SWCNTs with metallic chiralities has been established. However, although the majority of the SWCNTs are metallic, some semiconducting chiralities, predominantly the (9,4) chiraity and traces of others namely the (7,5) and (7,6), albeit in diminished amounts. These results were obtained after only a single pass in the VFD under continuous flow, and is a significant advancement in its own right. However, much needs to be done, including recycling the liquids through the VFD to convert all of the metallic SWCNTs to metallic SWCNTs.

Thin films under continuous flow in the presence of a pulsed laser at a 1064 nm wavelength convert (interconvert) the semiconducting and metallic chiralities of SWCNT without destroying the metallic chiralities, unlike for other methods,[27-34] and the method is devoid of any surfactants, and most importantly the complexity of the mixture and thus the separation requirements are diminished. What is the mechanism towards this conversion (interconversion)? The ballistic wave from the pulsed laser operating at 1064 nm and 260 mJ laser power overcomes the large barrier of energy, changing the magnitude and rolling vector of the semiconducting nanotubes, affording the metallic configuration. Even at this stage of the research, the use of the key semiconducting chiralities, namely the (9,4) is seemingly limitless, especially in biological imaging and for transparent flexible transistors.[27] What is next with this technology? Apart from the abovementioned aims, separating the (9,4) chirality itself would be worthwhile for a number of applications.

Besides length and diameter specificity, the research proceeded to establish a method to afford CNTs of varying diameters and to gain access to larger diameter CNTs. Upon slicing DWCNTs, there is evidence of *in situ* slicing and dethreading (removal of inner shells from the outer shells), but this work simply establishes the feasibility of dethreading. Further research here is a major focus in the Raston research group. The designer surfactants, *p*-phosphonated calix[n]arenes, facilitate the exfoliation and stabilization of graphene sheets in an aqueous solution, and the most conformational flexible of these macrocycles was used for the dethreading experiments, i.e *p*-phosphonated calix[8]arene. This *in situ* slicing of DWCNTs is in water, which in its own right is a remarkable innovation. Future work includes the use of other calixarenes of varied sizes and different functional moieties on the lower and upper rim to further understand the mechanism of dethreading.

Thus, it is evident that VFD mediated processing overcomes the many limitations of conventional processing, specifically the low dispersibility and high degree entanglement of the micron length CNTs. The method developed to shorten CNTs then leads to the development of sorting of the SWCNTs based on the specific chirality and diameter, avoiding the use of surface contaminating chemicals and tedious chromatographic methods. With the knowledge from previously patented technology within the Raston research group[35], a method was then developed to slice and dethread CNTs consisting of a number of concentric layers *in situ* using *p*-phosphonated calixarenes. The methods will then be further extended using the related *p*-sulfonated calixarenes. The method of dethreading will provide a novel pathway to gain access to larger diameter SWCNTs potentially for use in drug delivery applications and as protein delivery vehicles.[36]

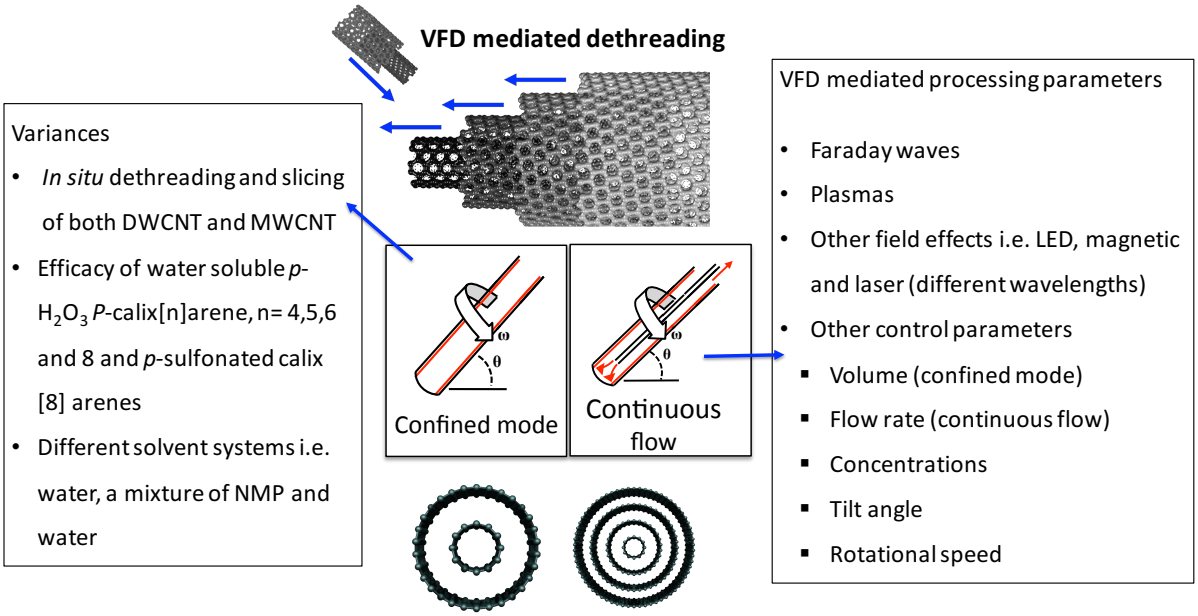

Figure 52 Schematic of the various conditions and parameters to be employed as future directions of this research

What is the future direction for the processing and technology developed in this thesis? The advancement of VFD mediated processing of nanocarbon thus far is still the 'tip of the iceberg'. This project has opened many exciting possibilities not only in the field of carbon nanomaterials but also other related 2D laminar materials, namely *hexagonal*-boron nitride (*h*-BN), molybdenum disulphide (MoS_2) and tungsten disulfide (WS_2), other laminar materials, and carbon nanoonions (CNO). Intensive shear within dynamic thin films in the VFD coupled with laser irradiation with tunable wavelengths or indeed combinations of wavelengths is destined to create limitless opportunities for the fabrication, manipulation and self-assembly of nanomaterials, developing methods and approaches without precedent, and as relative benign processes. This thesis provides preliminary guidelines of operating conditions established thus far for processing carbon nanomaterials, depending on the properties and applications. Overall, the VFD is poised to be revolutionary in nanotechnology and materials chemistry in specific, for a large number of applications, with potential of developing methods that are environmentally and economically sustainable, ensuring enhanced specificity, minimising energy usage and waste generation. Importantly VFD processing has scalability addressed up front, and for small niche applications of nanomaterials, a single VFD would suffice. For large scale processing, then a number of VFDs operating in parallel is envisaged, along the lines of conventional channel based microfluidic processing, but without the problems of clogging for such processing

7.1 References

1 Miyazawa, K., Kuwasaki, Y., Obayashi, A. & Kuwabara, M. C_{60} Nanowhiskers Formed by the Liquid–liquid Interfacial Precipitation Method. *Journal of Materials Research* **17**, 83-88, (2002).

2 Miyazawa, K., Minato, J., Yoshii, T., Fujino, M. & Suga, T. Structural characterization of the fullerene nanotubes prepared by the liquid–liquid interfacial precipitation method. *Journal of Materials Research* **20**, 688-695, (2005).

3 Liu, H. *et al.* Imaging As-Grown [C_{60}]Fullerene Nanotubes by Template Technique. *Journal of the American Chemical Society* **124**, 13370-13371, (2002).

4 Wang, L. *et al.* Highly Enhanced Luminescence from Single-Crystalline C_{60} m-xylene Nanorods. *Chemistry of Materials* **18**, 4190-4194, (2006).

5 Marappan, S. & Miyazawa, K. Size-Tunable Hexagonal Fullerene (C_{60}) Nanosheets at the Liquid−Liquid Interface. *Journal of the American Chemical Society* **129**, 13816-13817, (2007).

6 Akito, M., Zhenquan, T., Hitoshi, K., Hachiro, N. & Hidetoshi, O. Fullerene Fine Crystals with Unique Shapes and Controlled Size. *Japanese Journal of Applied Physics* **48,** (2009).

7 Jeong, J., Kim, W.-S., Park, S.-I., Yoon, T.-S. & Chung, B. H. Synthesis and Characterization of Various-Shaped C60 Microcrystals Using Alcohols As Antisolvents. *The Journal of Physical Chemistry C* **114**, 12976-12981, (2010).

8 Shrestha, L. K., Hill, J. P., Tsuruoka, T., Miyazawa, K. I. & Ariga, K. Surfactant-Assisted Assembly of Fullerene (C_{60}) Nanorods and Nanotubes Formed at a Liquid–Liquid Interface. *Langmuir* **29**, 7195-7202, (2013).

9 Iyer, K. S., Saunders, M., Becker, T., Evans, C. W. & Raston, C. L. Nanorings of Self-Assembled Fullerene C_{70} as Templating Nanoreactors. *Journal of the American Chemical Society* **131**, 16338-16339, (2009).

10 Liu, D., Yao, M., Wang, L., Li, Q., Cui, W., Liu, B., Liu, R., Zou, B., Cui, T., Liu, B., Liu, J., Sundqvist, B. & Wagberg, T. Pressure-induced phase transitions of C_{70} nanotubes. *The Journal of Physical Chemistry* **115,** 8918-8922, (2011).

11 Kim, J., Park, C. & Choi, C. Selective growth of a C_{70} crystal in a mixed solvent system: from cube to tube. *Chemistry of Materials* **27,** 2408-2413, (2015).

12 Zheng, S. & Lu, X. Formation kinetics and photoelectrochemical properties of crystalline C_{70} one-dimensional microstructures. *RSC Advances* **5,** 38202-38208, (2015).

13 Li, H., Guan, M., Zhu, G., Yin, G. & Xu, Z. Experimental observation of fullerene crystalline growth from mesocrystal to single crystal. *Crystal Growth Design* **16,** 1306-1310, (2016).

14 Nasibulin, A.G., Pikhitsa, P.V., Jiang, H., Brown, D.P., Krashenonnokov, A.V., Anisimov, A.S., Queipo, P., Moisala, A., Gonzales, D., Lientschnig, G., Hassanien, A., Shandakov, S.D., Lolli, G., Resasco, D.E., Choi, M., Tomanek, D. & Kauppinen, E.I. A novel hybrid carbon material. *Nature Nanotechnology* **2,** 156-161, (2007).

15 Kovtyukhova, N. I. *et al.* Non-oxidative intercalation and exfoliation of graphite by Brønsted acids. *Nature Chemistry* **6**, 957-963, (2014).

16 Hernandez, Y. *et al.* High-yield production of graphene by liquid-phase exfoliation of graphite. *Nature Nanotechnology* **3**, 563-568, (2008).

17 Matsumoto, M., Saito, Y., Park, C., Fukushima, T. & Aida, T. Ultrahigh-throughput exfoliation of graphite into pristine 'single-layer' graphene using microwaves and molecularly engineered ionic liquids. *Nature Chemistry* **7**, 730-736, (2015).

18 Zeng, F., Kuang, Y., Wang, Y., Huang, Z., Fu,C. & Zhou, H. Facile preparation of high quality graphene scrolls from graphite oxide by a microexplosion method. *Adv. Mater.* **23**, 4929-4932, (2011)

19 Shanfi, T., Gracia-Espino, E., Barzegar, H.R., Jia, X. Nitze, F, Hu, G., Nordblad, P., Tai, C.W. & Wagberg, T. Formation of nitrogen-doped graphene nanoscrolls by adsorption of magnetic Fe_2O_3 nanoparticles. *Nature Communications* **4,** (2013).

20 Hwang, D.Y., Yook, J.Y. & Suh, D.H. Inclusion and exclusion of self assembled molecules inside graphene scrolls. *RSC Advances.* **4,** (2014).

21 Liu, Z., Tabakman, S., Welsher, K. & Dai, H. Carbon nanotubes in biology and medicine: In vitro and in vivo detection, imaging and drug delivery. *Nano Research* **2**, 85-120, (2009).

22 Prato, M., Kostarelos, K. & Bianco, A. Functionalized Carbon Nanotubes in Drug Design and Discovery. *Accounts of Chemical Research* **41**, 60-68, (2008).

23 Sgobba, V. & Guldi, D. M. Carbon nanotubes-electronic/electrochemical properties and application for nanoelectronics and photonics. *Chemical Society Reviews* **38**, 165-184, (2009).

24 Katz, E. & Willner, I. Biomolecule-Functionalized Carbon Nanotubes: Applications in Nanobioelectronics. *ChemPhysChem* **5**, 1084-1104, (2004).

25 Beuerle, F., Herrmann, C., Whalley, A.C., Valente, C., Gamburd, A., Ratner, M.A. & Stoddart, J.F. Optical and vibrational properties of toroidal carbon nanotubes. *Chemistry European Journal* **17,** 3868-3875, (2011).

26 Mauro, A.D., Randazzo, R., Spano, S.F., Compagnini, G., Gaeta, M., Urso, L.D., Paolesse, R., Pomarica, G., Natale, C.D., Villari, V., Micali, N., Fragalo, M.E., Urso, A.D. & Purrello, R. Vortexes tune the chirality of graphene oxide and its non-covalent hosts. 10.1039/C6CC05177D (2016).

27 Yomogida, Y. *et al.* Industrial-scale separation of high-purity single-chirality single-wall carbon nanotubes for biological imaging. *Nature Communications* **7**, (2016).

28 Liu, H., Nishide, D., Tanaka, T. & Kataura, H. Large-scale single-chirality separation of single-wall carbon nanotubes by simple gel chromatography. *Nature Communications* **2**, (2011).

29 Takeshi, T., Hehua, J., Yasumitsu, M. & Hiromichi, K. High-Yield Separation of Metallic and Semiconducting Single-Wall Carbon Nanotubes by Agarose Gel Electrophoresis. *Applied Physics Express* **1**, 114001, (2008).

30 Tanaka, T., Urabe, Y., Hirakawa, T. & Kataura, H. Simultaneous chirality and enantiomer separation of metallic single-wall carbon nanotubes by gel column chromatography. *Analytical chemistry* **87**, 9467-9472, (2015).

31 Liu, H., Tanaka, T., Urabe, Y. & Kataura, H. High-efficiency single-chirality separation of carbon nanotubes using temperature-controlled gel chromatography. *Nano letters* **13**, 1996-2003, (2013).

32 Zheng, M. *et al.* DNA-assisted dispersion and separation of carbon nanotubes. *Nature Materials* **2**, 338-342, (2003).

33 Zheng, M. *et al.* Structure-Based Carbon Nanotube Sorting by Sequence-Dependent DNA Assembly. *Science* **302**, 1545-1548, (2003).

34 Krupke, R., Hennrich, F., Löhneysen, H. v. & Kappes, M. M. Separation of Metallic from Semiconducting Single-Walled Carbon Nanotubes. *Science* **301**, 344-347, (2003).

35 Hubble, L. J., Clark, T. E., Makha, M. & Raston, C. L. Selective diameter uptake of single-walled carbon nanotubes in water using phosphonated calixarenes and 'extended arm' sulfonated calixarenes. *Journal of Materials Chemistry* **18**, 5961-5966, (2008).

36 Mousavi, S.Z., Amjad-Iranagh, S., Nademi, Y. & Modarress, H. Carbon nanotube-encapsulated drug penetration through the cell membrane: an investigation based on

steered molecular dynamic simulation. *The Journal of Membrane Biology.* **246,** 697-704, (2013).

8 APPENDICES

A Journal formatted manuscript for the publication: **Vimalanathan, K.**, Gascooke, J.R., Martinez, I.S, Marks, N., Kumari, H., Garvey, C.J., Atwood, J.L, Lawrance, W.D. and Raston, C.L. Fluid dynamic lateral slicing of high tensile strength carbon nanotubes, *Sci. Rep.* **6***,* (2016)

B Journal formatted manuscript for the publication: **Vimalanathan, K.**, Chen, X. and Raston, C.L. Shear induced fabrication of intertwined single walled carbon nanotube rings. *Chem Commun.* **50**, 11295 (2014) **(Cover illustrated)**.

C Journal formatted manuscript for the publication: Wahid, M.H., Stroeher, U.H., Eroglu, E., Chen, X., **Vimalanathan, K.**, Raston, C.L. and Boulos, R.A. Aqueous based synthesis of antimicrobial decorated graphene. *J. Colloid and Interface Science* **444**, 88-96 (2014)

D Eggers, P., Eroglu, E., Becker, T., Chen, X., **Vimalanathan, K.**, Stubbs, K.A., Smith, S.M. and Raston, C.L. Nitrate uptake by p-phosphonic acid or p-(trimethylammonium) methyl calix[8] arene stabilized laminar materials. *RSC Adv.* **4**, 48348-48352 (2014).

E Supplementary information for: **Vimalanathan, K.**, Shrestha, R.G., Zhang, Z., Zou, J., Nakayama, T. and Raston, C.L. Surfactant-free fabrication of fullerene C_{60} nanotubules under shear. **Under Review** (2016)

F Supplementary information for: **Vimalanathan, K.**, Chen, X. and Raston, C.L. VFD induced templated graphene scroll formation from graphite. This section is the basis of a manuscript to be submitted for publication.

G Supplementary information for: **Vimalanathan, K.**, Gascooke, J.R., Martinez, I.S, Marks, N., Kumari, H., Garvey, C.J., Atwood, J.L, Lawrance, W.D. and Raston, C.L. Fluid dynamic lateral slicing of high tensile strength carbon nanotubes, *Sci. Rep.* **6***,* (2016)

H Supplementary information for: **Vimalanathan, K.**, Chen, X. and Raston, C.L. Shear induced fabrication of intertwined single walled carbon nanotube rings. *Chem Commun.* **50**, 11295 (2014)

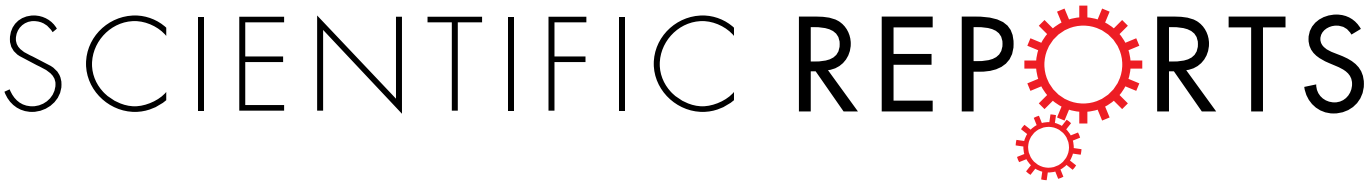

OPEN

Fluid dynamic lateral slicing of high tensile strength carbon nanotubes

Kasturi Vimalanathan[1], Jason R. Gascooke[1], Irene Suarez-Martinez[2], Nigel A. Marks[2], Harshita Kumari[3,4], Christopher J. Garvey[5], Jerry L. Atwood[3], Warren D. Lawrance[1] & Colin L. Raston[1]

Received: 15 October 2015
Accepted: 22 February 2016
Published: 11 March 2016

Lateral slicing of micron length carbon nanotubes (CNTs) is effective on laser irradiation of the materials suspended within dynamic liquid thin films in a microfluidic vortex fluidic device (VFD). The method produces sliced CNTs with minimal defects in the absence of any chemical stabilizers, having broad length distributions centred at *ca* 190, 160 nm and 171 nm for single, double and multi walled CNTs respectively, as established using atomic force microscopy and supported by small angle neutron scattering solution data. Molecular dynamics simulations on a bent single walled carbon nanotube (SWCNT) with a radius of curvature of order 10 nm results in tearing across the tube upon heating, highlighting the role of shear forces which bend the tube forming strained bonds which are ruptured by the laser irradiation. CNT slicing occurs with the VFD operating in both the confined mode for a finite volume of liquid and continuous flow for scalability purposes.

The processing of cylindrical carbon nanotubes (CNTs) for exploiting their exceptional thermal, mechanical, and electrical properties[1] poses a number of challenges. This includes overcoming a high degree of bundling and aggregation arising from their high aspect ratio and strong inter-tube van der Waals interactions. The CNTs are microns to millimetres in length, and may have single or multiple layers, described as single walled (SWCNTs), double walled (DWCNTs) or multi walled (MWCNTs). They have low density, and high stiffness and axial strength[2] with an exceptionally high Young's modulus, 1.0 to 1.28 TPa[3–5]. CNTs are produced using a number of techniques, including arc-discharge, laser ablation and chemical vapour deposition (CVD)[6–8], typically affording arrays of nanotubes in various lengths. However, the availability of shorter lengths without compromising quality is important for many applications, for example, in incorporating them into lipid bilayers for molecular sensing[2], and for enhancing the efficiency of electronic devices[3,4,9], for solar cell applications[10] and for chirality separation[11–13]. There has thus been considerable work directed at shortening CNTs towards sub-micron lengths, but this has proved challenging, currently requiring the use of high-energy sonication, lengthy processing times and the use of toxic chemicals[14–24]. Moreover, such conditions can chemically alter the surface of the CNTs with consequential change in their properties, thereby limiting their applications. Controlling the shortening of CNTs requires the use of a suitable processing medium in overcoming their tendency to aggregate, with some common solvents such as N-methyl-2-pyrollidone (NMP) and N,N-dimethylformamide (DMF) being effective dispersants for such purpose. The colloidal stability of individual CNTs usually requires polymer wrapping agents[25] and surfactants[26], and covalent end and/or sidewall functionalization[27,28].

We have established a new means to achieve shortening of CNTs that avoids many of these problems. Despite their high tensile strength, CNTs can be laterally sliced in solution by applying intense shear within dynamic thin films in a vortex fluidic device (VFD) while irradiating at 1064 nm using a pulsed Q-switch Nd:YAG laser (Fig. 1a). The VFD microfluidic platform generates controllable mechanoenergy within the liquid medium, as thin films around the internal walls of a rapidly rotating tube, which for practical purposes was a 20 mm diameter (ID 16.000 ± 0.013 mm) borosilicate nuclear magnetic resonance (NMR) glass tube. In general, the optimal performance of the VFD occurs at high rotational speeds (2000 rpm to 9000 rpm) and inclination angles, $\theta > 0°$, with

[1]Flinders Centre for NanoScale Science & Technology, School of Chemical & Physical Sciences, Flinders University, Adelaide SA 5001, Australia. [2]Nanochemistry Research Institute, Department of Physics and Astronomy, School of Science, Curtin University, Bentley Campus, Perth, WA 6102, Australia. [3]Department of Chemistry, University of Missouri, 601 South College Avenue, Columbia, Missouri 65211, United States. [4]James L. Winkle College of Pharmacy, University of Cincinnati, 3225 Eden Avenue, Cincinnati, Ohio, 42567, United States. [5]Bragg Institute, Australian Nuclear Science and Technology Organisation, New Illawarra Road, Lucas Heights, 2234, NSW. Correspondence and requests for materials should be addressed to C.L.R. (email: colin.raston@flinders.edu.au)

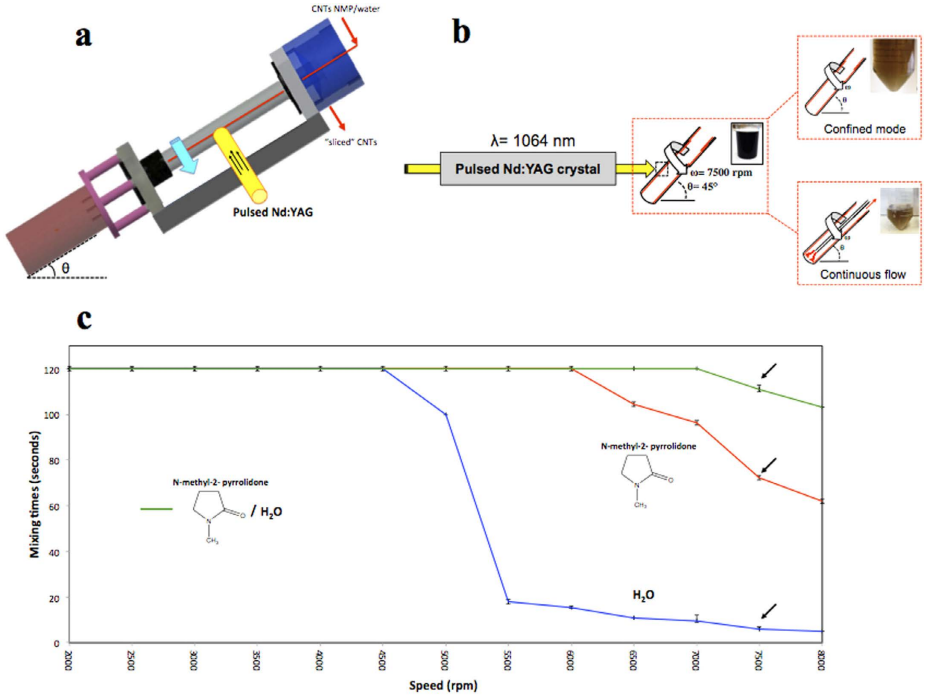

Figure 1. VFD laser processing and mixing times. (**a**) Schematic of the vortex fluidic device (VFD). (**b**) Experimental set up for laser Nd:YAG processing operating at 1064 nm wavelength, for confined and continuous flow modes of operation of the VFD. (**c**) Variation of mixing times of pure NMP, water and NMP/water at a 1:1 ratio. Mixing times were measured by placing 1 mL of the solvent in the VFD operating at an inclination angle of 45° and varying the rotational speed (2000–9000 rpm) and measuring the time taken for a drop of dye to uniformally mix with the bulk liquid (measured in triplicates).

a 45° tilt angle corresponding to the maximum cross vector of centrifugal force and gravity, being the optimum setting for a diverse number of applications of the device[29–35].

Results and Discussion

Both the confined and continuous modes of operation of the VFD are effective in slicing of the CNTs. In the confined mode a finite volume of liquid is wholly contained within the tube during processing while ensuring that a vortex is maintained to the bottom of the tube for moderate rotational speeds, and without any liquid exiting at the top of the tube. This minimises the formation of different shear regimes. In this mode, Stewartson/Ekman layers prevail in the resulting dynamic thin films, which arise from the liquid accelerating up the tube, with gravitational force acting against them[30]. In the continuous flow mode of operation of the VFD, jet feeds deliver one or more solutions (normally) to the bottom of the tube where there is intense micromixing, with instability of the liquid boundary layer in the hemispherical sphere at the bottom of the tube. The viscous drag as the liquid whirls up the tube creates shear, in addition to that from the Stewartson/Ekman layers. These unique fluidic properties of the VFD have led to a number of applications including control of chemical reactivity and selectivity in organic synthesis[29,30], exfoliating graphene and boron nitride[31], protein folding[32], fabricating toroidal arrays of SWCNTs[33], forming mesoporous silica at room temperature with control of pore size and wall thickness[34], and probing the structure of self organised processes[35–36].

The volume of liquid for confined mode studies was set at 1 mL with the speed and tilt angle varied to establish the lowest time for two liquids to homogenously mix. This was important to optimise exposure of the CNTs in the solution to the 8 mm diameter laser beam used in the 'slicing' experiments, as well as providing the maximum shear for debundling of the tubes. The minimum time taken for a homogenous mixture of water and NMP (1:1 ratio) to uniformly mix (visually estimated for solutions containing a dye, in the range 2000 to 9000 rpm, was for a rotational speed of 7500 rpm (Fig.1) for θ 45°. The choice of a 1:1 ratio of water and NMP was based on overcoming the low mixing time for NMP, in which the CNTs are readily dispersed, versus the fast mixing times in water, in which there is little dispersion of CNTs. These VFD parameters (θ 45°, 7500 rpm rotational speed) also correspond to the optimal processing parameters (*vide infra*).

Energy absorption from the pulsed laser source was essential to laterally slice the CNTs. The laser produces 1064 nm pulses of 5 ns duration and operates at a repetition rate of 10 Hz. In the confined mode, the optimised irradiation conditions were found to be a laser power of 260 mJ/pulse for, 30 minutes of processing. This was established by determining CNT length distributions using AFM on isolated samples (Supplementary Fig. S5). At high laser powers, $\geq$400 mJ, only small amounts of sliced nanotubes were evident, along with bundled and aggregated long nanotubes. Here the extra heat provided by the laser pulse disturbs the fluid flow, with a clear

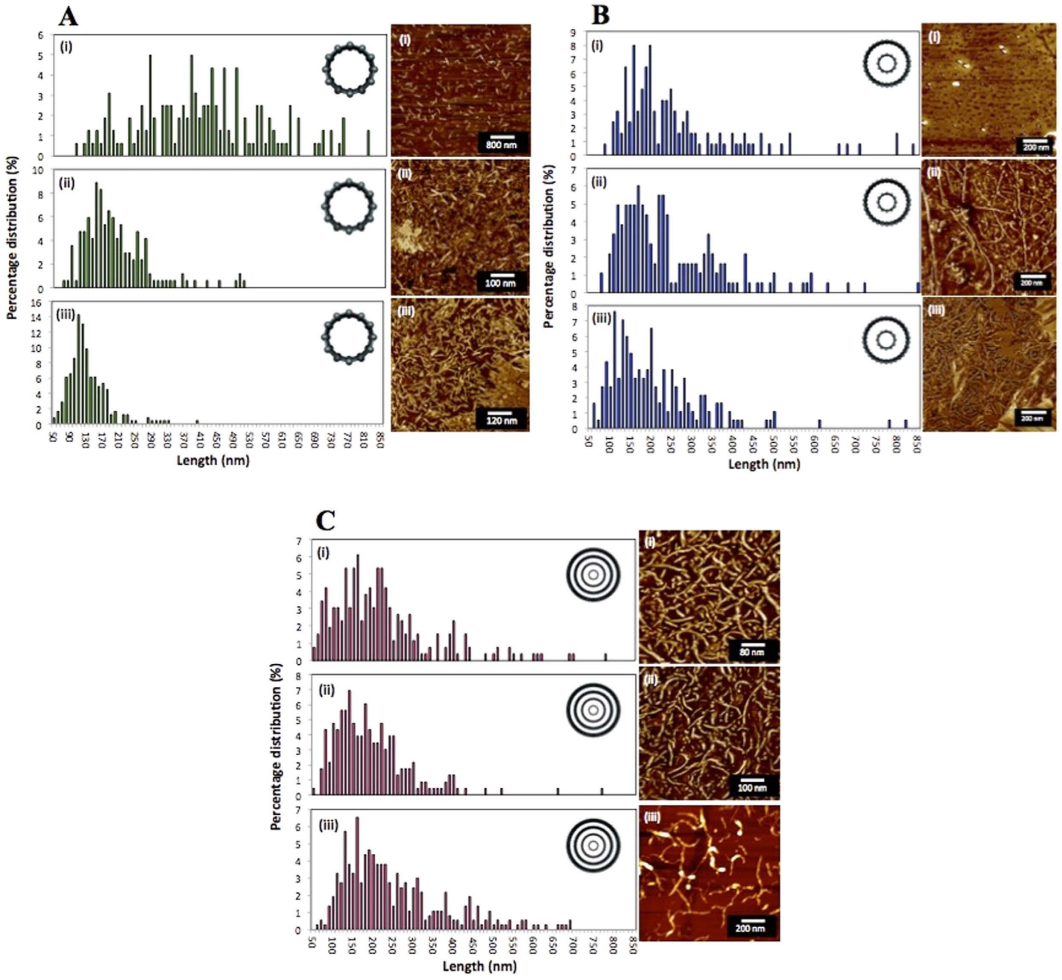

Figure 2. Slicing of SWCNTs, DWCNTs and MWCNTs at θ = 45° and rotational speed of 7500 rpm. AFM height images of laterally sliced CNTs using the confined mode of operation of the VFD, with associated length distribution plots for reaction times of (i) 10 min, (ii) 30 min and (iii) 1 hour for SWCNTs (**A**), DWCNTs (**B**), and MWCNTs (**C**).

band which is presumably largely devoid of CNTs at the point of laser irradiation. Decreasing the laser power to $<$200 mJ for 30 minutes was ineffective in slicing the CNTs and no clear band was observed at the irradiation site. (Supplementary Fig. S5).

The optimal VFD processing parameters (inclination angle θ and rotational speed) were determined following a number of control experiments. For rotational speeds below 6000 rpm, the as-received aggregated bundles of CNTs (SWCNTs, DWCNTs and MWCNTs) remained unaffected in both the presence and absence of laser irradiation. At 6000 rpm and 45° tilt, a significant amount of debundling of the nanotubes occurred (as shown through AFM observations), but laser irradiation led to non-uniformity of the sliced CNTs, and the persistence of longer tubes. Uniform slicing of the CNTs occurred between 7500 rpm and 8000 rpm when irradiated by the pulsed laser. A tilt angle of 45° angle was found to be optimal, with minimal lateral slicing at other angles between 0 and 90°. For these optimised VFD processing parameters (θ 45°, rotational speed 7500 rpm), in the absence of the laser pulses there was no evidence for slicing, with the length of the CNTs unchanged, although there was significant debundling (Supplementary Fig. S1). In decoupling the effect of the VFD and the laser irradiation, a pulsed laser beam of the same optimised power was directed towards the CNTs in a 1:1 mixture of water and NMP in a glass cuvette rather than in a VFD. This resulted in fragmentation of the CNTs nanotubes into (i) large and irregular shapes for the SWCNTs, (ii) large bundles and aggregates for the DWCNTs, and (iii) irregular slicing of MWCNTs with bundles and aggregates present (Supplementary Fig. S2). In addition, there was no evidence of slicing the CNTs with the laser wavelength set to 532 nm (Supplementary Fig. S3). Thus, the optimised parameters for laterally slicing the different CNTs to lengths below *ca* 450 nm are established as a 45° tilt angle of the VFD tube rotating at 7500 rpm under confined mode for 30 minutes, with the 10 Hz pulsed laser operating at a wavelength of 1064 nm and 260 mJ per 5 ns pulse. These conditions were found to be independent of the concentration of CNTs in the solution up to a maximum concentration of 0.1 mg/mL, above which presumably the dynamics in the thin film are affected by the CNTs.

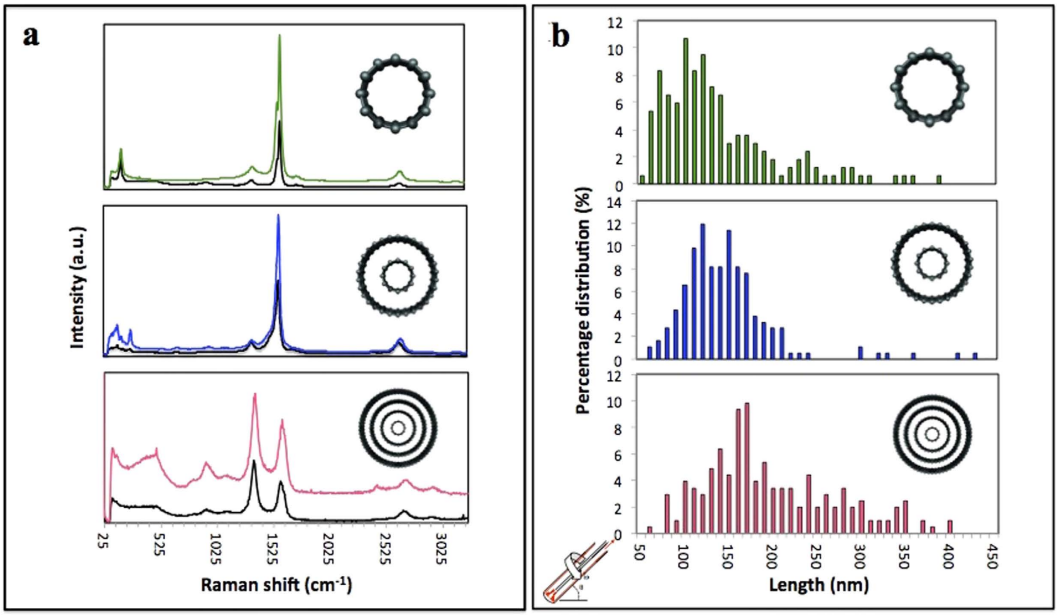

Figure 3. Raman spectroscopy and length distribution plots. (**a**) Raman spectra of SWCNTs, DWCNTs and MWCNTs, respectively, and the corresponding as received nanotubes (black). (**b**) Length distribution plots of the sliced SWCNTs, DWCNTs and MWCNTs under continuous flow operation of the VFD at a flow rate of 0.45 mL/min.

A time dependant study taking samples at 10 minute intervals during 1064 nm laser irradiation at 260 mJ/pulse, and the VFD operating in the confined mode, was also undertaken for the three types of CNTs. Over time, more slicing and debundling was observed, with SWCNTs resulting in a narrower length distribution, but not so for DWCNTs and MWCNTs (Fig. 2), although here slightly higher yields of sliced CNTs were evident.

Experiments under confined mode established the potential for laser irradiation of CNTs in a VFD to produce unbundled, short CNTs, but for generating practical quantities of the materials, continuous flow processing is desirable. Here a jet feed of CNTs dispersed in a 1:1 mixture of water and NMP was directed into the bottom of the rapidly rotating 20 mm tube at a low flow rate of 0.45 mL/min, using the same concentration of CNTs as for the confined mode. The low flow rate was necessary for sufficient exposure time of the CNTs to the 8 mm diameter laser beam, while ensuring droplets of the suspension of the CNTs were striking the hemispherical bottom of the tube rather than a continuous stream of the liquid. Such droplets result in instability of the resulting thin film, which imparts additional shear compared to the confined mode of operation of the VFD *(24)*. Under continuous flow there is a dramatic increase in yield of the sliced CNTs, typically 95%, with a length distribution of 100–400 nm, for SWCNTs, DWCNTs and MWCNTs (Fig. 3(b)). Also noteworthy is that all the samples are devoid of long bundled nanotubes, unlike the outcome for confined mode of operation of the VFD.

Raman analysis. Raman spectroscopy (Fig. 3(a)) established that any damage to the walls of the CNT products is minimal for confined mode and continuous flow operation of the VFD, irrespective of the number of shells of cylindrical graphene. Distinct peaks for CNTs include the radial breathing mode region (RBM), the tangential mode G band, its second harmonic G′ band and the disorder-induced D-band. The average ratio of intensities of the G and D bands (I_D/I_G) of the sliced SWCNT, DWCNT and MWCNT was ~0.2, ~0.3 and 1.2, respectively, which are similar to that of the starting pristine nanotubes which were ~0.2, ~0.2 and ~1.3, respectively, confirming that tube damage was minimal.

Small angle neutron scattering analysis. The average size of the sliced CNTs in solution was analysed using small angle neutron scattering (SANS). The radius of SWCNTs treated with the laser alone and laser and VFD (confined mode, 10, 30 and 60 min) was 0.7 ± 0.2 nm, which is consistent with AFM results (0.7 to 1.4 nm). For shorter treatment times the nanotubes were longer, and in the absence of VFD processing there is either complete disruption of SWCNTs or no slicing, with the results consistent with the AFM data (supplementary data). Overall, SWCNTs irradiated and subject to shear are broken down to smaller length scales (Fig. S9–S12), as is the case for the DWCNTs (Fig. S13) and MWCNTs (Fig. S14), to 160 nm and 171 nm respectively (Table S1), which is again consistent with AFM data.

Theoretical calculations. CNTs subjected to the shear forces created in the VFD result in local bending, as established by the observation that toroidal arrays of SWCNTs are produced in a mixture of toluene and water in the VFD in the absence of laser irradiation[33]. Bending is not surprising given the very high aspect ratio for SWCNTs, and when combined with heating from the laser it is likely to result in rupture of multiple bonds. To explore this further in understanding the mechanism of slicing, molecular dynamics simulations were carried out

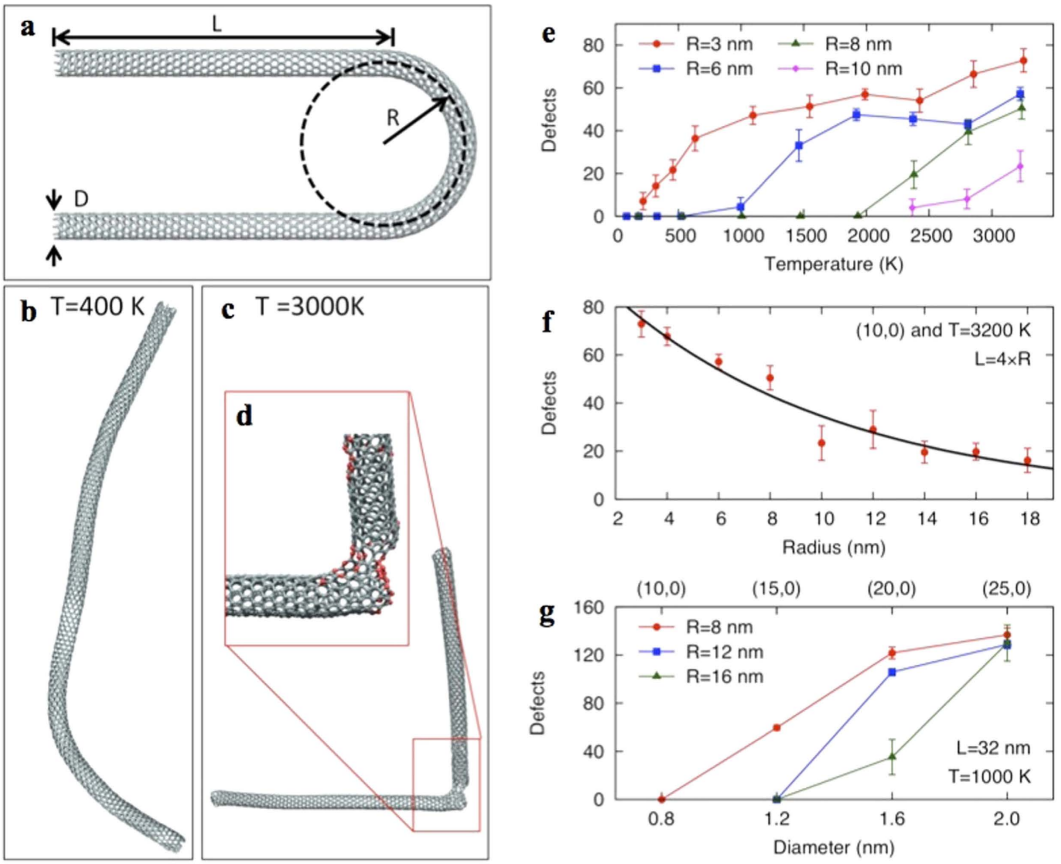

Figure 4. Theoretical calculations. (**a**) Initial bent structure of geometrical model of a nanotube showing the bending radius, R. and an arm-length, L, and nanotube diameter, D. (**b**,**c**) Snapshots of a (10, 0) nanotube model after annealing at 400 K and 3000 K respectively, with inset (**d**) showing a zoom-in of the defected sliced part of the nanotube. (**e**) Plot of the number of defects as a function of temperature for the (10, 0) nanotube with different bending radii. (**f**) Plot of the number of defects as a function of radius for the (10, 0) nanotube at a constant temperature of 3200 K. (**g**) Plot of number of defects at constant temperature as a function of diameter for different chiralities.

for SWCNTs, with hairpin-shaped tubes created to mimic the bending occurring in the VFD. Figure 4a shows a (10, 0) nanotube with a bending radius R of 2.5 nm and an arm-length L of 10 nm. When relaxed near room temperature (Fig. 4b and Movie S1), the hairpin unfolds and no defects are created. However, when the system is raised to a high temperature (Fig. 4c,d and Movie S2) a large tear occurs in the bent region and other defects appear nearby. The damage is produced by the extra energy provided by the elevated temperature resulting in breaking of bonds that are already strained.

The number of defects induced has been explored for different bending radii as a function of temperature. Figure 4e shows data for the same (10, 0) chirality with four bending radii, R = 3, 6, 8 and 10 nm. Ten simulations were performed at each temperature and radius to gather statistics. Defects are counted as atoms with a potential energy 10% higher than the cohesive energy of graphene or with a coordination number other than three. Below a critical temperature few defects are created, and in many instances no damage is created at all. As the radius increases, the critical temperature above which many defects are created becomes higher, as the bonds are less strained and require additional thermal activation to damage the nanotube. At large radii few defects are observed (Fig. 4f), even at high temperatures. These observations explain the experimental result that slicing occurs in the VFD with the laser irradiation but not with laser irradiation alone. Without the shear forces provided by the VFD, there is no localized bending or strained bonds for the laser to rupture. The simulations also suggest that the diameter D of the nanotube plays a role. Experimentally, this varies between 1 and 2 nm for the SWNTs. Figure 4g shows defect-vs-diameter data for three different bending radii. Chiralities of (10, 0), (15, 0), (20, 0) and (25, 0) were chosen with diameters spanning 0.78 to 2.0 nm. All three tubes were heated at 1000 K while bent in a hairpin-shape with radii of 8, 12 and 16 nm. For all three bending radii shown, the number of defects increases for nanotubes with larger diameter. Larger diameter tubes require less bending (i.e. larger bending radii) to be damaged. For example, while a (10, 0) nanotube heated at 1000 K needs to be bent to a radius less than 8 nm in order to show any defects, a (15, 0) nanotube shows damage at 8 nm but recovers for larger radii. This occurs due to the smaller inner bending radii (R-D/2) which arises for larger diameter tubes, while bonds at the outer bending radii are correspondingly stretched, with an outer radius of R + D/2. Therefore, tubes of larger diameter are

more easily sliced. We expect that these simulations of SWCNTs are also applicable to DWCNTs and MWCNTs. Outer tubes will be damaged first, as they have a larger diameter. Once the outer tube of the MWCNT is breached then the mechanical force either side would provide a point for spontaneously slicing through the inner tubes.

In summary, we have established the ability to laterally slice carbon nanotubes within dynamic thin films, irrespective of the number of concentric layers in the material. This is without precedent, and further highlights the unique capabilities of the recently developed vortex fluidic device. Importantly, the method minimises the generation of defects on the CNTs, producing pristine material devoid of chemical stabilisers, and we have demonstrated that there is potential for scalability of the process under continuous flow mode of operation of the VFD. Controlling the lengths of the shorter nanotubes is more significant for SWCNTs, under confined mode, affording a narrow size distribution at a length scale suitable for drug delivery applications. In general, the availability of short single, double or multi-walled CNTs is poised for the advancement of their applications where specific length scale is paramount.

Methods

Preparation of aqueous suspensions of sliced CNTs. SWCNTs were purchased from Thomas Swan & Co (UK), as chemical vapour deposition prepared material with an as-received purity >90%, DWCNTs were purchased from Carbon Allotropes with an as received purity >99% and the MWCNTs were purchased from Sigma Aldrich with an as received purity >98%. Sample preparation included the addition of the CNTs (1 mg) into a sample vial containing a mixture of NMP and water (6 mL) at a 1:1 ratio. The solution mixture was then ultrasonicated for 10 minutes, affording a black stable dispersion. Under the confined mode operation, the solution mixture (1 mL) was then placed in the 20 mm borosilicate NMR glass tube (ID 16.000 ± 0.013 mm) and placed in the vortex fluidic device (VFD), under the optimized rotating speed of 7500 rpm, at a tilt angle of 45 degrees. Simultaneously, a nanosecond pulsed laser processing system with an energy of approximately 260 mJ was applied to the rapidly rotating system for a period of time (10 minutes, 30 minutes and 1 hour), depending on the resulting length distribution. Under continuous flow mode, jet feeds with a flow rate at 0.45 mL/min (optimised) deliver the CNT suspension (mixture CNTs in NMP/water at a 1:1 ratio-similar concentration, as for the confined mode) into the rapidly rotating tube. Centrifugation (g 3.22) of the resulting solution for the confined mode of operation was required to remove any large agglomerates, unsliced bundled CNTs and impurities in the sample. The centrifugation step was not necessary for the continuous flow mode of operation with *ca* 95% of the material isolated as sliced CNTs.

Computational details. Starting coordinates were obtained by geometrically mapping the coordinates of a straight carbon nanotube onto a semicircle of a given radius linked with two straight sections to give a U-shape. Molecular Dynamics (MD) simulations were performed using the Environmental-Dependent Interaction Potential (EDIP) for carbon[37]. Prior to the MD step, the structures were relaxed using steepest descent optimization to remove any forces associated with the mapping. All MD simulations were performed in the NVE (constant particle-volume-energy) ensemble with an integration timestep of 0.35 fs. The simulations were initialized with velocities drawn from a Maxwell-Boltzmann distribution at a prescribed temperature and the entire system was allowed to evolve for 35 ps. Due to equipartition, the system temperature during the simulation was very close to half the initial value. Note that all temperatures reported here are system averages, and not the starting value. Steepest descent optimization was again applied to the final structures to remove any displacements due to thermal vibrations. The resultant structure was then analysed for defects. Atoms were defined as defects if their coordination number (defined by Equation 9 in Ref. 37) differed by more than 0.1 from the perfect value of 3 or if potential energy was more than 10% less than the perfect value of −7.361 eV for graphite.

Instrumentation. TEM characterizations were carried out using the Phillips CM 200 operating at 200 kV, in the Adelaide Microscopy at the University of Adelaide. SEM analysis was carried out on the FEI Quanta 450 in Adelaide Microscopy. AFM, Raman characterizations and UV-Vis analysis were performed at Flinders University. SANS characterizations were carried on QUOKKA at the Bragg Institute, ANSTO.

References

1. Wong, E. W., Sheehan, P. E. & Lieber, C. M. Nanobeam Mechanics: Elasticity, Strength and Toughness of Nanorods and Nanotubes. *Science*. **277,** 1971–1975 (1997).
2. Liu, L., Yang, C., Zhao, K., Li, J. & Wu, H. C. Ultrashort single walled carbon nanotubes in a lipid bilayer as a nanopore sensor. *Nature Commun*. **4,** 2989 doi: 10.1038/ncomms3989 (2013).
3. Treacy, M. M. J., Ebbesen, T. W. & Gibson, J. M. Exceptionally high Young's modulus observed for individual carbon nanotubes. *Nature*. **381,** 678–680 (1996).
4. Krishnan, A., Dujardin, E., Ebbesen, T. W., Yianilos, P. N. & Treacy, M. M. J. Young's modulus of single walled nanotubes. *Phys. Rev. B.* **58,** 14013–14019 (1998).
5. Kashyap, K. T. & Patil, R. G. On Young's modulus of multiwalled carbon nanotubes. *Bull. Mater. Sci.* **31,** 185–187 (2008).
6. Ebbesen, T. W. & Ajayan, P. M. Large scale synthesis of carbon nanotubes. *Nature*. **358,** 220–222 (1992).
7. Guo, T., Nikolaev, P., Thess, A., Colbert, D. T. & Smalley, R. E. Catalytic growth of single walled nanotubes by laser vaporisation. *Chem. Phys. Lett*. **243,** 49–54 (1995).
8. Endo, M. *et al.* The production and structure of pyrolytic carbon nanotubes. *J. Phys. Chem. Solids*. **54,** 1841–1848 (1997).
9. Javey, A. *et al.* High Field Quasiballistic Transport in Short Carbon Nanotubes. *Phys. Rev. Lett.* **92,** 16804 1–4 (2004).
10. Kalita, G. *et al.* Cutting carbon nanotubes for solar cell applications. *Appl. Phys. Lett.* **92,** 12358 doi: 10.1063/1.290349 (2008).
11. Farkas, E., Anderson, M. E., Chen, Z. & Rinzler, A. G. Length sorting cut single walled carbon nanotubes by high performance liquid chromatography. *Chem. Phys. Lett*. **363,** 111–116 (2002).
12. Sanchez-Valencia, J. R. *et al.* Controlled synthesis of single chirality carbon nanotubes. *Nature*, **512,** 61–64 (2014).
13. Casey, J. P., Bachilo, S. M., Moran, C. H. & Weisman, R. B. Chirality-resolved length analysis of single walled carbon nanotube samples through shear aligned photoluminescence anisotropy. *ACS Nano*, **2,** 1738–1746 (2008).

14. Minati, L. *et al.* Investigation on the Electronic and Optical Properties of Short Oxidised Multiwalled Carbon Nanotubes. *J.Phys. Chem. C.* **114,** 11068–11073 (2010).
15. Tran, M. Q., Tridech, C., Alfrey, A., Bismarck, A. & Shaffer, M. S. P. Thermal oxidative cutting of multiwalled carbon nanotubes. *Carbon*. **45,** 2341–2350 (2007).
16. Wang, C., Guo, S., Pan, X., Chen, W. & Bao, X. Tailored cutting of carbon nanotubes and controlled dispersion of metal nanoparticles inside their channels. *J. Mater. Chem.* **18,** 5782–5786 (2008).
17. Yudasaka, M., Zhang, M., Jabs, C. & Iijima, S. Effect of an organic polymer in purification and cutting of single walled carbon nanotubes. *App. Phys. A*. **71,** 449–451 (2000).
18. Zhang, J. *et al.* Effect of chemical oxidation on the structure of single walled carbon nanotubes. *J. Phys. Chem. B.* **107,** 3712–3718 (2003).
19. Liu, J. *et al.* Fullerene pipes. *Science.* **280,** 1253–1256 (1998).
20. Gu, Z., Hauge, R. H., Smalley, R. E. & Margrave, J. L. Cutting single walled carbon nanotubes through fluorination. *Nano Letters.* **2,** 1009–1013 (2002).
21. Pierard, N. *et al.* Ball milling effect on the structure of single walled carbon nanotubes. *Carbon*. **42,** 1691–1697 (2004).
22. Chen, Z. *et al.* Soluble ultra-short single walled carbon nanotubes. *J. Am. Chem. Soc.* **128,** 10568–10571 (2006).
23. Yi, X. J., Nadeem, A. M., Dong, B. H., Ying, L. H. & Tai, Y. W. Concentration and temperature controlled oxidation and cutting of single walled carbon nanotubes by ammonium persulfate. *Sci Chi*. **53,** 2026–2032 (2010).
24. Zhao, J., Liu, P., Yang, Z., Zhou, P. & Zhang, Y. One-step cutting of multiwalled carbon nanotubes using nanoscissors. *Nano-Micro Lett*. **2,** 86–90 (2011).
25. Manivannan, S. *et al.* Dispersion of single walled carbon nanotubes in aqueous and organic solvents through polymer wrapping functionalisation. *J. Mater. Sci.* **20,** 223–229 (2009).
26. Tkalya, E. E., Ghislandi, M., With, G. D. & Koning, C. E. The use of surfactants for dispersing carbon nanotubes and graphene to make conductive nanocomposites. *Curr. Opin. Coll. Inter.* **17,** 225–232 (2012).
27. Mickelson, E. T. *et al.* Solvation of flourinated single walled carbon nanotubes in alcohol solvents. *J. Phys. Chem. B.* **103,** 4318–4322 (1999).
28. Boul, P. J. *et al.* Reversible sidewall functionalisation of bucky tubes. *Chem. Phys. Lett.* **310,** 367–372 (1999).
29. Britton, J., Chalker, J. M. & Raston, C. L. Rapid vortex fluidics: Continuous flow synthesis of amides and local anaesthetic lidocaine. *Chem. Eur. J*. **21,** 10660–106665 (2015).
30. Britton, J., Dalziel, S. B. & Raston, C. L. Continuous flow Fischer esterifications harnessing vibrational-coupled thin films fluidics. *RSC Adv*. **5,** 1655–1660 (2015).
31. Chen, X., Dobson, J. F. & Raston, C. L. Vortex fluidic exfoliation of graphite and boron nitride. *Chem. Commun.* **48,** 3703–3705 (2012).
32. Yuan, T. Z. *et al.* Shear-stress-mediated refolding of proteins from aggregates and inclusion bodies. *ChemBioChem*. **16,** 393–396 (2015).
33. Vimalanathan, K., Chen, X. & Raston, C. L. Shear induced fabrication of intertwined single walled carbon nanotube rings. *Chem Commun.* **50,** 11295–11298 (2014).
34. Tong, C. L., Boulos, R. A., Yu, C., Iyer, K. S. & Raston, C. L. Continuous flow tuning of ordered mesoporous silica under ambient conditions. *RSC Adv*. **3,** 18767–18770 (2013).
35. Mo, J. *et al.* Shear induced carboplatin binding within the cavity of a phospholipid mimic for increased anticancer efficacy. *Sci. Rep*. **5,** 10414 doi: 10.1038/srep10414 (2015).
36. Iyer, K. S. & Raston, C. L. Fabrication of laterally 'sliced' metal plated carbon nanotubes under aqueous continuous flow conditions. *J. Mater. Chem.* **17,** 4872–4875 (2007).
37. Marks, N. A. Generalizing the environment-dependent interaction potential for carbon. *Phys. Rev. B*. **63,** 035401 doi: 10.1103/PhysRevB.63.035401 (2000).

Acknowledgements

The authors thank Dr. Paul Eggers for his technical assistance, and Associate Professor Amanda Ellis for discussions on the optical absorbance characterisations. The authors also thank Australian Research Council and The Government of South Australia for support of the work.

Author Contributions

K.V., J.R.G., W.D.L., N.M., I.S.M., H.K., J.L.A. and C.L.R. designed the experiments and wrote the paper, K.V. and J.R.G. performed the slicing experiments. K.V. carried out AFM, Raman and UV Vis analysis and analysed the data. N.M. and I.S.M. carried out the computational studies and the data analysis. H.K. and C.G. carried out SANS experiments and H.K. and J.L.A. carried out the data analysis based on the SANS results.

Additional Information

Supplementary information accompanies this paper at http://www.nature.com/srep

Competing financial interests: The authors declare no competing financial interests.

How to cite this article: Vimalanathan, K. *et al.* Fluid dynamic lateral slicing of high tensile strength carbon nanotubes. *Sci. Rep.* **6**, 22865; doi: 10.1038/srep22865 (2016).

Volume 50 | Number 77 | 7 October 2014 | Pages 11245–11422

ChemComm

Chemical Communications

www.rsc.org/chemcomm

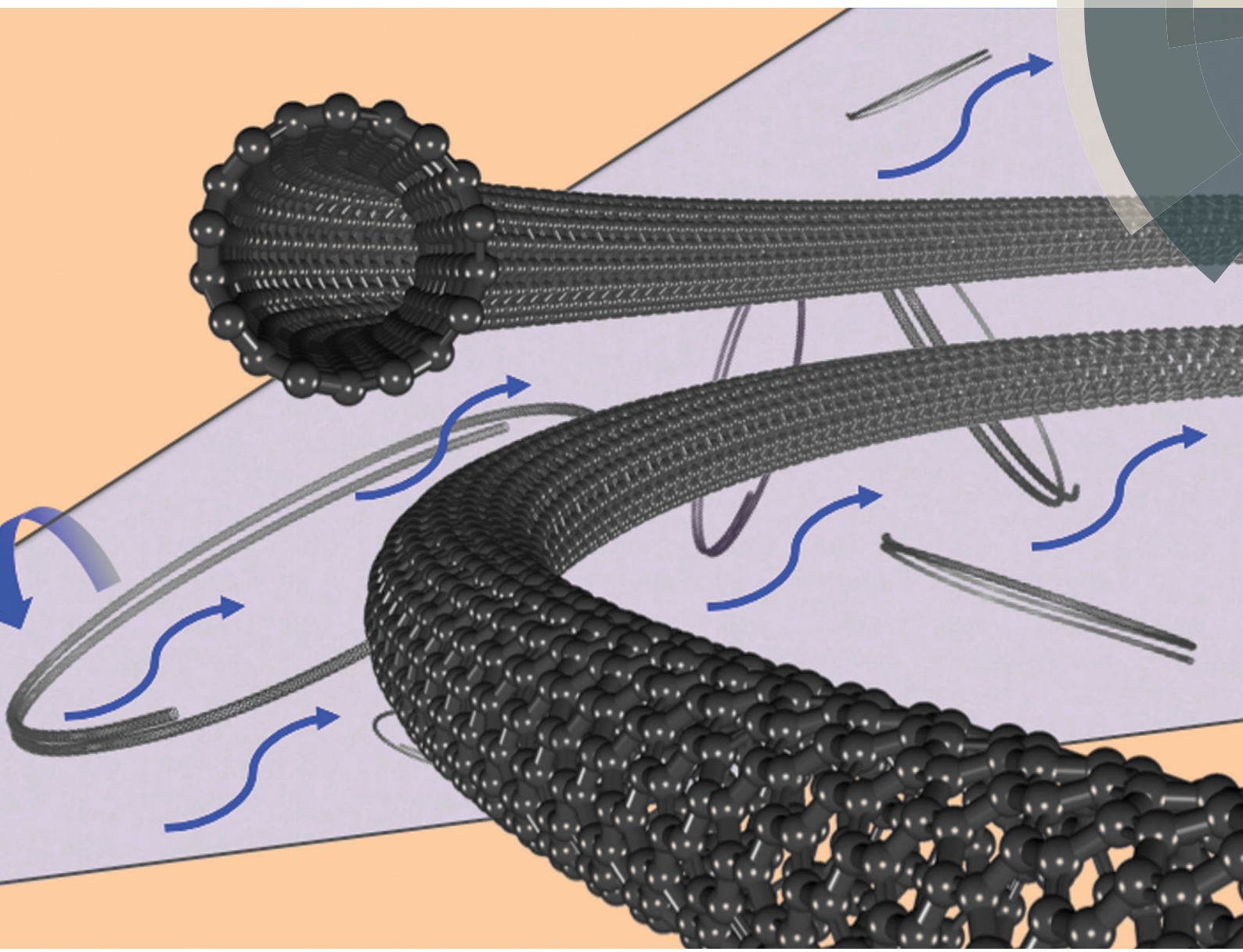

ISSN 1359-7345

ROYAL SOCIETY OF CHEMISTRY

COMMUNICATION

Colin L. Raston *et al.*

Shear induced fabrication of intertwined single walled carbon nanotube rings

ChemComm

COMMUNICATION

View Article Online
View Journal | View Issue

Cite this: *Chem. Commun.*, 2014, **50**, 11295

Received 28th April 2014,
Accepted 5th June 2014

DOI: 10.1039/c4cc03126a

www.rsc.org/chemcomm

Shear induced fabrication of intertwined single walled carbon nanotube rings†

Kasturi Vimalanathan, Xianjue Chen and Colin L. Raston*

Thin film microfluidic shearing of a mixture of toluene dispersed single walled carbon nanotubes (SWCNTs) and water in a vortex fluidic device results in SWCNT nanorings (and related structures), diameters 100 to 200 nm or 300 to 700 nm, for respectively 10 mm or 20 mm diameter rotating tubes.

Single walled carbon nanotubes (SWCNTs) continue to attract attention, having exceptional mechanical and electrical properties in high performance electronics[1] and applications in scanning probe microscopy,[2] fuel cells,[3] composites,[4] chemical,[5] biological,[6] and physical sensors.[7,8] They are available as long fibres, centimetres in length and beyond, and tend to aggregate into large bundles because of the relatively strong inter-SWCNT van der Waals interactions. Indeed, difficulties in generating individual strands of SWCNTs is an issue in optimizing their mechanical, thermal, and electronic properties.[9] Carbon nanotubes have in general extremely high flexural rigidity,[3,4] and permanently bending them in a controlled way into well-ordered nanorings/toroidal structures is challenging,[10] with the potential to circumvent or control the aforementioned aggregation[11] and impart different functionality. A variety of techniques have been reported on generating such structures with control over their diameters.[12–15] However, they mostly involve long periods of high-energy sonication, chemical modifications and lengthy physical processing as well as the use of highly reactive chemicals such as concentrated sulphuric acid and hydrogen peroxide, which are potentially damaging to the SWCNTs. In this context, the development of more benign methods is warranted, as is the ability to scale up the conversion of SWCNTs in particular, into the nanorings, with control over their diameter while maintaining a high level of purity. Hydrophobic carbon nanotubes and hydrophilic palladium nanowires form coils in the presence of a water–oil mixture, and this establishes the utility of an immiscible solvent mixture and the associated interfacial surface tension as an important consideration in overcoming high flexural rigidity of these one dimensional materials.[15]

We now report a simple and novel one-step method to produce nanorings of SWCNTs in high yield, where liquid–liquid interfacial tension involving a mixture of water and toluene is amplified using mechanoenergy from a recently developed energy efficient microfluidic vortex fluidic device (VFD), Fig. 1a.[16] Well-defined nanorings of SWCNTs with the average diameters depending on the diameter of the tube, being accessible down to *ca.* 100 nm. The ability to control the diameter of such rings, and the ability to scale up, has implications for applications in electronic devices.[10]

The VFD has a rapidly rotating tube, within which liquids form dynamic thin films for finite sub-millilitre volumes of

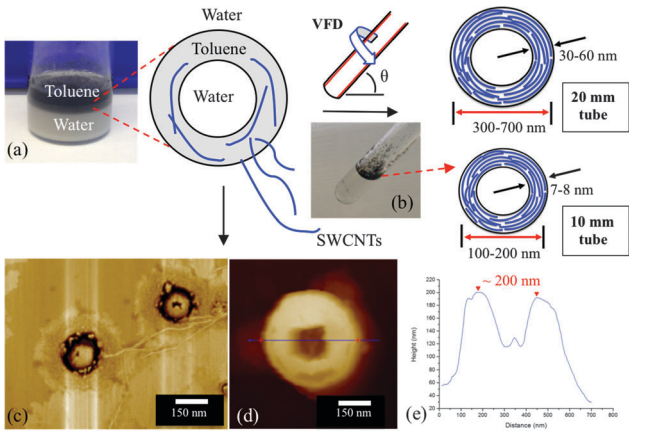

Fig. 1 (a) Synthesis and proposed templated mechanism of formation of nanorings of SWCNTs from a sonicated mixture of toluene and water, (b) photograph of SWCNT–toluene–water mixture post-VFD processing, θ = 45°; and pre-VFD processing AFM phase image, (c), height image (d), and associated height profile, (e), of a toroidal structure with radiating SWCNTs, formed on drop casting the mixture from (a).

Centre for NanoScale Science and Technology, School of Chemical and Physical Sciences, Flinders University, Bedford Park, SA 5042, Australia.
E-mail: colin.raston@flinders.edu.au

† Electronic supplementary information (ESI) available. See DOI: 10.1039/c4cc03126a

liquid, as the so-called confined mode of operation of the device.[16] The shear intensity in the films depends on a number of parameters, including inclination angle relative to the horizontal position, θ, and the rotational speed,[16] which collectively define the interplay between centrifugal and gravitational forces within the films.[17] The confined mode of operation of the VFD results in the formation of a thin film for a defined volume of liquid (herein 1 mL) within the tube, at least above a threshold speed such that a vortex is maintained to the bottom of the tube, otherwise there are different regimes of shear within the liquid.[16]

The VFD can also operate under continuous flow where jet feeds deliver solutions to the bottom of the tube which results in intense micro mixing, and collectively with the confined mode of operation, a number of applications of the device have been established. These include controlling chemical reactivity and selectivity in organic synthesis,[16] exfoliation of graphene and boron nitride,[17] generating mesoporous silica at room temperature with control of pore size and wall thickness,[18] controlling the decoration of palladium nanoparticles on carbon nano-onions and graphene sheets,[19] generating graphene algae hybrid material for nitrate removal,[20] and more.

SWCNTs produced by a catalytic chemical deposition synthesis method with $>90\%$ purity were purchased from Thomas Swan and Co. (UK), and used as received. Toluene was purchased from Sigma Aldrich and also used as received. SWCNTs (1.0 mg) were dispersed in toluene (3 mL) and added to MilliQ water (3 mL). Sonication for 10 minutes afforded a stable two-phase dispersion with the top phase black and the bottom phase milky (Fig. 1a). A 1 mL portion of the mixture under sonication was collected to ensure that it was a uniform mixture of the three components, and was placed in a 20 mm (I.D. = 16.000 $\pm$ 0.013 mm) or 10 mm (I.D. = 7.100 $\pm$ 0.013 mm) diameter VFD tube, as standard borosilicate glass NMR tubes.

A systematic evaluation of the operating parameters of the VFD was carried out to ascertain the optimal parameters for the formation of the nanorings. These were established as an inclination angle of 45° with the 20 mm VFD tube rotating at 7500 rpm, for a reaction time of 20 minutes. At other rotational speeds and inclination angles, *i.e.* higher or lower than the optimized conditions, the formation of the nanorings was either in low yield or not evident (see ESI† for details). The diameters of the rings produced were within the range of 300 to 700 nm, as established using atomic force microscopy (AFM) and transmission electron microscopy (TEM). Optimisation of the operating parameters were also established for a 10 mm diameter tube, which resulted in the formation of nanorings with a significantly smaller diameter range, 100 to 200 nm.

Overall the nanorings formation (Fig. 2 and 3) is at a high conversion. There was no evidence of non-coiled SWCNTs, with some different morphologies generated, namely nanorings, figure of "8" shaped rings and crossed lattice rings.[13] Processing in the smaller internal diameter tube afforded smaller rings, 100 to 200 nm in diameter, Fig. 3, for a reaction time of an hour under the same VFD operating parameters (namely 45 degree inclination angle, 7500 rpm rotational speed). Small amounts of toroidal structures based on a single SWCNT are also present

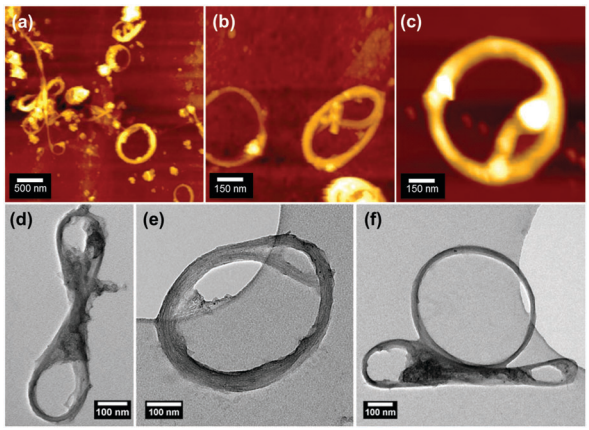

Fig. 2 SWCNT nanorings 300 to 700 nm in diameter, generated using a 20 mm VFD tube: (a–c) AFM height images of the rings, (d–f) TEM images of the different nanoring structures.

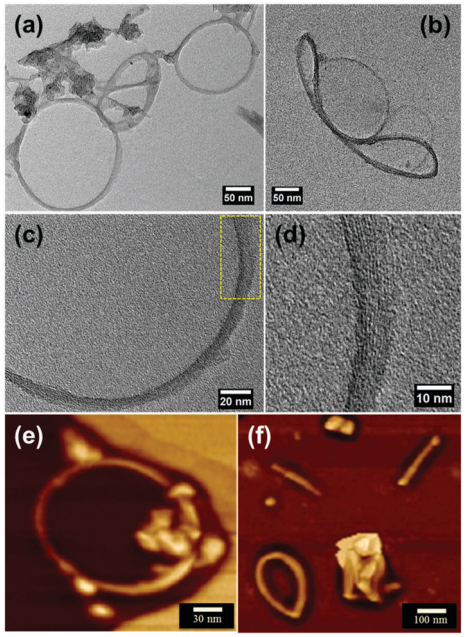

Fig. 3 SWCNT nanorings 100 to 200 nm in diameter (10 mm diameter VFD tube): (a and b) TEM images of the nanorings, (c and d) HRTEM images, AFM height images (e) nanoring, and (f) single SWCNT 'biting' its tail (lower left) along with some short SWCNTs, *ca.* 120 nm in length.

(Fig. 3f), where it appears that SWCNTs 'bite' their tail, with the diameter of the toroid at approximately 100 nm. This corresponds to a length of 314 nm for a straight SWCNT, from which the toroid presumably originates, Fig. 3f, and this has implications on the nature of processes involved in the dynamic thin films in the VFD. It is noted that the initial lengths of these as-received SWCNTs were approximately 1–2 μm, and thus in forming these structures based on a single SWCNT there has been some lateral slicing in generating shorter lengths.

Shear forces in the VFD are effective under both confined mode and continuous flow modes of operation in controlling

the fabrication of nanomaterials,[14–18] including exfoliation of carbon nanomaterials such as graphite.[17] In the confined mode at $\theta > 0^{\circ}$, centrifugal forces accelerate the emulsion droplets and nanotubes to the bottom of the tube. The ensuing shear forces can overcome the large van der Waals forces between the bundles of SWCNTs and thus facilitate exfoliation of individual SWCNTs, with the shear forces then also responsible for their lateral slicing.

Drop casting the interfacial SWCNT laden material in Fig. 1a affords toroids with radiating SWCNTs, as established using AFM, Fig. 1c–e. This suggests that toroids of toluene containing hydrophobically matched SWCNTs are present pre-VFD processing, and the subsequent shear forces result in compacting and intertwining the SWCNTs at their van der Waals limit, also drawing in the radiating SWCNTs into the nanorings. These nanorings were characterised using AFM and TEM, Fig. 2 and 3. They have smaller wall thickness (differences between the internal and external diameter) relative to the toroids formed from drop casting pre-VFD processing mixture. For 10 mm diameter VFD tubes, the external diameter of the nanorings dramatically reduces relative to the size of the toluene toroids, resulting is greater curvature in the SWCNTs.

Interestingly, the long axis of the figure of ''8'' structures is approximately twice the external diameter of the nanorings, and possibly arise from two toroids of SWCNT laden toluene in contact through common SWCNTs, at their limiting size under intense shear. Previous researchers have noted that the different structures of nanorings depend on the method of sample preparation, with rings collapsing at the edge of the substrate prior to solvent evaporation in forming the figure of ''8'' structure.[13] Formation of these structures has also been ascribed as resulting from further coiling and twisting of the toroid rings, as a secondary structure.[15]

As a control, sonication of a suspension of SWCNTs in toluene showed de-bundling of the nanotubes with occasional ring structures. However, these rings were unstable and slowly collapsed back to the post-sonication SWCNTs (see ESI† for details). Also SWCNTs in toluene, in the absence of water, and without the application of sonic energy, undergo aggregation/restacking. Clearly, sonication is essential to obtain well-dispersed SWCNT, and generating templating toroids of toluene laden with SWCNTs en route to forming the compact nanorings of SWCNTs under shear. VFD processing in the absence of the liquid–liquid interface under similar conditions, for a dispersion of SWCNTs in pure toluene, does not afford nanorings of SWCNTs, thereby establishing that the surface tension between the otherwise immiscible liquids is essential for generating nanorings of SWCNTs (see ESI† for details).

High-resolution TEM (HRTEM) images show that the nanorings are comprised of SWCNTs of diameters in the range 1 to 2 nm (Fig. 3c and d). These results are consistent with micro-Raman spectroscopy (Fig. 4), at an excitation wavelength of 532 nm ($\leq$5 mW).

The radial breathing mode (RBM) (Fig. 4 inset) as well as the G- and D-band on the spectra are markers for determining the diameters of the SWCNTs.[21] The peaks at 1353 cm^{-1} and

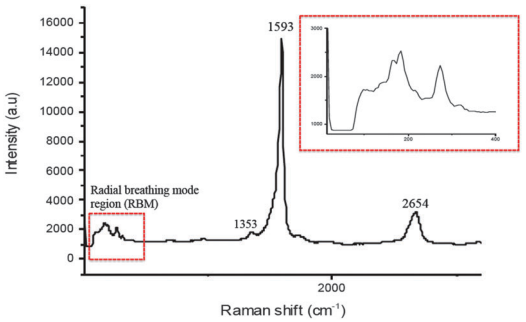

Fig. 4 Raman spectra of SWCNT nanorings deposited on a glass slide. Inset: radial breathing mode region whereby the frequencies correspond to diameter of the SWCNTs.[22]

the peak at 1593 cm^{-1} correspond to the D- and the G-bands respectively (Fig. 4). The D-band is the disorder-induced band which provides information regarding amorphous impurities and is a measure of the amount of disorder and defects on the walls of the nanotubes, whereas the G-band (graphite band) corresponds to the graphite E_{2g} symmetry band, affirming the structural integrity of the sp^2 hybridized carbon atoms of the nanotubes.[22] Focusing on the RBM of the spectra, the frequencies at *ca.* 97.3 cm^{-1}, 164.1 cm^{-1}, 182.1 cm^{-1} and 277.8 cm^{-1} respectively, $\nu_{RBM} = A/d_t + B$, where the RBM frequency is in cm^{-1}, d_t is the diameter of the CNT, and A = 223.5 cm^{-1} and B = 12.5 cm^{-1} which have been determined experimentally,[23] enable the determination of the diameter of the SWCNTs forming the rings. Thus, the frequencies of the RBM region correspond to SWCNTs present approximately 2.64 nm, 1.47 nm, 1.32 nm and 0.86 nm in diameter respectively, in accordance with HRTEM data. The irregular thicknesses (Fig. 2 and 3) of the ring walls relate to aggregation of more than one nanotube, consisting of semiconducting and metallic nanotubes of a range of diameters, stacked at the van der Waals limit. The rings produced in the 20 mm VFD had a nanoring wall thickness of *ca.* 30 to 60 nm, comprised of approximately 20 to 30 stacks of nanotubes of diameters between 1 to 2 nm, noting that some of the nanotubes are likely to coil more than once in each nanoring. The smaller diameter rings, generated using a 10 mm diameter VFD tube, have 7.0 to 8.0 nm thick walls, being similarly built up of about 3 to 8 stacks of nanotubes of 1 to 2 nm in diameter.

In summary, we have developed a simple and novel one-step method to fabricate SWCNT nanorings using the shear generated in thin films within a vortex fluidic device. This is under ambient conditions and avoids the use of reactive chemicals for processing, and the need for surfactants to stabilize the nanorings, with the ability to control the ring size, depending on the diameter of the rapidly rotating tube. Nanorings of SWCNT have promise in a number fields including in polymer composites,[11] sensing devices[8] and more importantly electronic circuits,[12–14] and this is closer to a realization with the availability of such material herein, which can be readily scaled up, noting the ability for the VFD to operate under continuous flow conditions.[16]

The authors gratefully acknowledge support of this work by the Australian Research Council and the Government of South Australia, and the Australian Microscopy & Microanalysis Research Facility (AMMRF) at the Centre for NanoScale Science and Technology, Flinders University.

Notes and references

1 J. Appenzeller, *Proc. IEEE*, 2008, **483**, 201–211.
2 H. Dai, J. H. Hafner, A. G. Rinzler, D. T. Colbert and R. E. Smalley, *Nature*, 1996, **384**, 147–150.
3 M. M. J. Treacy, T. W. Ebbesen and J. M. Gibson, *Nature*, 1996, **381**, 678–680.
4 E. W. Wong, P. E. Sheehan and C. M. Lieber, *Science*, 1997, **277**, 1971–1975.
5 J. H. Hafner, C. L. Cheung and C. M. Lieber, *J. Am. Chem. Soc.*, 1999, **121**, 147–150.
6 G. Girishkumar, T. D. Hall, K. Vinodgopal and P. V. Kamat, *J. Phys. Chem.*, 2006, **110**, 107–114.
7 O. Breuer and U. Sundararaj, *J. Phys. Chem.*, 2004, **25**, 630–645.
8 E. S. Snow, F. K. Perking, E. J. Houser, S. C. Badescu and T. L. Reinecke, *Science*, 2005, **307**, 1942–1945.
9 B. L. Allen, P. D. Kichambare and A. Star, *Adv. Mater.*, 2007, **19**, 1439–1451.
10 J. R. Wood and H. D. Wagner, *Appl. Phys. Lett.*, 2000, **76**, 2883–2885.
11 T. Hasan, V. Scardaci, P. Tan, A. G. Rozhin, W. I. Milne and A. C. Ferrari, *J. Phys. Chem. C*, 2007, **111**, 12594–12602.
12 L. Song, L. Ci, L. Sun, C. Jin, L. Liu, W. Ma, D. Liu, X. Zhao, S. Luo, Z. Zhang, Y. Xiang, J. Zhou, W. Zhou, Y. Ding, Z. Wang and S. Xie, *Adv. Mater.*, 2006, **18**, 1817–1821.
13 W. Wang, E. D. Laird, Y. Gogotsi and C. Y. Li, *Carbon*, 2012, **50**, 1769–1775.
14 R. Martel, H. R. Shea and P. Avouris, *J. Phys. Chem.*, 1999, **103**, 7551–7556.
15 L. Chen, S. Yu, H. Wang, J. Xu, C. Liu, W. H. Chong and H. Chen, *J. Am. Chem. Soc.*, 2012, **135**, 835–843.
16 L. Yasmin, X. Chen, K. A. Stubbs and C. L. Raston, *Sci. Rep.*, 2013, **3**, 2282.
17 X. Chen, J. F. Dobson and C. L. Raston, *Chem. Commun.*, 2012, **48**, 3703–3705.
18 C. L. Tong, R. A. Boulos, C. Yu, K. S. Iyer and C. L. Raston, *RSC Adv.*, 2013, **3**, 18767–18770.
19 F. M. Yasin, R. A. Boulos, B. Y. Hong, A. Cornejo, K. S. Iyer, L. Gao, H. T. Chua and C. L. Raston, *Chem. Commun.*, 2012, **48**, 10102–10104.
20 M. H. Wahidd, E. Eroglu, X. Chen, S. M. Smith and C. L. Raston, *Green Chem.*, 2012, **15**, 650–655.
21 M. S. Dresselhaus, G. Dresselhaus, R. Saito and A. Jorio, *Phys. Rep.*, 2005, **409**, 47–99.
22 L. J. Hubble, T. E. Clark, M. Makha and C. L. Raston, *J. Mater. Chem.*, 2008, **18**, 5961–5966.
23 S. M. Bachilo, M. S. Strano, C. Kittrell, R. H. Hauge, R. E. Smalley and R. B. Weisman, *Science*, 2002, **298**, 2361–2366.

Journal of Colloid and Interface Science 443 (2015) 88–96

Contents lists available at ScienceDirect

Journal of Colloid and Interface Science

www.elsevier.com/locate/jcis

Aqueous based synthesis of antimicrobial-decorated graphene

M. Haniff Wahid [a], Uwe H. Stroeher [b], Ela Eroglu [c,d], Xianjue Chen [a], Kasturi Vimalanathan [a], Colin L. Raston [a,*], Ramiz A. Boulos [a,*]

[a] Centre for NanoScale Science and Technology, School of Chemical and Physical Sciences, Flinders University, Bedford Park, SA 5042, Australia
[b] School of Biological Sciences, Flinders University, Bedford Park, SA 5042, Australia
[c] Centre for Strategic Nano-Fabrication, School of Chemistry and Biochemistry, The University of Western Australia, Crawley, WA 6009, Australia
[d] ARC Centre of Excellence in Plant Energy Biology, The University of Western Australia, 35 Stirling Highway, Crawley, WA 6009, Australia

ARTICLE INFO

Article history:
Received 9 October 2014
Accepted 17 November 2014
Available online 25 November 2014

Keywords:
Graphene
Exfoliation
Ramizol
Ultra-sonication
Non-covalent functionalization
Antibacterial
Antimicrobial

ABSTRACT

Ramizol® (1,3,5-tris[(1E)-2′-(4′-benzoic acid)vinyl]benzene) is a potent amphiphilic anti-microbial agent. It is essentially a planar molecule and can interact with the surface of graphene *via* extended π–π interactions. Herein we demonstrate the utility of Ramizol® in potentially acting as a molecular 'wedge' to exfoliate graphene and stabilise it in water. The non-covalent attachment of Ramizol® on the graphene surface enables release of Ramizol® by altering the pH of the solution. Furthermore, the stabilised composite material demonstrates antibacterial activity against *Staphylococcus aureus* which leads to potential in biomedical applications with graphene acting as a drug carrier as well as enhancing the structural strength of the composite material.

1. Introduction

The remarkable properties of graphene such as high electron mobility, high mechanical strength, flexibility and transparency, has led to extensive research efforts to produce the 2D material on a large scale [1–4]. Exfoliation is possible directly from graphite as a relatively cheap and abundant material, which requires overcoming relatively strong van der Waals interactions between the graphitic layers [5,6]. Developing processes to assist this exfoliation, as well as stabilising the sheets after exfoliation is important in advancing the diversity of applications of graphene, which includes its use as an antimicrobial agent in its own right [7,8]. Also important is avoiding the use of harsh chemical reagents or the production of toxic by-products, for developing sustainable technologies for the future.

Various methods have been reported for the production of graphene, from chemical vapour deposition [9], reduction of graphite oxide [10], micromechanical cleavage of graphite [11], ultra-sonication in an organic solvent such as N-methyl-2-pyrrolidone [12] or in water with the addition of a surfactant [13–16], dissolution in super acid [17], to the use of high shear forces [4,18]. We recently established the synthesis of multi-layer graphene from graphite in water using shear within a thin film microfluidic vortex fluidic device, without the need for a stabilising surfactant [19]. Given the antimicrobial property of graphene [7,8], we sought to use an antimicrobial agent to enhance this property of graphene, and also to facilitate the exfoliation process as well as acting as a stabilising agent at physiological pH. Ramizol® (1,3,5-tris[(1E)-2′-(4′-benzoic acid)vinyl]benzene) is a potent and non-toxic synthetic antimicrobial agent [20–22], and features in this study, in developing a composite with graphene, along with the choice of water as the reaction medium. The latter was deemed important in incorporating green chemistry metrics into the synthesis from the outset.

Ramizol® is essentially a planar molecule and can in principle interact with the surface of graphene *via* extended π–π interactions, with potential then for stabilising the graphene in water. Intense shear and high cavitation forces [23–25] induced by ultrasonic mechanoenergy act on the bulk graphite, resulting in exfoliation [25]. In addition, the shape of Ramizol® lends itself to facilitate exfoliation of graphene from graphite in potentially act-

Abbreviations: 2D, two-dimensional; 3D, three dimensional; FITC, fluorescein isothiocyanate; TEM, transmission electron microscopy; AFM, atomic force microscopy; SEM, scanning electron microscopy; ESI, electronic supplementary information.

* Corresponding authors. Fax: +61 8 8201 2905.
E-mail addresses: haniff.wahid@flinders.edu.au (M. Haniff Wahid), uwe.stroeher@flinders.edu.au (U.H. Stroeher), ela.eroglu@uwa.edu.au (E. Eroglu), xianjue.chen@flinders.edu.au (X. Chen), kasturi.vimalanthan@flinders.edu.au (K. Vimalanathan), colin.raston@flinders.edu.au (C.L. Raston), ramiz.boulos@flinders.edu.au (R.A. Boulos).

http://dx.doi.org/10.1016/j.jcis.2014.11.043
0021-9797/

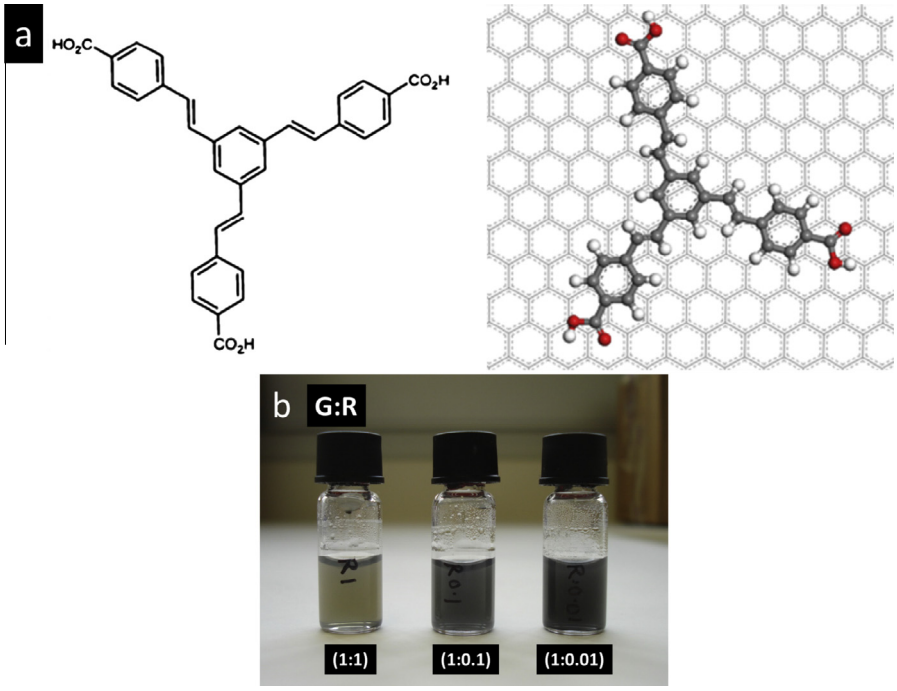

Fig. 1. (a) Structure of Ramizol® (1,3,5-tris[(1E)-2′-(4′-benzoic acid) vinyl]benzene and a molecular dynamic simulation of it on the surface of graphene (ESI-S1). (b) Photograph of solutions derived from sonication of mixtures of different ratios of graphite and Ramizol® in water (G:R).

ing as a molecular 'wedge' during sonication (Fig. 1 and ESI-S1), where the graphene sheets are prized apart. Such a process during sonication is likely to result in the exfoliation of graphene in water, as a related process to that established in the exfoliation of graphene in the presence of *p*-phosphonic acid calix[8]arene [15] and pyrene derivatives [13,14,16]. The presence of the ionisable carboxylic groups on the pendant arms of Ramizol® renders the molecule soluble in water at pH > 7. Ramizol® also exhibits antioxidant properties, similar to α-tocopherol (vitamin E), as a standard antioxidant [22], adding to its potent antimicrobial activity.

Functionalizing graphene with a biological active molecule is a design strategy for greater efficacy, noting composite nanomaterials are gaining prominence in applications in medicine [26–28]. Graphene and its derivative, namely graphene oxide, exhibit antibacterial property towards the Gram-negative bacteria, *Escherichia coli*, where it effectively cuts through the cell membrane of the bacteria releasing phospholipids, resulting in death of the bacteria [7]. In addition, composite materials of graphene, or graphene oxide with silver nanoparticles, and glutaraldehyde, are effective in killing *E. coli* and Gram-positive bacteria, *Staphylococcus aureus* [29–31]. More recently a composite of graphene oxide and curcumin has been developed for cancer therapy [32]. However, despite graphene oxide being more favourable for many applications because of its colloidal stability in aqueous media, the presence of oxygen containing functional groups on its surface is a concern for biomedical applications [33]. Administration of graphene oxide into the lungs of mice results in severe and persistent lung injury [33]. In addition, graphene oxide increases the rate of mitochondrial respiration and the generation of reactive oxygen species, activating inflammatory and apoptotic pathways of the cells. This is in contrast to pristine graphene which has minimal toxicity, which is reduced further by coating and stabilising the graphene with block copolymer Pluronic [33]. Overall, the use of graphene in biomedical applications is advancing, for example, in the development of biocompatible graphene-based antibacterial paper [8].

We have established the facile exfoliation and stabilisation of graphene sheets in water at pH 10 by non-covalent functionalisa-

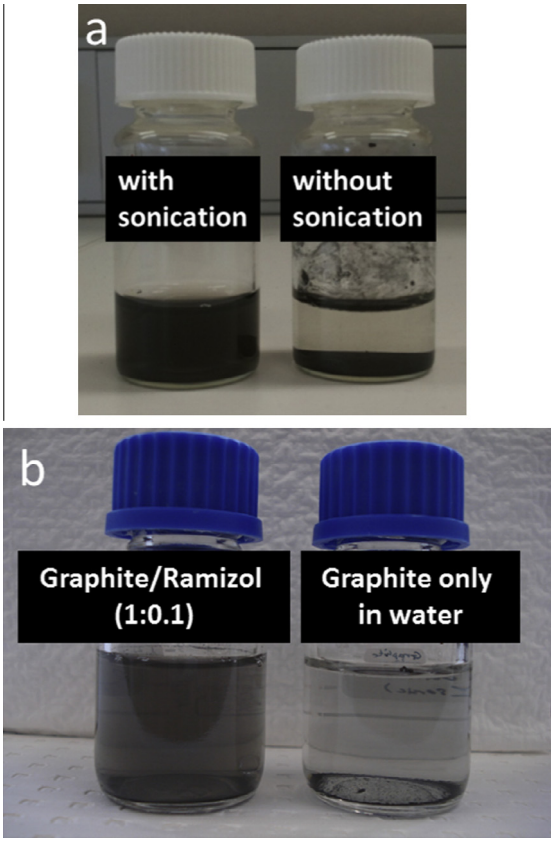

Fig. 2. (a) Graphene/Ramizol® sample at the initial graphite to Ramizol® ratio, G:R (1:0.1) produced after sonication (image on the left) and a control sample prepared with the same starting material without sonication (image on the right). Sonication was carried out following the reported procedure, and the sample prepared without sonication involved manual shaking and left overnight, and (b) Photograph image of graphite in water, in the presence and absence of Ramizol®. Samples were sonicated following the described procedure and left overnight. In the case where no Ramizol® is present, any exfoliation is followed by rapid restacking.

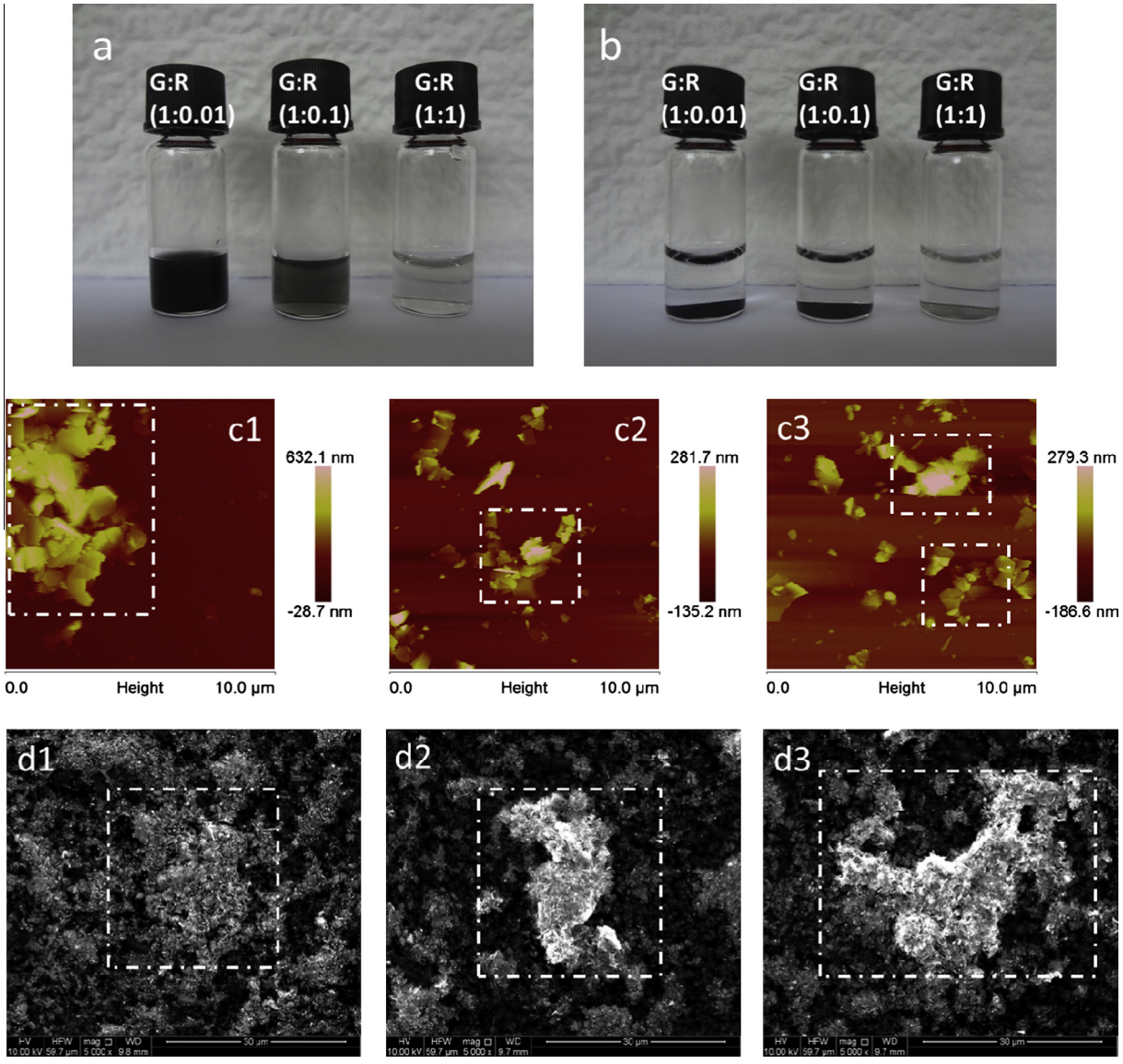

Fig. 3. Photograph images of stabilised graphene/Ramizol® solutions, (a) before addition of aqueous NaOH (1 M), and (b) after the addition followed by mild sonication and centrifugation. AFM (c1-3) and SEM (d1-3) images at different regions of graphene/Ramizol® sample (initial graphite to Ramizol® ratio, G:R (1:0.1)) upon addition of NaOH followed by mild sonication and centrifugation. Rectangular dotted loops show formation of aggregates of restacked graphene sheets.

tion with Ramizol®, with the resulting graphene/Ramizol® hybrid material exhibiting antibacterial properties. The exfoliated material is stable for more than 1 month, and unlike covalently functionalised graphene, the extended π conjugation on the graphene surface is maintained, and thus the electrical properties of the 2D sheets is preserved [34]. Interestingly Ramizol® is also fluorescent [21,22] and this was useful in terms of characterisation of the composite materials with graphene. From the perspective of drug delivery, the non-covalent functionalised graphene provides a platform for high drug loading and controlled release of the drug [26,35], with antimicrobial and antioxidant activity. Apart from acting as a drug carrier, graphene and multi-layer graphene can also impart mechanical stability, thermal conductivity [36] and flame retardant properties [37] which are promising for widespread applications.

2. Experimental section

2.1. Materials

Ramizol® was synthesised following the literature procedure with minor changes to the method [38]. Ethyl acetate (20%) in hexane was used for monitoring the progress of the Heck cross coupling reaction between 1,3,5-tribromobenzene and ethyl 4-vinylbenzoate, using TLC and 20:80 ethyl acetate–dichloromethane for eluting the product. Purification of the final product from the saponification reaction involved column chromatography using a 20:80 methanol–tetrahydrofuran solvent system, followed by the addition of diethyl ether as an anti-solvent to wash the product [38]. Graphite flakes (99%, particle size 7–10 µm in lineal dimension of the planar flakes) were purchased from Alfa Aesar and used as received.

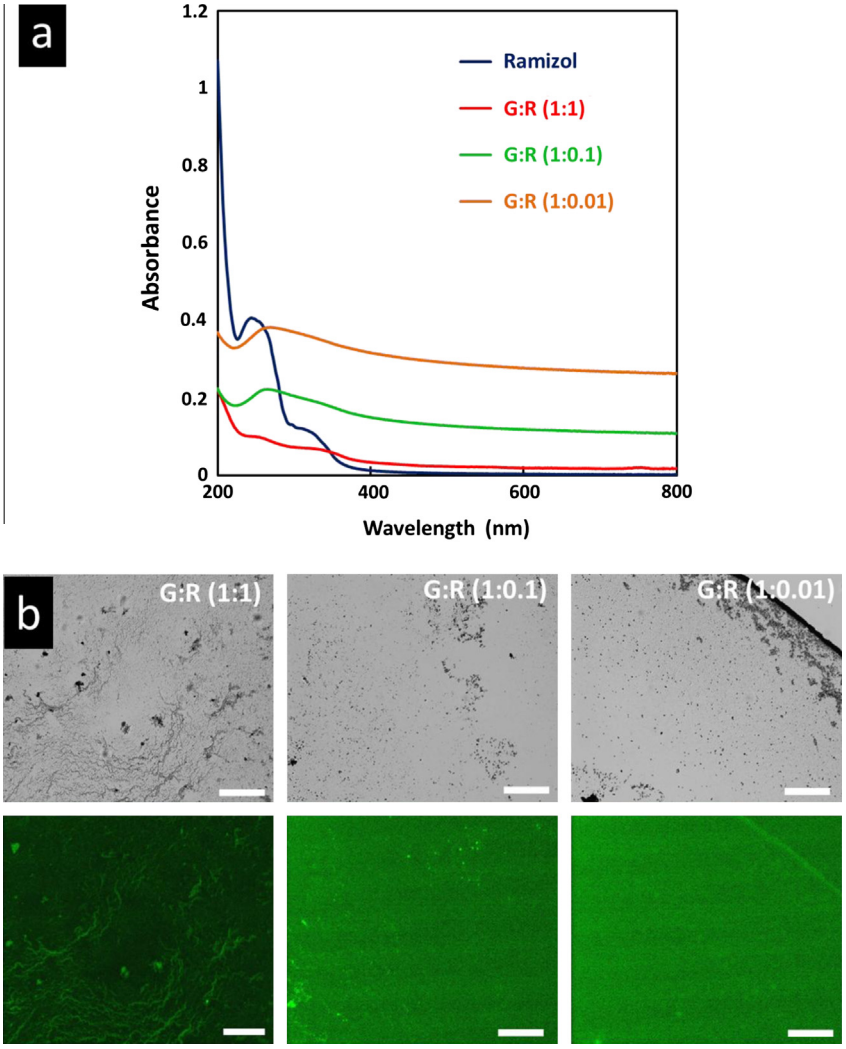

Fig. 4. (a) UV–visible spectra of Ramizol® and graphene/Ramizol® composites at different ratios of graphite to Ramizol® (G:R) after centrifugal washing and redispersing in Milli-Q water. (b) Bright field image (top row) of Ramizol® functionalised graphene and the corresponding fluorescence microscopy images (bottom row) at different w/w ratios of G:R (1:1), (1:0.1) and (1:0.01), respectively. (Scale bar: 100 μm).

2.2. Sample preparation

Ramizol® was dissolved in Milli-Q water at a concentration of 0.1 mg mL^{-1} after the addition of 0.1 M NaOH, such that the final pH of the solution was 10, noting Ramizol® has limited solubility at pH $\leqslant$ 7. Graphite flakes were added to the solution at a weight to weight (w/w) ratio of graphite to Ramizol® (G:R) of 1:1, 1:0.1 and 1:0.01 in a total of 20 mL of 0.1 mg mL^{-1} Ramizol® solution (ESI-S2). The graphite–Ramizol® mixtures were then ultrasonicated using a Sonics Vibra Cell ultrasonic liquid processor (130 Watt, 20 kHz) at 50% of the amplitude for 2 h, whereupon they were centrifuged at 453*g* for 30 min to remove residual graphite flakes. Excess Ramizol® in the processed solution was removed from each reaction mixture by centrifugal washing with Milli-Q water at 18,730*g* for 30 min. The final isolated mixture containing the exfoliated graphene sheets was redispersed in Milli-Q water, initially for characterisation purposes.

2.3. Characterisation

UV–Vis spectra of the samples were recorded using a Varian Cary 50 Bio UV/visible spectrophotometer. Raman spectra were acquired using a WITec alpha300R confocal Raman microscope at 532 nm excitation wavelength. Transmission electron microscopy

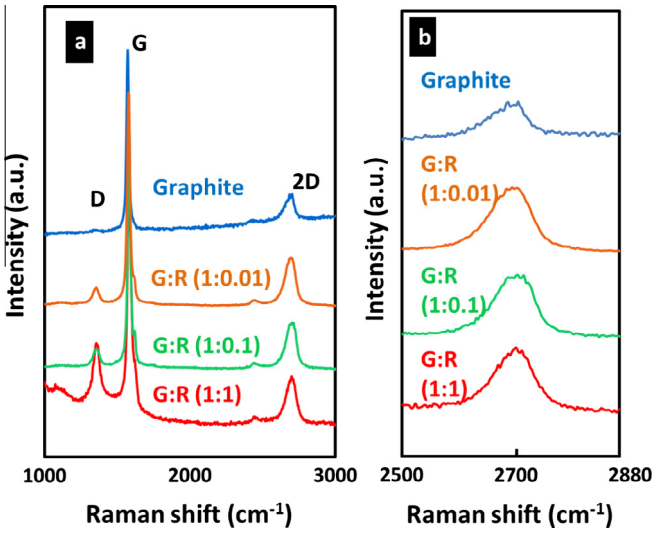

Fig. 5. (a) Raman spectra at 532 nm of graphite flakes and graphene/Ramizol® composites at different ratios of graphite to Ramizol® (G:R). Dotted loops indicate a shoulder at 1900 cm^{-1}, and (b) comparison of scaled 2D band of the samples.

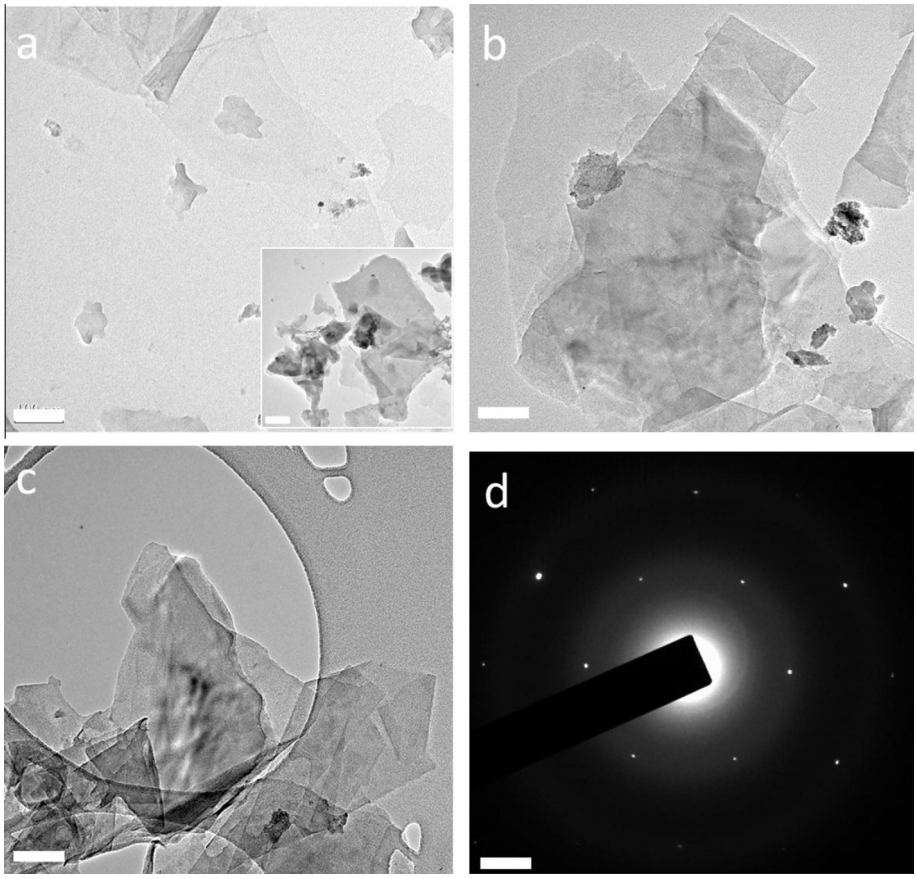

Fig. 6. TEM images of graphene sheets prepared at different w/w ratios of graphite to Ramizol® (G:R). (a) 1:1. The inset TEM image shows significant traces of Ramizol® observed on graphene sheets from different area of the sample (b) 1:0.1 and (c) 1:0.01, and (d) electron diffraction pattern of a selected area in sample (c) (Scale bar: 100 nm).

(TEM) characterisation was carried out using the JEOL 2100 instrument operating at 120 kV. Atomic force microscopy (AFM) analysis in tapping mode was performed with a multimode AFM head and a NanoScope V controller (Digital Instruments, Veeco, Santa Barbra, USA) in ambient conditions. Scanning electron microscopy (SEM) analysis was performed on the FEI Quanta 450, with high voltage, 10 kV, and working distance, 10 mm. Antibacterial activity of graphene/Ramizol® against *S. aureus* was investigated by monitoring the cell density by optical density measurements at 600 nm for a period of 20 h.

3. Results and discussion

Ultrasonic mechanoenergy applied for 2 h to the mixture of graphite and Ramizol® in water results in the exfoliation of graphite into multiple layers of graphene, affording a stable grey suspension, for all graphene:Ramizol® ratios (Fig. 1b). It is noteworthy that sonic energy and Ramizol® are both necessary for the exfoliation of graphene sheets. As shown in Fig. 2, the use of Ramizol® in the absence of the sonic energy (Fig. 2a) or the use of sonic energy in the absence of Ramizol® (Fig. 2b), no exfoliation and graphene stabilisation occurred. The yield of exfoliated graphene sheets was determined by weighing the remaining graphite sediments after sonication, and subtracting it from the weight of initial graphite. This establishes an average yield of between 40% and 50% yield for G:R at 1:1 and 1:0.1, whereas for G:R 1:0.01 the yield was ca. 10%, presumably because of insufficient Ramizol® for effective graphene exfoliation and stabilisation of the colloidal particles. For the same ratio, increasing the concentration of Ramizol® to 0.15 mg mL^{-1} resulted in a modest 4% increment in yield. Despite the high yields obtained for higher ratios, the thickness of graphene sheets obtained varied for different concentrations of Ramizol®. Importantly excess Ramizol® can be recovered and reused which is an advantage of using this processing method. A simple test to affirm that Ramizol® is non-covalently attached to at least the flat surface of the graphene, involved adding 0.1 mL of 1 M NaOH to 0.5 mL of the resulting solution, followed by mild sonication. This resulted in sedimentation of graphite following centrifugation at 453g, which is consistent with restacking of the previously stabilised colloidal solutions of graphene (Fig. 3). The formation of aggregates of restacked sheets due to the hydrophobic nature of graphite was verified using AFM and SEM (Fig. 3c and d).

Ultraviolet (UV)–visible spectra of the graphene/Ramizol® composites are shown in Fig. 4a. Pure Ramizol® (blue)[1] shows strong absorption peaks at ~250 nm and ~320 nm which are weak for G:R 1:1 sample (red). For G:R 1:0.1 (light green) and G:R 1:0.01 (orange), the absorption peak of graphene at ~260 nm [39] is present which is consistent with the higher graphene to drug ratio. The effect of different graphene to Ramizol® ratios is also evident for fluorescence microscopy under FITC filters; green coloured regions represent Ramizol® within the sample (Fig. 4b). For samples containing higher Ramizol® content, the contrast was clearer due to a higher drug concentration on the surface of graphene sheets (Fig. 4b).

Raman spectra of the graphene-containing samples were recorded using a 532 nm laser excitation wavelength, Fig. 5. The prominent features of graphite/graphene are the G (~1580 cm^{-1}),

[1] For interpretation of color in Fig. 4, the reader is referred to the web version of this article.

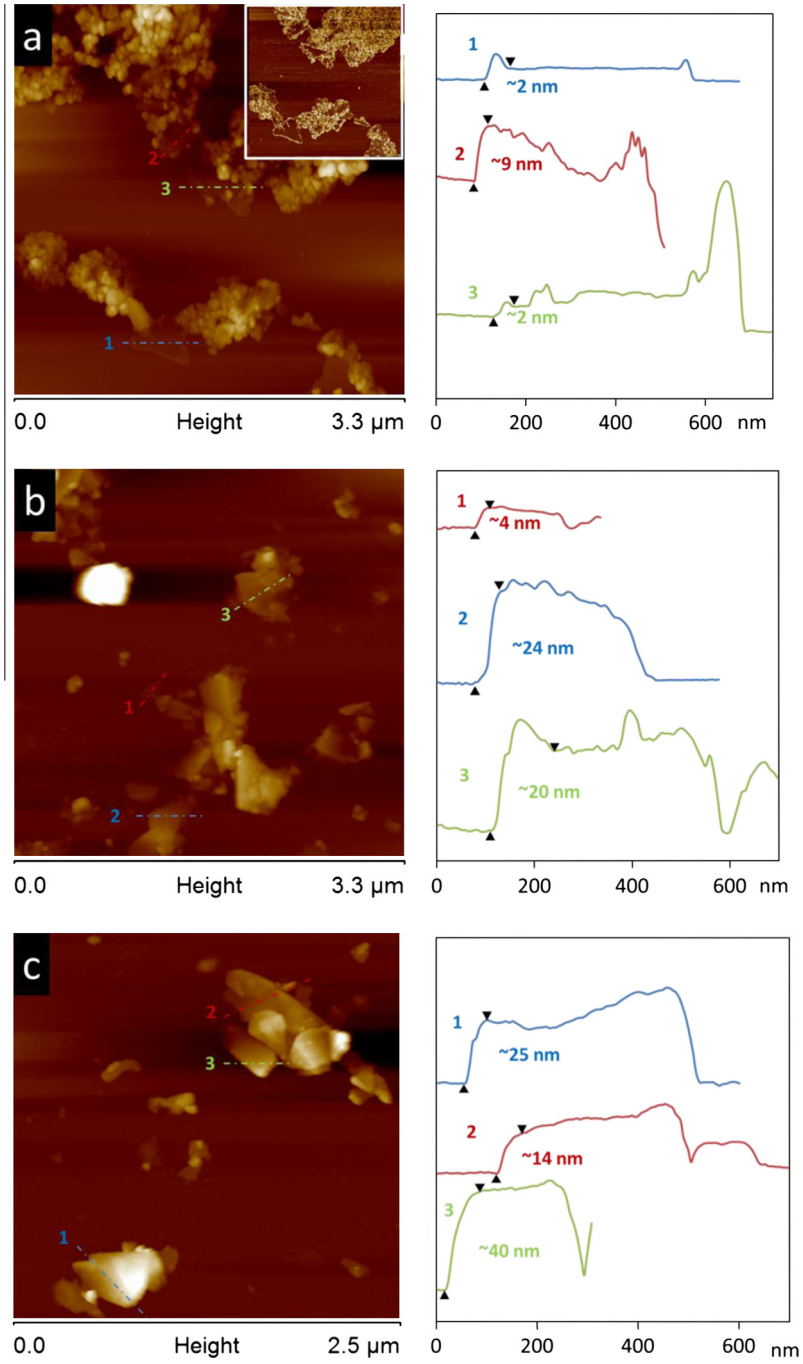

Fig. 7. AFM height images of graphene/Ramizol® G:R (1:1) (a) with phase image in the inset, (1:0.1) (b), and (1:0.01) (c), respectively.

D (~1350 cm^{-1}) and 2D (~2700 cm^{-1}) bands [40], which are clearly observed for all samples. The D band represents graphitic disorder which is likely due to the edge effect and also structural defects introduced to graphene during the sonication process [15,40]. The integrated intensity ratio, I_D/I_G for the D and G band, which is a measure of graphene defects [41], is higher for samples with a lower graphite concentration most likely due to smaller quantity of graphite being exposed to the sonic energy leading to deformation compared to graphite at a higher concentration. A small shoulder at 1900 cm^{-1} can be attributed to the presence of Ramizol® and/or partial oxidation of graphene arising from the sonication [15]. The 2D band profiles, Fig. 5b, shows the composite materials have narrower peaks compared to graphite, which is consistent with the few layers of graphene, as expected [40]. Raman spectra of graphene sheets composed of 5 layers or more are harder to distinguish from bulk graphite [40] and consequently transmission electron microscopy (TEM), atomic force microscopy (AFM) and scanning electron microscopy (SEM) were used as complementary tools to investigate the thickness of the sheets in such samples.

TEM images of the final product revealed few layers of graphene sheets with clear traces of Ramizol®, particularly for G:R 1:1, Fig. 6a, which corresponds to the highest loading of the compound. For G:R 1:1, the graphene sheets are more transparent compared to the other samples. For lower ratio of Ramizol®, i.e. G:R 1:0.1, and G:R 1:0.01, possible partial restacking during sonication is evident

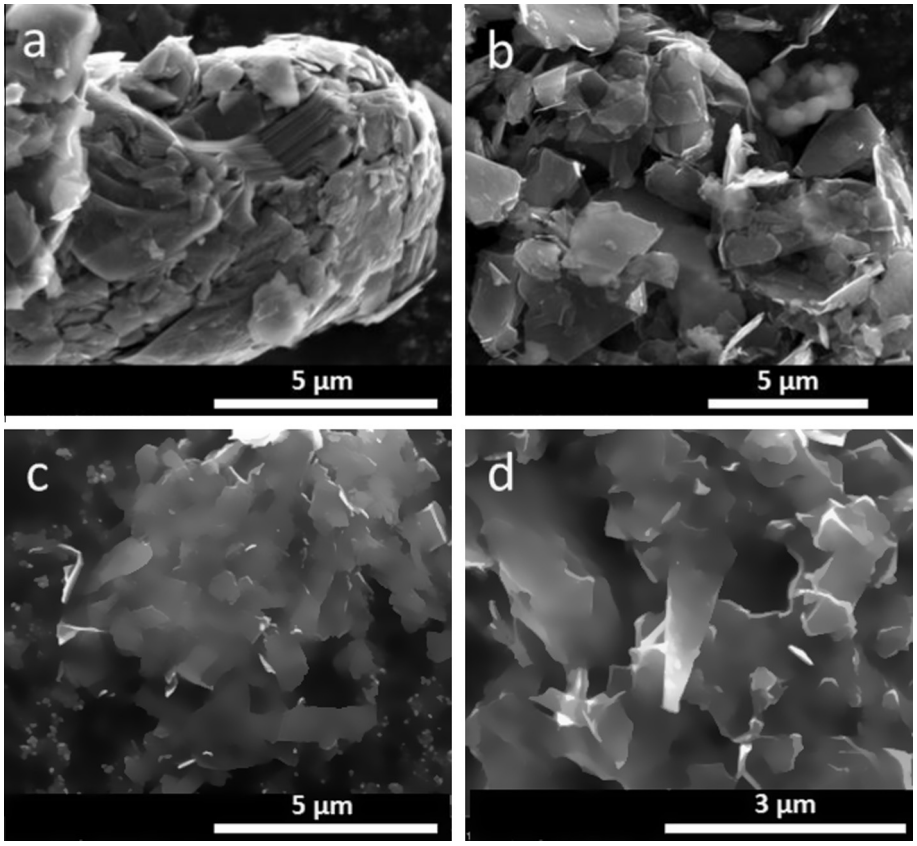

Fig. 8. SEM images of (a) pristine graphite and graphene/Ramizol® samples; (b) G:R (1:1), (c) G:R (1:0.1) and (d) G:R (1:0.01) respectively (scale bar: 5 µm).

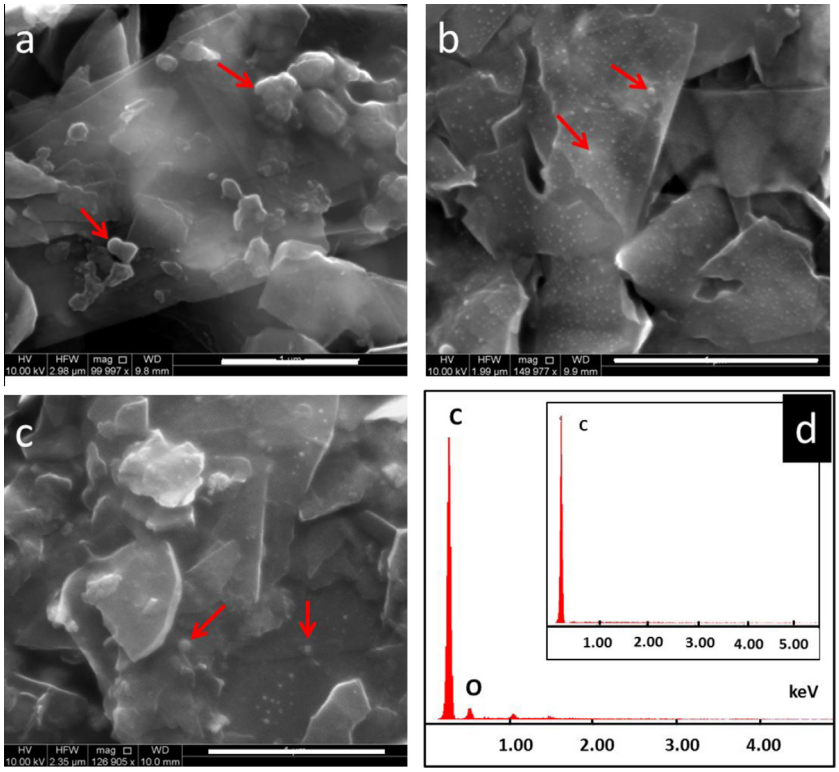

Fig. 9. SEM images of graphene/Ramizol®, G:R (a) 1:1, (b) 1:0.1 and (c) 1:0.01, and (d) EDS analysis of lumpy sites in (a) and inset image showing EDS analysis on a clear surface for comparison. Red arrows indicating lumpy features on graphene sheets (scale bar: 1 µm). (For interpretation of the references to colour in this figure legend, the reader is referred to the web version of this article.)

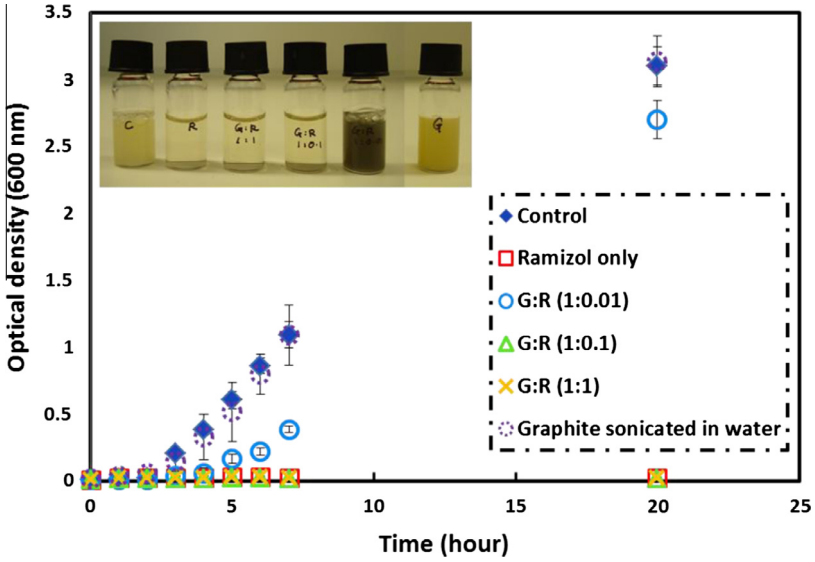

Fig. 10. Bacterial growth monitoring by optical density measurements at 600 nm for pure Ramizol®, pure graphite sonicated in water and graphene/Ramizol® composites of *S. aureus* in Mueller–Hinton media over a period of 20 h. Inset photograph shows image of samples after incubation for 20 h. First image on the left is bacteria only in media followed by pure Ramizol®, G:R 1:1, G:R 1:0.1, G:R 1:0.01 and ultrasonicated graphite in water with bacteria in media, respectively.

by the presence of randomly stacked arrays, on the basis that a lower relative amount of Ramizol® is present to assist the exfoliation and stabilisation of graphene sheets. Electron diffraction of a selected area in Fig. 6c displays the typical six-fold symmetry expected for graphite/graphene structure, Fig. 6d. Sonication in water alone without any surfactant (Ramizol®) is significantly less effective in forming thin graphene sheets (Fig. 2b). Overall, the presence of Ramizol® is important in stabilising the graphene against restacking.

AFM images using tapping mode revealed graphene sheets either partially or fully covered with Ramizol® which confirms the stabilising nature of the molecule, Fig. 7. This is particularly evident for G:R 1:1, where the presence of Ramizol® can be clearly observed in both height (Fig. 7a) and phase (inset of Fig. 7a) AFM images. In all samples, the exfoliated graphene sheets have lateral dimensions of several hundred nanometers to ~1 μm. However, the presence of Ramizol® made it difficult to determine the thickness of graphene sheets especially for G:R 1:1. For G:R 1:1, the graphene sheets are discernible with different thicknesses ranging from 2 nm to 10 nm which is consistent with the presence of a few layers of graphene sheets. The effect of different ratios of drug to graphite towards the yield of graphene is consistent with the results discussed above, i.e. thicker sheets are more prevalent as the amount of drug decreases. As expected, the presence of Ramizol® became less evident as the relative amount of compound decreased. Even though thin sheets (<5 nm) are present, thicker sheets (>20 nm) are common (Fig. 7b and c). Interestingly, some sheets have a higher height profile at the periphery compared to the centre and this is possibly due to the multi-layered stacking of drug molecules at the edges of the sheets which is in accord with computational energy minimisation studies (ESI-S3).

SEM was used to explore the surface decoration of graphene with Ramizol®. Even without coating, clear images can still be observed which indicates that the effect of exfoliation process on the electrical conductivity of graphene is minimal (Figs. 8 and 9). The difference in thickness of the sheets after exfoliation in the presence of Ramizol® is also significantly different to that of bulk pristine graphite (Fig. 8). SEM results are consistent with the TEM and AFM analyses, where at G:R 1:1, Fig. 9a, Ramizol® is aggregated, with lumpy structural features. However, aggregation becomes less evident for G:R 1:0.1 and G:R 1:0.01 where Ramizol® is present as small particles, ~2 nm in height based on AFM analysis. Elemental analysis for sample shown in Fig. 6a using energy dispersive electron spectroscopy (EDS), shows the presence of oxygen and carbon peaks for the lumpy site which coincides with the elements in Ramizol® (Fig. 9d) whereas only carbon peak was observed for clear surface of the same sample (Fig. 9d inset).

The antibacterial property of the graphene/Ramizol® composite material was investigated using the model Gram-positive bacteria *S. aureus* (ESI-S4). Optical density of the samples in media containing *S. aureus* was monitored at 600 nm after every 1 h from 0 to 8 h followed by the final measurement after overnight incubation. Preliminary test results in Fig. 10 shows that effective bacterial growth inhibition was achieved with pure Ramizol®, G:R 1:1 and G:R 1:0.1, whereas the antibacterial effect became less effective for higher graphene concentrations, i.e. G:R 1:0.01 and for graphite sonicated in water in the absence of Ramizol®, the bacteria growth was hardly affected. Noteworthy mentioning is that the concentration of graphite alone in water was the same for the starting amount of graphite in sample G:R 1:1 (0.1 mg mL^{-1}). The lack of efficacy is a direct result of the restacking of graphene sheets in water to afford graphite, which unlike graphene, does not have antibacterial properties (Fig. 2b). Results are consistent with the high affinity of the drug to graphite reducing its bioavailability, and the low yield of exfoliated graphene sheets as a result of a low drug:graphite ratio. Both factors affect the observed antibacterial activity and at low concentrations of Ramizol® and graphene, the antibacterial activity of the G:R 1:0.01 mixture is thus quenched. The inset image displays the mixtures after 20 h of incubation. For the control, a cloudy suspension is clearly observed which indicates uninhibited growth of the bacteria. With addition of Ramizol®, a clear suspension was obtained due to the antibacterial effect which inhibits the growth of the bacteria. This was also observed for G:R 1:1 and G:R 1:0.1. However for G:R 1:0.01 and pure graphite sample a cloudy suspension was observed which suggests a lower antibacterial activity in this mixture.

4. Conclusion

Facile graphene exfoliation in water was successful in the presence of Ramizol® under sonication. The composite material incorporates the remarkable properties of graphene and Ramizol®, with

the latter being an antimicrobial and an antioxidant agent. This material has potential for developing wound dressing materials where graphene functions as a drug carrier as well as to impart toughness to the material. In addition this material may also be used for antibacterial coatings or other biomedical applications.

Acknowledgments

We gratefully acknowledge support of this work by the Australian Research Council, the National Health and Medical Research Council and the Government of South Australia. TEM, SEM and AFM studies were carried out using facilities in the Centre for Microscopy, Characterisation and Analysis, The University of Western Australia and Flinders University, supported by the Australian Microscopy and Microanalysis Research Facility. M.H. Wahid would like to thank the Malaysian Government and University Putra Malaysia for the Ph.D. research funding.

Appendix A. Supplementary material

Supplementary data associated with this article can be found, in the online version, at http://dx.doi.org/10.1016/j.jcis.2014.11.043.

References

[1] A.K. Geim, Science 324 (2009) 1530–1534.
[2] J.C. Meyer, A. K Geim, M.I. Katsnelson, K.S. Novoselov, T.J. Booth, S. Roth, Nature 446 (2007) 60–63.
[3] M.J. Allen, V.C. Tung, R.B. Kaner, Chem. Rev. 110 (2010) 132–145.
[4] K.R. Paton, E. Varrla, C. Backes, R.J. Smith, U. Khan, A. O'Neill, C. Boland, M. Lotya, O.M. Istrate, P. King, T. Higgins, S. Barwich, P. May, P. Puczkarski, I. Ahmed, M. Moebius, H. Pettersson, E. Long, J. Coelho, S.E. O'Brien, E.K. McGuire, B.M. Sanchez, G.S. Duesberg, N. McEvoy, T.J. Pennycook, C. Downing, A. Crossley, V. Nicolosi, J.N. Coleman, Nat. Mater. 13 (2014) 624–630.
[5] X. Yang, J. Zhu, L. Qiu, D. Li, Adv. Mater. 23 (2011) 2833–2838.
[6] R. Zacharia, H. Ulbricht, T. Hertel, Phys. Rev. B 69 (2004) 155406.
[7] Y. Tu, M. Lv, P. Xiu, T. Huynh, M. Zhang, M. Castelli, Z. Liu, Q. Huang, C. Fan, H. Fang, R. Zhou, Nat. Nanotechnol. 8 (2013) 594–601.
[8] W. Hu, C. Peng, W. Luo, M. Lv, X. Li, D. Li, Q. Huang, C. Fan, ACS Nano 4 (2010) 4317–4323.
[9] A. Reina, X. Jia, J. Ho, D. Nezich, H. Son, V. Bulovic, M.S. Dresselhaus, J. Kong, Nano Lett. 9 (2009) 30–35.
[10] S. Stankovich, D.A. Dikin, R.D. Piner, K.A. Kohlhaas, A. Kleinhammes, Y. Jia, Y. Wu, S.T. Nguyen, R.S. Ruoff, Carbon 45 (2007) 1558–1565.
[11] K.S. Novoselov, A.K. Geim, S.V. Morozov, D. Jiang, Y. Zhang, S.V. Dubonos, I.V. Grigorieva, A.A. Firsov, Science 306 (2004) 666–669.
[12] Y. Hernandez, V. Nicolosi, M. Lotya, F.M. Blighe, Z. Sun, S. De, I.T. McGovern, B. Holland, M. Byrne, Y.K. Gun'Ko, J.J. Boland, P. Niraj, G. Duesberg, S. Krishnamurthy, R. Goodhue, J. Hutchison, V. Scardaci, A.C. Ferrari, J.N. Coleman, Nat. Nanotechnol. 3 (2008) 563–568.
[13] M. Zhang, R.R. Parajuli, D. Mastrogiovanni, B. Dai, P. Lo, W. Cheung, R. Brukh, P.L. Chiu, T. Zhau, Z. Liu, E. Garfunkel, H. He, Small 6 (2010) 1100–1107.
[14] D.-W. Lee, T. Kim, M. Lee, Chem. Commun. 47 (2011) 8259–8261.
[15] X. Chen, R.A. Boulos, P.K. Eggers, C.L. Raston, Chem. Commun. 48 (2012) 11407–11409.
[16] F. Zhang, X. Chen, R.A. Boulos, F.M. Yasin, H. Lu, C.L. Raston, H. Zhang, Chem. Commun. 49 (2013) 4845–4847.
[17] N. Behabtu, J.R. Lomeda, M.J. Green, A.L. Higginbotham, A. Sinitskii, D.V. Kosynkin, D. Tsentalovich, A.N.G. ParraVasquez, J. Schmidt, E. Kesselman, Y. Cohen, Y. Talmon, J.M. Tour, M. Pasquali, Nat. Nanotechnol. 5 (2010) 406–411.
[18] X. Chen, J.F. Dobson, C.L. Raston, Chem. Commun. 48 (2012) 3703.
[19] M.H. Wahid, E. Eroglu, X. Chen, S.M. Smith, C.L. Raston, Green Chem. 15 (2013) 650–655.
[20] R.A. Boulos, A. Van Leeuw, J. Microb. 104 (2013) 155–167.
[21] R.A. Boulos, E. Eroglu, X. Chen, A. Scaffidi, B.R. Edwards, J. Toster, C.L. Raston, Green Chem. 15 (2013) 1268–1273.
[22] E. James, H. Viola, L. Hool, P.K. Eggers, C.L. Raston, R.A. Boulos, RSC Adv. 3 (2013) 7277.
[23] K.S. Suslick, Y. Didenko, M.M. Fang, T. Hyeon, K.J. Kolback, W.B. McNamara III, M.M. Mdleleni, M. Wong, Philos. Trans. R. Soc. London A. 357 (1999) 335–353.
[24] A. Esmaeili, M.H. Entezari, J. Colloid Interface Sci. 432 (2014) 19–25.
[25] A. Ciesielski, P. Samori, Chem. Soc. Rev. 43 (2014) 381–398.
[26] X. Yang, X. Zhang, Z. Liu, Y. Ma, Y. Huang, Y. Chen, J. Phys. Chem. C 112 (2008) 17554–17558.
[27] K. Yang, S. Zhang, G. Zhang, X. Sun, S.-T. Lee, Z. Liu, Nano Lett. 10 (2010) 3318–3323.
[28] J. Yao, Y. Sun, M. Yang, Y. Duan, J. Mater. Chem. 22 (2012) 14313.
[29] J. Tang, Q. Chen, L. Xu, S. Zhang, L. Feng, L. Cheng, H. Xu, Z. Liu, R. Peng, ACS Appl. Mater. Interfaces 5 (2013) 3867–3874.
[30] M-C. Wu, A.R. Deokar, J-H. Liao, P-Y. Shih, Y-C. Ling, ACS Nano 7 (2013).
[31] B. Jiang, C. Tian, G. Song, W. Chang, G. Wang, Q. Wu, H. Fu, J. Mater. Sci. 48 (2013) 1980–1985.
[32] S. Some, A-R. Gwon, E. Hwang, G-H. Bahn, Y. Yun, Y. Kim, S-H. Kim, S. Bak, J. Yang, D-G. Jo, H. Lee, Sci. Rep. 4 (2014) 6314.
[33] M.C. Duch, G.R.S. Budinger, Y.T. Liang, S. Soberanes, D. Urich, S.E. Chiarella, L.A. Campochiaro, A. Gonzalez, N.S. Chandel, M.C. Hersam, G.M. Mutlu, Nano Lett. 11 (2011) 5201–5207.
[34] K.P. Loh, Q. Bao, P.K. Ang, J. Yang, J. Mater. Chem. 20 (2010) 2277–2289.
[35] D. Depan, J. Shah, R.D.K. Misra, Mater. Sci. Eng. C 31 (2011) 1305–1312.
[36] K.M.F. Shahil, A.A. Balandin, Nano Lett. 12 (2012) 861–867.
[37] B. Dittrich, K-A. Wartig, D. Hoffman, R. Mulhaupt, B. Schartel, Polym. Degrad. Stabil. 98 (2013) 1495–1505.
[38] N.A. Lengkeek, R.A. Boulos, A.J. McKinley, T.V. Riley, B. Martinac, S.G. Stewart, Aust. J. Chem. 64 (2011) 316–323.
[39] G. Wang, X. Shen, J. Yao, J. Park, Carbon 47 (2009) 2049–2053.
[40] A.C. Ferrari, J.C. Meyer, C. Casiraghi, M. Lazzeri, F. Mauri, S. Piscanec, D. Jiang, K.S. Novoselov, S. Roth, A.K. Geim, Phys. Rev. Lett. 97 (2006) 187401.
[41] M.A. Pimenta, G. Dresselhaus, M.S. Dresselhaus, L.G. Cancado, A. Jorio, R. Saito, Phys. Chem. Chem. Phys. 9 (2007) 1276–1291.

RSC Advances

COMMUNICATION

View Article Online
View Journal | View Issue

Cite this: *RSC Adv.*, 2014, **4**, 48348

Received 21st August 2014
Accepted 19th September 2014

DOI: 10.1039/c4ra09000d

www.rsc.org/advances

Nitrate uptake by *p*-phosphonic acid or *p*-(trimethylammonium)methyl calix[8]arene stablized laminar materials†

Paul K. Eggers,[ab] Ela Eroglu,[ac] Thomas Becker,[d] Xianjue Chen,[b] Kasturi Vimalanathan,[b] Keith A. Stubbs,[a] Steven M. Smith[ac] and Colin L. Raston*[b]

Graphite, BN, MoS_2 and WS_2 are readily exfoliated using probe sonication in the presence of *p*-(trimethylammonium)methyl-calix[8]arene resulting in few-layer laminar material. The positively charged material is effective in the removal of nitrate ions from waste effluent, as is the negatively charged corresponding material stablized by partially deprotonated *p*-phosphonic acid calix[8]arene, with scope for efficient recycling.

Two-dimensional (2D) materials such as graphene, hexagonal boron nitride (BN), molybdenum disulfide (MoS_2) and tungsten disulfide (WS_2) are gaining attention in biotechnology.[1–4] This is largely due to the development of improved methods of producing single sheets of these materials, allowing their novel properties to be elucidated and exploited. One such method uses sonic energy in the presence of *p*-phosphonic acid calix[8]-arene to exfoliate and stabilise the 2D materials in aqueous solutions.[5] The resultant single- and few-layer 2D materials are stable for months over a range of pH values, taking on negative charge associated with partial deprotonation of the upper rim phosphonic acid groups. Hereafter, in making reference to these calixarenes, referring to them as the phosphonic acid species, it is implied that they will be partially deprotonated. We note that the *p*-phosphonic acid calix[8]arene and the family of such calix[*n*]arenes, $n = 4$, 5, 6 and 8, are non-toxic,[6] with demonstrated potential in drug delivery applications.[7–9] This is an important factor for any applications, both for environmental and health concerns.

p-(trimethylammonium)methyl calix[8]arene *p*-phosphonic acid calix[8]arene

Another advantage to this exfoliation method is that the *p*-phosphonic acid calix[8]arene is non-covalently bound to the 2D material, limiting potential defects arising from covalent bonding to graphene for solubilisation purposes, while providing points of nucleation and growth of nanoparticles such as palladium, platinum and ruthenium into ordered arrays.[10–12] Of interest to us is the ability of graphene exfoliated and stablized by the same calixarene using this methodology[5] to absorb nitrate ions from waste water.[13] In general, 2D materials are optimum candidates as molecular absorbents given that the exposed surface area of the materials is at the highest theoretically limit.

Nitrate removal from waste water is an important aspect of water treatment due to its hazardous effects on the environment and human health.[14,15] Excess nitrate can result in the formation of toxic algal blooms, in disrupting an already strained environment.[16,17] What is of particular interest is how the charge of the calixarene affects the exfoliation and stabilisation of 2D materials, as well as the ability of the exfoliated 2D material to remove nitrate ions from waste effluent. Herein we demonstrate that a positively charged *p*-(trimethylammonium)methyl-calix[8]arene can also facilitate the exfoliation of graphite, BN, MoS_2 and WS_2 and that the resulting suspension of the composite material, along with the previously synthesised negatively charged *p*-phosphonic acid calix[8]arene exfoliated materials,[5] can be effectively used to remove nitrate from waste effluent.

[a]*School of Chemistry and Biochemistry, The University of Western Australia, Crawley, WA 6009, Australia*

[b]*Centre for NanoScale Science and Technology, School of Chemical and Physical Sciences, Flinders University, Bedford Park, SA 5042, Australia. E-mail: colin.raston@flinders.edu.au*

[c]*ARC Centre of Excellence in Plant Energy Biology, The University of Western Australia, 35 Stirling Highway, Crawley, WA 6009, Australia*

[d]*Nanochemistry Research Institute, Curtin University, Kent Street, Bentley, Australia*

† Electronic supplementary information (ESI) available: AFM images of graphene, MoS_2, WS_2 and BN exfoliated with *p*-phosphonic acid calix[8]arene and the synthetic procedure for *p*-(trimethylammonium)methyl-calix[8]arene. See DOI: 10.1039/c4ra09000d

Fabrication and characterisation of the 2D materials

p-Phosphonic acid calix[8]arene was synthesised according to literature procedures.[18] *p*-(Trimethylammonium)methyl-calix[8]arene was synthesised by mixing calix[8]arene, formaldehyde, acetic acid and dimethylamine in dimethylformamide at room temperature for 24 hours to afford *p*-(dimethylamine)methyl-calix[8]arene followed by mixing with iodomethane in dimethylformamide at room temperature for 4 hours (ESI†).

The exfoliation method used in the present study has been described previously.[5,13] In the general experiment the 2D material (2 mg mL^{-1}) and the calix[8]arene (10 mg mL^{-1} *p*-phosphonic acid calix[8]arene or *p*-(trimethylammonium) methyl-calix[8]arene) was dispersed in Milli-Q water. The dispersion was then sonicated for 2 hours using a probe sonicator (150 W at 70% amplitude, Sonifier cell disruptor, Model SLPt, Branson Ultrasonics Corporation). The dispersion was centrifuged at 1500 × *g* for 30 minutes and the liquid removed, with the resulting solid redispersed in Milli-Q water (10 mL) and separated equally into six centrifuge tubes. These were centrifuged at 18 400 × *g* for 30 minutes and the liquid removed with the solid redispersed in the same volume of Milli-Q water. This last step was repeated 5 times on the six tubes to remove excess calix[8]arene. The dry masses in each tube tended to be very small and hence the weights had significant errors associated with them. For this reason all the measurements were compared as a process and not to a mass. The resulting dispersions are shown in Fig. 1.

The purification of the material by centrifugation partitions the different thickness of the laminar material with the initial low speed centrifugation removing the largely un-exfoliated material. At the other extreme, the high speed centrifugation partitions the calixarene and the highly aqueous stablized single-layer material in supernatant from the few-layer and lower aqueous stablized single sheet material in the pellet. This is evident from the initial high speed centrifugation, with the supernatant retaining the colour of the exfoliated 2D material. Some colour remains in the supernatant after each subsequent centrifugation washing step, with the intensity decreasing approximately exponentially through each subsequent centrifugation until it is difficult to discern after the final centrifugation. As a result the finally isolated exfoliated 2D materials for both the *p*-phosphonic acid and *p*-(trimethylammonium) methyl-calix[8]arenes are expected to be at most a few layers with a low concentration of single-layer sheets.

Exfoliation in the presence of *p*-phosphonic acid calix[8]arene has been described in a previous report,[5] with the AFM images establishing the thickness of graphene, BN, MoS_2 and WS_2 at 2 nm, 4 nm, 5 nm and 5 nm respectively. The exfoliation method described herein increases the concentration of calixarene used from the original method, but produces a similar thickness of materials for both the *p*-phosphonic acid calix[8]arene (ESI†) and the *p*-(trimethylammonium)methyl-calix[8]arene (Fig. 2). The presence of *p*-(trimethylammonium)methyl-calix[8]arene appears to result in a greater exfoliation efficiency than in the presence of *p*-phosphonic acid calix[8]arene under identical exfoliation conditions. Qualitative evidence supporting this are the images of the suspended material in Fig. 1, where the optical density of the *p*-(trimethylammonium) methyl-calix[8]arene exfoliated materials are higher than the *p*-phosphonic acid calix[8]arene exfoliated materials. It should be noted that the experiments in the present study were designed around identical exfoliation procedures to analyse the nitrate uptake of the various materials for exfoliation agents of different charge. Single-layer sheets are not necessarily ideal in this case. As noted in the purification method the single-layer sheets are likely to be extremely stable in aqueous solution and require more time and energy to separate from the excess calix[8]arene.

The transmission electron microscopy (TEM) images (Fig. 3) show a significant number of *p*-(trimethylammonium)methyl-

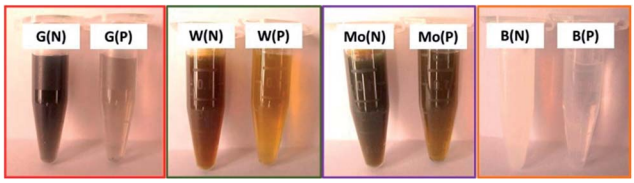

Fig. 1 Dispersions of the 2D exfoliated materials graphene (G), WS_2 (W), MoS_2 (Mo), and BN (B) exfoliated in the presence of either *p*-(trimethylammonium)methyl-calix[8]arene (N) or *p*-phosphonic acid calix[8]arene (P).

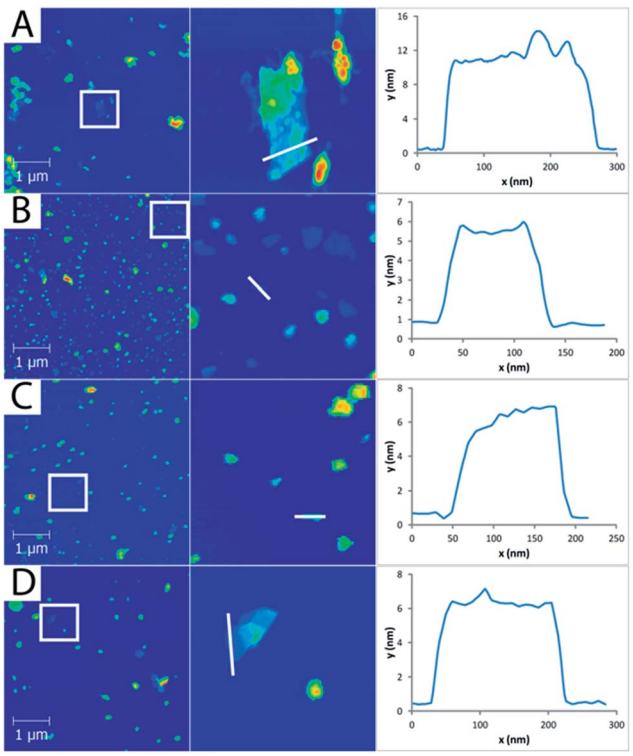

Fig. 2 Atomic force microscopy (AFM) images with 1 μm × 1 μm inset and line profile of 2D materials exfoliated with *p*-(trimethylammonium) methyl calix[8]arene. (A) Graphene, (B) MoS_2, (C) WS_2 and (D) BN.

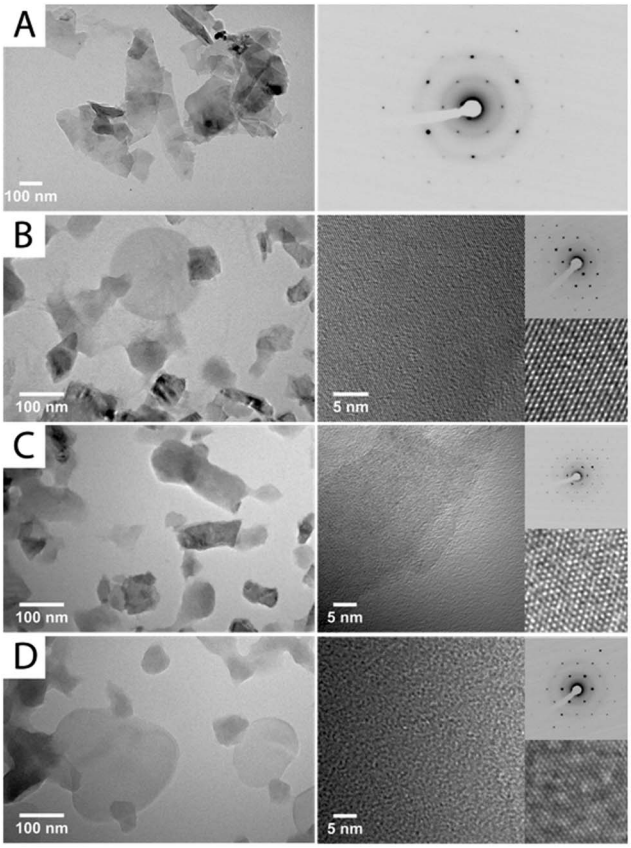

Fig. 3 TEM images with 5 nm × 5 nm inset and electron diffraction of 2D materials exfoliated with *p*-(trimethylammonium)methyl-calix[8]arene. (A) Graphene, (B) MoS_2, (C) WS_2 and (D) BN.

calix[8]arene exfoliated sheets from all 2D materials prepared. As in our previous report describing *p*-phosphonic acid calix[8]-arene exfoliated materials,[5] the TEM images in Fig. 3a–c show reduced widths of the sheets relative to the widths of the starting material, graphite, MoS_2 and WS_2 flakes, suggesting that the materials were fragmented in the exfoliation process. The fragmentation presumably arises from the high energy cavitation associated with sonication. The BN sheets do not appear to have undergone significant fragmentation, with the 2D material still retaining its original circular shape. As noted earlier, the lack of single-layer sheets observed in the AFM images may be due to the purification process. However, the electron diffraction and high resolution TEM images for all of the materials (Fig. 3) indicate that the exfoliated materials have a high degree of crystallinity. Thus, from the TEM and AFM images, it can be concluded that *p*-(trimethylammonium) methyl-calix[8]arene was effective in facilitating the exfoliation and stabilisation of graphene, BN, MoS_2 and WS_2 in water.

Nitrate removal

Removal of nitrate ions from effluent is legislated in many countries. According to the United States Environmental Protection Agency (EPA), the maximum level of nitrate-nitrogen [NO_3^--N] in drinking water is regulated so that it is below 10 mg L^{-1} (equivalent to approximately 45 mg L^{-1} as NO_3^-).[14,19] Nitrate-nitrogen [NO_3^--N] represents the amount of nitrogen (N) present in aqueous solutions yielding from nitrate ions (NO_3^-).[19] In the present study, nitrate uptake for the final mixtures of various 2D materials stablized by *p*-phosphonic acid calix[8]arene or *p*-(trimethylammonium)methyl-calix[8]arene was assessed. The final mixtures were diluted three times with Milli-Q water, centrifuged at 18 400 × *g* for 30 minutes and the majority of supernatant discarded. The remaining mixtures (0.25 mL) were then diluted with nitrate-containing aquatic effluent which is also composed of phosphates, carbonate buffer, vitamins, and some micronutrients (1.25 mL, pH 7.5).[20] The concentration of nitrate in the effluent was monitored at various time intervals (0, 3, 6, 12, 18 and 24 hours). Prior to nitrate analysis, each mixture was centrifuged at 18 400 × *g* for 30 minutes and the suspension-free supernatants were collected for spectrophotometric analysis.[21] The reusability of the materials for nitrate removal was tested after initially exposing the 2D materials to the effluent for 24 hours. The samples were then centrifuged at 18 400 × *g* for 30 minutes, the supernatant discarded, the solid re-dispersed in Milli-Q water and subjected to mild sonication (180 W) for 2.5 minutes.[13] These samples were then re-centrifuged at 18 400 × *g* for 30 minutes, the major part of the supernatant was then discarded (1.25 mL), and replaced with same amount of nitrate-containing aqueous media. This second cycle was analysed after exposure to the effluent for 24 hours following the same procedure as the first cycle.

For all eight of the laminar materials produced, regardless of which exfoliating compound was used, we observed a substantial amount of nitrate removal from the effluent media (Fig. 4). The WS_2 sample exfoliated with *p*-(trimethyl-ammonium)methyl-calix[8]arene (WN) had the highest removal at 66%, and removal by graphene and WS_2 exfoliated

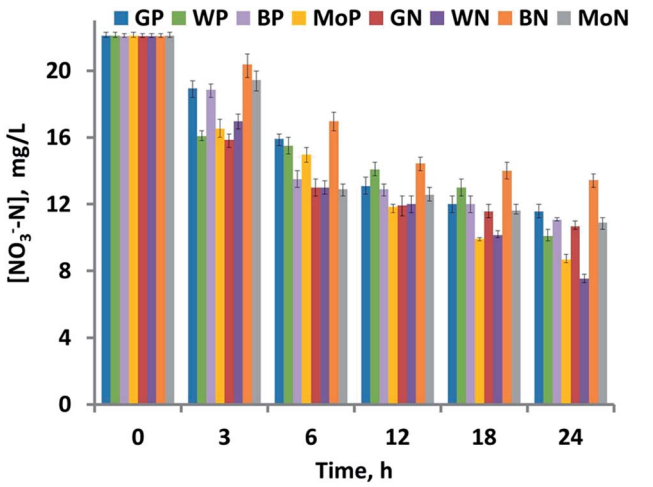

Fig. 4 Nitrate-nitrogen [NO_3^--N] content of liquid solution, exposed to various exfoliated laminar materials stablized by *p*-phosphonic acid calix[8]arene or *p*-(trimethylammonium)methyl-calix[8]arene, designated "P" and "N" respectively with G = graphene, W = WS_2, B = BN, Mo = MoS_2.

with *p*-(trimethylammonium)methyl-calix[8]arene were slightly more efficient than their *p*-phosphonic acid calix[8]arene exfoliated counterparts. Generally, the laminar materials exfoliated with *p*-(trimethylammonium)methyl-calix[8]arene reached higher nitrate removal rates within the first six hours of the experiment relative to *p*-phosphonic acid calix[8]arene exfoliated materials, with the exception of BN. The maximum nitrate removal efficiencies were consistent with our previous study of *p*-phosphonic acid calix[8]arene exfoliated graphene sheets reaching a maximum removal efficiency of 55.7% for different exfoliation conditions.[13]

The variations within the nitrate uptake are presumably related to the amount of exfoliated surfaces available, the functional groups of the calix[8]arenes and/or the manner in which the calix[8]arenes adsorb to the surface. As indicated by Fig. 1 and 5, the *p*-(trimethylammonium)methyl-calix[8]arene resulted in apparently greater exfoliation. Thus, given the difference in amount of material exfoliated and the differences in nitrate removal efficiencies, it would appear that the phosphonic acid calix[8]arene has a greater efficiency at nitrate removal per mass. This establishes that the negatively charged *p*-phosphonated calixarene is more effective at binding nitrate than the more electrostatically favoured trimethylammonium cation functionalised calixarene. However, the *p*-(trimethylammonium)methyl-calix[8]arene with WS_2 is the best material for nitrate removal as it yielded the lowest [NO_3^--N] concentration (7.5 mg L^{-1}) in the remaining effluent, under the same preparation procedures as for all other materials.

Nitrate removal efficiencies of these laminar materials after two consecutive cycles were also compared (Table 1). The recycling process was applied to the samples at a time-interval of 24 hours. These results indicate that all laminar materials were still effective for removing nitrate during their second cycle (Table 1), despite having a decrease in their removal efficiencies. Independent from its surface group, graphene was more stable in recycling than the other laminar materials, showing similar nitrate removal efficiencies for each consecutive cycle. In terms of overall nitrate removal efficiencies of two-consecutive cycles, MoP and WN gave the highest removal efficiencies of 53.2% and 51.8%, respectively.

Of interest in an industrial sense is that although these calixarene-exfoliated materials are stable for months prior to the addition of effluent, once the effluent is added the material begins to precipitate. We hypothesize that this may be the result of the nitrate ion acting as an intercalation agent between exfoliated sheets, creating a weak glue to bind the laminar sheets. Indeed, this precipitation of environmentally benign materials from effluent may be a viable method for lowering [NO_3^--N] content to below regulated concentrations.

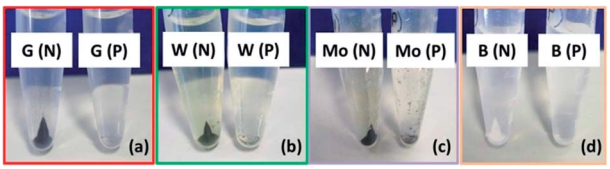

Fig. 5 Images of graphene (G), WS_2 (W), BN (B), MoS_2 (Mo) exfoliated by either *p*-phosphonated calix[8]arene (P) (G(P); W(P); B(P); Mo(P)) or *p*-(trimethylammonium)methyl-calix[8]arene (N) (G(N); W(N); B(N); Mo(N)) in a mixture with nitrate containing aqueous solution, followed by their centrifugation at 18 400 × *g* for 30 minutes.

Table 1 Nitrate-nitrogen [NO_3^--N] removal efficiencies of various laminar materials in two consecutive cycles using the same materials. The values represent the amount of nitrate-nitrogen [NO_3^--N] ions removed from solution (see Fig. 5 for abbreviations)

Sample	GP	GN	WP	WN	BP	BN	MoP	MoN
1st cycle (mg L^{-1})	10.6	11.0	11.5	14.0	11.5	9.0	13.5	10.5
2nd cycle (mg L^{-1})	9.5	8.5	6.5	8.8	4.9	6.6	9.9	8.0
Total (mg L^{-1})	20.1	19.5	18.0	22.8	16.4	15.6	23.4	18.5
Overall efficiency (%)	45.7	44.3	40.9	51.8	37.3	35.5	53.2	42.0

Conclusions

We have demonstrated the exfoliation of 2D materials from bulk materials with a positively charged calix[8]arene (*p*-(trimethylammonium)methyl-calix[8]arene). The synthesis is a simple two-step process from a known high yielding preparation of calix[8]arene. We have shown that laminar materials exfoliated with either positively charged or negatively charged calix[8]arenes were effective at removing nitrate from waste effluent, with WS_2 exfoliated in the presence of *p*-(trimethylammonium)methyl-calix[8]arene resulting in the highest decrease in nitrate content of the waste effluent. All materials show significant recyclability removing only slightly less nitrate after regeneration by mild sonication. One benefit of these abundant laminar earth minerals is they begin to precipitate after binding nitrate allowing a facile method of nitrate extraction.

Acknowledgements

We gratefully acknowledge the financial support of the Australian Research Council and the Government of South Australia. The TEM and AFM analyses were carried out in the Centre for Microscopy, Characterisation and Analysis at The University of Western Australia, and the Nanochemistry Research Institute at Curtin University, respectively.

Notes and references

1 Y. Wang, Z. Li, J. Wang, J. Li and Y. Lin, *Trends Biotechnol.*, 2011, **29**, 205–212.
2 K. Liu, J. Feng, A. Kis and A. Radenovic, *ACS Nano*, 2014, **8**, 2504–2511.
3 T. Lin, L. Zhong, Z. Song, L. Guo, H. Wu, Q. Guo, Y. Chen, F. Fu and G. Chen, *Biosens. Bioelectron.*, 2014, **62**, 302–307.
4 J. Wu and L. Yin, *ACS Appl. Mater. Interfaces*, 2011, **3**, 4354–4362.
5 X. Chen, R. A. Boulos, P. K. Eggers and C. L. Raston, *Chem. Commun.*, 2012, **48**, 11407–11409.

6 A. D. Martin, E. Houlihan, N. Morellini, P. K. Eggers, E. James, K. A. Stubbs, A. R. Harvey, M. Fitzgerald, C. L. Raston and S. A. Dunlop, *ChemPlusChem*, 2012, **77**, 308–313.
7 P. K. Eggers, T. Becker, M. K. Melvin, R. A. Boulos, E. James, N. Morellini, A. R. Harvey, S. A. Dunlop, M. Fitzgerald, K. A. Stubbs and C. L. Raston, *RSC Adv.*, 2012, **2**, 6250–6257.
8 E. James, P. K. Eggers, A. R. Harvey, S. A. Dunlop, M. Fitzgerald, K. A. Stubbs and C. L. Raston, *Org. Biomol. Chem.*, 2013, **11**, 6108–6112.
9 J. Mo, P. K. Eggers, C. L. Raston and L. Lim, *Anal. Bioanal. Chem.*, 2014, 1–9.
10 X. Chen, F. M. Yasin, P. K. Eggers, R. A. Boulos, X. Duan, R. N. Lamb, K. S. Iyer and C. L. Raston, *RSC Adv.*, 2013, **3**, 3213–3217.
11 X. Chen, W. Zang, K. Vimalanathan, K. S. Iyer and C. L. Raston, *Chem. Commun.*, 2013, **49**, 1160–1162.
12 X. Chen, K. Vimalanathan, W. Zang, A. D. Slattery, R. A. Boulos, C. T. Gibson and C. L. Raston, *Nanoscale*, 2014, **6**, 4517–4520.
13 E. Eroglu, W. Zang, P. K. Eggers, X. Chen, R. A. Boulos, M. H. Wahid, S. M. Smith and C. L. Raston, *Chem. Commun.*, 2013, **49**, 8172–8174.
14 EPA, *National Pesticide Survey: Project Summary*, U.S. Environmental Protection Agency, Washington D.C., 1990.
15 A. M. Fan, C. C. Willhite and S. A. Book, *Regul. Toxicol. Pharmacol.*, 1987, **7**, 135–148.
16 P. J. Thorburn, J. S. Biggs, K. L. Weier and B. A. Keating, *Agric., Ecosyst. Environ.*, 2003, **94**, 49–58.
17 M.-J. Zhou, Z.-L. Shen and R.-C. Yu, *Cont. Shelf Res.*, 2008, **28**, 1483–1489.
18 T. E. Clark, M. Makha, A. N. Sobolev, H. Rohrs, J. L. Atwood and C. L. Raston, *Chem.–Eur. J.*, 2008, **14**, 3931–3938.
19 E. Eroglu, V. Agarwal, M. Bradshaw, X. Chen, S. M. Smith, C. L. Raston and K. Swaminathan Iyer, *Green Chem.*, 2012, **14**, 2682–2685.
20 C. J. Bolch and S. I. Blackburn, *J. Appl. Phycol.*, 1996, **8**, 5–13.
21 APHA, *Standard methods for the examination of water and wastewater*, American Public Health Association, Washington DC, 18th edn, 1992.

APPENDIX E

Supplementary Information

Surfactant free formation of fullerene C_{60} nanotubules under shear

Kasturi Vimalanathan[a], Rekha G. Shrestha[b], Zhi Zhang[c], Jin Zou[c], Tomonobu Nakayama[b,d] and Colin L. Raston[a*]

[a] Flinders Centre for NanoScale Science & Technology (CNST) School of Chemical & Physical Sciences, Flinders University, Adelaide SA 5001, Australia

[b] International Centre for Materials Nanoarchitectonics (MANA) National Institute for Materials Science (NIMS), 1-1 Namiki, Tsukuba, Ibaraki, 305-0044, Japan

[c] Materials Engineering and Centre for Microscopy and Microanalysis, The University of Queensland, Brisbane, QLD 4072, Australia

[d] Graduate School of Pure and Applied Sciences, University of Tsukuba, 1-1 Namiki, Tsukuba, Ibaraki, 305-0044, Japan

*Corresponding author email: colin.raston@flinders.edu.au

Experimental methods:

In a typical experiment C_{60} (99685-96-8, 99+%, BuckyUSA) was added to toluene (2 mg/mL) and the mixture allowed to stand overnight, whereupon it was filtered to remove any undispersed C_{60} and impurities. A mixture of a toluene solution of C_{60} (0.5 mL) with water (0.5 mL) was placed in in a glass tube (as a readily available borosilicate nuclear magnetic resonance (NMR) tube (ID 16.000 ± 0.013 mm), which was spun for 30 minutes at an optimized speed of 7000 rpm and inclination angle of 45 degrees. For the confined mode of operation, a finite volume of total liquid is required which was set a 1 mL. This ensures that a vortex is maintained to the bottom of the tube for moderate rotational speeds, to avoid different shear regimes, and without any liquid exiting at the top the tube. Stewartson/Ekman layers prevail in the dynamic thin films, which arise from the liquid accelerating up the tube with gravitational force acting against them.[1] The scalability of the process was then investigated under continuous flow, using two jet feeds, one delivering the above toluene solution of C_{60}, the other water, both at the combined optimised flow rate of 1 mL/min with intense micromixing resulting in the formation of what appears to be a single phase with then with spontaneous phase separation as the liquid exits the tube. A systematic evaluation of the flow rates was carried out with

1mL/min affording the highest yield (~ 85 %) of hollow C_{60} nanotubules. The formation of the nanotubules is facilitated initially at the hemispherical bottom of the tube where there is instability of the liquid boundary layer.[1] The viscous drag as the liquid whirls up the tube creates shear and facilitates micromixing, along with that from the Stewartson/Ekman layers.

The C_{60} nanotubules were characterized by scanning electron microscopy (SEM) performed using a FEI Quanta 450 High Resolution Field Emission SEM, with a voltage of 10 kV, and working distance of 10 mm, transmission electron microscopy (TEM), Raman spectroscopy and powder X-ray diffraction (XRD). Raman scattering were recorded at an excitation wavelength of 532 nm (≤ 5mW) at room temperature. XRD patterns were collected on a Bruker Advanced D8 diffractometer (capillary stage) using Cu Kα radiation (λ= 1.5418 Å, 50 kW/40 mA, 2θ = 2 – 55°). Samples for XRD were prepared on clean XRD plates, and dried at 80°C under reduced pressure for 24 hours prior to characterization. Samples for SEM and Raman analysis were prepared on clean silicon wafers. Samples for TEM were prepared by drop-casting the dispersion of C_{60} material onto standard carbon coated copper grids prior to characterization. TEM, high-resolution TEM (HR-TEM) images and selected area electron diffraction (SAED) were taken on a JEM- 2100F (200 kV) equipped with an EDS module.

Quartz Crystal Microbalance (QCM) Test

Sample preparation for quartz crystal microbalance studies

QCM electrode was prepared as follows: 2.0 mg of C_{60} nanotube was dispersed in toluene (1 mL). The mixture was then sonicated for 3 minutes (mild intensity) in a bath sonicator, and the integrity of the nanotubles was confirmed using SEM. 3 µL of this dispersion was drop casted on the QCM Au electrodes. The electrode was dried at 60 °C in vacuum for 24 hours before measurements. The modified QCM electrode then was attached to the QCM instrument and exposed to the solvent in a sealed space to prevent the escape of the vapors during the adsorption measurements. Between measurements, the electrode was exposed to air to desorb the solvent vapor. The recovery of the initial frequency value was taken as an indication of complete desorption. The change in mass, m ($g.cm^{-2}$) of the material deposited on the surface of the QCM electrode (due to adsorption and desorption

of solvent molecules) is related to the change in the oscillating frequency of the quartz electrode. A resonance frequency of 9 MHz (AT-cut) was used and the frequency of the modified QCM electrode (fullerene coated on Au QCM electrode) was recorded upon exposure to different solvent vapors at 25 °C.

The frequency change (Δf) corresponds to the sample amount loaded (m) on the QCM electrodand can be calculated from Sauerbrey equation[2]

$$\Delta f = (2f_0^2 / \sqrt{\rho_Q \mu_Q})m \qquad \text{(Equation 1)}$$

where f_o (Hz) is the natural frequency of the quartz crystal, ρ_Q is the quartz density (2.649 g cm^{-3}), and μ_Q is the shear modulus (2.947 × 10^{11} g cm^{-1}s^{-2}).

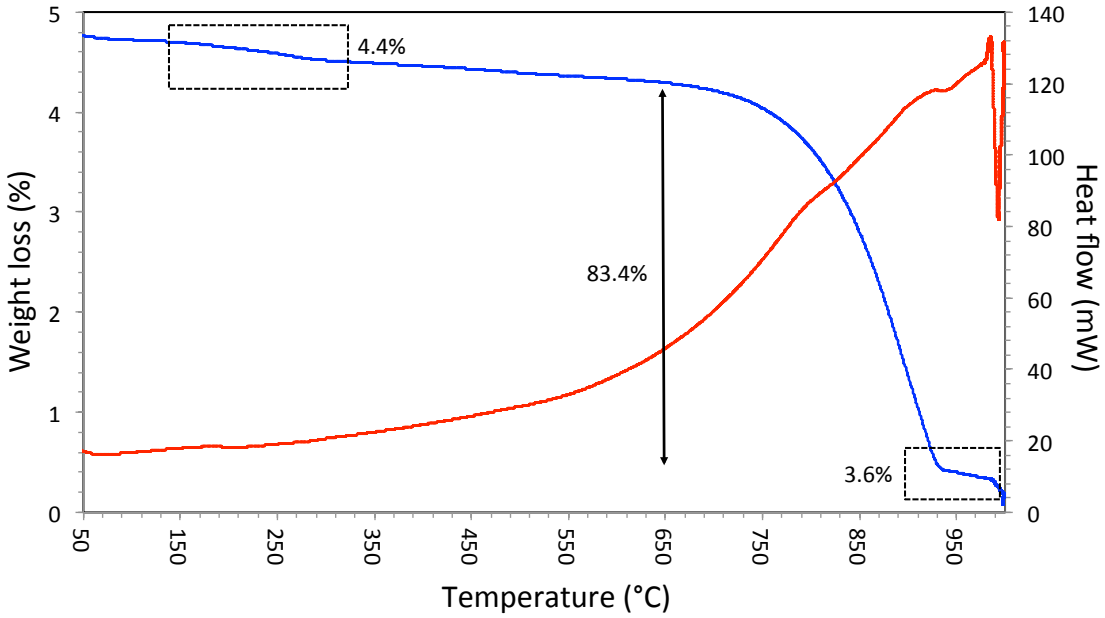

Figure SE1 TGA analysis of the C_{60} nanotubules with a 20°C/min rate of temperature increase in air.

Control Experiments:

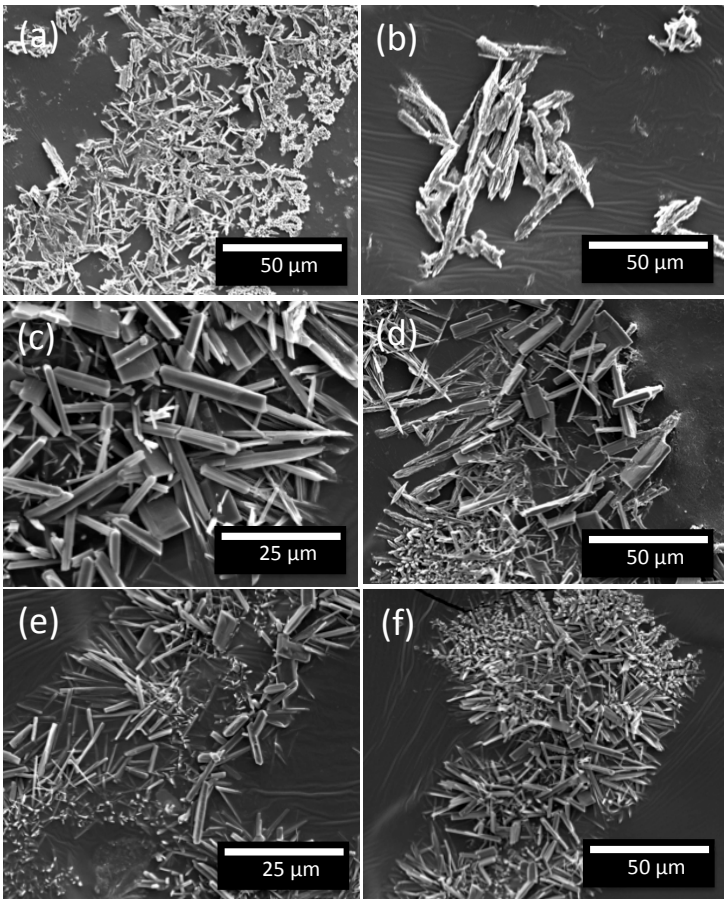

Figure SE2 SEM images of C_{60} dispersed in toluene at different concentrations with then the addition of water at a 1:1 volume ratio prior to sonication for 30 minutes (no VFD processing), which resulted in a change in colour from magenta to brown. (a-b), 1 mg/mL VFD flow rate VFD, (c-d), and 2 mg/mL VFD flow rate (e-f) 3 mg/mL.

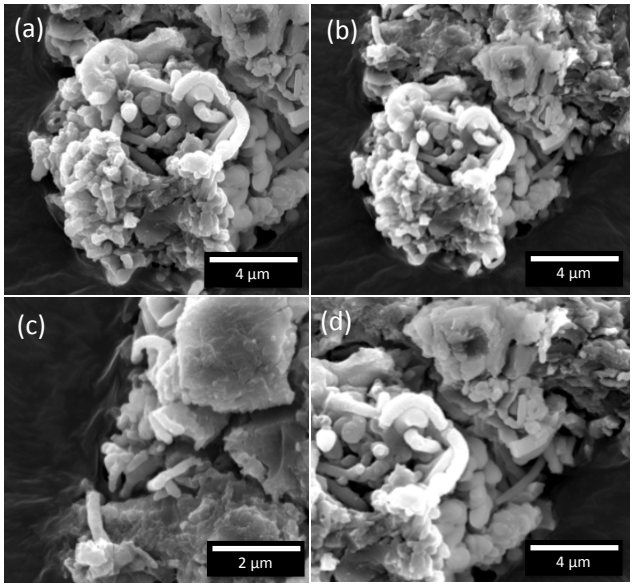

Figure E3 SEM images of C_{60} dispersed in toluene (1 mg/mL) with then the addition of water at a 1:1 volume ratio. 1 mL of the dispersion was then placed in the VFD at an inclination angle of 45° and a rotational speed of 7000 rpm for 30 minutes (confined mode).

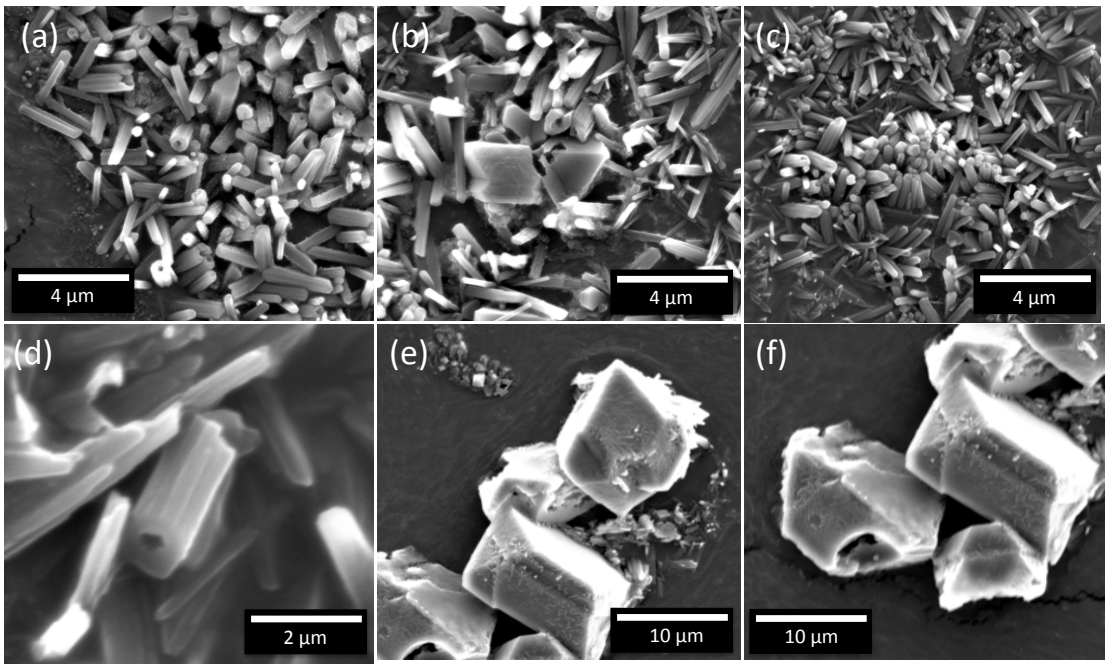

Figure E4 SEM images at different areas of the post VFD processed sample. The sample was prepared with C_{60} dispersed in toluene (2 mg/mL) with then the addition of water at a 1:0.5 volume ratio. 1 mL of the dispersion was then placed in the VFD at an inclination angle of 45° and a rotational speed of 7500 rpm for 30 minutes. The volume ratio was critical with control experiments establishing changing the volume ratios other that the 1:1 volume ratio, affording a mixture of different morphologies

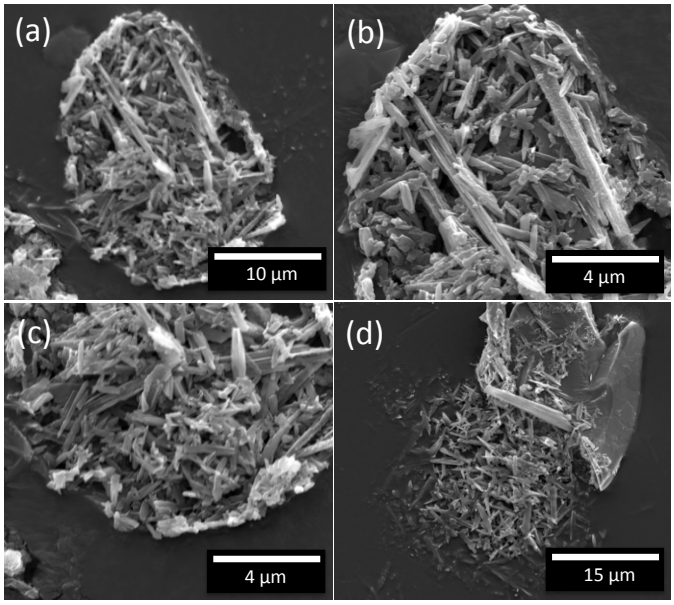

Figure E5 SEM images of C_{60} dispersed in toluene (2 mg/mL) with then the addition of water at a 1:1 volume ratio. 1 mL of the dispersion was then placed in the VFD at an inclination angle of 45° at different rotational speeds for 30 minutes. Different rotational speeds other then the optimized conditions afford a mixture of different morphologies (confined mode).

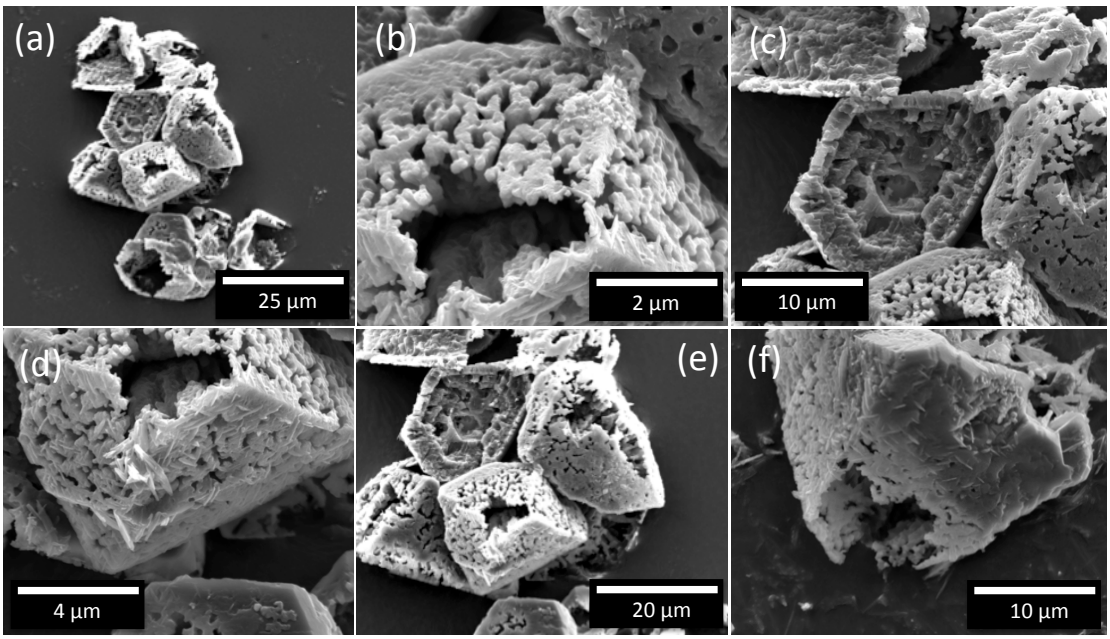

Figure E6 SEM images of C_{60} dispersed in toluene (3 mg/mL) with then the addition of water at a 1:1 volume ratio. 1mL of the dispersion was then placed in the VFD at an inclination angle of 45° and a rotational speed of 7000 rpm for 30 minutes (confined mode).

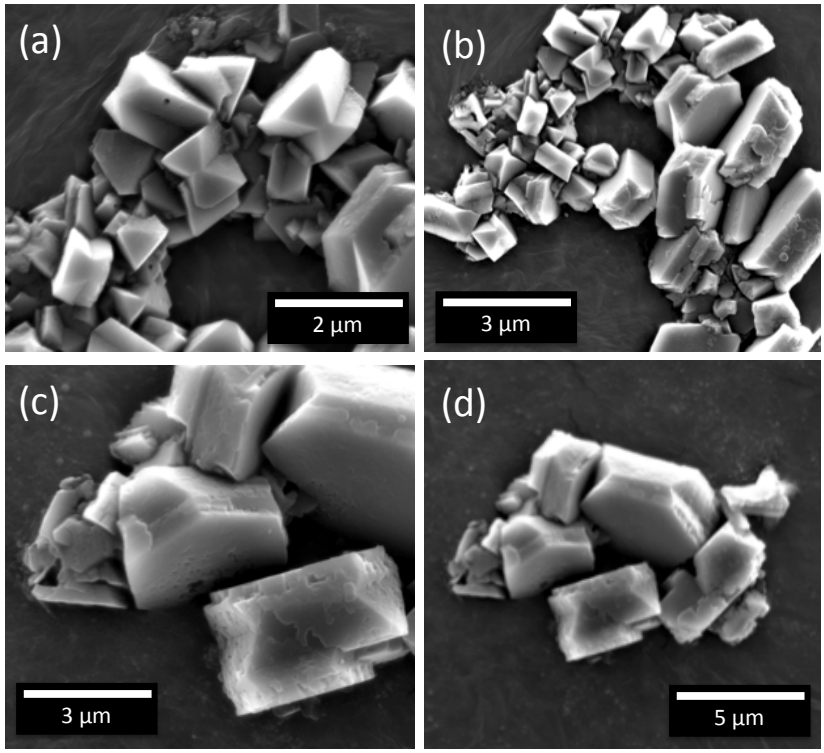

Figure E7 SEM images of C_{60} dispersed in toluene (3 mg/mL) with then the addition of water at a 1:1 volume ratio. 1 mL of the dispersion was then placed in the VFD at an inclination angle of 45° and a rotational speed of 7500 rpm for 30 minutes (confined mode).

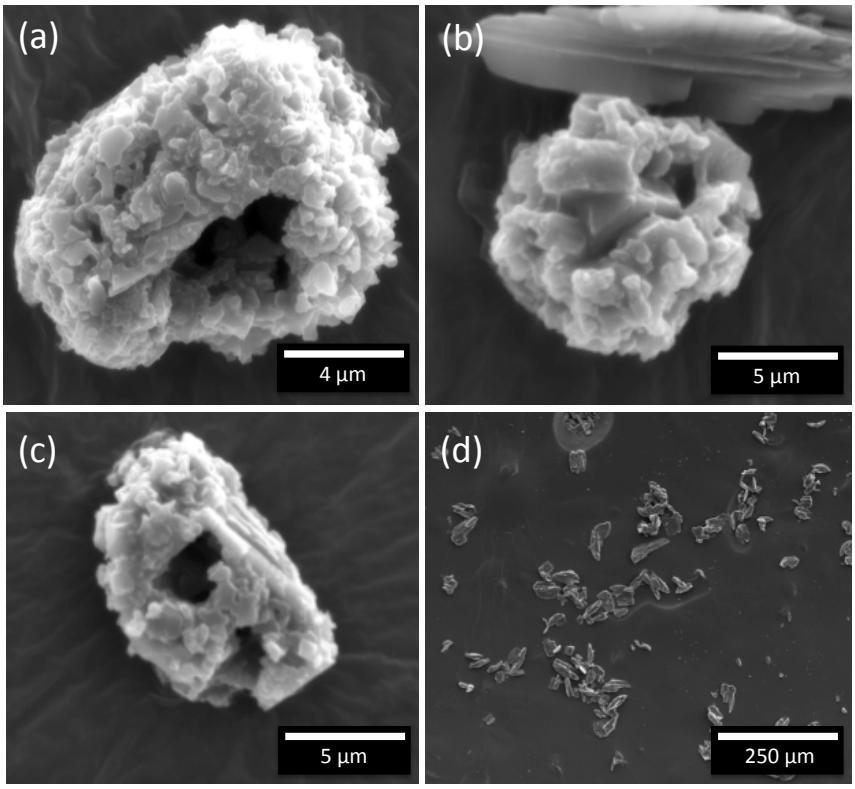

Figure E8 SEM images of C_{60} dispersed in toluene (3 mg/mL) with then the addition of water at a 1:1 volume ratio. 1 mL of the dispersion was then placed in the VFD at an inclination angle of 45° at other rotational speeds for 30 minutes. Different rotational speeds other then the optimized conditions afford a mixture of different morphologies (confined mode).

1D fullerene nanotubules were prepared using previously published method, as the liquid–liquid interfacial precipitation (LLIP) method.[3] These form at the interface of a saturated solution of C_{60} in mesitylene (0.99 $mgmL^{-1}$) and isopropyl alcohol (IPA), and the synthesis involves the slow addition of IPA to a saturated C_{60} solution in mesitylene. The mixture was stored in a temperature-controlled incubator at 25 ^{o}C for 24 h.

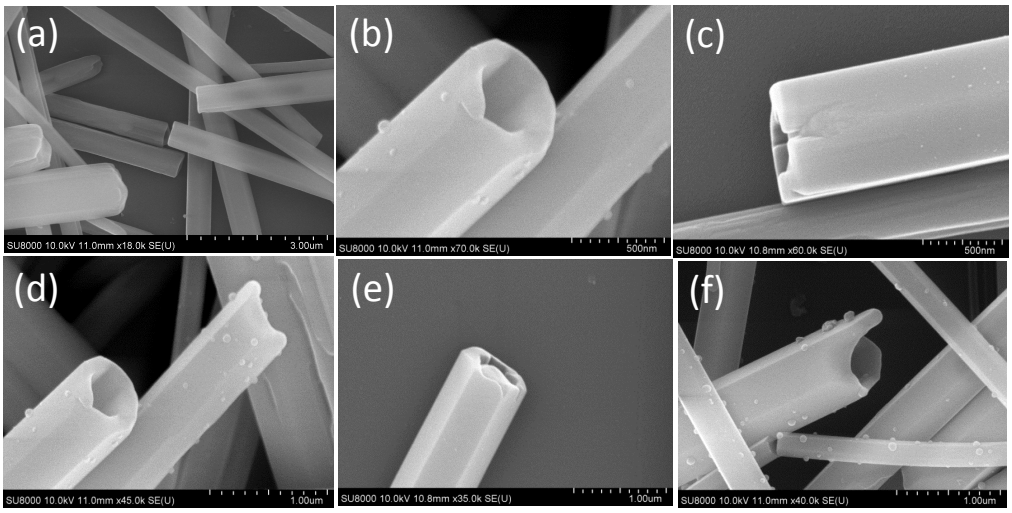

Figure E9 SEM images of C_{60} nanotubules prepared using the LLIP method.[3]

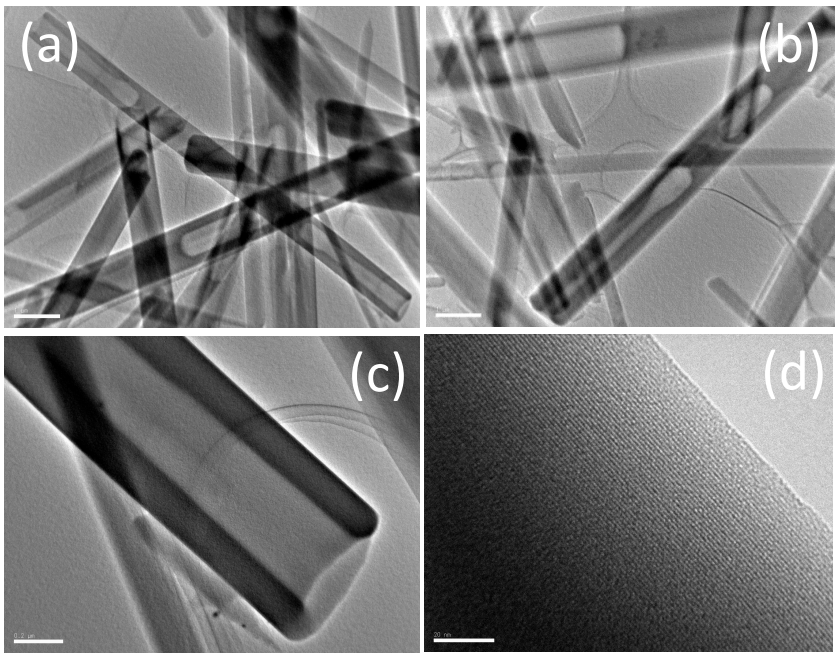

Figure E10 TEM and HRTEM of the C_{60} nanotubules prepared using the LLIP method.[3]

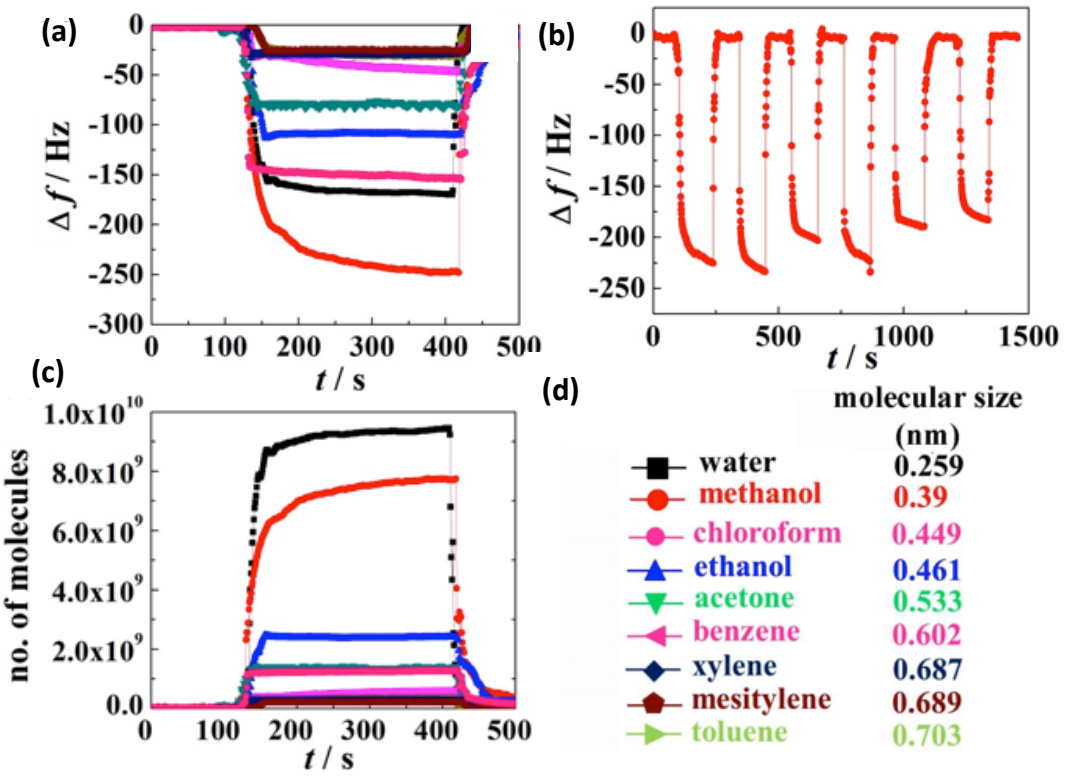

Figure E11 C_{60} nanotubules prepared using the LLIP method with no pores on the surface: (a) QCM frequency shifts for coated electrode upon exposure to different solvent vapors (water, methanol, ethanol, acetone, benzene, toluene, xylene, mesitylene, and chloroform), (b) repeatability test of the electrode upon exposure and removal of methanol vapors, (c) number of molecules adsorbed with time, and (d) the legends common for figures (a) to (c) shown in the order of their molecular sizes that are estimated by considering molecular structure and atomic radii of the solvents**.**

References:

[1] J. Britton, S.B. Dalziel, C.L. Raston, *RSC Adv*. **2015,** *5,* 1655-1660

[2] G.Z.Sauerbrey, *J. Physik* **1959**, *155*, 206–212.

[3] L.K. Shrestha, R.G. Shrestha, Y. Yamauchi, J.P. Hill, T. Nishimura, K. Miyazama, T. Kawai, S.Okada, K. Wakabayashi, K. Ariga, *Angew. Chem. Int. Ed*. **2015,** *54*, 951-955

APPENDIX F

Supplementary information

VFD induced templated graphene scroll formation from graphite

Kasturi Vimalanathan, Christopher T. Gibson, Xianjue Chen and Colin L. Raston*

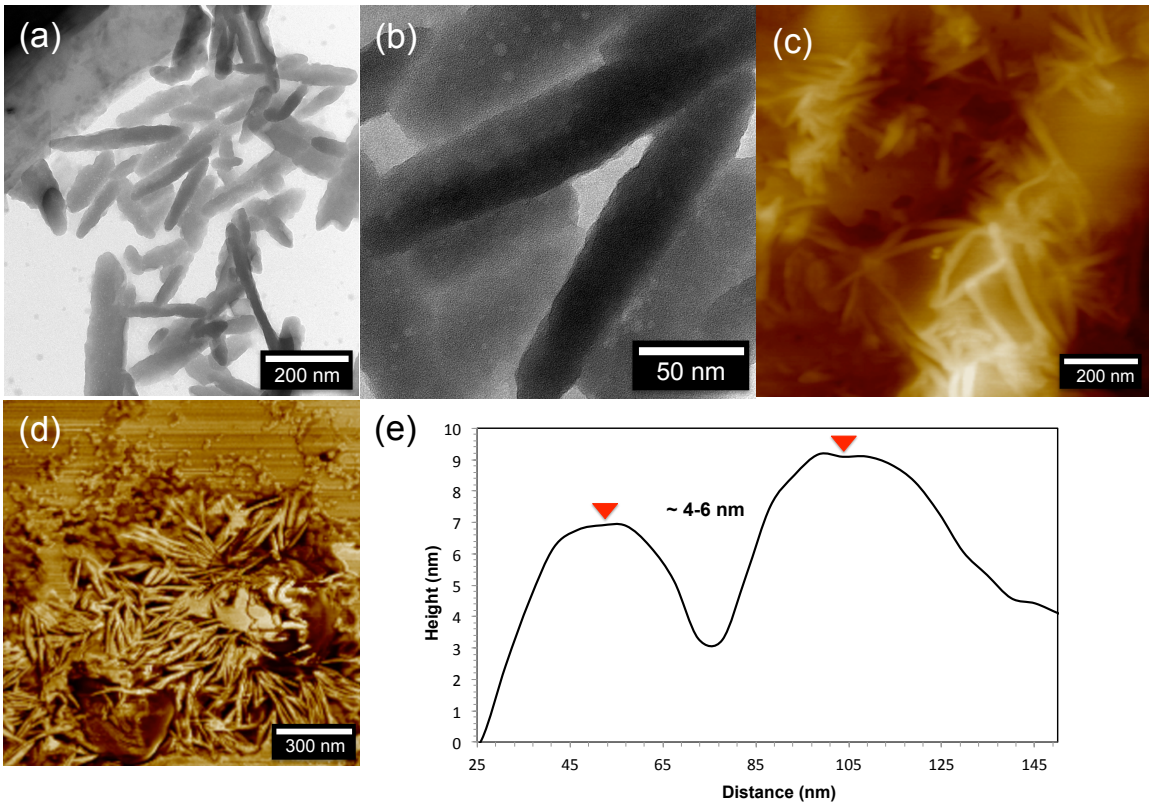

Figure F12 Graphite flakes in the immiscible solvent system mixture, toluene and water without the use of sonication the sample was characterized at the interphase of toluene and water; (a-b) TEM of the stable hydrophobic/hydrophilic rod templates of toluene and water, (c-d) AFM images of the rod templates, and (c) the associated height profile of the rod templates, with a height of *ca* 4-6 nm

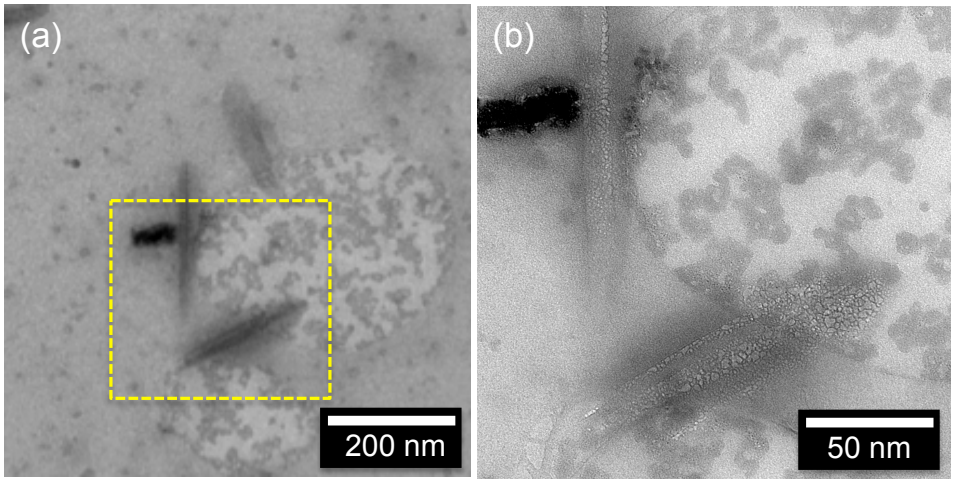

Figure F13 The immiscible solvent system mixture in the absence of graphite flakes, toluene and water without the use of sonication; the sample was characterized at the interphase of toluene and water; (a-b) TEM of the hydrophobic/hydrophilic rods which were unstable under high energy.

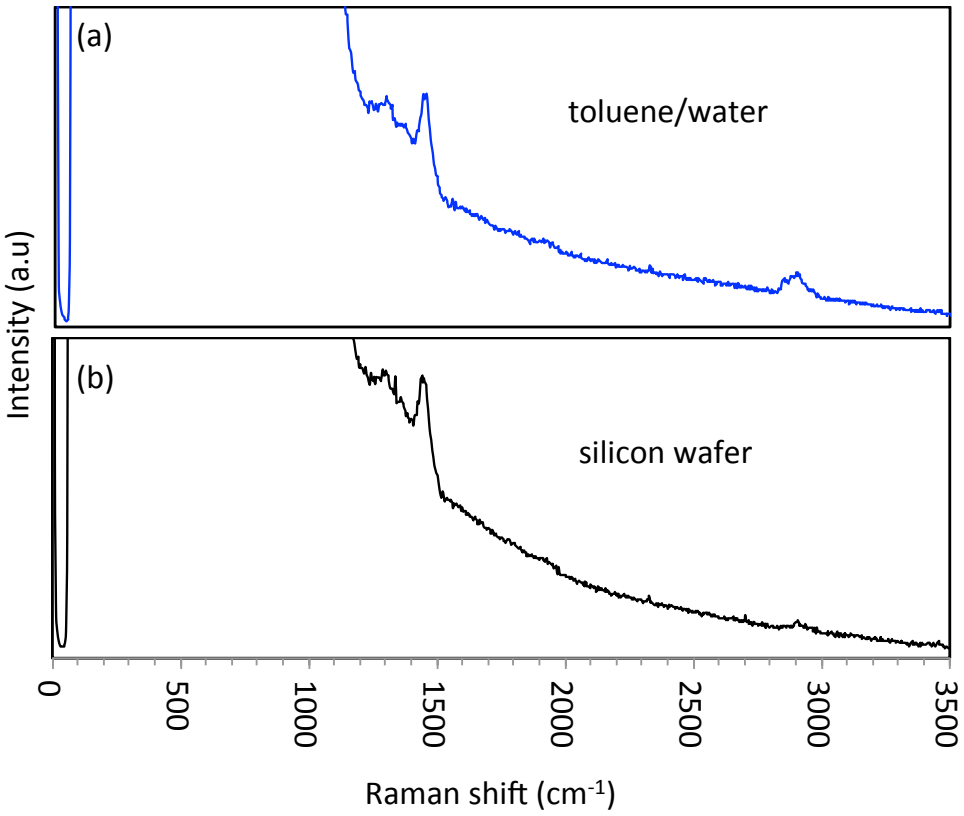

Figure F14 Raman spectroscopy of the control experiments for the assignment of the two additional peaks present in the scroll spectra; (a) toluene/water solvent system deposited on a silicon wafer, and (b) pure silicon wafer

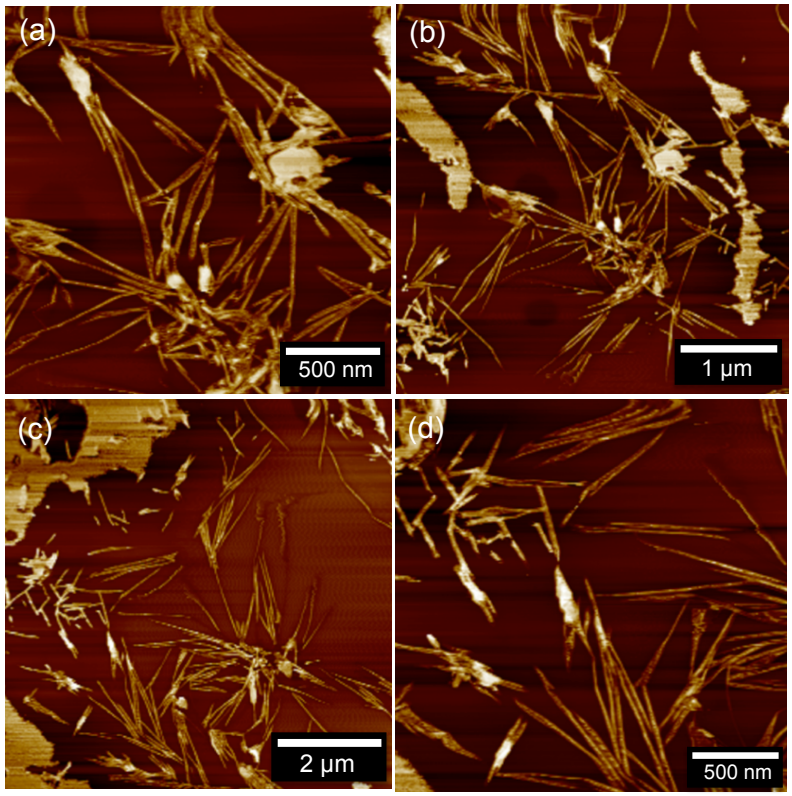

Figure F15 Additional AFM images of graphene scrolls afforded using toluene water at a 1:1 volume ratio. This was the optimised condition to afford high quantities of graphene scrolls.

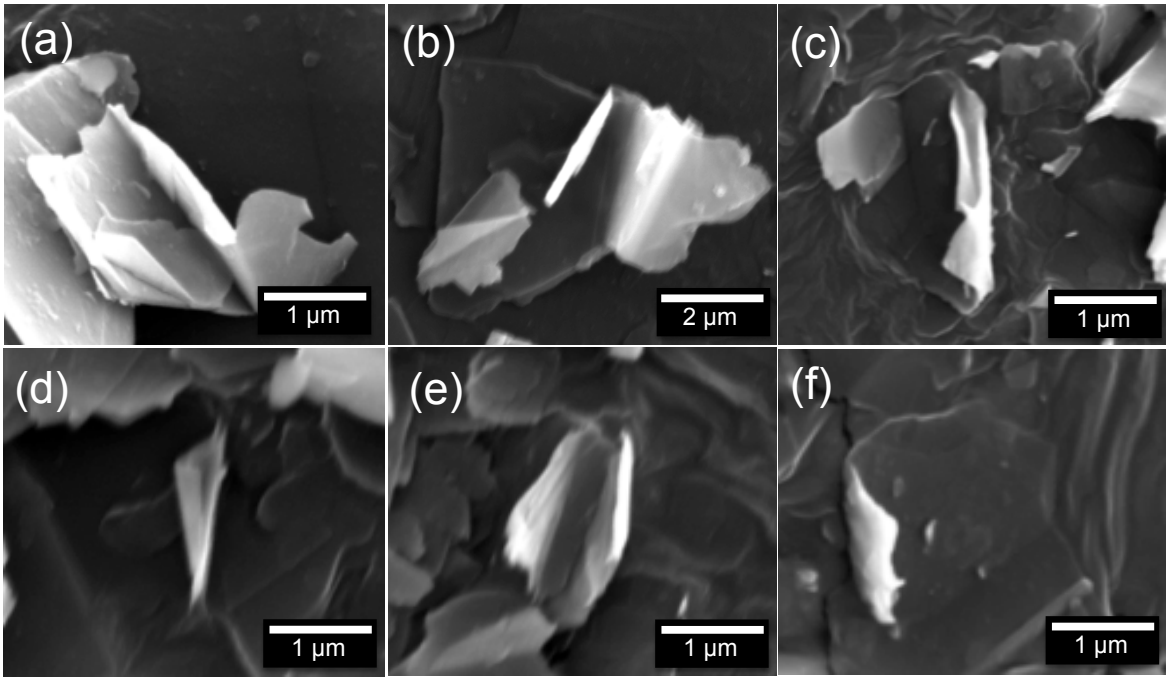

Figure F16 SEM images of partial/ unscrolled graphene sheets. Partial scrolled graphene sheets were afforded when changing the volume ratio of toluene and water other then the optimised condition (1:1 volume ratio).

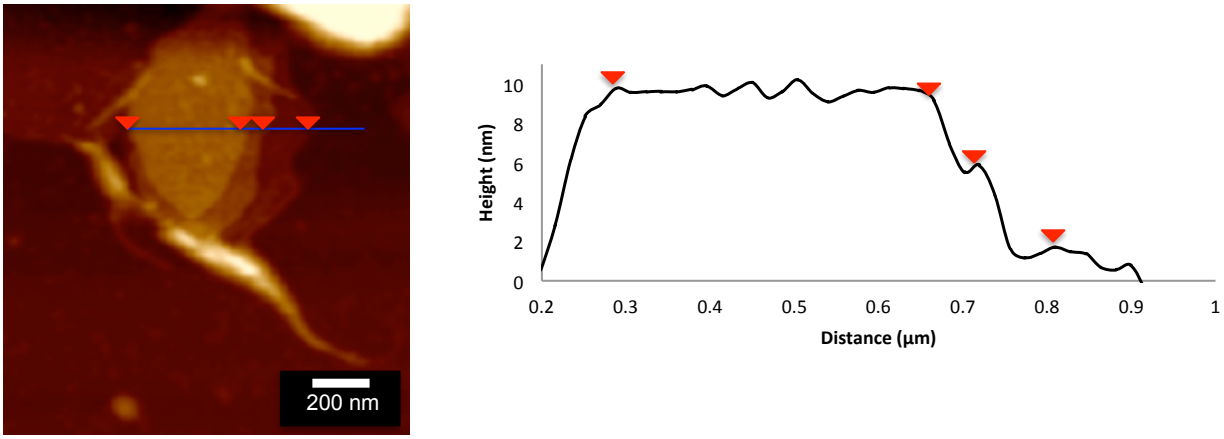

Figure F17 AFM of small amounts of exfoliated/partially exfoliated graphene sheets present post VFD processing, and the associated height profile. The graphene sheets were of smaller dimensions due to the intense shearing in the VFD, sufficient to be able to rip the graphene sheets into smaller dimensions**.**

APPENDIX G

Supplementary Information

Fluid dynamic slicing of super tensile carbon nanotubes

Kasturi Vimalanathan,[1] Jason R. Gascooke,[1] Irene Suarez-Martinez,[2] Nigel Marks,[2] Harshita Kumari,[3,4] Chris Garvey,[5] Jerry L. Atwood,[3] Warren D. Lawrance,[1] and Colin L. Raston[1*]

1 Flinders Centre for NanoScale Science & Technology, School of Chemical & Physical Sciences, Flinders University, Adelaide SA 5001, Australia

2 Nanochemistry Research Institute, Department of Physics and Astronomy, School of Science, Curtin University, Bentley Campus, Perth, WA 6102, Australia

3 Department of Chemistry, University of Missouri, 601 South College Avenue, Columbia, Missouri 65211, United States

4 James L. Winkle College of Pharmacy, University of Cincinnati, 3225 Eden Avenue, Cincinnati, Ohio, 42567, United States

5 Bragg Institute, Australian Nuclear Science and Technology Organisation, New Illawarra Road, Lucas Heights, NSW 2234

*Corresponding authors email: colin.raston@flinders.edu.au

Raman characterization

In a typical carbon nanotube Raman spectrum[1-3], the RBM frequencies correspond to the diameter of the nanotubes present in the sample, correlating to peak intensities within the specified region. Any disorder induced D-band conforms to damage/defects present within the walls/ends of individual CNTs, with the ratio of intensity of the G band and the disordered induced D band (I_D/I_G) determining the structural defects present on the walls of the nanotubes post-processing.

Supplementary Figure 1

AFM images of the as received SWCNTs, MWCNTs and DWCNTs respectively (in the absence of the VFD and laser) dispersed in a 1:1 mixture of NMP and water after batch processing in a round bottom flask (stirring)

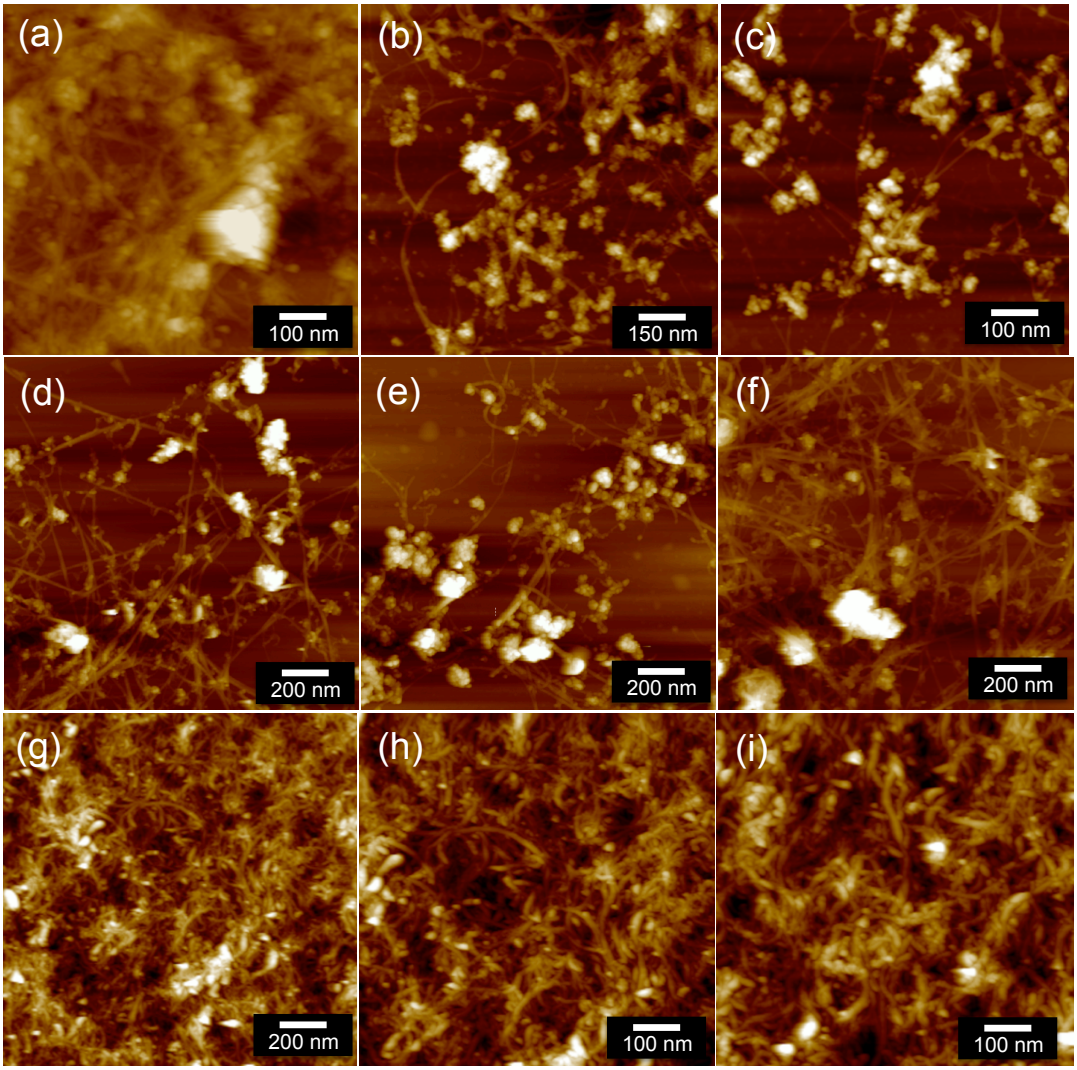

Figure G18 AFM images of the as-received carbon nanotubes (a-c) SWCNTs (d-f) DWCNTs, and (g-i) DWCNTs.

Supplementary Figure 2,3 and 4

Additional AFM images of the sliced carbon nanotubes, SWCNTs, DWCNTs and MWCNT

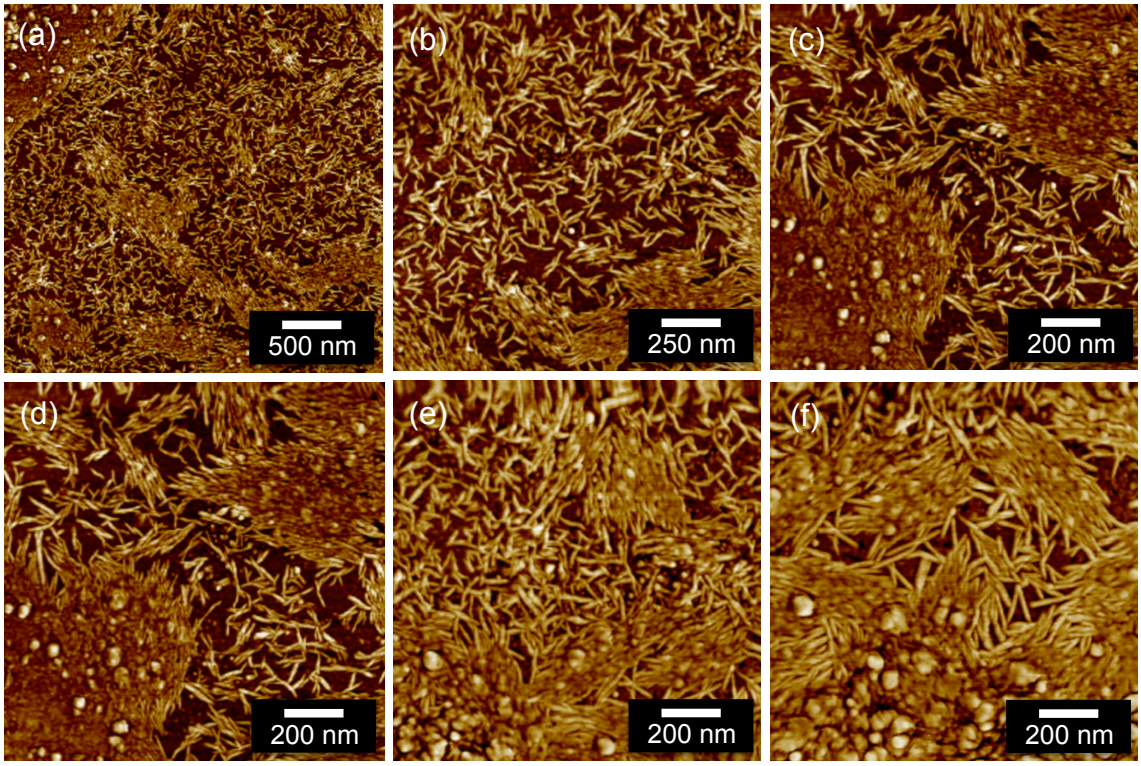

Figure G19 AFM images of the sliced SWCNTs

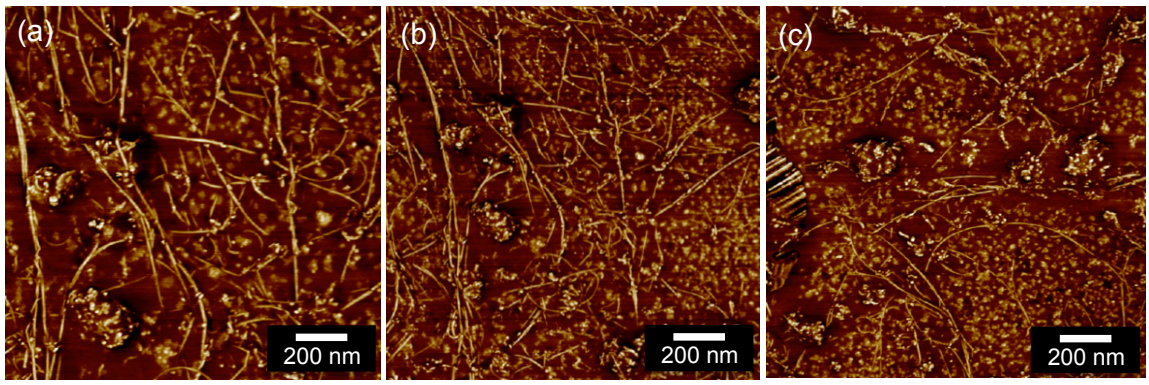

Figure G20 AFM images of the sliced DWCNTs

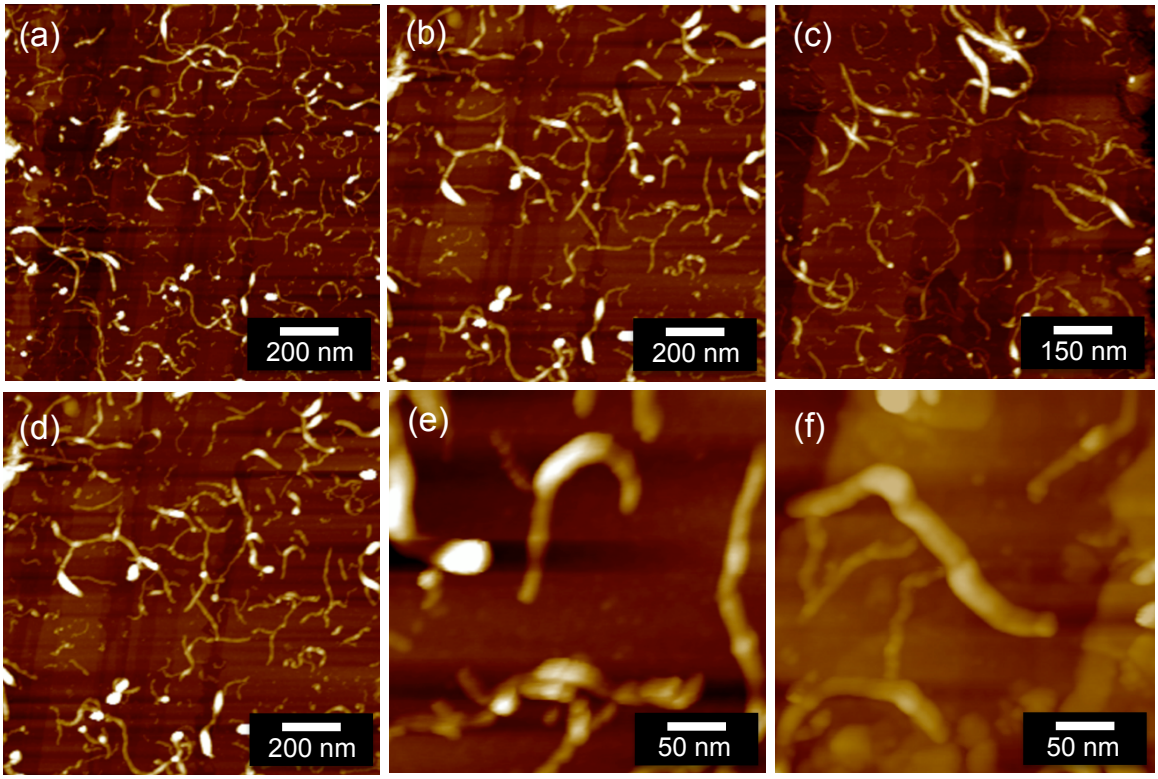

Figure G21 AFM images of the sliced MWCNTs

Supplementary Figure 5

AFM images SWCNTs, MWCNTs and DWCNTs respectively processed with the 1064 nm laser (in the absence of VFD processing) for a 30 minute processing time. A glass cuvette was filled with the respective CNT suspension (1:1 mixture of NMP and water) with a stirring bar beneath the vial to ensure continuous mixing of the suspension. The 8 mm pulsed laser was directed to the middle of the glass cuvette.

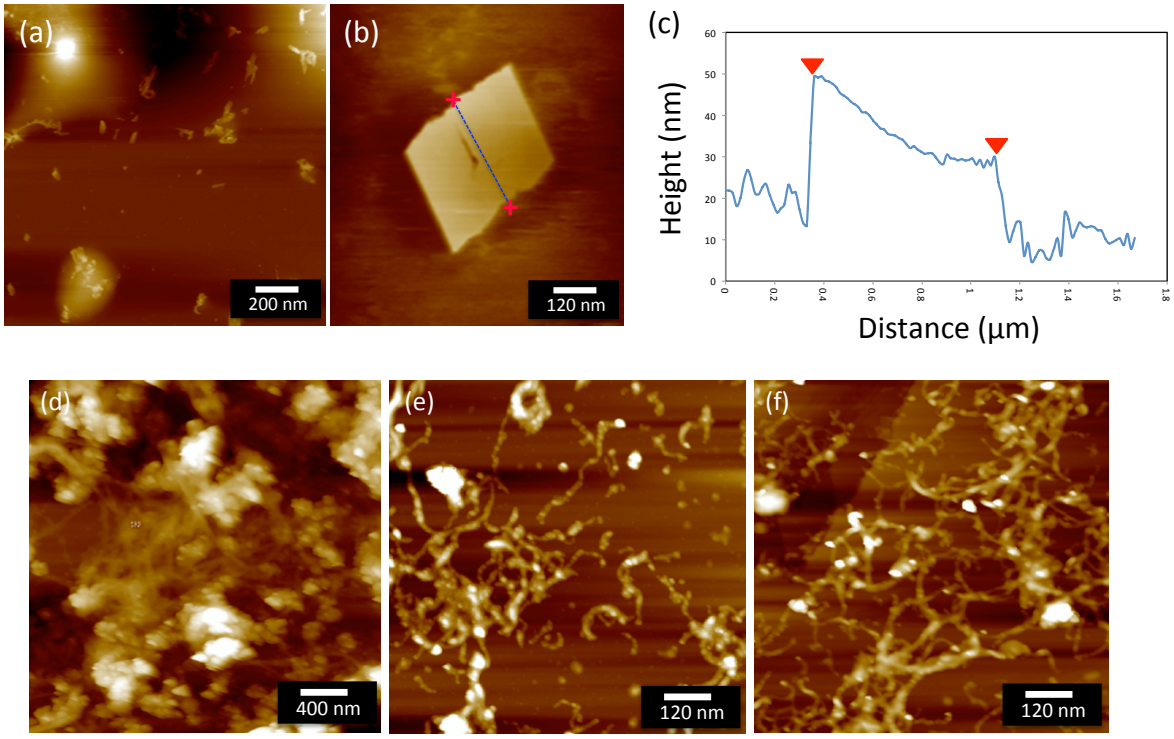

Figure G22 (a) AFM height images of the fragmented SWCNTs, (b) AFM height image of a SWCNT fragment and its (c) associated height profile, (d) AFM height image of DWCNTs, and (e-f) AFM height images of partially sliced MWCNTS with no uniformity in length with the presence of bundles and agglomerates.

Supplementary Figure 6

Control experiments to study the effects of changing the laser wavelength on the slicing of the CNTs at the optimised laser power, 260 mJ. The 532 nm wavelength (green light) showed no apparent slicing of the CNTs, single, doubled and multi walled under the same conditions.

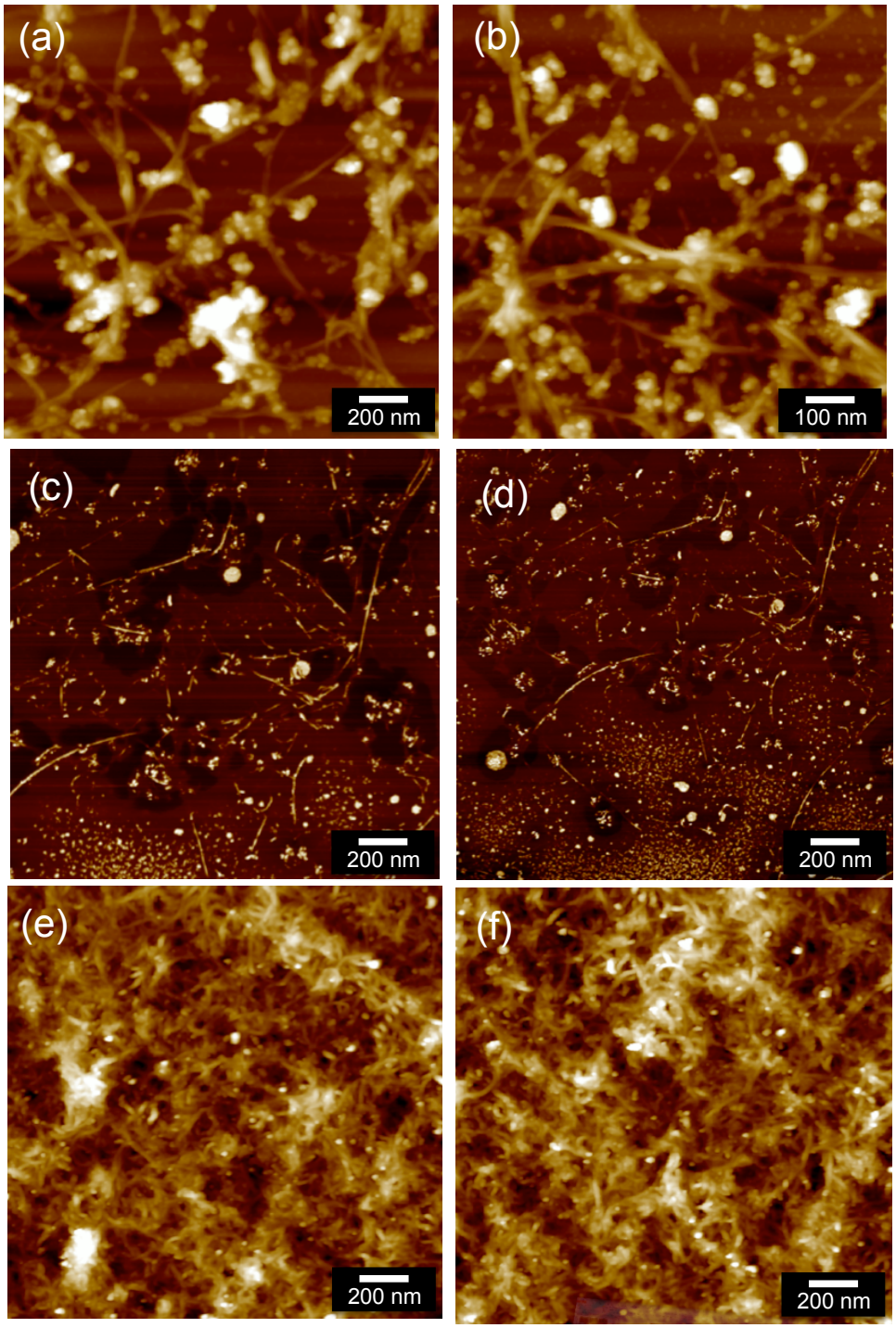

Figure G23 AFM images of the nanotubes; (a-b) SWCNT, (c-d) DWCNT, and (e-f) MWCNT

Supplementary Figure 7

Control experiments to establish the optimised power for the slicing process. At a laser power of 150 mJ, bundled SWCNT remained unaffected with debundling and some agglomerates still present, however no slicing was evident. At 450 mJ, there were large amounts of bundled and agglomerated SWCNTs still present within the sample; however, small amounts of sliced SWCNTs were observed (Figure (e)) albeit irregular in length.

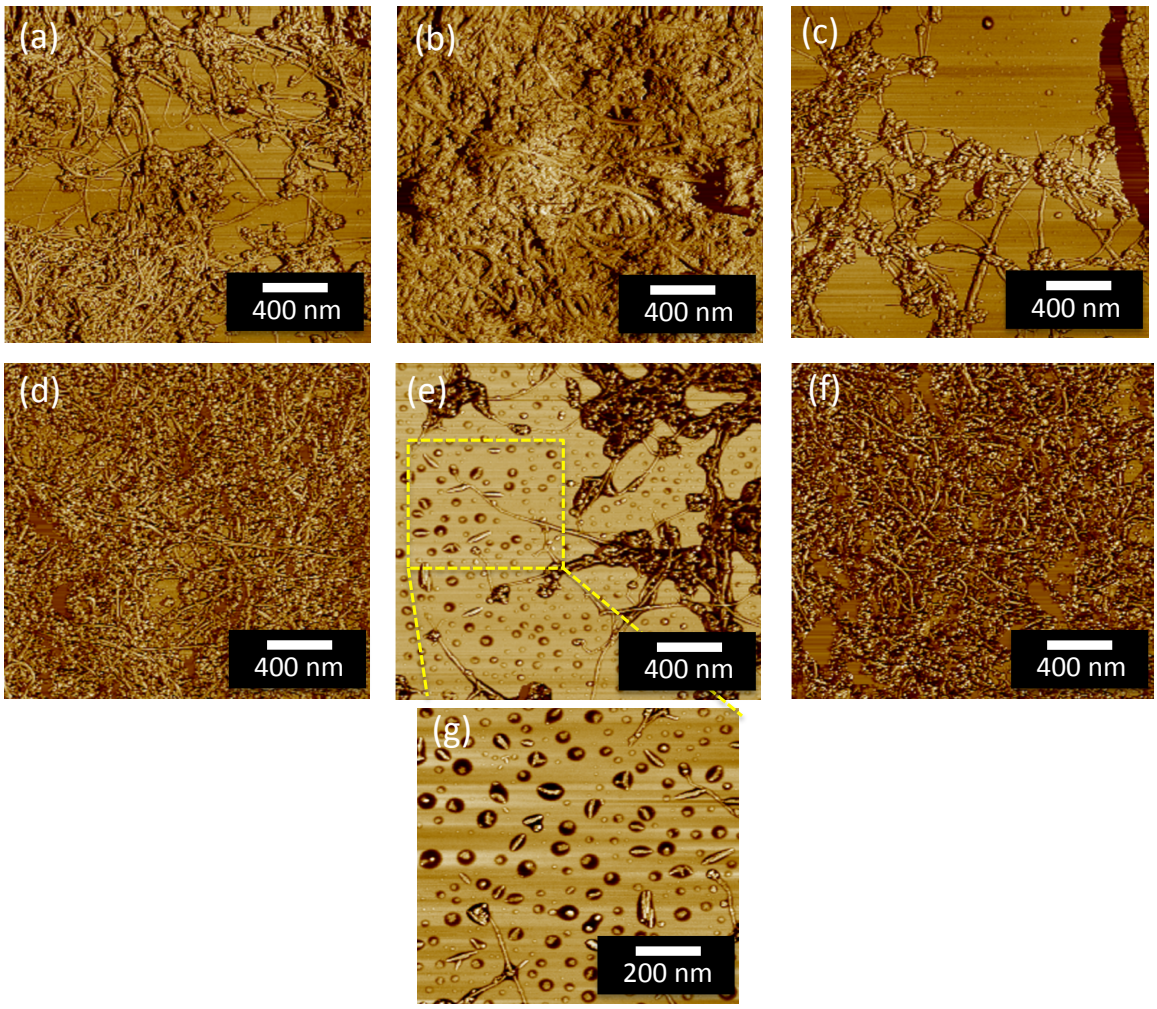

Figure G24 AFM images of SWCNT processed in the VFD (θ 45°, rotational speed 7500 rpm) at different laser powers for a 10 minute, 30 minute and 1 hour processing time respectively (VFD confined mode); (a-c) 150 mJ (a) 10 minutes, (b) 30 minutes, (c) 1 hour; (d-f) 450 mJ (d) 10 minutes, (e,g) 30 minutes- small amounts of sliced SWCNTs were observed, and (f) 1 hour

Supplementary Figure 8

Absorption spectrums of the sliced single, double and multi CNTs were observed to determine the concentration and their chiralities, present in the aqueous dispersions under both confined mode (Supplementary Fig. 6(a)) and continuous flow (Supplementary Fig. 6(b)). For SWNCTs there are four regions around 850-1350 nm, 500-850 nm, 330-450 nm and 300-400 nm, corresponding to the S_{11}, S_{22}, S_{33} and S_{44} optical transition of the semiconducting SWCNTs. The absorbance peaks observed between the regions 400-650 nm represent the first optical transition of metallic SWCNTs (M_{11}). As for the sliced CNTs for DWCNTs and MWCNTs, the absorption peaks were significantly broader compared to the peaks for SWCNTs. A much lower absorbance was observed specifically for the MWCNTs. The absorption peaks for DWCNTs and MWCNTs are in similar regions to the SWCNTs. The peaks between 950 and 1250 nm correspond to small amounts of semiconducting nanotubes for the S_{11} transition and dominated amounts of the S_{22} transition, corresponding to the smaller diameter inner wall nanotubes and the larger outer walls respectively. A typical absorption peak at 273 nm corresponds to the surface π-plasmon excitation of stable dispersed carbon nanotube dispersions, also known as the ultraviolet absorption characteristic of the nanotubes[4-5].

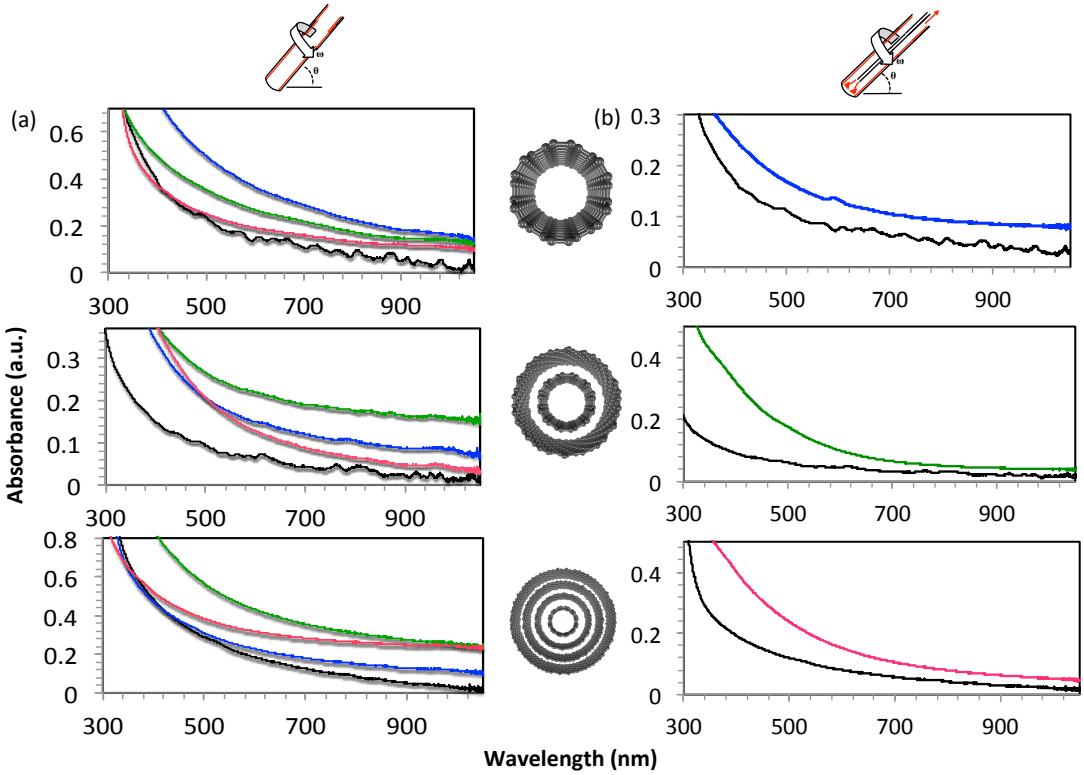

Figure G25 UV-Visible spectras of the sliced SWCNT, DWCNT and MWCNT compared to the respective as-received CNTs; (a) under confined mode, (b) under continuous flow.

Supplementary Figure 9-14

SANS measurement was performed along with AFM to compare the results from the two techniques and in two different solvents. While AFM provides 2-dimensional real space representation of structure with some limited statistics, SANS as a reciprocal space method where 3-dimensional real space information is reconstructed by modeling of scattering curves[6], provides a true statistical perspective on structure. The two techniques are therefore complementary. For this purpose, we evaporated NMP from sliced/pre-treated (shear+laser or laser only) nanotubes. The resultant material/nanotubes were re-dissolved in deuterated chloroform for SANS measurements. Deuterated solvent was used to lower the relative incoherent background scattering and the contrast between the solute and the solvent. SANS measurements were performed on QUOKKA at Braggs Institute, ANSTO. Neutrons of wavelength 5 Å were used with a wavelength spread/ full-width half maximum of $\Delta\lambda/\lambda$ = **12%**. The sample to detector distances of 1.3 m, 4.5 m, 13 m covered the overall q range of 0.013 $Å^{-1} < q < 0.534$ $Å^{-1}$. Here $q = (4\pi/\lambda) \sin(\theta/2)$ is the magnitude of the scattering vector and θ is the scattering angle. The sample scattering was corrected for the background, the empty cell scattering, and the sensitivity of the individual detector pixels. The corrected data sets were placed on an absolute scale and the structure was modeled using Igor Pro software[7].

Small-angle neutron scattering (SANS) data for single-walled-, double walled- and multi-walled carbon nanotubes, subjected to laser and shear at various time scales, have been reduced and fitted to cylindrical models. The quality of the fit and physical plausibility of the structural parameters was used to evaluate which structure was the most likely solution structure of the nanotubes. The scattering length densities (SLDs) for the nanotubes and solvent (*d3*-chloroform) were calculated and the analyses were done on Igor software provided by NIST. The data was collected at Bragg Institute, ANSTO. The data was fitted to cylinder model. In the smeared cylindrical fits (all 3 types), the SLDs for SWCNTs/ DWCNTs/ MWCNTs were free, whereas that for the solvent d_3-$CDCl_3$ was held fixed at the calculated values and the structural parameters common to each data set were optimized to provide the best fit. The scattering data indicates that vortex fluidic device (VFD) in combination with laser enabled the breaking of carbon nanotubes. A list of fits and individual fits with fitting parameters and notes are enlisted below.

In the smeared cylindrical fits, the scattering length densities/SLDs for the solvent d_3-$CDCl_3$ and length were held fixed at the calculated values and the structural parameters common to each data set were optimized to provide the best fit.

TABLE 1: RESULT SUMMARY

Sample	SLD	Radius	Length
SWCNT laser only	5.91621e-06 ±0.000724898	7 ± 0.502443	999.523±283.901
SWCNT laser +shear (10min)	4.71192e-06 ± 0.000482733	7 ± 2.2327	3700 ±0
SWCNT laser +shear (30min)	5.71086e-06 ± 0.000462135	7 ± 1.75552	1650 ±0
SWCNT laser +shear (60min)	5.9024e-06 ± 0.000740086	7 ± 2.6338	1100 ±0
DWCNT laser +shear(60min)	4.86312e-06 ± 0.00244807	20 ± 1.22684	1600 ±0
MWCNT laser +shear(60min)	4.42184e-06 ± 0.00369752	45 ± 1.72077	1710 ±0

Fit to SmearedCylinderForm,

Data file: a1_comb_ABS

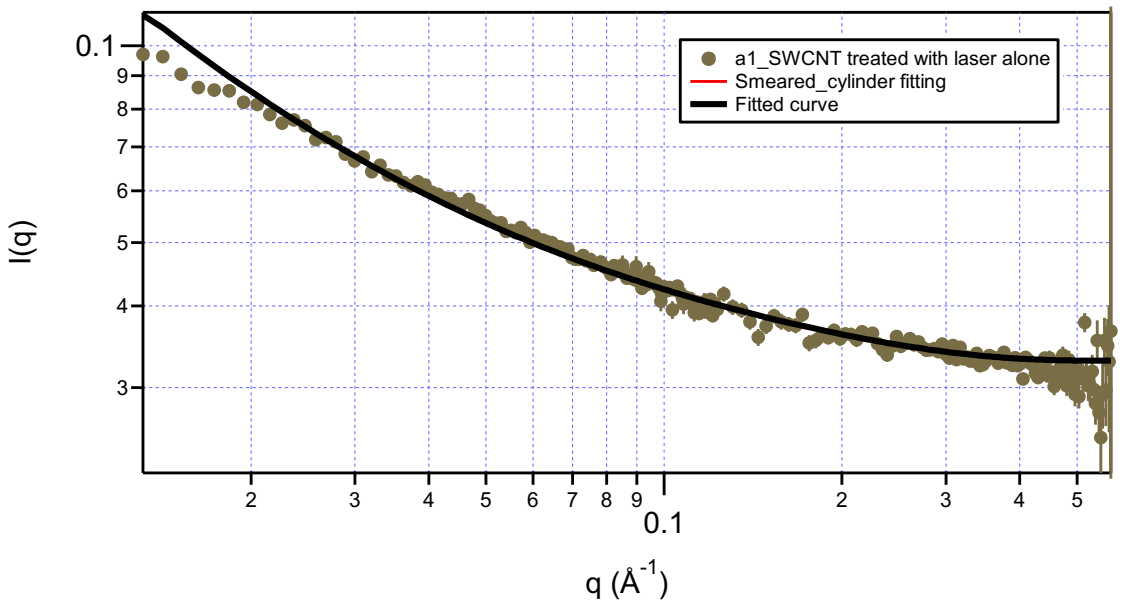

scale	0.00290988	±	1.5284
radius (Å)	7	±	0.502443
length (Å)	999.523	±	283.901
SLD cylinder (Å^{-2})	5.91621e-06	±	0.000724898
SLD solvent (Å^{-2})	3.156e-06	±	0
incoh. bkg (cm^{-1})	0.032984	±	0.000181443

chisq = 693.141

Npnts = 223 Sqrt(χ^2/N) = 1.76302

Fitted range = [0,222] = 0.0131333 < Q < 0.570667

FitError = No Error FitQuitReason = No decrease in chi-square

Figure G26 Smeared cylinder fitting for single-walled carbon nanotubes treated with laser only

Fit to SmearedCylinderForm,

Data file: a2_comb_ABS

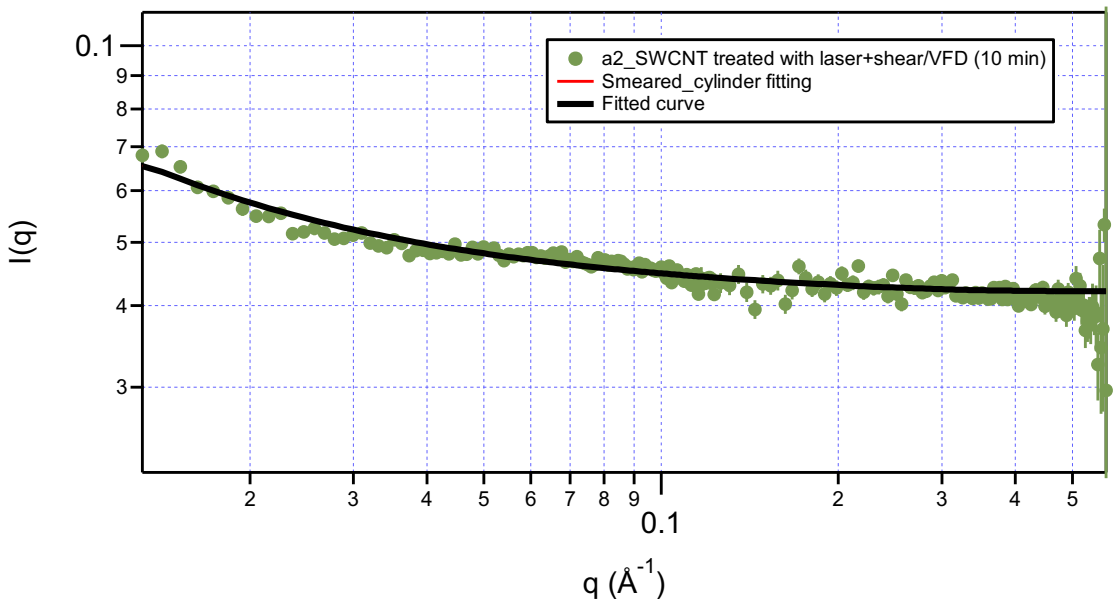

scale	0.00264772	±	1.64283
radius (Å)	7	±	2.2327
length (Å)	3700	±	0
SLD cylinder ($Å^{-2}$)	4.71192e-06	±	0.000482733
SLD solvent ($Å^{-2}$)	3.156e-06	±	0
incoh. bkg (cm^{-1})	0.0420775	±	0.000234206

chisq = 441.902

Npnts = 216 Sqrt(χ^2/N) = 1.43033

Fitted range = [0,215] = 0.0131333 < Q < 0.570667

FitError = No Error FitQuitReason = No Error

Figure G27 Smeared hollow cylinder fitting for single-walled carbon nanotubes treated with laser and shear 10 minutes

Fit to SmearedCylinderForm,

Data file: a3_comb_ABS

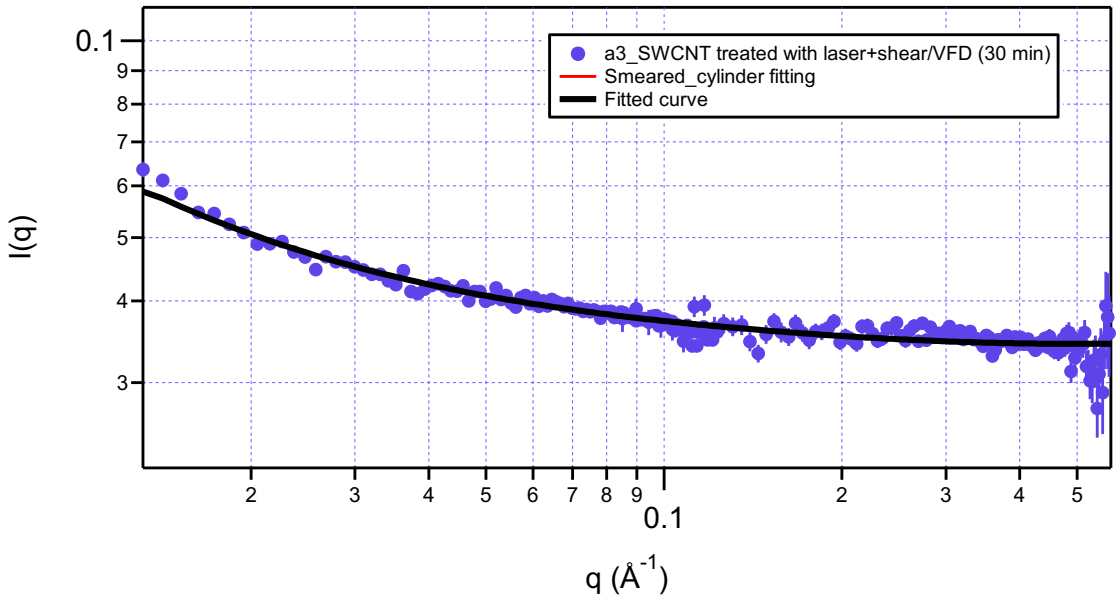

scale	0.00104287	±	0.377255
radius (Å)	7	±	1.75552
length (Å)	1650	±	0
SLD cylinder (Å^{-2})	5.71086e-06	±	0.000462135
SLD solvent (Å^{-2})	3.156e-06	±	0
incoh. bkg (cm^{-1})	0.0343739	±	0.000195543

chisq = 337.927

Npnts = 223 Sqrt(χ ^2/N) = 1.231

Fitted range = [0,222] = 0.0131333 < Q < 0.570667

FitError = No Error FitQuitReason = No Error

Figure G28 Smeared hollow cylinder fitting for single-walled carbon nanotubes treated with laser and shear 30 minutes

Fit to SmearedCylinderForm,

Data file: a4_comb_ABS

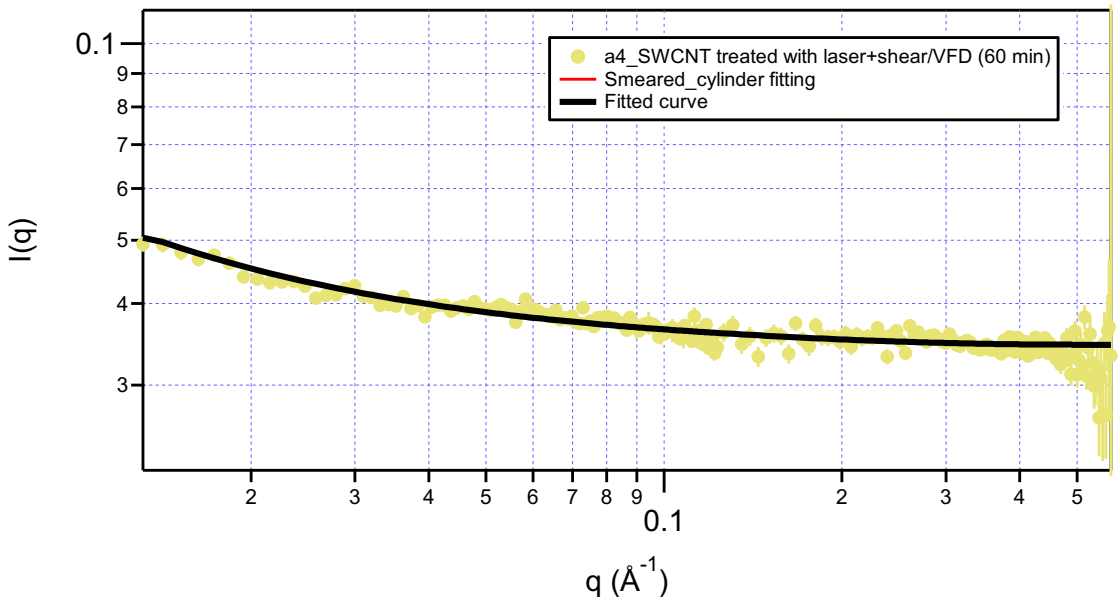

scale	0.00059959	±	0.323132
radius (Å)	7	±	2.6338
length (Å)	1100	±	0
SLD cylinder (Å^{-2})	5.9024e-06	±	0.000740086
SLD solvent (Å^{-2})	3.156e-06	±	0
incoh. bkg (cm^{-1})	0.0345868	±	0.000193535

chisq = 372.465

Npnts = 222 Sqrt(χ ^2/N) = 1.29529

Fitted range = [0,221] = 0.0131333 < Q < 0.570667

FitError = No Error FitQuitReason = No Error

Figure G29 Smeared hollow cylinder fitting for single-walled carbon nanotubes treated with laser and shear 60 minutes

Fit to SmearedCylinderForm,

Data file: a5_comb_ABS

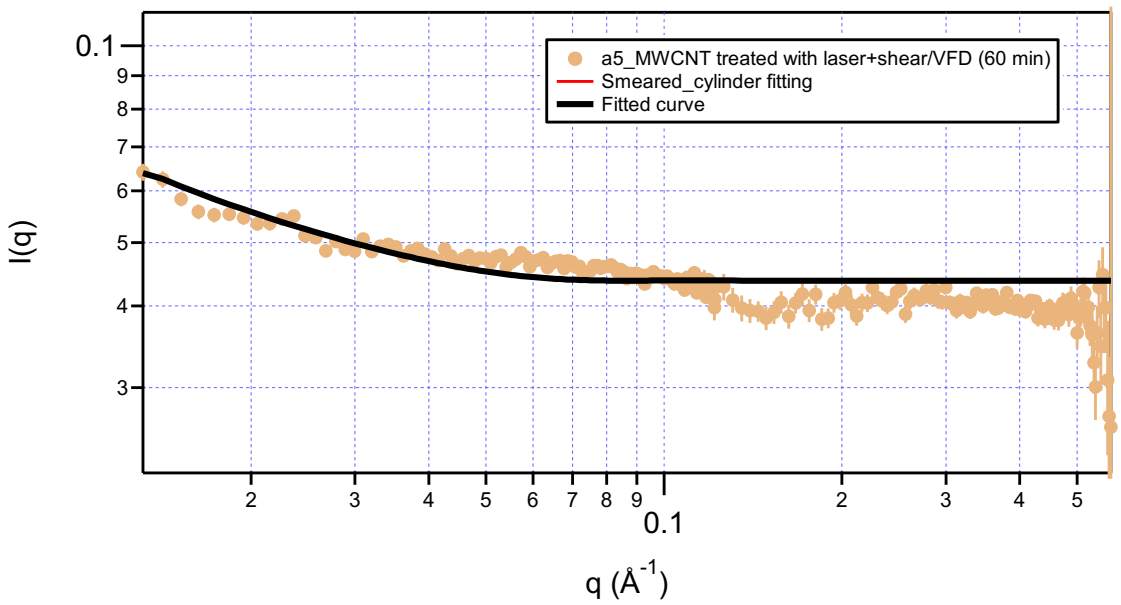

scale	9.24342e-05	±	0.540001
radius (Å)	45	±	1.72077
length (Å)	1710	±	0
SLD cylinder (Å^{-2})	4.42184e-06	±	0.00369752
SLD solvent (Å^{-2})	3.156e-06	±	0
incoh. bkg (cm^{-1})	0.0437142	±	6.81163e-05

chisq = 1616.97

Npnts = 216 Sqrt(χ ^2/N) = 2.73605

Fitted range = [0,215] = 0.0131333 < Q < 0.570667

FitError = No Error FitQuitReason = No Error

Figure G30 Smeared hollow cylinder fitting for multi-walled carbon nanotubes treated with laser and shear 60 minutes

Fit to SmearedCylinderForm,

Data file: a6_comb_ABS

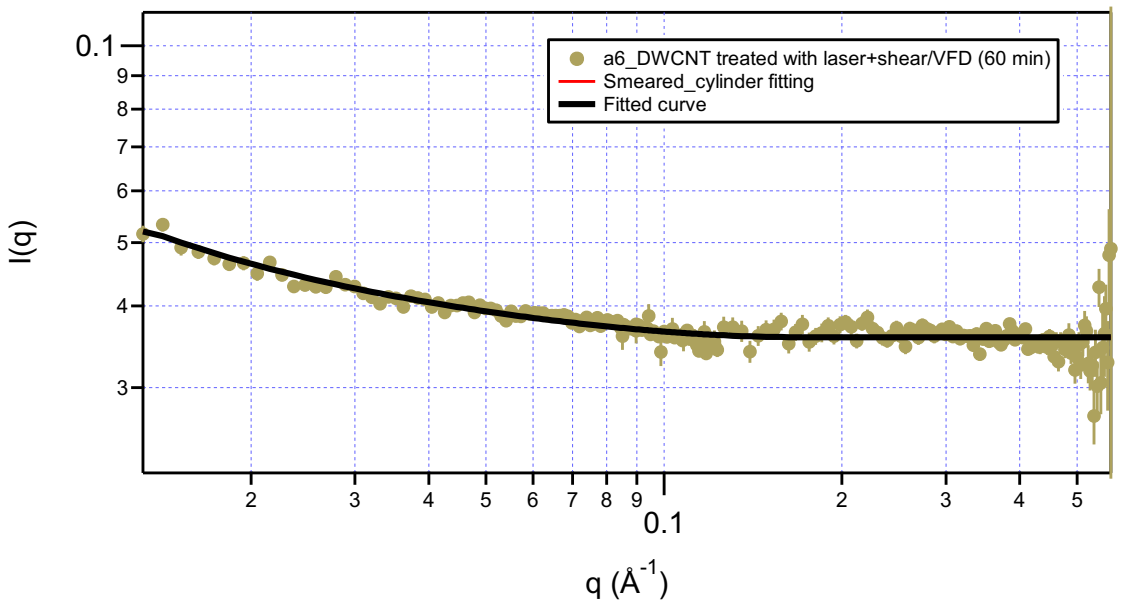

scale	0.000193797	±	0.555824
radius (Å)	20	±	1.22684
length (Å)	1600	±	0
SLD cylinder ($Å^{-2}$)	4.86312e-06	±	0.00244807
SLD solvent ($Å^{-2}$)	3.156e-06	±	0
incoh. bkg (cm^{-1})	0.0357999	±	9.45695e-05

chisq = 316.69

Npnts = 223 Sqrt(χ ^2/N) = 1.19169

Fitted range = [0,222] = 0.0131333 < Q < 0.570667

FitError = No Error FitQuitReason = No Error

Figure G31 Smeared hollow cylinder fitting for double-walled carbon nanotubes treated with laser and shear 60 minutes

References

[1] Dresselhaus, M.S., Dresselhaus, G., Saito, R. & Jorio, A. Raman spectroscopy of carbon nanotubes. *Phys. Rep.* **409**, 47-99 (2005)

[2] Hennrich, F., Krupke, R., Lebedkin, S., Arnold, K., Fischer, R., Resasco, D.E.Kappes,M.M. Raman spectroscopy of individual single walled carbon nanotubes from various sources. *J.Phys. Chem. B.* **109**, 10567-10573 (2005)

[3] Bokobza, L. & Zhang, J. Raman spectroscopy characterization of multiwall carbon nanotubes and of composites. *Poly. Lett.* **6**, 601-608 (2012)

[4] Hubble, L.J., Clark, T.E., Makha, M. & Raston, C.L. Selective diameter uptake of single-walled carbon nanotubes in water using phosphonated calixarenes and 'extended arm' sulfonated calixarenes. *J. Mater. Chem.* **18**, 5961-5966 (2008)

[5] Attal, S., Thiruvengatham, R. & Regev, O. Determination of the concentration of SWCNTs in aqueous dispersions using UV-Vis absorption spectroscopy. *Anal. Chem*. **78**, 8098-8104 (2006)

[6] Pedersen, J.S. Analysis of small-angle scattering data from colloids and polymer solutions: modelling and least squares fitting. *Adv. Colloid Interface Sci.* **70,** 171-210 (1997)

[7] Kline, S. R. Reduction and analysis of SANS and USANS data using IGOR Pro. *J., Appl. Crystallogr.* **2006**, *39*, 895.

APPENDIX H

Supplementary information

Shear induced fabrication of intertwined single walled carbon nanotube rings

Kasturi Vimalanathan, Xianjue Chen and Colin L. Raston*

A systematic evaluation was carried out to determine the optimized conditions required for the organization of the SWCNT rings under shear in the VFD. A dispersion of SWCNTs (0.1 mg/mL) was placed in the VFD tube, 20 mm diameter tube (I.D= 20.000 ± 0.013) and the 10 mm diameter tube (I.D= 7.100 ± 0.013 mm) at different rotational speeds, targeting 3000 rpm, 6000 rpm, 7000 rpm and 8000 rpm, and at different inclination angles, 0°, 30°, 45°, 60°, 75° and 90°.

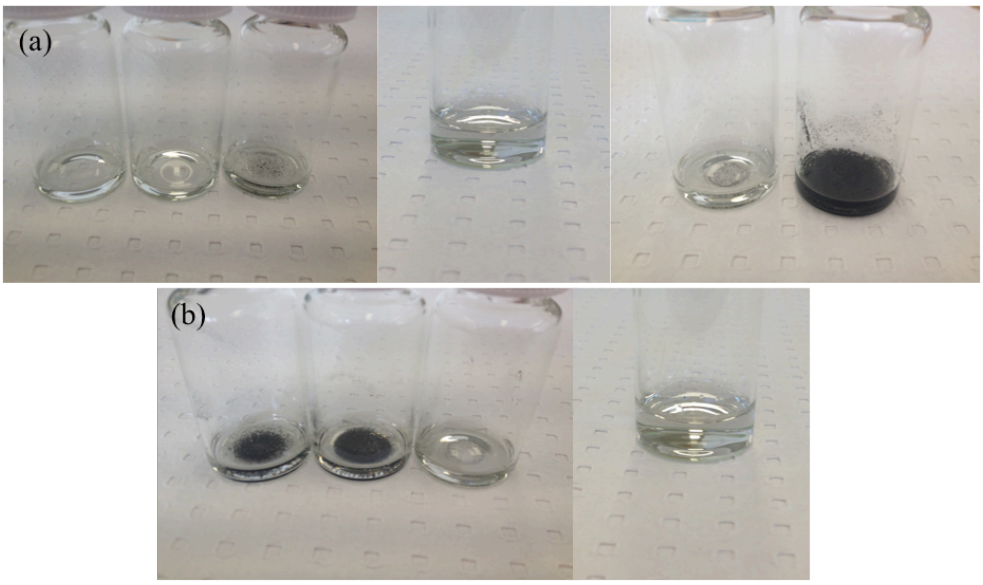

Figure H32 Photographs of the SWCNTs dispersion after the processing under shear; (a) at inclination angles 0°, 30°, 45°, 60°, 75° and 90°, respectively, and (b) at 3000 rpm, 6000 rpm, 7000 rpm and 8000 rpm rotational speeds, respectively (left to right).

The rotational speed of VFD was critical in the formation of the nanorings, with speeds above 6000 rpm effective in forming the nanorings. The highest yield of nanorings was observed at 7000 rpm and 8000 rpm. The rotational speed at 6000 rpm afforded nanorings but in minimal quantity. The choice of inclination angle of the tube was as significant as the choice of rotational speed for the microfluidic processing, which is consistent with other

applications of the VFD[16,17,18,19,20]. At low inclination angles (0° to 30°), there was limited formation of the nanorings. At 60° tilt angle nanorings resulted albeit in low yield, and higher angles (75° and 90°) were ineffective in forming such rings. The optimal conditions for the formation of the SWCNT nanorings is for the tube inclined at 45° and rotating at 7500 rpm.

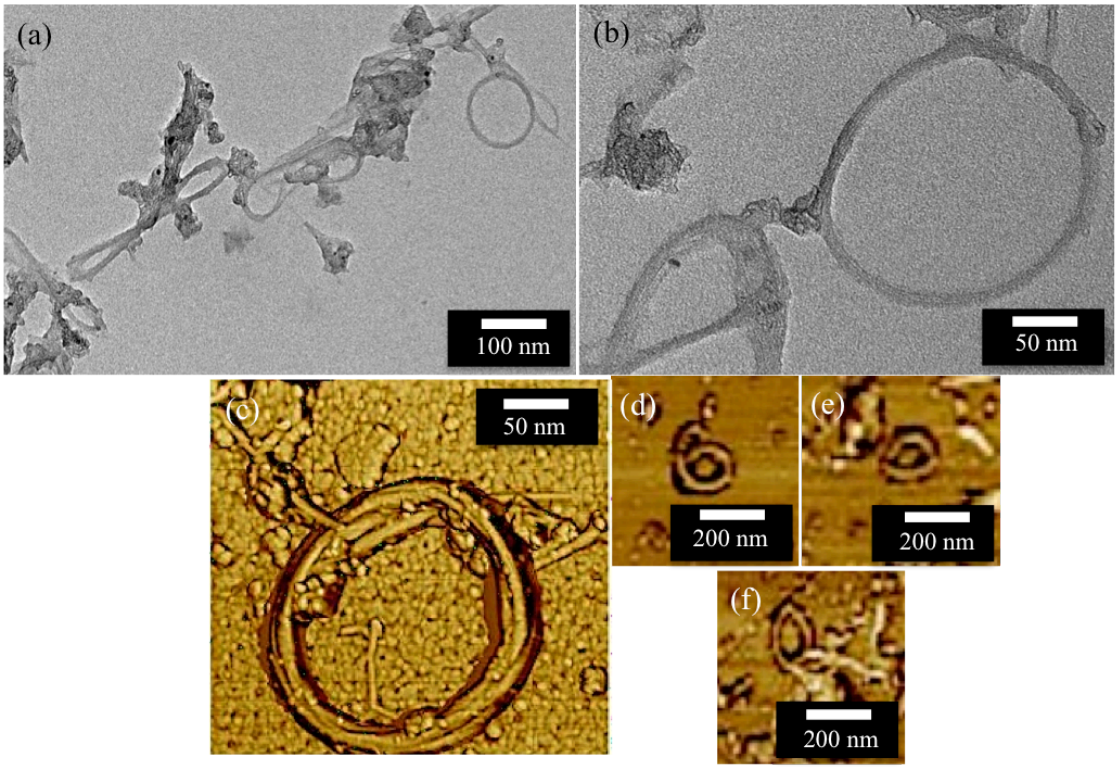

Figure E33 Images of SWCNTs rings 100 to 200 nm in diameter derived from (a) TEM (b) AFM (phase images), (d-f) AFM phase images of single SWCNT appearing to 'bite' their tail

Control experiments:

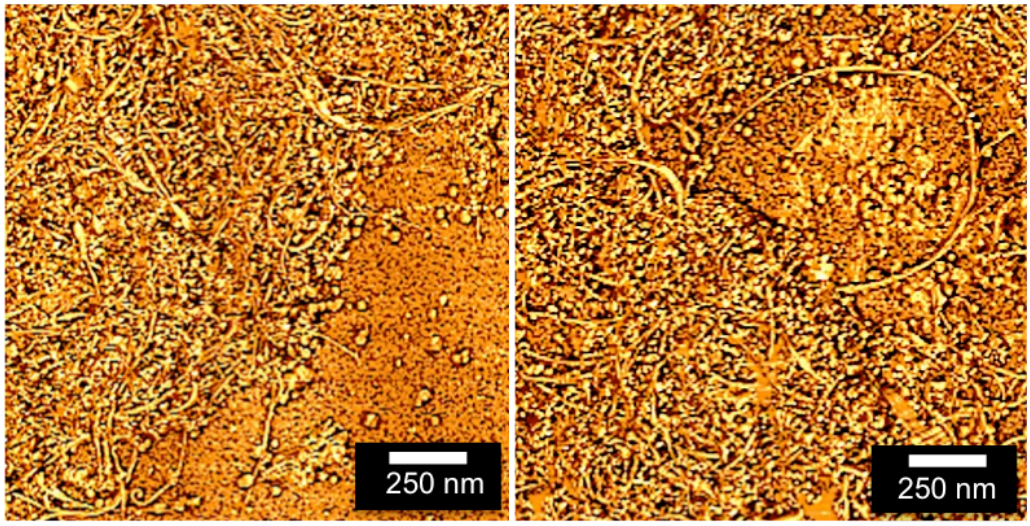

Figure H34 AFM phase images: SWCNT dispersion in toluene/water in the absence of shear (i.e. no VFD processing).

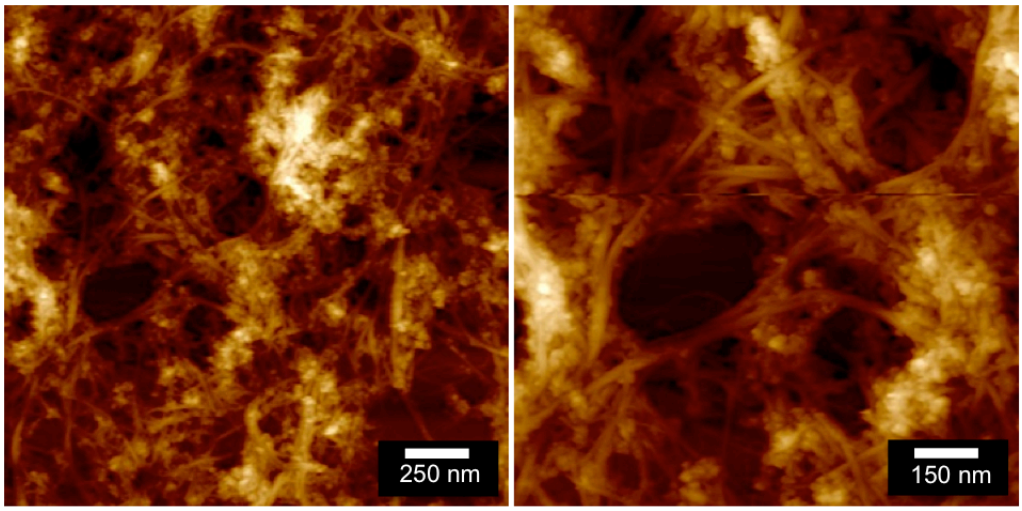

Figure H35 AFM height images: SWCNT dispersion in pure toluene.

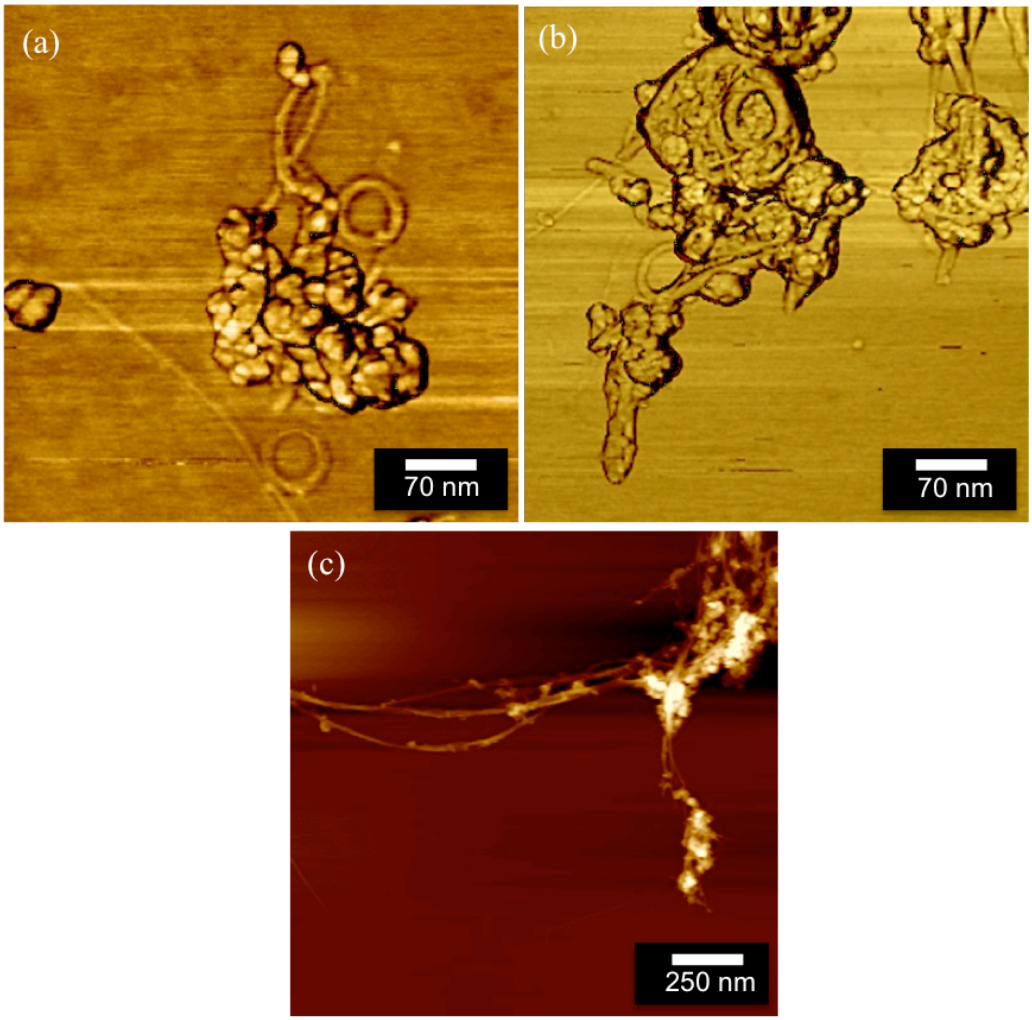

Figure H36 AFM images: (a and b) for a colloidal dispersion drop cast immediately form a mixture under sonication (phase image); (c) for a colloidal dispersion drop cast after sonication (10 minutes) (height image); small amounts of SWCNT rings were noticed immediately post-sonication collapsed back to those in (c). The rings in (a) and (b) are ca 70-90 nm in diameter.